UNIVERSITY OF STRATHCLYDE
DEPARTMENT OF CHEMICAL AND PROCESS ENGINEERING

Particles in Oscillatory Flows: Jamming of Concentrated Particulate Suspensions and the Response of Swimming Algae

Alexander Hope

A thesis submitted to the Department of Chemical and Process Engineering, University of Strathclyde in fulfilment of the requirements for the degree of Doctor of Philosophy

2014

Declarations

‘This thesis is the result of the author’s original research. It has been composed by the author and has not been previously submitted for examination which has led to the award of a degree.’

Signed:

Date:

Acknowledgements

I would like to thank my supervisor Mark Haw for reading through this thesis in great detail.

I would also like to thank Otti Croze and Martin Bees for all their assistance in all things related to algae.

I would also like to thank Claire and Carol Forsyth for inspiring me through their commitment to their research.

Additional thanks to Joy for selling my hats on eBay.

I must also thank Andrew Schofield for supplying colloidal PMMA dispersions to my supervisor at cost value.

Publications

J. Leckie**, A. Hope**, M. Hughes, S. Debnath, S. Fleming, A.W. Wark, R.V. Ulijn and M.D. Haw, Nanopropulsion by Biocatalytic Self-assembly, *ACS Nano*, 2014, 8, 9580-9589.

A. Hope, Ottavio A. Croze, Wilson C. K. Poon, Martin A. Bees,4 and Mark D. Haw, Unexpected Ordering of Swimmer Trajectories in Oscillatory Flows, *in preperation*.

Abstract

This document describes an experimental investigation of two different particle systems under conditions of oscillatory flow. The 1st system being concentrated suspensions of non-motile particles and the 2nd system being dilute suspensions of swimming algae. This document focuses on the study of the jamming of concentrated suspensions of particles (primarily in oscillatory flows), and the response of swimming algae to oscillatory shear flows.

The flow characteristics of concentrated colloidal and granular suspensions are known to display a variety of interesting flow characteristics such as shear thinning and discontinuous shear thickening. These depend on a wide range of parameters such as concentration, particle size, rate of deformation and many more. During the flow of concentrated suspensions, they can change from behaving like a fluid and flowing to behaving like a solid which can fracture or yield. Many aspects of this transition are still not understood. This phenomenon has important applications in process flow of slurries, the development of light weight bullet proof vests and as a dampening fluid within vehicle suspensions.

This thesis shows that when concentrated colloidal and granular suspensions are subjected to oscillatory squeeze film flow, they display reversible local flow field distortions and macroscopic shape changes which are likely related to jamming. It highlights a range of unreported behaviours of suspensions in oscillatory squeeze film flows.

This document also provides rheological data on the discontinuous shear thickening and jamming of a wide variety of different suspensions in both continuous and oscillatory shear flows.

Swimming micro-organisms are currently used in a wide variety of health and cosmetic products. They are also being researched for use in the production of biodiesel. Swimming algae are grown within photo-bioreactors where their swimming characteristics can have a major impact on the reactors overall efficiency. Additionally a major issue in the production of swimming algae is the need for them to be concentrated using centrifugation which is energy intensive.

This thesis shows that in oscillatory shear flows, gravitactic swimming algae can order their swimming directions in the vorticity directions of the oscillating flow field. This has potential applications in the development of a method to encourage micro-swimmers to self-concentrate. Suggestions of other investigations into the ordering behaviour of swimming micro-organisms are also provided.

This document also displays a unique and cheap method for applying oscillatory squeeze film flows while allowing samples to be viewed underneath a microscope. It also makes suggestions on how this method could be enhanced. This device has applications in carrying out squeeze film tests to examine the rheological properties of fluids.

Contents

List of Symbols and Abbreviations

A	Contact area
$Actual\_dm_{solvent}$	Actual mass of solvent added to a particle sediment
A_D	Maximum displacement of the top plate of the shear cell from its initial position
CST	Continuous shear thickening
d	Particle diameter
DST	Discontinuous shear thickening
$\underline{\hat{e}_x}, \underline{\hat{e}_y}, \underline{\hat{e}_z}$	Unit vectors pointing in the direction of a relevant axis
ESC	Electromechanical squeeze cell
F	Force
f_d	Frequency of oscillation
g	Gravity
G'	Elastic/storage modulus
G''	Viscous/loss modulus
k_B	Boltzmann's constant
M_0	Mass of sediment after centrifugation
$\underline{n}$	A unit vector that some algae rotate around due to an intrinsic torque
N	Number of frames
N_1	1st normal stress difference
N_2	2nd normal stress difference
$\underline{r}$	Position vector
r, r_p	Radius of particle
R	Ordering ratio
R_s	Radius of sample
Re	Reynolds number
p	Equivalent pressure
P	Absolute pressure
$\underline{p}$	A unit vector that points in the direction that the cell is swimming in
$P_{Atmospheric}$	Atmospheric pressure
PAM	Polyacrylamide
Pe	Peclet number
$PMMA$	Poly(methyl methacrylate)
$N_{Particles}$	Total number of particles within the system
$OSFF$	Oscillatory squeeze film flow
PSC	Piezoelectric squeeze cell
S	Displacement of bottom plate of electromechanical squeeze cell from its initial position
SMF	Solid mass fraction

SVF	Solid volume fraction
SFF	Squeeze film flow
t	Time
Δt	Lag time
T	Temperature
$Target\_dm_{solvent}$	Target mass of solvent to add
u	Velocity
V	Upward velocity of bottom plate of the electromechanical squeeze cell
v_t	Terminal velocity
V_{System}	Total volume of system
V_P	Velocity of top plate of shear cell
$V_{Particles}$	Total volume of particles within the system
$\underline{X_P}$	Position vector of the centre of the top plate of the shear cell
η	Viscosity of fluid
η_0	Viscosity of suspending fluid
$\lvert\eta\rvert$	Complex viscosity
τ	Stress
τ_p	Peak stress
τ_{MAX}	Maximum stress before sample breakup during discontinuous shear thickening
τ_{xx}	Normal stress on a surface with a normal in the x-direction
τ_{yy}	Normal stress on a surface with a normal in the y-direction
τ_{zz}	Normal stress on a surface with a normal in the z-direction
$\acute{\Gamma}$	Surface tension
$\dot{\gamma_c}$	Critical shear rate at which shear thickening begins
$\dot{\gamma}$	Rate of deformation
$\dot{\gamma_R}$	Rate of deformation at sample edge
ρ_c	Density of colloidal particles
$\rho_{solvent}$	Density of dispersing medium
$\Delta\rho$	Density difference
σ_{normal}	Upthrust force on upper plate during shear
μ_k	A fitting constant
Φ	Solid volume fraction of sediment
Φ_{Solid}	Solid volume fraction of total suspension
Φ_C	Critical solid volume fraction of suspension
Φ_T	Target solid volume fraction of suspension
ω_D	Angular frequency of oscillation
ω_G	Magnitude of gravitactic torque
ω_H	Magnitude of intrinsic torque
$\underline{\omega}$	Vorticity vector

Ω	Angular speed
$\underline{\Omega}$	Angular velocity

Thesis Layout

As a general outline, this thesis begins with 3 introductory chapters. These introduce the reader into the areas of the jamming of concentrated suspensions, oscillatory flows and the response of swimming algae to complex flows. It then describes the techniques used to examine both concentrated suspensions of non-motile particles and swimming microalgae, which primarily took place in oscillatory flows. It then finishes with chapters describing the results obtained from these investigations.

Chapter 1 begins by describing some of the general features of colloidal suspensions and the rheological behaviour of particle suspensions in general. It then describes some of the literature surrounding the jamming and discontinuous shear thickening of concentrated particle suspensions. This is relevant to chapters 5 and 6.

Chapter 2 begins by briefly describing parallel disk shear flow rheometry. It then goes on to describe mathematically oscillatory parallel plate shear flow for Newtonian fluids which is relevant to chapters 3, 4 and 7. It then goes on to mathematically describe oscillatory squeeze film flow for Newtonian fluids which is relevant to chapters 4, 6 and 7.

Chapter 3 starts with a description of what algae are in general and their industrial significance. It then goes on to describe features of swimming algae and in particular the species *Dunaliela Salina*. The chapter ends with a model describing the motion of gravitactic algae and an example of how this model could be applied to the oscillatory parallel plate shear flow described previously in chapter 2.

Chapter 4 concerns the experimental apparatus and procedures used throughout the PhD. It begins by describing the design of electromechanical squeeze cell and how it was calibrated. It then goes on to describe the electromechanical shear cell and the piezoelectric squeeze cell and their relevant procedures (these were also used to induce oscillatory flows upon suspensions of algae). It then discusses the materials used in this PhD and how they were prepared. It finishes by describing particle tracking and how

particle tracking data was analysed to identify the swimming directions of *D.Salina* in oscillatory flows.

Chapter 5 presents results from continuous shear and large amplitude oscillatory shear experiments that were carried out on a range of concentrated colloidal dispersions and granular suspensions. These were obtained using a strain controlled rheometer. The results are then compared to similar experiments involving different particle systems in the literature.

Chapter 6 displays results obtained from applying oscillatory squeeze film flow on concentrated colloidal and granular suspensions. This was done using the electromechanical squeeze cell described in chapter 4. The results are then compared with results from the previous chapter and are discussed in the context of the surrounding literature.

Chapter 7 shows the results obtained from subjecting *Dunaliela Salina* to oscillatory shear flows in a range of experimental setups detailed in chapter 4. The results are then discussed in the context of the surrounding literature.

Chapter 8 states the overall conclusions that can be drawn from the work presented in this thesis. Future work is also suggested for anyone who may be interested in carrying out similar works.

Chapter 1 Introduction to the Jamming of Particulate Suspensions

1.1 Chapter Summary

In this chapter a general introduction to the stress induced jamming of colloidal dispersions and granular suspensions is given. It starts with an introduction to the jamming of particulate systems and why they are relevant to study. It then goes on to examine the literature surrounding the properties of concentrated suspensions and in particular colloidal dispersions. The rest of the chapter discusses the flow behaviours of particulate systems and in particular the shear thickening and jamming of particle suspensions.

1.2.1 A Brief Introduction to Jamming Concepts

Colloidal dispersions are loosely defined as consisting of solid particles of around 0.01-10 μm in size dispersed in a fluid. In this case, size usually refers to the diameter of its smallest significant dimension. Granular suspensions are composed of particles larger in size than around 10 μm, while nanoparticle dispersions are composed of particles smaller than 0.01 μm [1,2]. The reasons behind these distinctions are given in section 1.3.

In the literature there are a variety of different definitions for what a jammed system is. One definition of a jammed substance is as an amorphous solid (one that does not possess a long range order) that deforms elastically under an applied stress that is lower than the yield stress, but can flow like a fluid when the yield stress is surpassed. Yet another definition is a material that is microscopically disordered yet can macroscopically support its own weight while only deforming elastically [3-5].

It is important to mention that emulsions (liquid dispersed in another immiscible liquid) and foams (a gas dispersed in a liquid) are also capable of possessing a yield stress and can therefore also be referred to as jammed materials [5].

With these definitions in mind, jamming can be loosely defined as the conversion of a fluid system into such a jammed system; however there are two slightly different definitions on the jamming of colloidal and granular systems that can be found in literature [6].

Jamming is therefore broadly defined by some authors as the non-equilibrium conversion of a fluidic system to an amorphous system with a yield stress. This is characterised in colloidal and granular suspensions of particles by most particles becoming effectively trapped and unable to move relative to each other easily due to the lack of local free volume [3,4].

Some authors define jamming more restrictively as the arrest of a flowing particulate system of a volume fraction below the random close packing fraction. This is due to the formation of load bearing structures within the system due to the application of stress. This is a different and more restrictive view point which is probably better suited to tackle the problem of jamming of industrial slurries and suspensions during flow caused by an applied stress [7-10].

Colloidal dispersions that have undergone a jamming transition can sustain forces applied to them by transmitting forces through chains and/or clusters formed by inter-particle contact. This is described later in section 1.6. Jammed particulate suspensions are often referred to as fragile; this is because their structures can be very heterogeneous and although they may support a stress in one direction they may break apart if stress is applied in another direction [7,11].

The main questions around the jamming of suspensions are how, why and under what conditions is it likely to occur to a given system if at all [11,12]. The relationship between jamming and discontinuous shear thickening (DST) where the viscosity of a suspension increases drastically with shear rate is also still to be definitively identified [13-16].

1.2.2 Why is the Jamming of Particulate Systems Important to Industry?

More than 40% of the value added to products from the chemical industry is linked to particle technology and 50% of all products sold are either contain colloidal or granular particles or involve the processing of granular/colloidal materials at some stage of production [17].

Examples of finished products that consist of particulate suspensions are; toothpaste, latex paint, pen ink, sunscreen, soybean paste and many more.

All of the products mentioned above and many others such as pharmaceutical tablets, will inevitably at some point have a stage that involves processing the particulate systems in some way (e.g. coating, mixing and compression), or at the very least involves the transportation of a particulate system through pipes or channels.

When the solid volume fraction of particulate systems is high, the system can change from responding like a fluid to responding like a solid. As this has the potential to cause blockage in pipes and clog equipment and reduce productivity, it would be beneficial to processing industries to gain a better understanding of how and why it happens. Controlling the occurrence of discontinuous shear thickening and jamming is also important in drilling for oil and in designing of new cement formulations [18-20].

There have also been attempts to make use of particulate suspensions that can jam and unjam to create useful products. One product being developed is a gripping arm capable of holding almost any shape of object. It essentially consists of a bag containing granular particles dispersed in a gas. The bag and its contents can be made to flow around an object to be picked up while in the fluid phase, and then made to contract and jam by sucking the gas out of the bag. The contents of the bag can then transmit forces allowing the object to be picked up [21,22].

There have also been attempts to make use of the ability of concentrated suspensions to show jamming and shear thickening behaviour only when the applied shear rate is fast enough. One application of this has found its place in bullet and stab proof vests and other personal protection equipment that only jam under great stress such as when struck by a bullet or knife [23-27]. This is currently being researched by many of the world's largest defence companies such as BAE systems, although similar products that use polymers instead have been in use since 2005 [28]. It has also been shown by the United States military that impregnating Kevlar with colloidal particles can greatly improve its effectiveness [24].

1.3 Colloidal Systems

Colloidal systems are comprised of at least two different phases with one phase dispersed within another. In order to meet the definition of colloidal system one of these phases must have a significant dimension less than approximately 1-10 microns in size but larger than 10 nanometre in size [2,29].

The size restriction is in place to ensure the following:

1. That the dispersed phase has a large surface area.
2. That the force of gravity on the particle is weak enough that Brownian motion and forces imposed by the dispersion medium are still significant.
3. That the particles are large enough that interactions between them and the molecules of the dispersing medium are negligible and quantum effects can be ignored. Additionally the dispersing medium can be considered a continuum relative to the colloidal particles.

The table below shows examples of multi-phase colloidal systems

Dispersing Medium	Dispersed Phase	Term	Industrial Examples	Natural Examples
Gas	Liquid	Aerosol	Febreeze, Deodorant	Clouds, mist
Gas	Solid	Aerosol	Some antiperspirants	Volcanic Smoke
Liquid	Gas	Foam	Shaving foam, whipped cream	Vacuoles
Liquid	Liquid	Emulsion	Mayonnaise, margarine	Milk
Liquid	Solid	Colloidal Sol or dispersion	printing ink, toothpaste	Mud, magma
Solid	Gas	Solid Foam	Styrofoam, Insulating foam	Zeolites
Solid	Liquid	Porous material or solid emulsion	Ice cream, Bituminous road paving	Opals, pearls
Solid	Solid	Solid Suspension	Some alloys and chocolate	Wood

Table 1 Examples of the various types of colloidal systems [2,29].

1.4 Colloidal Dispersions

Colloidal dispersions are systems in which solid colloidal particles are dispersed in a fluid medium. They differ from granular suspensions in that Brownian motion is significant which hinders sedimentation and allows particles to diffuse through the dispersion. This difference is best shown by considering the rate of sedimentation compared to the rate of diffusion of a given particle [1,2].The terminal velocity of a sedimenting spherical particle can be estimated from Stokes law as shown by Equation 1, where r_p is the radius of the particle, g is the acceleration due to gravity, $\Delta\rho$ is the density difference between the fluid and the particle and η is the fluid viscosity. This shows that the larger the particle, the faster it sediments:

$$v_t = \frac{2\Delta\rho r_p^2 g}{9\eta}$$

Equation 1

The mean squared displacement (MSD) is a measure of the average displacement of a particle due to diffusion. The MSD of a spherical particle can be estimated using Stokes-Einstein-Sutherland equation as shown in Equation 2, where k_B is Boltzmann's constant, Δt is the lag time and D is the diffusion coefficient. This shows that the smaller the particle the higher the distance travelled by diffusion in the time Δt:

$$\langle r^2 \rangle = 6D\Delta t = \frac{k_B T}{\pi\eta r_p}\Delta t$$

Equation 2

As an example, over a period of 10 seconds and at room temperature, a colloidal PMMA particle of 0.1 µm in radius suspended in decalin at terminal velocity will have sedimented a distance of $3.1\text{x}10^{-4}$ µm. Over the same period, the square root of the MSD would be $8\text{x}10^{-3}$µm. A PMMA particle of 10 microns in radius suspended in decalin at terminal velocity will sediment a distance of 3.1 µm over 10 seconds while the root of the MSD over the same period would only be $8\text{x}10^{-4}$µm. This example shows that Brownian motion becomes insignificant as the suspended particles in a suspension approach granular sizes. The length scale over which gravity and sedimentation are important can be estimated by the scale height shown in Equation 3. This is the ratio of the thermal energy of a particle

compared to the gravitational force acting on the particle [30]. As the particle size increases, the scale height decreases meaning that sedimentation becomes more important over smaller and smaller length scales.

$$z_0 = \frac{3k_B T}{4\pi \Delta \rho r_p^3 g}$$

Equation 3

1.4.1 Colloidal Interactions

Colloidal particles can interact with each other by a variety of different mechanisms.

Surface Forces

These are forces that come into effect when the surfaces of different particles come close enough together, where the surfaces may be charged, have adsorbed ions, surfactants or polymer molecules [1,31].

Dispersion Forces

These result from quantum mechanical effects caused by fluctuations in the electron clouds surrounding atoms or molecules of which the colloidal particles are made and are usually referred to as van der Waals forces. In a colloidal dispersion it is possible to stabilize colloidal particles against aggregation due to van der Walls forces by matching the refractive index of the medium to that of the dispersed particles. The range of these forces is very short, of the order 10nm however these forces are usually many times larger than the thermal energy of colloidal particles due to Brownian motion, meaning that they can cause aggregation [32].

Depletion Forces

This force is present in situations where colloidal particles are surrounded by soluble polymer molecules or smaller particles that cannot access the space between larger colloidal particles within a colloidal dispersion. This effectively results in an osmotic pressure that can push the larger colloidal particles together [1].

Hydrodynamic Interactions

These arise from disturbances in the flow field surrounding a particle caused by another particle. Hydrodynamic interactions cease to exist if the flow field is perfectly stagnant. In the study of shear thickening and jamming of colloidal dispersions and granular suspensions, this type of interaction is extremely important**.** A great deal of work on characterising hydrodynamic interactions has been done in the literature [31,33,34].

Friction Forces

If the surfaces of neighbouring particles make physical contact then friction can become significant depending on the friction coefficient of the particles. Additionally, as suspensions become highly concentrated, inter-particle friction can become the dominant form of interaction between particles within a suspension [15,35,36].

1.4.2 Stabilization of Colloidal Dispersions

If a colloidal dispersion is termed unstable it means that any repulsion forces between the particles are insufficient to overcome attractive forces causing them to stick together in the event of collisions over a given time period. This causes particles to aggregate irreversibly. Even van der Walls attractions are enough to cause aggregation if no stabilisation forces are present. Dispersions can be stabilised through electrostatic repulsions and steric hindrance [2].

Steric Stabilisation

This is where particles are coated with strands of long chain polymers. Only one end of the polymer is attached to the particle and the other end is free to move in the dispersing medium by Brownian motion. The polymer segments are attached by chemicals bonds or physical interactions. If particles come close enough together such that their polymer strands overlap, they interact with each other resulting in a region where the polymer concentration is high. This results in an osmotic force that acts to keep the colloidal particles apart. The magnitude of this force is dependent on the polymer graft density, the polymer length and the strength of the interactions between the polymer and the solvent. For the polymer to stabilize the dispersions, the solvent must be a good solvent for the

polymer strands so that polymer strands don't attract each other causing flocculation and phase separation [32].

Electrostatic Double Layer Repulsion

When colloidal particles are dispersed in a solvent they may obtain a surface charge due to adsorbing ions from the solution or due to adsorbed chemical groups ionizing. This can result in a given colloid being surrounded by a region of dissolved free ions that effectively neutralises the charges on the surface of the colloidal particle.

The colloids are therefore essentially surrounded by a region in which the ion concentration is higher than in the bulk solution. When such colloidal particles come close enough together it creates a region with an even higher ion concentration. This results in an osmotic pressure that acts to separate the colloidal particles [1,37].

Electrostatic Stabilisation

Simply put, if the surfaces of particles all become either positively or negatively charged, then this will provide a force to keep them apart. This is significant when charged colloidal particles are dispersed in a non-polar solvent where the double layer is insignificant.

1.4.3 Volume Fractions and Packings of Hard Spheres

An important variable used in the examination of the rheological properties of colloidal dispersions and granular suspensions is the solid volume fraction or packing fraction ϕ_{solid} . This is the fraction of the volume of the total system which is occupied by solid particles. This is shown in Equation 4, where $V_{Particles}$ is the volume of solid particles within the system and V_{System} is the total volume of the system:

$$\phi_{solid} = \frac{V_{Particles}}{V_{System}}$$

Equation 4

If the particles are spherical, then the solid volume fraction is given by Equation 5 where $N_{Particles}$ is the number of particles within the system:

$$\Phi_{solid} = \frac{4r_P^3 N_{Particles}}{3V_{System}}$$

Equation 5

This parameter has a huge effect on the flow characteristics of a particulate system. At low volume fractions of less than 0.1, the viscosity of a particulate suspensions of spherical particles can be estimated well by Einstein's equation assuming Stokes flow. Einstein's equation is shown below in Equation 6 where η is the suspension viscosity and η_0 is the viscosity of the liquid medium.

$$\eta = \eta_0(1 + 2.5\phi_{solid})$$

Equation 6

At higher volume fractions predicting the shear viscosity of suspensions and dispersions at a given set of flow conditions becomes extremely complicated due to many body hydrodynamic interactions. Throughout the literature there are many examples that show how the viscosity of particulate systems diverges as the solid volume fraction increases [1,2,31].

Random Loose Packing (RLP) Volume Fraction

This is the lowest volume fraction for which a particulate system is mechanically stable against gravity. This means that it can support its own weight. The RLP is poorly defined as it depends to some extent on the attractive forces between the particles as well as the density difference between the continuous and dispersed phases. The lowest value is for spherical particle suspensions is said to be around 0.55 by many authors [38,39]. Some authors however argue that there is no such thing as a lowest packing fraction [40].

The RLP could therefore in a sense be related to the yield stress of the system. Perhaps an alternative definition is the volume fraction for which the yield stress of the system is high enough to resist the gravitational stress on the system.

Random Close Packing (RCP) Volume Fraction

This is the densest packing of spheres having a random structure or the densest packing of non-crystalline spheres where the particles have no room to move. It is defined as a jammed state as particles are unable to move relative to each other. This is quoted as approximately 0.64 for a system of mono-disperse spheres by a large number of authors but no exact number has yet to be given [17,41,42].

Torquato's group has done work on the jamming of hard sphere packings which focuses on how closely packed a particulate system has to be before it can be considered permanently jammed without application of any stress [43,44].

They defined a given particle as being jammed if it cannot be translated while fixing all the positions of all the other particles in the system. They therefore defined the entire system as being jammed if each particle and each surrounding particle is jammed. The volume fraction at which this occurs is approximately equal to the RCP.

Critical Jamming Volume Fraction

This is the solid volume fraction at which a particulate system obtains a yield stress denoted by ϕ_C. This typically takes a value of approximately 0.5-0.6 for spherical particles [31,45]. This is important as it has been proposed that discontinuous shear thickening only occurs in particulate systems with volume fractions above and around ϕ_C [46]. Work carried out by Egres and Wagner shows that the value of ϕ_C for a given suspension is

extremely sensitive to the aspect ratio of its constituent particles, while as the aspect ratio increases the packing fraction required for DST decreases [46,47].

1.4.4 Crystallization of Colloidal Dispersions

Non-interacting hard sphere colloids dispersed in a fluid can spontaneously undergo crystallisation to increase the entropy of the system. By forming an ordered arrangement, the colloidal spheres on average obtain a greater free volume in which they can diffuse around than when the particles are arranged in a disordered state as is shown in Figure 1 below [30,32,48].

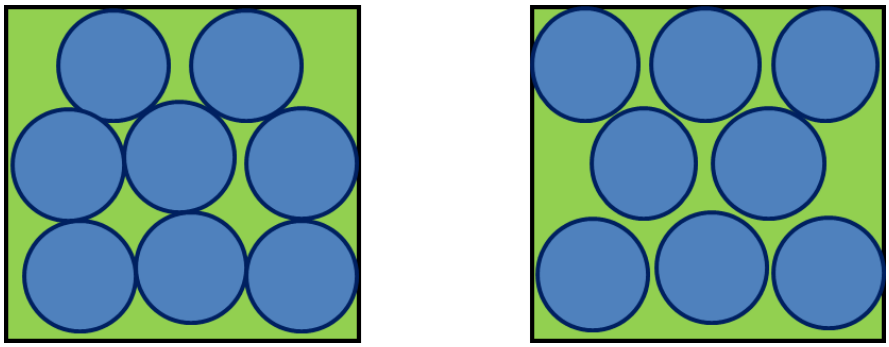

Figure 1 Illustration of how each particle can obtain greater local free space to explore when the system crystallises (forms an ordered arrangement).

The system gains greater entropy due to the increase in available volume than it loses configurational entropy due to the system gaining long range order[1].

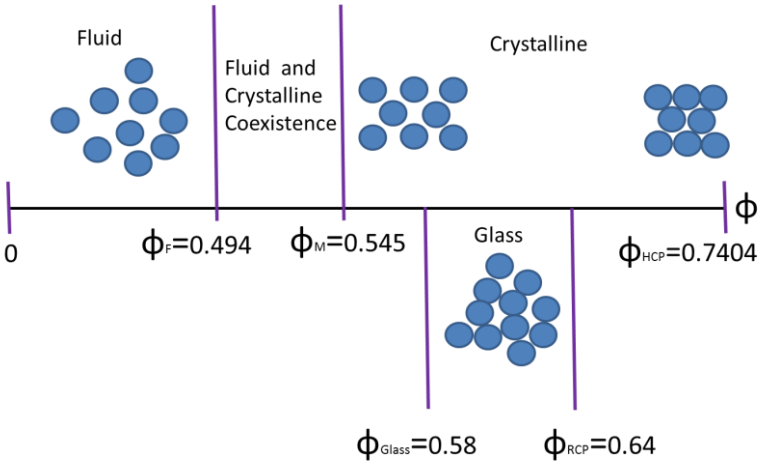

Figure 2 Adapted from [49]. This shows the possible phase changes of hard sphere colloid dispersions with increasing volume fraction.

At high solid volume fractions, dispersions of hard sphere colloidal particles can adopt a long range crystalline structure. It should be noted that the absolute maximum volume fraction obtainable for monodisperse hard spheres is well known to be 0.7404 which is achieved by the face centred cubic (FCC) or hexagonally close packed (HCP) crystalline arrangement [1]. Crystallisation in this case is referring to the point that the particle system obtains a long range order and this crystallisation transition is an order-disorder transition and not a liquid solid transition [1,30,32].

As is illustrated by Figure 2**,** it has been reported that mono-disperse colloidal dispersions with a solid volume fraction below 0.494 (referred to as the freezing volume fraction) have a disordered structure. However once the volume fraction has passed this threshold volume fraction of around 0.494 a phase transition occurs where the dispersions separates into 2 phases one of which has a volume fraction of 0.494 and the other has a volume fraction of 0.545 (referred to as the melting volume fraction). Above a global volume fraction of 0.545 the dispersion can become fully crystalline [32,48].

It is more correct to say however that crystallisation is thermodynamically favourable above a certain volume fraction. The particles will only crystallise if they are given enough time to rearrange themselves.

It is theoretically possible given a long enough time period for a dispersion to crystallise up to a volume fraction of 0.7404. However initially disordered hard sphere suspensions above a volume fraction of around 0.58 cannot form a crystalline structure in practice due to the particle's inability to jump into the necessary positions. Only up to this volume fraction can the suspension form a crystalline structure as they have the necessary space to reach the most thermodynamically stable arrangement [5].

1.4.5 Glass Transition of Colloidal Dispersions

As the solid volume fraction of dispersions of solid colloidal particles approaches the value of around 0.58, colloidal dispersions can undergo the colloidal glass transition where the effects of Brownian motion can no longer move particles past their closest neighbours. This is because insufficient free volume is present and in order for a given particle to move it requires co-operative motion of many other particles as is shown by Figure 3 below.

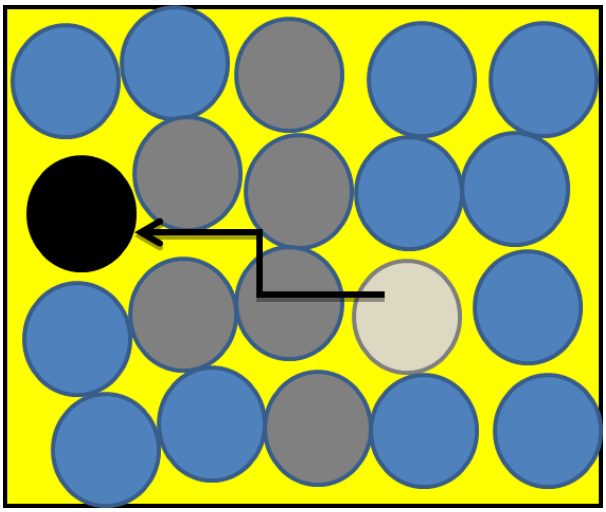

Figure 3 For the white particle to move to the position where the black particle is, it requires the co-operative rearrangement of most of the grey particle which is statistically very unlikely to happen spontaneously.

As the volume fraction increases the ability of the particles to re-arrange themselves decreases. It has been shown by microscopy that near the glass transition, at any point in time the particles that are moving to the greatest extent always do so only when their neighbours are moving in the same direction [5,30]. As glassy substances are not in a state of equilibrium, as time goes on they are known to slowly age (change their structure) which results in their physical properties changing over long enough time periods [1,30,50].

This colloidal glass transition resembles the glass transition that takes place in simple pure molecular liquid if cooled at a rate sufficiently greater than the speed at which the liquids molecules can re-arrange themselves into their crystallisation positions. If molecules lack the vibrational energy to jump out of their initial positions then they are effectively stuck in a trapped state as are colloidal particles in a dispersion of high enough volume fractions [1].

The glass transition of colloidal dispersions is also characterised in the rheological sense by the relaxation time and viscosity of the dispersions increasing extensively [30]. The glass transition is relevant to the discontinuous shear thickening and jamming of colloidal dispersions because it is at these high volume fractions that these effects are most prominent [51].

Colloidal glasses are formed by increasing the solid volume fraction beyond 0.58 rapidly (by centrifugation for example as will be discussed in chapter 4) which bypasses the crystallisation region as the particles are too crowded together for them to adopt a long range ordered arrangement. It has been suggested that a slight poly-dispersity between the particles is required in order to achieve the glass transition as it essentially inhibits the suspension's ability to crystallise [5].

1.5 General Rheology of Concentrated Dispersions

Colloidal dispersions show a variety of complex non-Newtonian behaviour such as shear thinning, shear thickening, viscoelasticity, and non-zero normal stress differences. Descriptions of each of these effects will be given along with explanations taken from the surrounding literature as to why they occur. It should be noted that flocculated colloidal dispersions can show other non-Newtonian behaviour such as thixotropy but this is not relevant to this thesis as dispersions under investigation are stabilised [31].

The most distinctive feature of the rheology of concentrated colloidal dispersions is that an individual sample can give a Newtonian, shear thinning or shear thickening response depending on the applied stress or rate of deformation due to changes in the microstructure of the system. This is illustrated in Figure 4[31]:

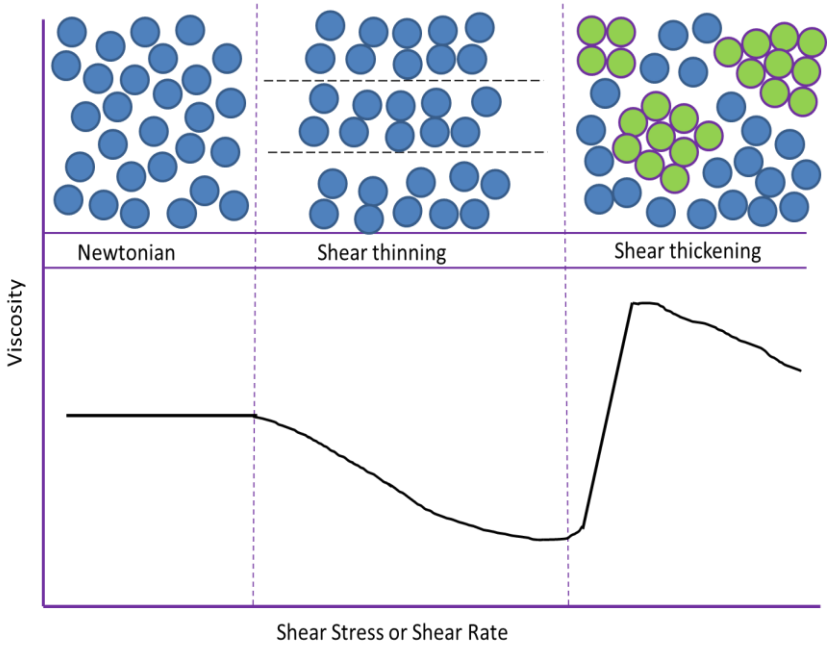

Figure 4- Illustration of changes in microstructure and viscosity of colloidal dispersions commonly observed with changes in the applied stress [31].

At very high shear rates and applied stresses it is possible for some particulate suspensions to even undergo a change from showing shear thickening behaviour to showing shear thinning behaviour again. This is due to the deformation of the constituent particles within the system [24].

1.5.1 Non-Zero Normal Stress Differences of Colloidal Dispersions

In this subsection, normal stress differences are briefly discussed as they are mentioned frequently throughout this thesis. When a Newtonian fluid undergoes pure shear flow between two parallel plates due to movement of the top plate, shear stresses are produced within the fluid that act to drag adjacent layers along in the direction of the applied shear. Excluding hydrostatic pressure there are no other stresses present in this situation. Some fluids such as concentrated suspensions however, generate normal stresses even when subjected to pure shear flows. These stresses are illustrated in Figure 5. In practice normal stress differences are measured rather than direct normal stresses.

The 1st normal stress difference (NSD) is given by:

$$N_1 = \tau_{XX} - \tau_{YY}$$

The 2nd NSD is given by:

$$N_2 = \tau_{YY} - \tau_{zz}$$

Where τ_{XX} is the normal stress on a plane where the normal points in the direction of the shear stress. τ_{YY} is the normal stress on a plane where the normal points in the direction of the velocity gradient. τ_{ZZ} is the normal stress on a plane where the normal points in the direction of the vorticity [52]. For a Newtonian fluid, the values of the 1st and 2nd NSD are zero.

The 1st NSD is commonly observed during the shear of concentrated colloidal and granular suspensions. If the 1st NSD is positive, this means that during simple shear flow it has the effect of pushing the plates apart as if to increase the gap distance [53]. The 1st NSD can be measured using a plate-plate or cone and plate rheometer by measuring the normal force being exerted on the plate or cone by the sample as it is sheared [31,52]. The 2nd NSD is difficult to visualise and measure and so it is rarely mentioned in literature compared to the 1st NSD which is relatively easy to measure.

At low to moderate shear rates, colloidal dispersions have been observed to generate positive 1st and 2nd normal stress differences due to the presence of viscoelasticity. However it has been observed that both of the NSD's become negative at higher shear

rates. For non-Brownian suspensions under shear, the 1st and 2nd normal stress differences are generally both negative and of comparable magnitude [31].

At high volume fractions however the 1st NSD of colloidal and granular suspensions has been observed to become large and positive during discontinuous shear thickening (DST) by Lootens and Fall [15,54]. This is likely caused by dilation of the sample being sheared exerting an upward force on their rheometer. It has been proposed that DST and stress induced jamming are caused by presence of constraints that can act against the large positive NSDs produced at high rates of deformation in particulate systems [10,13]. This will be discussed in more detail later in this chapter. In literature and in the rest of this thesis, it is generally the case that when the term normal stress is used it is referring to the upthrust that a sample is exerting on a top plate during shear flow.

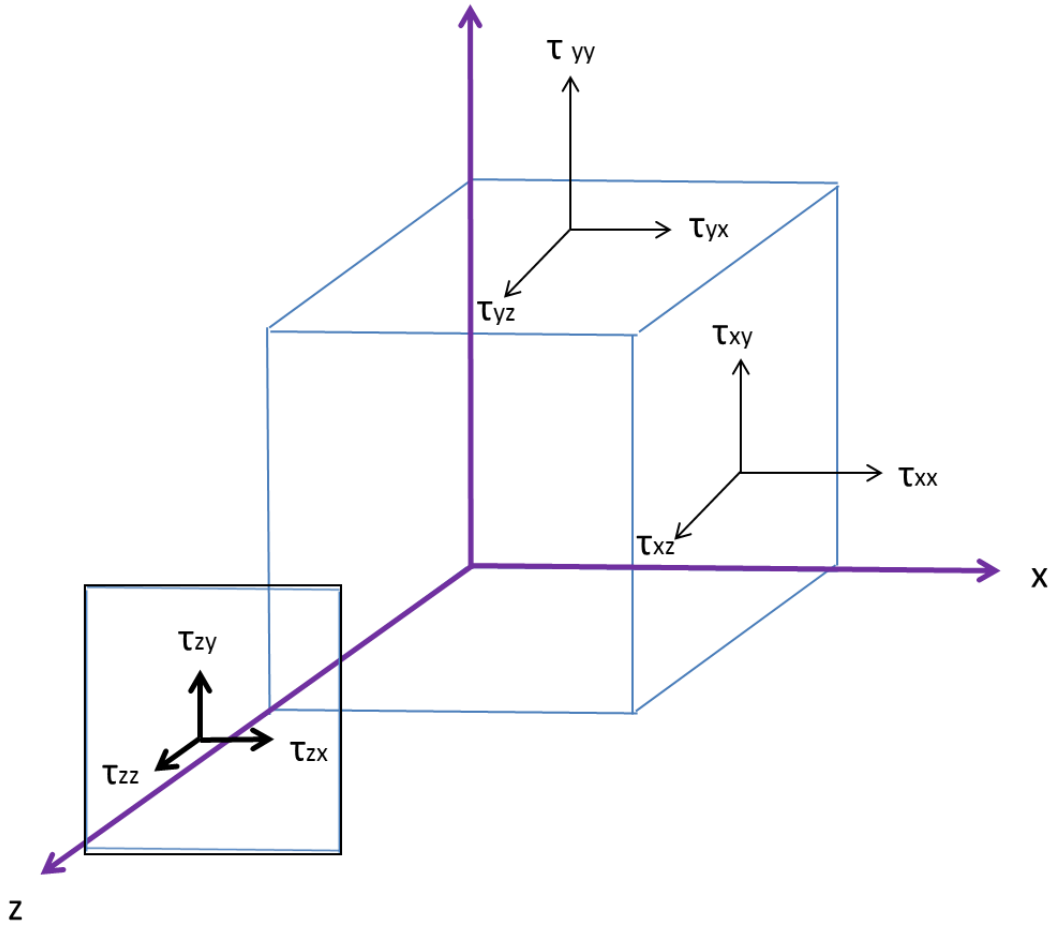

Figure 5 Diagram representing how stress can be defined with a material at a point. The normal stress terms can be thought of as acting perpendicular on a surface as to stretch or compress the cube which represents and infinitesimal volume within a fluid. The 1st subscript designates the direction of the normal to the plane and the 2nd subscript designates the direction of the force acting on the plane.

1.5.2 Shear Thinning

Shear thinning is the term applied to a material that shows a decrease in shear viscosity as the shear rate increases. Some materials are also said to be extensionally thinning if their elongational viscosity decreases as the rate of elongation increases. Shear thinning is sometimes referred to as inverse plasticity, and many products are engineered to have this property so that they are solid like at rest but still able to flow under a weak stress. Examples of this are shampoos and liquid detergents [24].

Shear thinning is an effect most commonly observed while shearing polymer solutions but is also commonly displayed by particulate suspensions within certain ranges of shear rates. It is associated with changes in microstructure of the material being deformed. This occurs when the rate of deformation surpasses the rate at which the material can return to its equilibrium state. This is best characterised by the dimensionless group known as the Peclet number. In the rheology of colloidal dispersions, the Peclet number is defined as the ratio of the rate of the applied deformation of the material to the rate of diffusion of the materials constituent particles.

$$Pe = \frac{Shear\ Rate}{Diffisive\ Transport\ Rate} = (Relaxation\ Time) \times (Shear\ Rate)$$

Equation 7

The relaxation time as applied to colloidal dispersions is essentially the time it takes a particle to diffuse a distance equal to its own radius (denoted by τ_D) as shown below in Equation 8, where r_p is the radius of the particle, η_0 is the dispersing fluid viscosity, D is the diffusion coefficient of the particle and k_B is Boltzmann's constant.

$$\tau_D = \frac{r_p^2}{6D} = \frac{\pi \eta_0 r_p^3}{k_B T}$$

Equation 8

The Peclet number for pure shear flow can therefore be expressed as shown below in Equation 9, where $\dot{\gamma}$ is the shear rate:

$$Pe = \frac{\pi \eta_0 r_p^3 \dot{\gamma}}{k_B T}$$

Equation 9

When Pe<< 1, Brownian motion can restore the microstructure fast enough so that the microstructure remains in its original equilibrium configuration, its rheological properties therefore remain unchanged by the flow. The reason that colloidal dispersions can show Newtonian like behaviour is essentially due to the fact that the particles are capable of randomizing their positions, and therefore their microstructure at low rates of deformation [1].

As Pe approaches unity then the flow begins to change the microstructure of the material and shear thinning becomes evident. When Pe>> 1 Brownian motion cannot restore the microstructure of the material and the system is almost completely out of equilibrium [1,24].

In colloidal dispersions, shear thinning is often said to be caused by change in the dispersion's microstructure where ordered layers of particles are formed that can slide over each other resulting in fewer particle interactions for a given amount of deformation of the dispersion. This leads to less energy being dissipated as friction resulting in a decrease in the observed shear viscosity. The formation of ordered layers has been observed using microscopy, light scattering and neutron scattering techniques [55-59]. There is still some debate however on whether shear thinning is a direct consequence of this observed ordered layering [60].

1.5.3 Shear Thickening

Shear thickening is the term applied to a material that shows a reversible increase in shear viscosity with an increase in shear rate. Materials are also said to be extensionally thickening if their elongational viscosity increases as the rate of elongation increases.

A material that shows shear thickening is often alternatively referred to as being rheologically dilatant. The reason for this is that most materials that are shear thickening also happen to be concentrated particulate systems. Concentrated suspensions often need to expand their total volume in order to flow as show in Figure 6. Dilatancy can be observed by visual roughening of the free surface of a particle suspension during flow due to particles being forced to poke out of the surface [61].

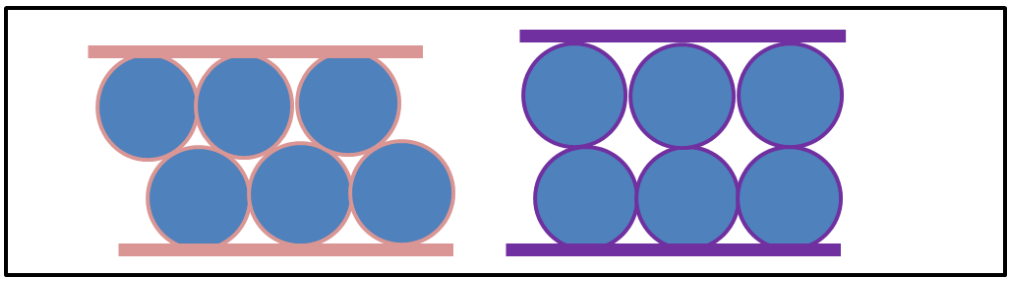

Figure 6 Simple example of how particulate systems can dilate under shear

The most commonly cited example of a shear thickening fluid is corn-starch suspensions (also known as corn-flour suspensions) which are composed of polydisperse granular particles approximately 15 microns in size. The exact size distribution is dependent on manufacturer. Corn-starch is composed of roughly 75% amylopectin and 25% amylose depending on the plant used to produce it.

Early work on shear thickening was done in the 1930's by Williamson and Heckert where corn-starch suspensions were placed within a viscometer. The load exerted by the viscometer would increase showing a gradual increase in viscosity. Eventually a point would be reached where increasing the load would no longer increase the flow rate. In other words as the applied stress increased the suspension refused to flow any faster [62].

A few years later experiments in which a sphere was pulled through various colloidal dispersions were carried out by Freundlich and Roder. Their results also showed shear thickening behaviour as the applied load increased, they also confirmed that at high enough loads the colloidal dispersion refused to deform any faster [63]. This effect is now called discontinuous shear thickening by some authors and is characterised by a rapid increase in the rate at which the observed shear viscosity increases with shear stress or shear rate.

1.5.3.1 Types of shear thickening

Many authors such as Brown and Cates define two main types of shear thickening behaviour that primarily concern colloidal and granular suspensions. These are continuous shear thickening (CST) and discontinuous shear thickening (DST)[10,13].

Continuous shear thickening (CST)

CST is essentially mild shear thickening where the viscosity only increases by several tens of per cent as the shear rate increases over a few decades. Continuous shear thickening has been observed in colloidal dispersions of volume fractions as low as approximately $\phi = 0.3$, although it is by far most prominent at higher volume fractions [31]. Shear thickening is generally preceded by shear thinning at lower rates of deformation and is characterised by significant changes in the microstructure that occur when $Pe \gg 1$, where the rate of deformation is relatively high. At high enough rates of deformation, where CST is encountered, Brownian motion has been found to be insignificant and hydrodynamic interactions dominate [31]. The shear rate and applied stress at which shear thickening begins are termed the critical shear rate and critical stress respectively by many authors, however it is argued that it is better to state the critical stress rather than the critical shear rate as the former is more independent of the packing fraction [46,64]. Some authors denote the critical shear stress as τ_{MIN} and at the same time define a maximum shear stress as τ_{MAX} above which CST and/or DST is no longer seen and often gives way to other effects such as shear thinning and fracturing [13,65].

Discontinuous shear thickening (DST)

DST is a type of shear thickening where the shear viscosity increases discontinuously by orders of magnitude over a narrow range of applied shear rates or shear stresses beyond a given applied shear stress or shear rate. This is observed above a critical volume fraction near the RCP where the suspensions obtain a yield stress ϕ_c [13,45,66]. DST has been shown to evolve from continuous shear thickening as the applied stress increases, assuming solid volume fraction is greater than a critical value [45,66,67]. Additionally work done by Fall and Lootens showed that when DST is observed, large fluctuations in the shear stress can also be observed that are strongly correlated to fluctuations in the normal stress (due to dilation). It has been suggested that this indicates that frictional interactions are highly relevant to DST [15,54,68].

Inertial shear thickening

Some authors refer to an additional type of shear thickening called inertial shear thickening. This is due to increasing turbulence and the formation of rotating eddies at high shear rates resulting in greater energy dissipation and therefore a higher viscosity. This type of shear thickening can even be observed in Newtonian liquids during flows at high Reynolds numbers and therefore is usually not even referred to as a form of shear thickening [16].

1.5.3.2 Traditional Theories for Cause of Continuous Shear Thickening

There are two main theories that have traditionally been used to explain shear thickening. Both theories have had some success in predicting the minimum stress for shear thickening of suspensions but neither of them have had much success in predicting the large increases in viscosity observed when DST occurs [13,16,31]. Because CST can occur at very low solid volume fractions compared to DST and DST unlike CST, is extremely sensitive to the variations of the solid volume fraction, it has been proposed that CST and DST have a different mechanism [13,15]. A proposed mechanism for DST will be discussed in section 1.5.3.5.

Hydroclustering

This theory was introduced by Brady and Bossis in 1985, and it is the most heavily represented view in the literature. It proposes that the characteristic change in the microstructure that initiates shear thickening is the formation of stress bearing groups of particles separated by a thin layer of solvent termed hydroclusters as illustrated in Figure 4 [31,69].

Hydroclusters are correlated groupings of particles in regions of the dispersion where the particle density is higher than average. They are not aggregates but rather shear induced fluctuations in the local particle density that are continuously forming and breaking up due to the flow. Hydroclusters form because applied shear pushes particles close together, and in order for them to move away from each other they must overcome large viscous drag forces from neighbouring particles. This makes it difficult for particles to leave a cluster by diffusion but they can still continuously leave and join a given hydrocluster [31].

When the shear has ceased, Brownian motion can rapidly randomize the microstructure as only slight adjustments separate the equilibrium microstructure from the shear thickened microstructure. This gives an indication as to why continuous shear thickening is reversible. Most authors in the literature take the view that dominance of hydrodynamic forces at high rates of deformation results in the formation of these hydroclusters [70,71].

Within hydroclusters the particle concentration is higher than the average concentration of the system. This puts the fluid within the clusters under great stress due to hydrodynamic forces that must be overcome in order to move particles past each other by squeezing fluid through the spaces between particles. This change in microstructure also means that large hydrodynamic forces must be overcome in order to make hydroclusters themselves move past each other. This results in greater energy being dissipated for a given amount of deformation resulting in an increase in viscosity. This increase in hydrodynamic forces is considered to be enough to cause continuous shear thickening without an order disorder transition or aggregation [70-74]. It has been verified by both Rheoptics experiments carried out by Bender and Wagner, and Stokesian dynamics simulations carried out Brady that at high Pe, the lubrication hydrodynamic interactions between particles increase dramatically giving weight to this theory [71,75-77]. Recently, confocal rheology measurements have shown that the existence of particle clusters coincide with the shear thickening regime [78].

Order-Disorder Transition

This theory was first proposed by Hoffmann. He found that the transition to CST often coincided with the transition from an ordered microstructure with ordered layers at low shear rates to a disordered structure at higher shear rates. It has now been shown that CST can occur without an order disorder transition and that the change in microstructure is mainly coincidental [47,73,74,79].

1.5.3.3 How do Suspension Properties Affect the Onset of Shear Thickening?

A broad literature review of the factors effecting shear thickening was done by Barnes in 1989 which demonstrated that particle size, particle shape, polydispersity and volume fraction, had strong effects on the onset of shear thickening of non-flocculated granular and colloidal suspensions [53].

The factors affecting the critical shear rate and critical stress to bring about shear thickening in a given colloidal dispersion of spherical particles have also been investigated more recently by Wagner and co-workers through a number of publications using colloidal silica dispersions. They also demonstrated that the critical shear rate and the critical shear stress were primarily dependent on particle size, interparticle interactions and of course, the solid volume fraction [80,81].

It has been show that increasing the polydispersity of suspensions can have a strong effect on the critical shear rate as well as the relative viscosity of a suspension of a given volume fraction. It also has the effect of increasing the maximum packing fraction of a given suspension which was shown by Chong [82]. Most investigations on the effect of polydispersity have involved studying bimodal mixtures of varying size ratios. It has been shown that adding smaller particles roughly 25% of the diameter of larger particles has the effect of greatly increasing the critical shear rate and reducing the relative viscosity [53].

As particle size increases it was shown by Maranzano and Wagner that the critical stress and critical shear rate scales inversely with particle radius cubed. They suggested that this results from hydrodynamic interactions dominating in the shear thickening regime [31,80,81].

If colloidal particles are strongly repulsive or are coated with polymer strands then this causes the extent of shear thickening to decrease as particles cannot come close enough for hydrodynamic interactions to dominate as much. This pushes the onset of shear thickening to higher shear rates and applied stresses [80,81,83].

Experiments using a variety of different particle shapes such as rods, platelets and hooked rods have shown that particle shape can have a strong effect on the critical volume fraction

and critical stress at which shear thickening and jamming occur. This is to be expected as changing the shape has a dramatic effect on how close particles can pack together [53,84].

1.5.3.4 Are Dilatancy and Shear Thickening Linked?

Dilatancy is a direct consequence of collisions between particles. In order to accommodate the flow, the grains have to roll over each other in the direction of the velocity gradient, and therefore the material will tend to expand in this direction and exert normal stresses in the process. Cates and Fall suggested, that the maximum confinement pressure due to surface tension at a free surface associated with dilation should be of the order of the surface tension divided by the particle size. This confinement pressure is of the same order of magnitude as the typical normal stresses measured by Fall near the onset of the shear thickening shear thickening regime of particle suspensions, which indicates a connection between shear thickening, dilation and the occurrence of normal stresses [10,14].

There is a good deal of literature that discusses how dilatancy and shear thickening may be related which started in the late 1950's. Metzner and Whitlock subjected dispersions of TiO_2 spheres in water of various volume fractions to shear flow in couette cell geometry and through a capillary over a wide range of shear rates. They observed that dilatancy could occur at lower shear rates than what was required to bring about shear thickening and that many samples showed shear thickening without displaying any visible dilatancy effects. However they also carried out experiments on granular suspensions of glass spheres that showed dilation without showing shear thickening [61].

They also found that the critical shear rate to bring about CST decreased with decreasing medium viscosity. As altering the medium viscosity should not affect the extent to which dilatancy can occur they concluded that shear thickening and dilatancy can occur completely separately from each other. It should be noted that at this point however, that some authors have found that altering the medium viscosity has little effect on the critical shear rate of dispersions of solid spherical spheres, although it will of course increase the applied stress required to bring about a given shear rate as the suspension viscosity is dependent on the medium viscosity [83].

Brown recently interpreted the conclusion made by Metnzer and Whitlock from their results differently; he concluded that dilatancy can occur without shear thickening; however shear thickening cannot occur without dilatancy. He suggested that the reason Metzner and Whitlock observed some samples showing dilatancy without showing shear thickening was because shear thickening can be hidden by shear thinning or yield stress effects [13,85]. Many authors suspect that discontinuous shear thickening is a form of jamming and both may be closely related to dilatancy but this will be discussed in detail in section 1.6 [7,10,13,86].

1.5.3.5 DST due to Constrained Dilation

It has been proposed by Brown and Jaeger [13,16] that DST of particulate systems is caused by dilation. They also propose the range of applied stresses over which DST is observed depends on the confining stresses that surround the particulate system, and on the dominant stress scale within the system, which is in agreement with results from mode coupling theory(MCT) carried out by Cates and co-workers [10,87]. MCT is based on the idea that at high solid volume fractions there is a nonlinear feedback mechanism by which fluctuations in the local structure of a fluid cannot relax to equilibrium because particles are caged by their neighbours. MCT has been used to describe aspects of the glass transition well and some authors have extended the use of MCT to describing concentrated particle systems undergoing flow [32].

Brown and Jaeger proposed that discontinuous shear thickening occurs when a suspension tries to dilate but is unable to fully do so due to constraints surrounding the system. Examples of these constraints are walls containing the sample being sheared and capillary forces resulting from dilation. These confining stresses are transmitted into the system being sheared through frictional interactions between particles or force bearing chains of particles creating additional resistance to flow and therefore an increase in the observed viscosity [13].

The mechanism proposed by Brown is given below [13]:

1. Dilation: The particulate system must dilate as it is sheared. This means that the suspension must have a high volume fraction.

2. Frustration: Geometric constraints must at the very least partially prevent the dilation attempt, in other words the sample must not be able to dilate as fully as it would if there were no constraints. These constraints could be surface tension at the liquid-air interface, particle stiffness or the walls surrounding the system. Frustration therefore requires high packing fractions.
3. Confining stress: The constraints must supply confining stress such that the least rigid constraint produces an opposing force to the dilation that increases as the dilatational strain of the sample increases. In other words the weakest constraining surface must provide a constraining stress that increases as the sample increasingly dilates.
4. Dominance: The confining stress must be much greater than all the stresses that prevent shear between particles and dilation. Examples of such stresses are gravity and interparticle interactions. If this is not the case, then there will not be enough of a stress increase due to dilation to result in a positive gradient on a viscosity curve and the global rheology of the system could be shear thinning.

Brown and Jaeger also proposed that the onset stress for shear thickening τ_{MIN} is set by the stress required to prevent two neighbouring particles from being moved apart. For example if the dominant stress of the system is due to attractive inter-particle attractions, then τ_{MIN} is set by the force required to roughly overcome the two-particle attractive force and pull the particles apart by shear. If the dominant stress of the system is due to repulsive inter-particle attractions then τ_{MIN} is set by the force required to push particles past each other.

If a colloidal system is stabilised by electrostatic potential then τ_{MIN} is set by the electrostatic repulsion force per cross sectional unit area of the particle. If a suspension consists of heavy settling particles, then τ_{MIN} is set by gravity and the stress needs to exceed the weight of a particle per cross sectional area as well as any relevant inter-particle friction forces [13].

Using evidence that normal and shear stresses during shear flow are coupled by dilation [14,54,88,89], Brown and Jaeger proposed that the maximum stress at which DST is observed τ_{MAX} (above which sample fracture occurs), can be predicted by the confining stress that is exerted by the least stiff boundary constraining the system. The least stiff boundary is usually the liquid-air interface, as the geometry of most rheometers has open

sections that result in a liquid air interface around the sample being examined. The maximum stress is therefore often set by the surface tension [13]. When dilation occurs, particles create bumps in the liquid surface and thus create additional surface area resulting in capillary forces that essentially try to pull the particle back inside the suspending fluid to minimize surface area. This maximum capillary force has been estimated by both Brown and Cates to be of the order of the surface tension of the suspending fluid divided by the diameter of the dispersed particles. This is shown in Equation 10 where *d* is the diameter of the particle and Γ́ is the surface tension of the fluid medium.

$$\tau_{MAX} = Maximum\ constraining\ capillary\ stress \approx \frac{\acute{\Gamma}}{d}$$

Equation 10

Below are some examples of predicted values of τ_{MAX} using the above equations, which are relevant to this PhD.

For a suspension of corn starch of roughly 14µm in diameter particles dispersed in water at room temperature being sheared in an open geometry the value of τ_{MAX} can be estimated as shown below:

$$\tau_{MAX} = Maximum\ constraining\ capillary\ stress \approx \frac{72.8 \times 10^{-3}\left[\frac{N}{m}\right]}{14 \times 10^{-6}[m]} = 5200[Pa]$$

For a dispersion of PMMA particles of 574nm in radius dispersed in decalin at room temperature being sheared in an open geometry the value of τ_{MAX} can be estimated as shown below:

$$\tau_{MAX} = Maximum\ constraining\ capillary\ stress \approx \frac{31.5 \times 10^{-3}\left[\frac{N}{m}\right]}{1.148 \times 10^{-6}[m]} = 27500[Pa]$$

Using a wide range of data from the literature on the shear flow of particulate systems within open rheometers, Brown and Jaeger showed that the values of τ_{MAX} experimentally observed compared well with (0.1Γ́/d) and so were roughly 10 times smaller than expected. They also showed that when the system is surrounded by walls such that there is no liquid-air interface that τ_{MAX} scales with the most compliant confining stress [13].

It has been put forward by Fall that shear thickening cannot take place without normal and confining stresses being present [14]. Fall carried out shear flow on suspensions using a special rheometer capable of keeping the 1st normal stresses constant by altering the gap distance. Results showed that allowing a shear thickening suspension to dilate without resistance from confining stresses resulted in the elimination of shear thickening altogether [15].This supports the mechanism for DST proposed by Brown and Jaeger.

Discontinuous extensional thickening and dilation has also been observed using an extensional rheometer by Smith and co-workers [90]. The value of stress required to bring about extensional thickening τ_{MIN}, compares well with that required to bring about shear thickening, however the equivalent rate of extension for uniaxial extensional is much lower than that for shear flow. The value of τ_{MIN} in extensional flows has been observed to be independent of the extensional rheometer gap distance used, however the critical extensional rate is dependent on the gap distance. The value of τ_{MAX} is generally larger for uniaxial extensional flow than for shear flow but is still limited to the capillary stresses that can maintain the fluid element [31]. Above this stress, the filament breaks and yields but this still corresponds well with shear flow situations where the system is open to the air where τ_{MAX} corresponds to the surface tension [13,91].

Another factor that has been shown to limit the maximum value of τ_{MAX} in shear flow and results in a second region of shear thinning at high stresses is referred to as the elastohydrodynamic deformation of suspended particles. This is due to the fact that colloidal particles have a finite elastic modulus [31]. At high enough stresses, two elastic particles in a suspension can deform with a very thin layer of fluid in between them. As DST leads to extremely high forces acting between particles within hydroclusters, it makes sense that an abrupt change from DST to shear thinning could occur as particles yield [31].

Evidence for this second round of shear thinning due to particle yielding has been observed in experiments involving shear flow of relatively soft particles at high shear rates [92-94]. Suspensions of silica particles and minerals also show this behaviour at very high stresses beyond what standard rheometers can supply [95]. Systems of highly deformable particles (including emulsions) have shown similar behaviour that limits τ_{MAX} and that sufficient softness can even result in the elimination of the shear thickening regime altogether [31,96-99].

1.5.4 Viscoelasticity of Colloidal Systems

A viscoelastic substance is one that can respond both viscously and elastically to an applied stress or shear. When a small amplitude oscillatory shear (SAOS) is applied to a viscoelastic substance, the resulting stress or deformation has both an elastic and a viscous component which are out of phase with each other [31,52]. Viscoelasticity is a feature most commonly displayed by polymer solutions but colloidal dispersions with volume fractions greater than roughly 0.2 have also been shown to display this behaviour under oscillatory shear [31]. SAOS is carried out in the linear viscoelastic regime, where a resulting stress increases linearly with applied strain and the micro-structure is not being altered from equilibrium [31,100].

An elastic modulus first appears when the applied probing frequency becomes much greater than the inverse of the characteristic time for Brownian motion of the constituent colloidal particles, or in other words the relaxation time. This is because the deformation is acting on a shorter time scale than the material can randomize its own microstructure by diffusion and so it cannot flow as a fluid would in response to the probing deformation [31]. Elasticity of colloidal dispersions arises from Brownian forces and other inter-particle interactions if present, which act like elastic springs between particles that store some of the energy used to deform the microstructure.

As the volume fraction of a colloidal dispersion increases, then hydrodynamic forces slow the movement of particles, which results in a reduction in the diffusivity of the dispersed particles causing the relaxation time to increase. This means that more concentrated particulate systems display elastic moduli at lower frequencies of oscillatory shear. If the volume fraction is high then particles cannot move with respect to each other fast enough without generating large hydrodynamic forces due to their close proximity. As the particle size increases, this also results in an increase in relaxation time due to a decrease in diffusivity resulting in an elastic modulus being observed at lower applied shearing frequencies [32].

Theory developed by Lionberger and Russel compares extremely well with experimental results which examined the linear viscoelastic properties of colloidal dispersions by applying SAOS. They showed that as the system becomes crowded calculating the elastic modulus becomes complicated due to hydrodynamic coupling which is not an issue in

polymer solutions. This is because in order for a particle to move, some of the dispersing medium must be displaced. They predicted that as the volume fraction approaches the RCP, the elastic storage modulus of dispersions diverges due to an increase in hydrodynamic interactions which fits in well with experimental observations [31,101,102].

1.5.5 Oscillatory Shear Thickening of Particle Suspensions

Shear thickening has been observed in colloidal and granular suspensions when they are subjected to large amplitude oscillatory shear (LAOS) [103-106]. LAOS is similar to SAOS except that larger strains are used that can result in non-reversible alteration of the microstructure which generally makes the interpretation of results much more difficult. LAOS experiments can also be complicated due to sample slip at high strains and frequencies [31].

Wall slip has been commonly observed in the rheology of concentrated particle suspensions and dispersions which is often unaccounted in results presented in the literature. Wall slip occurs when the flowing material fails to adhere to rheometer or pipe walls and is most likely to occur when these walls are smooth [107-111].

The magnitude of the complex viscosity (the difference between the in phase and out of phase viscosities [52,148]) of colloidal and granular suspensions during LAOS experiments has been shown to compare reasonably well with the shear viscosity observed during steady shear experiments [92,105,112]. In the case of nearly hard sphere dispersions, the critical applied stress to cause shear thickening in steady shear flow compares extremely well with the root mean square of the applied stress that causes shear thickening in LAOS experiments [103].

It has been observed by many authors that shear thickening is only observed during LAOS above minimum strain amplitude Υ_c, which is inversely proportional to the frequency of the applied shear [103,113]. There are conflicting views in the literature as to whether this minimum strain amplitude to bring about shear thickening is completely or partially due to wall slip [103,114]. Oscillatory shear experiments on corn-starch suspensions carried out by Fall showed that shear thickening did not occur unless the shear strain amplitude was greater than around 1. Fall suggested that in order for shear thickening to be observed in

oscillatory flows, the strain must be high enough that neighbouring particles experience a relative motion of the order of a particle diameter [15].

1.6 Jamming of Particulate Systems

The literature surrounding the various different types of jamming is discussed in this section. An attempt is made at untangling the different viewpoints and definitions that authors use when examining the transformation of a fluid particulate system to a solid particulate system.

In the literature surrounding jamming, many authors have a habit of not explicitly stating what specific type of jamming they are referring to. In order to make sense of the surrounding literature it is important to keep in mind what the author is really meaning when they use the term jamming by closely examining the context.

For example when referring to the jamming transition in the context of a fluid dispersion transforming to a solid by an increase in the volume fraction of the dispersed phase an author could mean a number of things. They could be referring to the volume fraction at which a system becomes mechanically stable against gravity (ϕ_{Solid}=RLP) or the value of ϕ_{Solid} at which the system first obtains a yield stress often called the critical jamming fraction ϕ_c [13,38,40,54]. They could also be referring to the point at which any given constituent particle cannot move without displacing its neighbours (ϕ_{Solid}=RCP) [115].

Another source of confusion that arises when considering stress induced static jamming of a yield stress fluid is that two different jammed regimes can be observed. As the applied stress acting on a glassy particulate system is increased it can yield to undergo a solid-fluid transition and at higher stresses, the system can undergo a fluid-solid transition into a statically jammed metastable system. This system remains jammed even when the applied stresses are removed which has been termed static jamming by the application of a stress. In order to clarify this confusion some authors have referred to this effect as re-entrance to the jammed state [9,14]. This refers to the fact that an initial applied stress is required to overcome the yield stress (due to attractive forces between the particles or inter-particle friction) and then as the applied stress increases to some critical value, the system effectively becomes a brittle solid that can yield at higher stresses.

There is also a difference between systems that are statically jammed and dynamically jammed although both depend on the formation of force chains. A statically jammed system remains in the jammed state whether or not the applied stresses are removed as is seen in granulation. Dynamic jamming is essentially temporary solidification of a particulate system in response to a stress applied over a short enough time scale [16]. Both of these types of jamming are discussed in this section.

1.6.1 Force Chains and Static Jamming of Particulate Systems

Some authors insist that the term jamming as applied to particulate systems, should be reserved for the process by which such a systems stops flowing when a high enough stress is applied. Some authors refer to this type of jamming as dynamic jamming or shear induced jamming as opposed to jamming where a system can obtain a yield stress just by increasing the solid volume fraction [7].

With this definition in mind authors agree that jamming involves the formation of force chains that transmit stress from the system boundaries impeding flow as long as the force is not too large to cause yielding as is shown in Figure 7. This view point has been largely proven through the use of suspensions containing photo-elastic disks which alter their refractive index when put under stress, allowing stress bearing chains to be directly identified [5,116-118].

By modelling stress transmission through particulate systems under applied stresses, Cates and co-workers showed that these force chains can only support forces in specific directions. If a force in a non-compatible direction is applied, the load bearing structure will rearrange itself to support the new force forming a new jammed fragile state [7,10,86,119].

When a particulate suspension with surfaces open to air transforms into a solid, it essentially becomes a pasty lump. Due to dilation causing particles to stick out of the surface, the system takes on a dry appearance and loses its shine compared to the fluid state, due to increased light scattering by the surface [10,90].

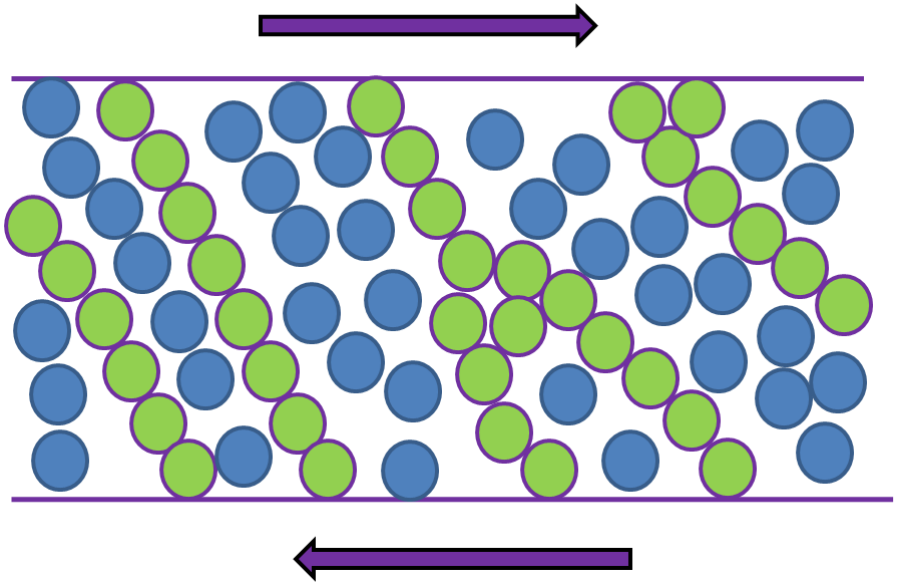

Figure 7 Illustration of force bearing chains opposing flow. Particles that are part of a force bearing chain are highlighted green.

Once jammed by the application of a high enough stress, systems are observed to be stable unless new outside forces alter the microstructure or additional solvent is added [10,51]. For example if the jammed system is lightly vibrated then it will re-fluidise because the force chains cannot support stresses from multiple directions. If a jammed granule is placed beside a granule that has been re-fluidised they will merge into one liquid like drop. A granule that has re-fluidised can be transformed back into a solid granule by re-applying a stress [8,10,12].

Because these jammed systems can maintain their arrested state after flow has ceased, these statically jammed states cannot be explained by hydrodynamic forces alone as these forces fade when the flow ceases. Increasingly authors are proposing that these statically jammed states are maintained by strong capillary stresses that exceed the characteristic stress scale of the system, and that these capillary forces also have a role to play in DST [10,13].

These strong capillary forces can be caused by sample dilation. During dilation, particles are partially protruding from the surface, this means that the surface tension forces acting inwards on the sample are greater. This has an effect of exerting additional compressive stresses on stress transmitting chains and preventing them from falling apart as long as no additional external forces come into play [10].

Cates suggests that dilation within a fixed volume of dispersing liquid involves the formation of force transmitting chains of hydroclusters that grow throughout the system and eventually causes particles to encounter the air-liquid interface. This results in large capillary forces at free surfaces, which can balance the normal inter-particle forces and resist further motion. The particles therefore form clusters that span the system in close contact, jamming the sample and showing visible dilation effects. The jammed system may then yield and fracture into jammed granules. The process of granulation involves applying a high enough stress to the particulate system such that it jams and then fractures into small granules by the ingress of air. These granules remain jammed and may each contain thousands of particles and a given amount of solvent [7,9,10,87,90].

The process of shear induced jamming of a droplet from a colloidal dispersion as suggested by Cates from mode coupling theory is illustrated in Figure 8. At low applied stresses the colloidal dispersion remains fluid like. However as the applied stress increases dilation occurs resulting in capillary forces that oppose motion and are transmitted through the system by load bearing chains resulting in DST. Once the applied shear stress is much larger than the characteristic Brownian force acting to keep particles apart, particles can be forced into close contact creating force bearing chains that span the droplet and are maintained by the capillary forces. The system is then permanently jammed unless a large outside force overwhelms the capillary force causing the microstructure to fracture. This is illustrated in Figure 8.

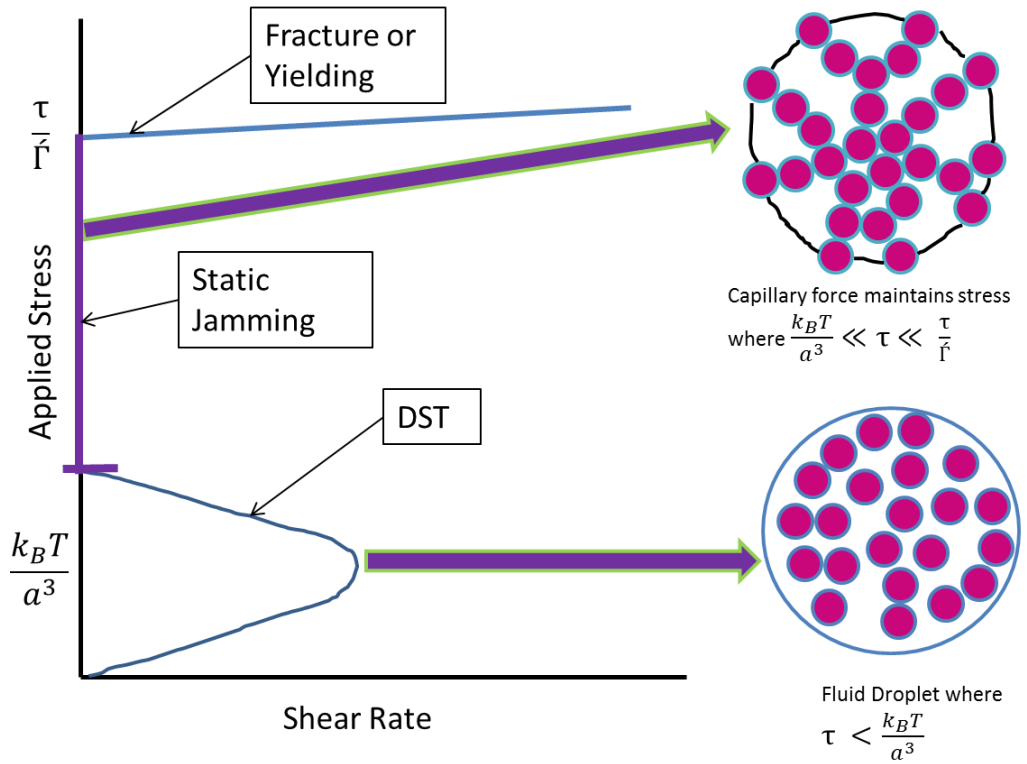

Figure 8 Illustration of jamming and yielding of a droplet from a colloidal disperion suggested by Cates where Γ́ represents the surface tension of the fluid and τ is the applied stress.

1.6.2 Shear Induced Jamming as the Limiting Extent of DST by Dilation

There are a lot of examples of rheological data on colloidal and granular systems in the literature that show that the viscosity of particulate suspensions can increase discontinuously over a narrow range of shear rates over a small range of applied shear rates. Additionally jammed systems can yield at high enough stresses and possibly give a shear thinning response from that point onwards as was indicated by Brown. This raises an important question, when does discontinuous shear thickening end and jamming begin [45,61,87].

Experiments carried out by Fall on concentrated corn-starch and laponite suspensions and on other suspensions by Bertrand and co-workers [15,120], showed that as the applied stress was increased, a point was reached at the end of the discontinuous shear thickening regime were the samples were transformed into a solid and refused to flow [12,14,120].

In granular systems undergoing flow, it has been observed that force chains that are restricting flow and cause the system to jam, can often buckle and break. This results in the suspension unjamming followed by the formation of new force chains which themselves break at a later time [121]. This behaviour explains the massive shear and normal stress fluctuations due to the formation of force chains during DST observed by Lootens and Fall using concentrated colloidal and granular suspensions respectively [14,15,54]. If a system momentarily jams and increases its resistance to flow and unjams decreasing its resistance to flow, then a rheometer would display fluctuating resistance to flow as stress fluctuations.

Stokesian dynamic simulations carried out by Melrose and co-workers on sterically stabilised hard sphere colloidal dispersions compare well with experimental observations made by Lootens [122-124]. They showed that during strong shear thickening large networks of stress bearing particles are formed that can span the system and lead to large fluctuations in the stress. They also proposed that shear thickening should be regarded as the initial approach to the jamming of the dispersion.

Experiments carried out by Smith and co-workers showed strong evidence that jamming and DST are also linked in extensional flows [90]. In these experiments concentrated

colloidal PMMA dispersions of volume fractions between 0.59-0.62 were subjected to wide range of rates of extension. At low rates of extension no dilation was observed, at high enough rates of extensional thickening and dilation was observed, followed by jamming and fracturing at higher rates. As the volume fraction increases, they showed that rate of elongation required for jamming was seen to decrease. From the literature discussed in this section so far; it is likely that DST is a form of jamming where the applied stresses are strong enough to dislodge force chains, or that the chains are not stable.

Theoretical work on concentrated suspensions under stress carried out by a number of authors also suggests that shear induced jamming evolves from DST at high enough applied stresses and volume fractions [10,11,125,126]. Using mode coupling theory where hydrodynamic interactions were neglected, Cates and Holmes predicted that colloidal dispersions under shear could display a wide range of behaviours observed experimentally in literature as shown in Figure 9. Their models were based on 2 theoretical parameters; one was called the jammability by stress denoted by (α) and the glassiness denoted by (v).

The jammability is a measure of how easy the system can be made to jam by application of stresses. An example of a practical way to increase jammability of the system could be to decrease the Brownian motion by increasing the particle size to make force chain formation easier. The glassiness controls how far away the system is from becoming a static glass and increases as the system approaches an arrested state. As the glassiness increases, the system is less able restore its microstructure to its equilibrium state following a disturbance. A potential way to increase the glassiness could be to increase both the packing fraction and particle size to limit the effects of Brownian motion. As the glassiness increases the system will either become a brittle or a yielding glass.

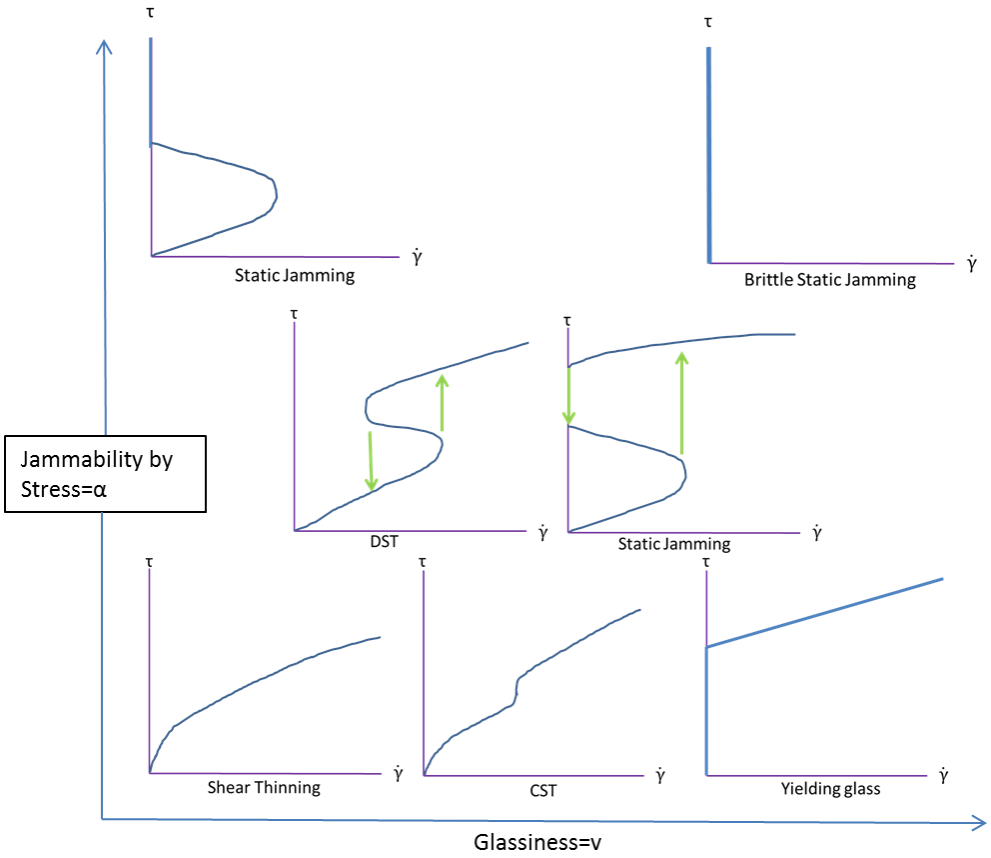

Figure 9 Illustration of the various curves predicted by Cates and co-workers using MCT that colloidal dispersion can display and of how altering the jammability and glassiness results in DST and jamming curves predicted.

From their models they predicted the various rheological behaviours seen in the literature by altering the values of the glassiness and jammability as illustrated in Figure 9. Areas where the curves take on negative gradients are mechanically unstable resulting in discontinuous jumps in the stress with a marginal increase in shear rate when these segments are reached. This is illustrated by the arrows that show the direction of discontinuous stress jumps. Over the regions where the curve is unstable, increasing the applied stress results in no increase in shear rate which is what is observed experimentally during DST. Their model also showed that jamming evolves from DST as the jammabilty is increased. The main difference with the curves displaying DST and the curves displaying jamming is that the jamming curve replaces a region with constant shear rate with a region where there is no flow.

1.6.3 Broadly Defined Jamming and the Universal Phase Diagram

Jamming is most broadly defined as the conversion of a fluidic system into an amorphous solid system. With this definition in mind, jamming of a concentrated colloidal dispersion can be brought about by various methods. Increasing the volume fraction of dispersion would eventually create a paste like system with a yield stress. In some cases decreasing the temperature of the system could create a glassy system. The application of a stress can cause a solid particulate system to jam and applying too high a stress to a jammed system could also cause it to yield and flow.

There have been attempts by many authors to characterise a sort of universal phase diagram to sum up the sets of conditions that will bring about the jamming of various types of particulate systems whether they are particulate dispersions or emulsions [3,4,6,127,128]. Whether or not a particulate system jams depends on the combination of the temperature and volume fraction of the system as well as the applied stress.

For example unless a particulate system is concentrated enough (has a high enough volume fraction) then there is no way for particles to come together and form force chains or clusters to transmit resisting forces implying that there is a critical volume fraction before jamming can occur.

These attempts to create such a generalised phase diagrams envisage the glass transition as being a limit of a generic non-equilibrium fluid-solid transition [29]. There is however very little experimental evidence to support this idea except for experiments carried out by Trappe where the volume fraction, attraction strength and applied stress were altered to bring about jammed states. In each case an elastic modulus was observed [3].

In the literature regarding universal jamming phase diagrams, it is important to note that when the term jamming transition is used, it refers to jamming by increasing the solid volume fraction and not by the application of a force. A related issue with the phase diagrams of suspensions presented in the literature so far is that, although they represent yielding at high enough applied stresses they do not represent stress induced jamming of a fluid system.

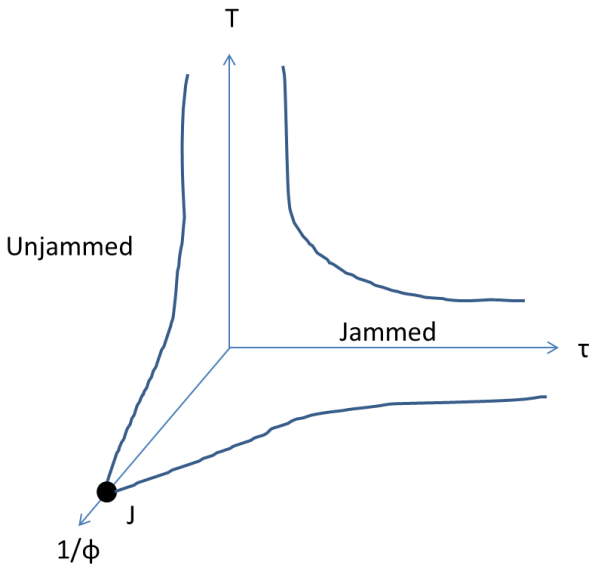

Figure 10 Proposed Jamming phase diagram by O'Hern [128]

Figure 10 shows an example of a simple phase diagram. The blue lines enclose a region where a system can be considered solid and outside the region the system can be considered to be a fluid. Point J represents the RLP where the system has just become mechanically stable. Looking at the density and load axis on Figure 10 it can be seen how this represents the yield stress as the solid volume fraction increases. If the density of the suspension is too low then it will not support any applied stress and will melt but if the solid volume fraction is above the RLP then it will possess a yield stress. Increasing the temperature of the system T, gives more energy to particles reducing the probability they will become locally jammed [5,128].

1.6.4 Dynamic Jamming by Impact

On YouTube it is easy to find videos showing humans running across pools filled with concentrated corn-starch in water suspensions. It has been shown that as someone runs over such a suspension fast enough, it behaves as a solid and supports the stress exerted on it due to the person running. However if they stop running they can be seen to sink as the suspensions rigidity vanishes over time. The stress required to stop a person from sinking can be shown to be well above 40 kPa which is far beyond the highest values of τ_{MAX} for corn-starch suspensions which was shown to ≈10000Pa[13]. This means that the jamming models described by Brown and Cates cannot be used to explain the impact resistance shown by many particulate suspensions. Hydrodynamic forces are also unable to generate this level of stress [13].

Waitukaitis and Jaeger showed that when an object rapidly impacts onto a free surface of a dense suspension it can result in a propagating density front where the particle concentration is above average as is illustrated in Figure 11 [129,130].

These regions where the volume fraction is high essentially become a temporarily jammed solid and so the density wave can be referred to as a jamming front. Once the density wave reaches a solid boundary it can transmit a reaction force through force chains. From a normal impact the jamming front propagates radially as well as downward through the suspension resulting in drag forces acting on the jammed solid allowing the suspension to support normal stresses even before the jamming front reaches a boundary [129,130].

It has been shown that some systems of solid particles can sustain extremely high impact stresses of up to tens of MPa at strain rates of 100,000/s. At high enough impact stresses, the response becomes dominated by the elastic modulus of the dispersed particles and at higher stresses the suspension can fracture [95,131]. Petal and co-workers showed that applying ballistic impact speeds of 1000m/s on suspensions of SiC particles, generated transient shear stresses of around 0.5GPa which indicates stress transmissions by solid-solid contacts provided by force chains that are limited by the elastic moduli of the particles themselves [132].

After fast impacts it was shown visually that the jammed solid melts away, as do visible signs of fracture on the surface of the system [133]. Dynamic jamming was also observed

by Kann as a sphere was allowed to sink in a concentrated corn-starch suspension. As a sphere sunk its velocity slowed down and stopped due to a solid jammed region forming in front of it. The solid region eventually melted away as the sphere velocity slowed allowing the sphere to sink faster which in turn caused the solid region to reform as the sphere picked up speed. This resulted in stop-start motion of the sphere [134].

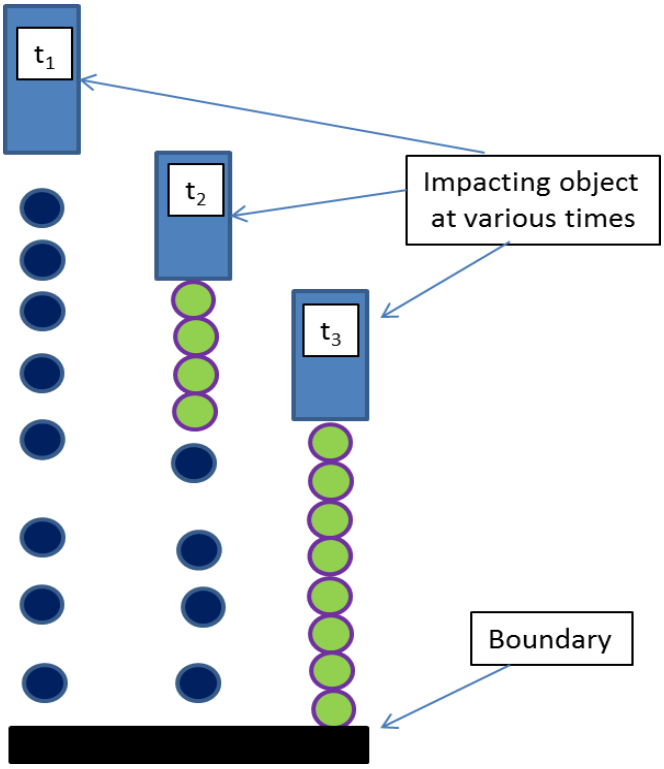

Figure 11 Simple illustration of the formation of a jamming front by an impacting object.

1.6.5 Unusual Behaviour during Vibration of Particle Suspensions

When concentrated suspensions are placed on top of a loudspeaker or on top of a vibrating plate with sidewalls to contain them, it can be seen that if the vibration is at a high enough frequency and peak force, stable fingers can stick out from the suspensions surface and holes can form within the concentrated suspension. These holes and fingers persist over many vibration cycles. These holes can expand, split and replicate [135-137].

When Newtonian fluids undergo vibration, fingers formed from disturbances in the fluids surface cannot persist due to gravity and surface tension pulls them back towards the surface as there are no other forces to oppose them. It was originally thought these persistent fingers and holes were due to shear thickening. However experiments carried out by Falcon showed that yield stress fluids that did not display shear thickening could show this behaviour as well [138].

Oscillatory shear experiments and simulations carried out by Deegan suggested that when concentrated suspensions are subjected to an oscillatory flow beyond a critical shear rate, they display stress hysteresis [139]. Stress hysteresis means that resulting stress corresponding to a given rate of deformation is changing over time. Stress hysteresis of particle suspensions under oscillatory shear was also observed by Barnes. He proposed that this hysteresis was due to shear induced changes in the microstructure being formed in high shear rate regions of the loop that persisted and were still present during low shear rate regions of the loop [53].

Experiments carried out by Ebata showed concentric convection like flow towards the wall of a cell containing concentrated suspensions as the suspensions were subjected to vertical oscillation as well as persistent holes. The strength of this convection like flow was shown to scale with acceleration of the vibrating plate, vibration frequency, particle size, solid volume fraction, and viscosity of the suspending fluid [140].

During the vibration of corn starch in water suspensions, this unusual behaviour has been shown to roughly coincide with the beginning of the DST regime [135]. However during the vibration of non-shear thickening yield stress viscoplastic fluids, Shiba and co-workers observed persistent holes and fingers when the critical inertial stress coincided with the

yield stress of the material [141]. This could indicate that the initiation of persistent holes and fingers behaviours could be related to the fluid-solid transition.

1.6.6 Stochastic Jamming During Pressure Flow

An example of an industrially relevant form of jamming is that of a particulate system as it flows through a pipe or constriction. During this type of flow arches of particles can form somewhat randomly, that span the cross section of the pipe restricting flow. In the literature, simulations and experiments carried out on granular and colloidal systems have shown that a form of jamming can occur during pipe flow at volume fractions below the critical jamming fraction ϕ_{C} , where the suspensions obtains a yield stress [142-147].

Work carried out by Haw showed that some colloidal dispersions of volume fractions above ϕ_{Solid}=0.56, flowing through a narrow constriction due to a pressure gradient can self-filtrate [144]. This is due to jamming taking place causing some of the colloidal particles to get stuck while the fluid passes though. During flow, jamming and unjamming events of the colloidal dispersion were repeatedly seen in the region of the entrance of the constriction corresponding with decreases and increases in the flow rate respectively. At high volume fractions, flow of the colloidal dispersion was highly intermittent and travelled in shocks. Fracturing of the jammed colloidal system could also be directly observed corresponding to an increase in the flow rate. As the volume fraction was lowered the period for which regions remained jammed decreased until eventually no jamming or self-filtration was seen [144].

Further work carried out by Campbell and Haw in which colloidal dispersions were sucked into a syringe at a constant applied pressure showed similar behaviour [145]. They showed that this jamming and unjamming behaviour was observed at solid volume fractions as low as ϕ_{Solid}=0.505. They also showed that the dispersions could unjam due to formation of vortices that likely break up force chains due to their fragility [145].

Simulations carried out by Brand and co-workers on the pressure driven pipe flow of granular suspensions, showed that jamming was observed at high solid volume fractions when particles did not order into layers, which compared well to experimental results in the literature [142,146,147].

Chapter 2 Introduction to Shear and Squeeze Film Flows

2.1 Chapter Summary

In this section, the different types of flows encountered during experiments carried out in this PhD are described in detail. It begins with a brief description of parallel disk drag flow. This is followed by a detailed mathematical description of the parallel plate oscillatory shear flow used on dilute suspensions of swimming microalgae which are essentially Newtonian. This is then followed by a mathematical description of oscillatory biaxial squeeze film flows of Newtonian fluids where the no-slip condition is satisfied, which was another flow type carried out during this PhD on a variety of fluids including particle and algae suspensions. The existing literature on squeeze film flow is also briefly explored.

2.2 Parallel Disk Drag Flow Rheometry

Rheometry refers to a wide range of experimental techniques used to determine the rheological flow properties of materials. The goal of rheometry is to determine relationships between applied stresses and the resulting flow or vice versa for a given flow condition. Rheometry is generally carried out using one of a few standard geometries. The reason for this is that it can often be extremely difficult to make comparisons between results using different geometries. In this subsection, parallel disk drag flow as shown in Figure 12, is briefly described as it is particularly relevant to this thesis, more detailed descriptions can be found in many rheology textbooks [52,148].

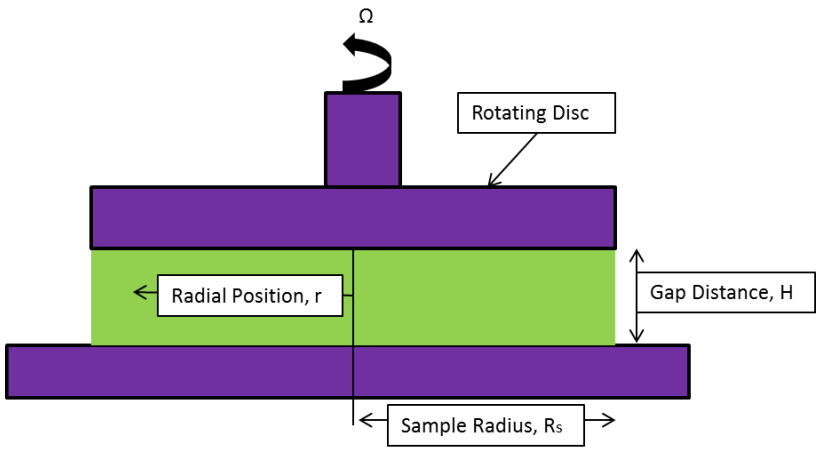

Figure 12 Shows an illustration of parallel disk drag flow where the gap distance is exaggerated for clarity.

In laminar parallel disk drag flow, the shear rate can be described by Equation 11, where Ω is the angular velocity of the rotating disc and v_θ is the tangential velocity. The shear rate varies from zero at the centre to its highest value at the outer edge. The shear rate at a given radial distance, r is independent of the height within the gap.

$$\dot{\gamma}(r) = \frac{v_\theta(r)}{H} = \frac{r\Omega}{H}$$

Equation 11

The viscosity at the outer edge is given by Equation 12, where *T* is the motor torque and $\dot{\gamma}_R$, is the shear rate at the outer edge:

$$\eta(\dot{\gamma}_R) = \frac{\frac{T}{2\pi R^3}}{\dot{\gamma}_R}\left[3 + \frac{dln\left(\frac{T}{2\pi R^3}\right)}{dln(\dot{\gamma}_R)}\right]$$

Equation 12

In the derivation of Equation 12 it is assumed that the viscosity does not vary with shear rate. In the case of suspensions and polymers where the viscosity is often a function of shear rate, the measured viscosity is a combination of the actual viscosity at each radial distance [52]. Typically when the shear rate is controlled at a given value, it refers to the shear rate at the outer edge of the rotating disc.

In oscillatory experiments using parallel disks the strain varies linearly with the radial distance from the centre. Typically when the strain amplitude is controlled at a given value, it refers to the strain at the outer edge.

The normal stress can be easily calculated using this geometry using the thrust of the sample on the upper plate and knowing the area of the plate.

2.3 Oscillatory Parallel Plate Shear Flow without Slip

An illustration of the oscillatory parallel plate shear flow carried out in this PhD on dilute suspensions of *D.Salina (*discussed in chapter 3), which satisfies the no slip condition, is given in Figure 13. The apparatus that was used to carry out such flow is described in chapter 4. In this flow, a top plate moves forwards and then backwards along the x-direction causing a velocity gradient within the fluid in the y-direction. In this subsection, a mathematical description of this flow is given below [52]. The flow field described in this subsection will be later substituted into a model in chapter 3 which describes many aspects of *D.Salina's* behaviour.

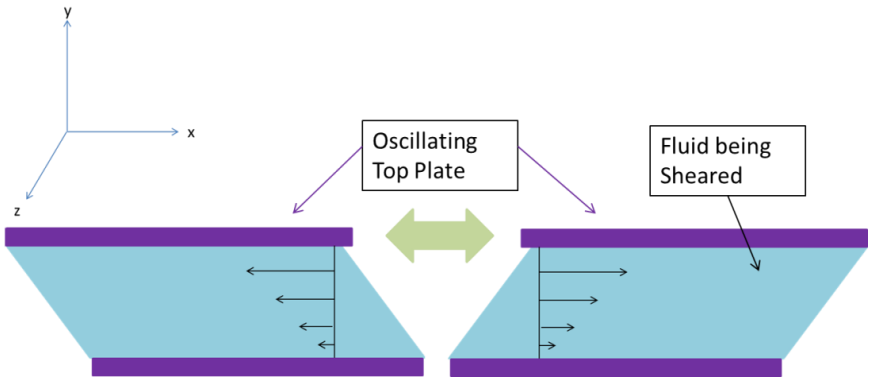

Figure 13 Shows an illustration of oscillatory shear flow and of the co-ordinate system used.

Assumptions

1. There is no variation of properties in the z direction, see Figure 13:

$$\rightarrow \frac{\partial u_z}{\partial z} = 0$$

2. The flow is laminar and is at steady state at each point in time even though the flow is transient. This is observed to be valid over the range of conditions used in this PhD.

Boundary Conditions

Using the no slip condition, the velocity u, at the bottom and top plates can be easily determined. The gap distance between the plates is denoted H, and the velocity of the top plate is V_p.

$$y = 0 \rightarrow u_x = 0$$

$$y = H \rightarrow u_x = V_p$$

The position of the top plate X_p, oscillates backwards and forwards in the x-direction and can be described by Equation 13 where A_D is the maximum displacement of the top plate from its initial position, ω_D is the angular frequency of the top plates motion, t is the time and $\underline{\widehat{e_x}}$ is a unit vector in the x-direction:

$$\underline{X_p}(t) = A_D Sin(\omega_D t)\underline{\widehat{e_x}}$$

Equation 13

The velocity of the oscillating top plate is therefore given by Equation 14:

$$\underline{V_p} = \frac{d\underline{X_p}(t)}{dt} = A_D \omega_D Cos(\omega_D t)\underline{\widehat{e_x}}$$

Equation 14

The components of the flow field due to the oscillatory shear are always zero in the y and z-directions. The velocity of a given plane in the x-direction is a function of its elevation from the bottom plate and can therefore be represented by Equation 15.

$$\underline{u} = (u(y), 0,0)_{x,y,z}$$

Equation 15

Governing Equations

Assuming the that fluid being sheared is incompressible and mass is conserved, Equation 16 is a valid governing equation:

$$0 = \nabla \cdot \underline{u} = \frac{\partial u_x}{\partial x} + \frac{\partial u_y}{\partial y} + \frac{\partial u_z}{\partial z}$$

Equation 16

As the velocity components of the flow field in the y and z-directions are zero, the above equation implies that there is no velocity gradient in the x –direction as expected:

$$\rightarrow \frac{\partial u_x}{\partial x} = 0$$

Equation 17

To carry out a momentum balance on the system, the Navier-Stokes equation can be used as shown below assuming the fluid is Newtonian, where ρ is the fluid density, g is gravity and P is the pressure:

$$\rho\left(\frac{\partial \underline{u}}{\partial t} + \underline{u}\cdot\nabla\underline{u}\right) = \nabla P + \eta\nabla^2\underline{u} + \rho\underline{g}$$

Equation 18

Substituting known information into the Navier-Stokes equation expressed in vector form gives:

$$\rho\left(\begin{pmatrix}\frac{\partial u_x}{\partial t}\\0\\0\end{pmatrix}_{x,y,z} + \begin{pmatrix}0\\0\\0\end{pmatrix}_{x,y,z}\right) = \begin{pmatrix}-\frac{\partial P}{\partial x}\\-\frac{\partial P}{\partial y}\\-\frac{\partial P}{\partial z}\end{pmatrix}_{x,y,z} + \eta\begin{pmatrix}\frac{\partial^2 u_x}{\partial y^2} + \frac{\partial^2 u_x}{\partial z^2}\\0\\0\end{pmatrix}_{x,y,z} + \begin{pmatrix}0\\-\rho g\\0\end{pmatrix}_{x,y,z}$$

Equation 19

Examining the individual components of the above equation gives:

$$\frac{\partial P}{\partial y} = \rho g$$

Equation 20

$$\rho\frac{\partial u_x}{\partial t} = -\frac{\partial P}{\partial x} + \eta\left(\frac{\partial^2 u_x}{\partial y^2} + \frac{\partial^2 u_x}{\partial z^2}\right) = \eta\left(\frac{\partial^2 u_x}{\partial y^2}\right)$$

Equation 21

As there is no pressure gradient in the x-direction and no velocity gradient in the z direction then:

$$\rho\frac{\partial u_x}{\partial t} = \eta\left(\frac{\partial^2 u_x}{\partial y^2}\right)$$

Equation 22

This implies that both sides of the equation are independently equal to some constant:

$$\rho\frac{\partial u_x}{\partial t} = \eta\left(\frac{\partial^2 u_x}{\partial y^2}\right) = C_1$$

Equation 23

$$\rightarrow u_x = \frac{C_1}{2\eta}y^2 + C_2 y + C_3$$

Equation 24

Using the assumptions and boundary conditions, the integration constants can be found:

$$C_1 = C_3 = 0$$

Equation 25

$$C_2 = \frac{V_p}{H}$$

Equation 26

Inserting the integration constants into Equation 24 leads to Equation 27 which gives the flow field as a function of the y-position within the sample. The magnitude of the velocity is greatest near the oscillating top plate and decreases towards zero as the stationary bottom plate is approached.

$$u_x = A_D \omega_D \frac{y}{H} Cos(\omega_D t)$$

Equation 27

The flow field is therefore a function of vertical position and time.

$$\rightarrow \underline{u}(y) = A_D \omega_D \frac{\mathrm{y}}{\mathrm{H}} Cos(\omega_D t) \widehat{\underline{e_x}}$$

Equation 28

The shear rate is constant throughout the gap at a given point in time.

$$\left| \frac{\partial \underline{u}(y)}{\partial y} \right| = \left| A_D \omega_D \frac{1}{\mathrm{H}} cos(\omega_D t) \right|$$

Equation 29

The Newtonian constitutive equation is given by:

$$\underline{\underline{\tau}} = \eta \underline{\underline{\dot{\gamma}}} = \eta \left[\nabla \underline{u} + (\nabla \underline{u})^T \right]$$

Equation 30

By substituting the velocity field into the above equation gives the relevant stress tensor as shown in Equation 31 which contains only shear components as expected.

$$\underline{\underline{\tau}} = \eta \begin{pmatrix} 0 & \frac{\partial u_x}{\partial y} & 0 \\ \frac{\partial u_x}{\partial y} & 0 & 0 \\ 0 & 0 & 0 \end{pmatrix}_{x,y,z} = \eta \begin{pmatrix} 0 & \frac{V_p}{H} & 0 \\ \frac{V_p}{H} & 0 & 0 \\ 0 & 0 & 0 \end{pmatrix}_{x,y,z}$$

Equation 31

$$\rightarrow \underline{\underline{\tau}} = \eta \begin{pmatrix} 0 & \frac{A_D \omega_D cos(\omega_D t)}{H} & 0 \\ \frac{A_D \omega_D cos(\omega_D t)}{H} & 0 & 0 \\ 0 & 0 & 0 \end{pmatrix}_{x,y,z}$$

Equation 32

$$\underline{\omega} = \nabla \wedge \underline{u} = \widehat{\underline{e_y}} \wedge \widehat{\underline{e_x}} \frac{\partial u}{\partial y}$$

Equation 33

$$\underline{\omega} = -\frac{A_D \omega_D}{\mathrm{H}} Cos(\omega_D t) \widehat{\underline{e_z}}$$

Equation 34

The above equation shows that during oscillatory shear flow, the direction of vorticity of the flow field oscillates between the positive and negative z-directions as expected. This has important consequences that will be discussed in chapter 3 and chapter 7.

The vorticity vector of a given flow field describes the local spinning motion due to a flow field. It points in the direction of the axis about which an object in the flow field at a given position and point in time would rotate around.

2.4 Squeeze Film Flows (SFF)

Squeeze film flow tests are carried out in the food and polymer industry frequently. The purpose of these tests is usually to obtain values of a material's yield stress or simply to test samples from a product line to see if they deform as expected for quality control purposes [149]. These are usually carried out at fixed squeezing force where the resulting deformation is observed, alternatively the squeezing rate is kept constant and the resulting normal force is recorded [150-153].

More advanced squeeze flow experiments have been devised in recent years which use piezoelectric transducers to sinusoidally squeeze and un-squeeze materials while recording the normal force to calculate the viscoelastic moduli at a range of frequencies [154-160]. It should be noted that at this time, there are few examples of apparatus that have been made commercially available due to their high expense and additional complexity when compared to more traditional rheometers.

The main exception to this is the Micro Fourier Rheometer (MFR) that was created in 2001 by the Australian company GBC [52,155]. It works by applying oscillatory squeeze film flow at random frequencies with a given peak strain and measuring the resulting oscillatory normal stress [158,161,162].

The term squeeze film flow (SFF) is used rather than squeeze flow to describe situations where very thin samples are being squeezed. Squeeze film flow has been described mathematically for Newtonian fluids and some standard viscoelastic and yield stress fluids [163-165]. However, little work has been done in comparison that connects how concentrated colloidal dispersions of particles flow during squeeze flow to their rheological properties, with a few exceptions [166].

Squeeze film flows where the no-slip condition is satisfied differ substantially from SFF where it is not satisfied. When perfect slip occurs such as when the squeezing plates are lubricated, then the flow is purely extensional and extensional flow properties can be directly measured. When the no slip condition is satisfied then the flow is more complicated due to shear and extensional flow taking place. It is however still possible to correct for shear stress terms to work out extensional components [167].

In this PhD, oscillatory squeeze film flow where the no-slip condition is satisfied was carried out upon a range of fluid systems. In these experiments however the shear components dominated the extensional components as will be shown in the next section.

2.5 Mathematical Description of Oscillatory Squeeze Film Flow Without Slip

An illustration of the main type of oscillatory squeeze film flow (OSFF) carried out in this PhD, which satisfies the no slip condition, is given in Figure 14. In this section a mathematical description of oscillatory squeeze film flow of a Newtonian fluid is outlined as it highlights a number of important issues that are relevant to later chapters.

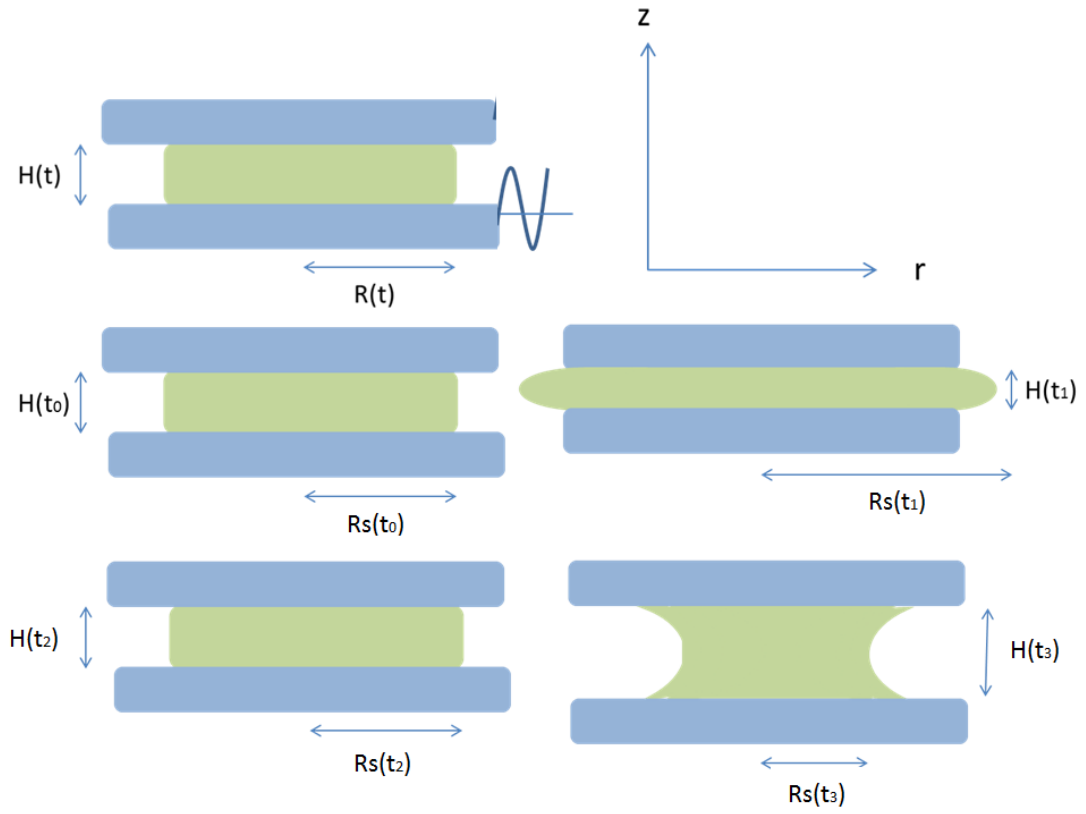

Figure 14 Example of squeeze film flow without wall slip initiated at t_0, the bottom plate oscillates upwards and downwards changing the gap distance resulting in the sample being squeezed and stretched. Note that in the experiments carried out in this PhD the radius of the samples compared to the height were many orders of magnitude greater than illustrated here.

2.5.1 Oscillatory Squeeze Film Flow without Slip Constraints

As the height of the sample being squeezed is decreased, the width of the sample in the *r* direction increases in order to conserve volume [168]. This type of flow has both shear and elongational components. If perfect slip where to occur instead in such squeeze flow, which occurs in lubricated biaxial extension flows, there would be only be extensional components[52]. The apparatus used to carry out this oscillatory squeeze film flow is shown in chapter 4.

Assumptions

1. There is no rotation of the fluid as it is squeezed and stretched which is observed to be the case and there is no variation of properties with angular position around the squeezing axis(θ is the angle around the z-axis):

$$\rightarrow \frac{\partial u_\theta}{\partial \theta} = 0$$

2. There is no significant curvature of the fluid surface as it is stretched and squeezed so that surface tension effects can be ignored.
3. The flow is steady at each point in time even though it is transient. This is valid for Re <<1.

Boundary Conditions

Fluid adheres to bottom plate(z=0) without slip where *V(t)* is the velocity of the oscillating bottom plate:

At $z = 0$: $u_z = V(t)$, $u_r = 0$

Fluid adheres to the top plate (z=H) without slip:

At *z= H*: $u_z = u_r = 0$

Governing Equations

Assuming the fluid being squeezed is incompressible and mass is conserved ,Equation 35 is a valid governing equation expressed in cylindrical cordinates:

$$0 = \nabla \cdot \underline{u} = \frac{1}{r}\frac{\partial (r u_r)}{\partial r} + \frac{1}{r}\frac{\partial u_\theta}{\partial \theta} + \frac{\partial u_z}{\partial z}$$

Equation 35

As there is no rotation, Equation 35 can be simplified:

$$\nabla \cdot \underline{u} = \frac{1}{r}\frac{\partial(ru_r)}{\partial r} + \frac{\partial u_z}{\partial z} = 0$$

Equation 36

The momentum balance on the system using Navier-Stokes equation expressed in cylindrical co-ordinates is shown in Equation 38 below where *p* is the equivalent pressure, where:

$$p = P - \rho g z$$

Equation 37

$$\rho\left(\begin{pmatrix}\frac{\partial u_r}{\partial t}\\ 0\\ \frac{\partial u_z}{\partial t}\end{pmatrix}_{r,\theta,z} + \begin{pmatrix}0\\0\\0\end{pmatrix}_{r,\theta,z}\right) = \begin{pmatrix}-\frac{\partial p}{\partial r}\\ 0\\ -\frac{\partial p}{\partial z}\end{pmatrix}_{r,\theta,z} + \eta\begin{pmatrix}\frac{\partial}{\partial r}\frac{1}{r}\frac{\partial(ru_r)}{\partial r} + \frac{\partial^2 u_r}{\partial z^2}\\ 0\\ \frac{1}{r}\frac{\partial}{\partial r}\frac{\partial(ru_z)}{\partial r} + \frac{\partial^2 u_z}{\partial z^2}\end{pmatrix}_{r,\theta,z}$$

Equation 38

At the bottom plate, the fluid motion is either uniformly in the positive or negative z-directions and is independent of the radial position. This implies that the z-component of the flow at a given position and moment in time can be represented as a function of z-position.

$$u_z = f(z)$$

Equation 39

2.5.2 Determination of the Squeeze Film Flow Velocity Gradients

From the mass conservation equation (Equation 36):

$$\frac{1}{r}\frac{\partial(ru_r)}{\partial r} = -\frac{\partial f(z)}{\partial z}$$

Equation 40

Integrating Equation 40 gives:

$$u_r = -\frac{r}{2}\frac{df(z)}{dz} + \frac{constant}{r}$$

Equation 41

The constant in Equation 41 must be zero to ensure that at r=0, u_r is finite.

$$u_r = -\frac{r}{2}\frac{df(z)}{dz}$$

Equation 42

Examining the components of Equation 38 and substituting in Equation 39 and Equation 42 gives Equation 43 and Equation 44:

$$0 = -\frac{\partial p}{\partial r} - \frac{1}{2}\eta r\frac{d^3 f(z)}{dz^3}$$

Equation 43

$$0 = -\frac{\partial p}{\partial z} + \eta\frac{d^2 f(z)}{dz^2}$$

Equation 44

Differentiating Equation 43 with respect to z gives Equation 45:

$$0 = -\frac{\partial^2 p}{\partial r \partial z} - \frac{1}{2}\eta r\frac{d^4 f(z)}{dz^4}$$

Equation 45

Differentiating Equation 44 with respect to r gives Equation 46:

$$0 = -\frac{\partial^2 p}{\partial r \partial z}$$

Equation 46

Substituting Equation 46 into Equation 45 gives Equation 47:

$$\frac{d^4 f(z)}{dz^4} = 0$$

Equation 47

Integrating Equation 47 with respect to z gives Equation 48:

$$f(z) = a + bz + cz^2 + dz^3$$

Equation 48

Using Equation 39 and Equation 42, the boundary conditions can be restated in a more convenient form.

Restated Boundary Conditions

Fluid adheres to bottom plate

$$\text{At } z = 0\text{: } f(z) = V(t), \frac{\partial f(z)}{\partial z} = 0$$

Fluid adheres to the top plate

$$At\ z = H(t)\text{: } f(z) = \frac{\partial f(z)}{\partial z} = 0$$

Using the boundary conditions, the constants *a,b,c* and *d* can be evaluated allowing the velocity field to be found as shown in Equation 49 and Equation 50:

$$u_z = f(z) = \left[V(t) - 3V(t)\left[\frac{z}{H(t)}\right]^2\left[1 - \frac{2}{3}\frac{z}{H(t)}\right]\right]$$

Equation 49

Equation 50 is obtained by substituting Equation 49 into Equation 42:

$$u_r = -\frac{r}{2}\frac{df(z)}{dz} = \frac{3rzV(t)}{(H(t))^2}\left[1 - \frac{z}{H(t)}\right]$$

Equation 50

$$\left|\frac{\partial u_r}{\partial z}\right| = \left|\frac{3rV(t)}{(H(t))^2}\left[1 - \frac{2z}{H(t)}\right]\right|$$

Equation 51

The above equation shows that the shear rate is zero when $z = 0.5H(t)$ and when $r = 0$. Additionally the shear rate increases with radial position and is greatest at the top and bottom plates at $z = H(t)$ and at $z = 0$ respectively. These facts are important to note, as they have consequences during the OSFF of suspensions of *D.Salina* as will be discussed in Chapter 7.

Substituting Equation 49 and Equation 50 into Equation 52 gives the extra stress tensor, which defines the stresses within the fluid at a given point [52].

$$\underline{\underline{\tau}} = \eta\underline{\underline{\dot{\gamma}}} = \eta\left[\nabla\underline{u} + (\nabla\underline{u})^T\right]$$

$$= \eta\begin{pmatrix} 2\left[\frac{\partial u_r}{\partial r}\right] & \left[r\frac{\partial\left(\frac{v}{r}\right)}{r\partial\theta} + \frac{1}{r}\frac{\partial u_r}{\partial\theta}\right] & \left[\frac{\partial u_r}{\partial z} + \frac{\partial u_z}{\partial r}\right] \\ \left[r\frac{\partial\left(\frac{v}{r}\right)}{r\partial\theta} + \frac{1}{r}\frac{\partial u_r}{\partial\theta}\right] & 2\left[\frac{1\partial u_z}{r\partial\theta} + \frac{\partial u_r}{r}\right] & \left[\frac{1\partial u_z}{r\partial\theta} + \frac{\partial u_\theta}{\partial z}\right] \\ \left[\frac{\partial u_r}{\partial z} + \frac{\partial u_z}{\partial r}\right] & \left[\frac{1\partial u_z}{r\partial\theta} + \frac{\partial u_\theta}{\partial z}\right] & 2\left[\frac{\partial u_z}{\partial z}\right] \end{pmatrix}_{r,\theta,z}$$

Equation 52

$$\underline{\underline{\tau}} = \eta\begin{pmatrix} \frac{6zV(t)}{(H(t))^2}\left[1-\frac{z}{H(t)}\right] & 0 & \left[\frac{3rV(t)}{(H(t))^2}\left[1-\frac{2z}{H(t)}\right]\right] \\ 0 & \frac{6zV(t)}{(H(t))^2}\left[1-\frac{z}{H(t)}\right] & 0 \\ \left[\frac{3rV(t)}{(H(t))^2}\left[1-\frac{2z}{H(t)}\right]\right] & 0 & -\frac{12zV(t)}{(H(t))^2}\left[1-\frac{z}{H(t)}\right] \end{pmatrix}_{r,\theta,z}$$

Equation 53

Equation 53 highlights another important issue. In squeeze film flow, when the radial distance is much greater than the gap distance, the shear terms (the terms in the top right and bottom left corners) generally dominate the extensional terms (the leading diagonal terms). This is important because in this PhD, a typical gap distance used for OSFF experiments was 1000µm while a typical sample radius was around 1.5cm.

2.5.3 Determination of Squeezing Forces and Velocities

Substituting Equation 49 into Equation 43 and rearranging gives:

$$\frac{\partial p}{\partial r} = -\frac{1}{2}\eta r\frac{d^3 f(z)}{dz^3} = \frac{6\eta V(t) r}{H^3}$$

Equation 54

Integrating Equation 54 with respect to *r* gives Equation 55 where *g(z)* is an unknown function of *z:*

$$p = -\frac{3\eta V(t) r^2}{H^3} + g(z)$$

Equation 55

Rearranging Equation 44 and integrating with respect to z gives where *h(r)* is an unknown function of *r* :

$$p = \eta \frac{\partial f(z)}{\partial z} + h(r) = -\frac{6\eta V(t) z}{H^2}\left(1 - \frac{z}{H(t)}\right) + h(r)$$

Equation 56

Combining Equation 55 and Equation 56 gives:

$$p = p_0 + \frac{3\eta V(t)}{H}\left(2\frac{z}{H(t)}\left(\frac{z}{H(t)} - 1\right) - \frac{r^2}{H^2}\right)$$

Equation 57

Additional Boundary Condition

At the outer edge at the top surface, the value of P is equal to the atmospheric pressure, where τ_{zz} is the normal stress on a plane whose normal points in the z-direction:

$$\text{At } z = H(t), \mathrm{r} = \mathrm{R}_s\text{: } 0 = \tau_{zz} = -P + 2\eta \frac{\partial u_z}{\partial z}$$

Equation 58

Substituting Equation 57 into the above initial condition gives Equation 59:

$$\text{At } z = H(t), \mathrm{r} = \mathrm{R}_s\text{: } 0 = \tau_{zz} = -p_0 + \frac{3\eta V(t) R_s^2}{H^3}$$

Equation 59

Inserting Equation 59 into Equation 57 gives an expression of the equivalent pressure scalar field:

$$p(r,z) = \frac{3\eta V(t)}{H}\left(2\frac{z}{H(t)}\left(\frac{z}{H(t)} - 1\right) - \frac{R_s^2 - r^2}{H^2}\right)$$

Equation 60

Neglecting the weight of the sample being squeezed, the force required by the bottom plate to move the bottom plate at a given velocity can be calculated by integrating the pressure at the bottom plate over the contact area:

$$F = \int_0^{Rs} 2\pi r p(r,0) dr = \int_0^{Rs} \frac{3\eta V(t)}{H^3}(R_s^2 - r^2) 2\pi r dr = \frac{3\pi\eta V(t) R_s^4}{2H^3}$$

Equation 61

The applied stress is therefore:

$$\tau = \frac{F}{A} = \frac{3\eta V(t) R^2}{2H^3}$$

Equation 62

Assuming the fluid droplet takes on a circular shape then:

$$F = \frac{3\pi\eta V(t) R_s^4}{2H^3}$$

Equation 63

In squeeze film flow, as the flat plates come closer together, the force required to further squeeze the fluid increases as is described by Equation 63. This effect needs to be considered during squeeze flow and for a Newtonian fluid the squeezing force is described here. The sinusoidal force exerted by the bottom plate during OSFF can be represented by Equation 64, where τ_p is the peak stress.

$$F = \tau_p Sin(\omega_D t)$$

Equation 64

Rearranging Equation 63 and substituting in Equation 64 gives:

$$V(t) = \frac{\tau 2H^3}{3\eta R_s^2} = \tau_p Sin(\omega_D t) \frac{2H^3}{3\eta R_s^2}$$

Equation 65

Integrating the above equation with respect to time gives the displacement of the bottom plate as shown below (care must be taken when applying this equation over a given interval as the above equation changes from being positive to being negative).

$$S(t) = \int \tau_p Sin(\omega_D t) \frac{2H^3}{3\eta R_s^2} dt = -\frac{\tau_p}{\omega_D} cos(\omega_D t) \frac{2H^3}{3\eta R_s^2}$$

Equation 66

Equation 65 gives the velocity of the bottom plate. As the gap distance decreases so does the velocity. Substituting Equation 65 into Equation 53 gives Equation 67 which defines the stress tensor at each point in the fluid.

$$\underline{\underline{\tau}} = \eta \begin{pmatrix} \frac{8z\tau H}{\eta R_s^2}\left[1-\frac{z}{H(t)}\right] & 0 & \left[\frac{4r\tau H}{\eta R_s^2}\left[1-\frac{2z}{H(t)}\right]\right] \\ 0 & \frac{8z\tau H}{\eta R_s^2}\left[1-\frac{z}{H(t)}\right] & 0 \\ \left[\frac{4r\tau H}{\eta R_s^2}\left[1-\frac{2z}{H(t)}\right]\right] & 0 & -\frac{16z\tau H}{\eta R_s^2}\left[1-\frac{z}{H(t)}\right] \end{pmatrix}_{r,\theta,z}$$

Equation 67

Equation 67 shows that as the applied stress increases, so does the shear and normal stress terms as expected.

2.5.4 Reynolds Number and Practical Considerations

As will be detailed in chapter 4 and chapter 6, glycerol (a viscous Newtonian fluid) was often subjected to OSFF as a baseline before concentrated suspensions were subjected to the same OSFF. It is useful here to show some example calculations that describe some experimental parameters during the OSFF of glycerol.

A typical peak applied squeezing stress was 1000Pa and the typical sample radius was approximately 1.5cm, the gap distance used was 1000 microns. The viscosity of glycerol at standard conditions is 1.42Pa.s [169], which is of a similar order to the concentrated suspensions examined in this thesis except sometimes when extreme DST was occurring.

Substituting this data into Equation 65 shows that the maximum instantaneous velocity the bottom plate should be able to achieve during squeezing/stretching is around 2000 µm.s^{-1} as shown below.

$$V(t) = \frac{(\pm 1000)[Pa]\,2(0.001)^3[m]^3}{3(1.42)[Pa.s](0.015)^2[m]^2} \approx \pm 0.002[m.s^{-1}] = \pm 2000[\mu m.s^{-1}]$$

The corresponding maximum displacement of the bottom plate during such an OSFF cycle at 40Hz from its initial position can be estimated from Equation 66 as shown below:

$$S(t) = \frac{(\pm 1000)[Pa]2(0.001)^3[m]^3}{2\pi 40[s^{-1}]3(1.42)[Pa.s](0.015)^2[m]^2} \approx \pm 8[\mu m.s^{-1}]$$

This means that during an OSFF cycle the maximum peak to peak displacement of the bottom plate is ≈16µm. This shows the displacement of the bottom plate is small relative to the gap distance. This has an important consequence that will be discussed in chapter 4.

It is important to have an idea of what the maximum shear stress occurring within a sample during OSSF is at a given peak squeezing or stretching stress applied by the bottom plate. Substituting the relevant data Equation 67 into allows the maximum shear stress term during OSFF to be calculated (which occurs at the top and bottom plates where r=R).

$$\tau_{zr} = \frac{4r\tau_p H}{\eta R_s^2}\left[1 - \frac{2z}{H(t)}\right] = \frac{4[0.0015]1000(0.001)}{1.42[0.0015]^2}\left[1 - \frac{2(0)}{0.001}\right] \approx 1900[Pa]$$

From this example we see that, the maximum shear stress within the sample is actually higher than the applied squeezing or stretching stress.

In order for the initial assumption of stokes flow to be valid, the value of the Reynolds number for squeeze flow needs to be much less than 1 as shown in Equation 68[168].

$$Re = \frac{4\tau_p \rho H^4}{3\eta^2 R_s^2} \ll 1$$

Equation 68

As mentioned previously, the maximum peak applied stress used was around 1000Pa, a typical sample radius was 1.5cm and the gap distance was 1000 microns. Substituting this data into Equation 68 shows that the assumption of Re <<1 is valid when squeezing glycerol.

$$Re = \frac{4(1000)[Pa]1261[Kg.m^{-3}](0.001)^4[m]^4}{3(1.42)^2[Pa.s]^2(0.015)^2[m]^2} \approx 0.004$$

Because the concentrated suspensions examined in this PhD had viscosities of a similar order to glycerol or higher, then we can be certain that the Reynolds number was always very small meaning that the assumption of Re <<1 was always valid.

2.6 Summary of Oscillatory Squeeze Flow

- As the gap distance decreases, then for a given applied squeezing or stretching stress, the magnitude of the plate velocity decreases rapidly as it is directly proportional to the gap distance cubed.
- At a given point in time the shear rate is dependent on radial and vertical positions within a sample. The shear rate is zero on the central vertical axis where $r=0$, and on the central horizontal plane where $z=H/2$.
- At the central horizontal plane within the sample, the shear rate is zero at all radial positions. However on all other horizontal planes the shear rate increases with radial position within the sample.
- On a given horizontal plane where $r\neq0$, as vertical distance away from the central horizontal axis increases the magnitude of the shear rate increases.
- On a given horizontal axis where $z\neq H/2$, as radial distance away from the central vertical axis increases, the magnitude of the shear rate increases.

Chapter 3 Introduction to Microalgae in Complex Flows

3.1 Chapter Summary

In this chapter a brief introduction to microalgae and their current and potential uses is given. Special attention is focused on swimming microalgae grown industrially and in particular the species known as *Dunaliella Salina*. The existing literature on the behaviour of swimming algae in a variety of flow conditions is briefly explored. A model from literature which describes many aspects of *D.Salina's* behaviour is also explored and is applied to the situation of parallel plate oscillating shear flow described in the previous chapter. In contrast to colloidal particles and emulsions *etc,* suspensions of swimming algae are essentially suspensions of particles that are motile, *ie* impose their own transport as well as being transported by flow. Hence one expects the response of motile particles to potentially differ from how non-motile particles respond in a variety of flow situations.

3.2 What are Algae?

Algae is a very vague and broad term that can be applied to a diverse range of chlorophyll containing organisms that are primarily Eukaryotic and are usually classed as being from the kingdom Protista. There are almost 100,000 different known species, many of which are unicellular and are called microalgae while others are multicellular and may grow well over 20 metres in size such as the giant Kelp. Algae are distinguished from plants by the fact they lack roots and other structures, however like plants they can use sunlight to produce their own food using carbon dioxide and water through photosynthesis. Most algae are aquatic although some are capable of living on land. Some live in fresh water while others live in salt water. Some types of microalgae can be described as being flagellate, meaning that they possess one or more flagella which are relatively long thin whip like appendages used to propel themselves through suspending media. Textbooks are available that describe the various known types of algae in great detail [170].

3.3 Current Uses of Microalgae

Microalgae are currently grown on an industrial scale in photo-bioreactors of various designs for use in health foods, vitamin supplements and cosmetics. Due to food safety

regulations and commercial factors, the market for microalgae is dominated by three species; *Chlorella, Spirulina and Dunaliella Salina*. *Chlorella* and *Spirulina* are commercially grown because their protein content can be as high as nuts and they contain high amounts of β-carotene and vitamins A and B as well as a wide range of other vitamins and nutrients in smaller amounts. *Dunaliella Salina* is grown for industrial production of β-carotene and vitamin A. *D. Salina* can manufacture 50-times the β-carotene that *Spirulina* can produce and can tolerate extremely high salt concentrations that most potential contaminants cannot survive in, making cultivation relatively easy [171].

3.4 Potential Uses of Microalgae

Microalgae are currently being investigated for biofuel production, carbon capture and wastewater treatment. Microalgae have simple growing requirements such as light, CO_2 and the elements N, P, and K. Through photosynthesis they can produce lipids, carbohydrates and proteins within their structures that can then be processed into biofuels. Microalgae and in particular *D.Salina* have the potential to produce biofuels in higher yields than even the best oilseed crops currently being used to produce biofuels as they can be grown all year long. They have the added advantage that they need less water than terrestrial crops and can be cultivated in brackish water on non-fertile land meaning that using microalgae, unlike crops, to produce biofuels would not necessarily have an adverse effect on food supplies. It has yet to be shown that production of biofuels from microalgae is economically feasible. This is partly due to the fact that cells currently need to be concentrated through the use of centrifuges which are energy intensive [172]. As a result of this, there is interest in developing methods to promote self-concentration of swimming algae [173]. Research is also being done on the possibility of increasing the profitability of such processes through the collection of valuable co-products. Additionally just as crops have been the targets of genetic engineering experiments to enhance their productivity and tolerance limits so have algae, which could increase their industrial potential [171,174].

3.5 Important Behaviours of Swimming Microorganisms

Swimming microorganisms are known to show a variety of interesting behaviours and responses that separate them from lifeless passive particles. The term bioconvection refers to the formation of patterns of swimming microorganisms within a suspension. Bioconvection is a result of certain 'taxes' exhibited by certain swimming microorganisms. A taxis is a movement of a given organism in response to certain stimuli found in its surrounding environment such as the presence of light and heat sources for example. There are a variety of different taxes that can cause organisms to bias their movements in certain directions. In principle the taxes that a given cell exhibits can be used to guide that cell.

Some swimming algae can be referred to as being gyrotactic. Gyrotaxis describes the way in which the swimming directions of a microorganism may be guided by how gravitational and viscous forces act on an organism whose mass is distributed asymmetrically [175]. Many microorganisms like *D.Salina* are bottom heavy. When bottom heavy organisms are within a flow field, their swimming direction is heavily influenced by the combination of the viscous drag, which generally acts to orientate them in the direction where the flow is most rapid and the gravitational torque which acts to orientate them upwards [176,177].

Microrganisms can be referred to as phototactic if they are sensitive to light intensity gradients, that is, they move towards or away from the stimulus of light. Organisms which require light for photosynthesis generally display positive phototaxis which means they swim towards regions of higher light intensity, however if the light intensity is too high then they can also display negative phototaxis. This has consequences in designing bio-reactors for phototactic microorganisms as they have a tendency to swim towards surfaces in search of light and in so doing fouling the surface. This blocks light for the rest of the microrganisms within the reactor [173].

Chemotaxis is the movement in response to the presence of certain chemicals in the surrounding environment. Positive chemotaxis is said to occur if the movement of the organism is in the direction of increasing concentration of the chemical in question, while negative chemotaxis is said to occur if the movement is in the direction of decreasing

concentration. Many organisms have evolved displaying positive chemotaxis towards chemicals which they feed upon. *E.coli* for example swims along oxygen gradients [178].

3.6 Swimming Microorganisms in Flows

In both natural and industrial environments, microorganisms reside within fluids which undergo flow. Recent investigations of micro swimmers in flows have resulted in a number of bioconvection patterns that could potentially be relevant to the design of photobioreactors and an understanding of how suspensions of micro-swimmers can self-organize [179-181].

For example recent investigations by Garcia and co-workers have shown that it is possible exploit the combination of gyrotactic and phototactic biases of micro-swimmers in Poiseuille flows [173]. In their experiments they showed that by using the right combination of light stimuli and flow vorticity that it was possible to influence their swimming directions and force the algae to self-concentrate at the centre of a channel. This has the potential to reduce the accumulation of algae at pipe walls and prevent fouling of surfaces due to adhesion.

The classical Taylor dispersion of passive particles has been shown to be very different from that involving gyrotactic algae in that they drift faster and disperse less [180]. The rheology of suspensions containing dispersed swimming microorganisms has also shown counterintuitive results. Recently it has been discovered that bacterial suspensions containing live cells are less viscous than bacterial suspensions containing only dead cells, while algal suspensions of live swimming algae are more viscous than suspensions containing only dead algae cells [182].

3.7 Description of Dunaliella Salina

In this PhD we are primary concerned with a specific species of green biflagellate single celled algae called *Dunaliella Salina* that belongs to the phylum Chlorophyta. It is a halophile meaning that it prefers to live in media of high salt concentrations; however it can adapt to live in very low salt concentrations. The behaviour and chemical composition of *D.Salina* is highly dependent on the salt concentration in its suspending media. *D.Salina* primarily reproduces asexually through cell division, however at low salt concentrations sexual reproduction is also significant [183].

D.Salina lacks a rigid cell wall and in order to protect the cell from osmotic pressure associated with living in high salinity environments, it produces glycerol to balance osmotic forces and also maintains enzyme activity. *D.Salina* also produces β-carotene to inhibit the formation of free radicals due to interaction with ultraviolet light. It has been found that glycerol and β-carotene production is highly dependent on the salinity of the medium and is greatest at high NaCl concentrations in the range of 1.5-5M. *D.Salina* also has a very wide pH tolerance ranging from a pH of 1-11, and is tolerant to environmental temperatures ranging from below 0^0C to around 45^0C. It is therefore one of the most environmentally tolerant known eukaryotic organisms which is a major industrial selling point [183].

The shape of *D. Salina* varies depending on environmental conditions, but those used in this PhD were partially ellipsoidal in shape. It is bottom heavy, this means that in a stagnant body of water they are biased to swim upwards due to a gravitational torque that acts to make cells face upwards. There is also a sedimentation torque due to the fact that their bodies are denser than their flagella. This effect of certain algae tending to swimming upward on average is known as gravitaxis [175].

D.Salina is morphologically similar to *Chlamydomonas reinhardtii* which is a commonly used microorganism for experiments in literature. The main difference is that C. *reinhardtii* possesses a rigid cell wall. Both possess flagella of equal length and both are of similar shape and size (roughly 12 microns in diameter). Both display chemotactic, phototactic, gravitactic, and gyrotactic behaviour [183,184].

D.Salina swims at a modal speed of around 60μm/s by pulling itself forward in a breaststroke like fashion by beating its flagella at around 50Hz. As it swims it rotates at a frequency of 2Hz along the longitudinal axis and traces out a helical path [185].

3.8 Swimming Microalgae Literature

A model describing how the orientation of gravitactic helical swimming algae is dependent on flow parameters and characteristics of the algae was given by Bearon[186]. The model was based on a species of spherical swimming algae called *Heterosigma akashiwa* which switches between straight and helical swimming patterns. This alga has a leading flagellum that sends waves along its length and pulls the organism forward. This organism also has a 2nd flagellum at its side however it is not clear what its function is. The model is valid for other species of algae as long as certain parameters that correspond to unique characteristics of the algae under consideration are changed. Similar models which neglect helical swimming have been qualitatively successful at predicting the observed phenomenology of gravitactic algae [181,187].

In this model $\underline{V}$ is the local fluid velocity, $\underline{p}$ is a unit vector that points in the direction that the cell is swimming in, $v\underline{p}$ is the swimming velocity vector. The 2nd flagellum produces an intrinsic torque (due to the way in which the alga beats its flagella resulting in a rotational torque) which points in direction of the unit vector $\underline{n}$ resulting in helical motion [186]. The unit vector $\underline{n}$ can be thought of as the axis which the alga rotate around as they swim in the direction of $\underline{p}$. This is illustrated in Figure 15.

The change in cell position $\underline{r}$, can be given by the following equation:

$$\frac{d\underline{r}}{dt} = \underline{V} + v\underline{p}$$

Equation 69

The cell rotates with an angular velocity, $\underline{\Omega}$, given by Equation 70 where ω_G and ω_H represent the strength of the gravitactic and intrinsic torques respectively. The symbol Λ represents the vector cross product and ω is the vorticity of the surrounding local flow field.

$$\underline{\Omega} = \omega_G \underline{p} \wedge \underline{\hat{e}_y} + \omega_H \underline{n} + \frac{1}{2}\underline{\omega}$$

Equation 70

Equation 71 represents how swimming direction changes with time which is given by the cross product of the swimming direction and the cell's angular velocity.

$$\frac{d\underline{p}}{dt} = \underline{\Omega} \wedge \underline{p}$$

Equation 71

Equation 72 represents how the direction of the intrinsic torque changes with time, which is given by the cross product of the cell's angular velocity and direction of the intrinsic torque.

$$\frac{d\underline{n}}{dt} = \underline{\Omega} \wedge \underline{n}$$

Equation 72

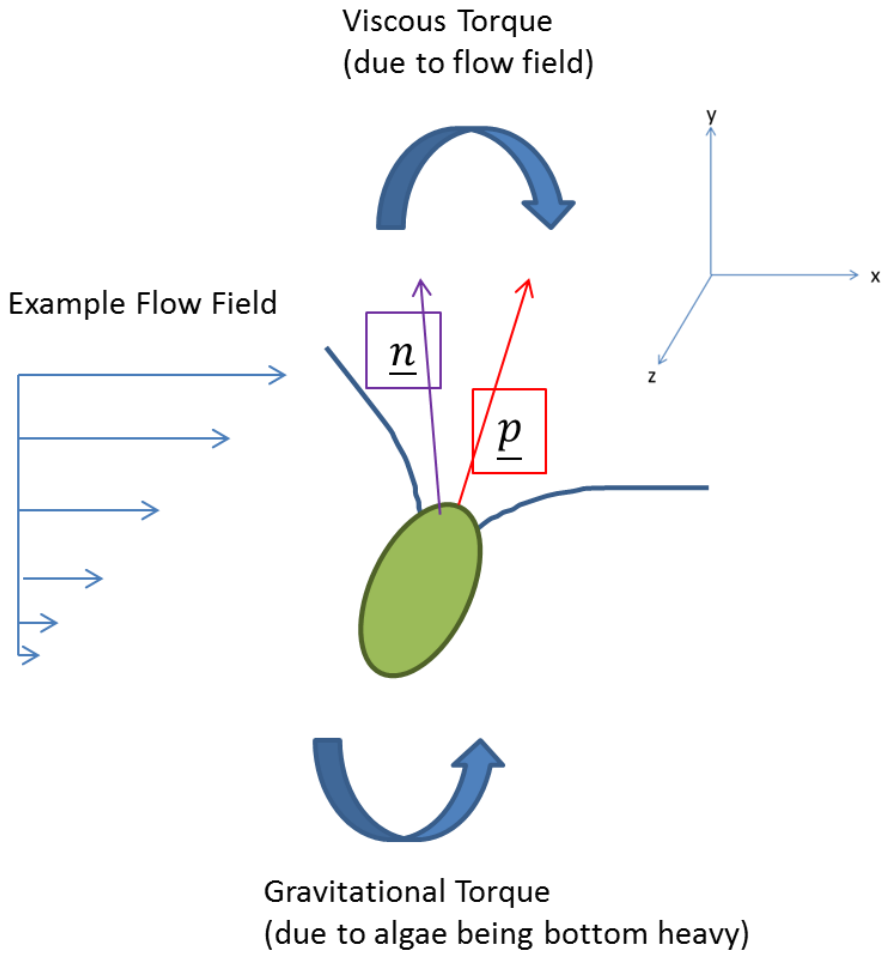

Figure 15 Illustration of a bottom heavy biflagellate algae swimming through a flow field corresponding to parallel plate shear flow. In this case shear flow causes a viscous torque that acts to rotate the alga downwards while the gravitational torque acts to rotate the alga upwards. The alga swims in the direction of p but rotates as it does so around n. This results in helical swimming as the swimming direction also rotates around n.

3.9 Model of *D.Salina* in Parallel Plate Oscillatory Shear Flow

In this PhD, the motion of *D.Salina* in oscillatory parallel plate shear and squeeze film flows was examined experimentally. In this section, the oscillating flow field described in section 2.3 and the ranges of the experimental parameters described in section 4.5, relevant to the parallel plate shear experiments carried out in suspensions of *D.Salina* are substituted into Bearon's model [185-186].

3.9.1 Relevant Scales

It is first useful to define some scales to make the analysis easier.

The significant time period is given by the period of oscillation of the top plate:

$$\tau = \frac{1}{\omega_D}$$

Equation 73

The significant length scale is given by amplitude of displacement of the top plate:

$$l = A_D$$

Equation 74

Dimensionless displacement is given by:

$$r' = \frac{r}{l} = \frac{r}{A_D}$$

Equation 75

Dimensionless time is given by:

$$t' = \frac{t}{\tau}$$

Equation 76

3.9.2 Dimensionless Mixed Equations

By substituting the scales defined in the previous section, Equation 70 and the flow field defined by Equation 28, into Equation 69, Equation 71 and Equation 72 respectively, gives the following dimensionless mixed equations[189]. The unit vectors in the x, y and z directions are given by $\underline{\hat{e}_x}$, $\underline{\hat{e}_y}$ and $\underline{\hat{e}_z}$ respectively:

$$A_D\omega_D\frac{d\underline{r}'}{dt'} = \omega_D y'\frac{A_D}{H}Cos(t')\underline{\hat{e}_x} + v\underline{p}$$

Equation 77

$$\omega_D\frac{d\underline{p}}{dt'} = \left[\omega_G\underline{p}\wedge\underline{\hat{e}_y} + \omega_H\underline{n} - \omega_D\frac{1}{2}\frac{A_D}{H}Cos(t')\underline{\hat{e}_z}\right]\wedge\underline{p}$$

Equation 78

$$\omega_D\frac{d\underline{n}}{dt'} = \left[\omega_G\underline{p}\wedge\underline{\hat{e}_y} + \omega_H\underline{n} - \omega_D\frac{1}{2}\frac{A_D}{H}Cos(t')\underline{\hat{e}_z}\right]\wedge\underline{n}$$

Equation 79

Grouping together the constant coefficients from Equation 77 to Equation 79 gives the following new dimensionless parameters.

$$\alpha = \frac{A_D}{H}, \beta = \frac{v}{A_D\omega_D}, \Omega_G = \frac{\omega_G}{\omega_D}, \Omega_H = \frac{\omega_H}{\omega_D}$$

Dropping the primes, and substituting in the above parameters into Equation 77 to Equation 79 gives:

$$\frac{d\underline{r}}{dt} = \alpha y\frac{A_D}{H}Cos(t')\underline{\hat{e}_x} + \beta\underline{p}$$

Equation 80

$$\frac{d\underline{p}}{dt} = \left[\Omega_G\left(\underline{p}\wedge\underline{\hat{e}_y}\right)\wedge\underline{p} + \Omega_H\underline{n}\wedge\underline{p} - \frac{1}{2}\alpha Cos(t)\underline{\hat{e}_z}\wedge\underline{p}\right]$$

Equation 81

$$\frac{d\underline{n}}{dt} = \left[\Omega_G\left(\underline{p}\wedge\underline{\hat{e}_y}\right)\wedge\underline{n} - \frac{1}{2}\alpha Cos(t)\underline{\hat{e}_z}\wedge\underline{n}\right]$$

Equation 82

3.9.3 Example Parameters

In this subsection, the experimental parameters relevant to the oscillatory parallel plate shear flow experiments carried out during this PhD are substituted. The purpose of this is to show the relative importance of the parameters involved on the movement of the algae.

The gap distance used in parallel plate shearing experiments was always 400µm, therefore:

$$H = 400\mu m$$

The displacement of the top plate during parallel plate shearing experiments was in the range of 55-262µm, therefore:

$$A_D = 55 - 262\mu m$$

The range of shearing frequencies used during parallel plate shearing experiments in the range of 0.5-6Hz, therefore:

$$\omega_D = 2\pi f_D = 2\pi(0.5 - 6s^{-1}) = 3.1 - 38s^{-1}$$

The gravitactic reorientation time of *D.Salina* is approximately 10 seconds [185], therefore:

$$\omega_G = \frac{1}{2\tau_G} = 0.05s^{-1}$$

The frequency at which *D.Salina* rotates is around 2Hz [185].

$$f_H = 2s^{-1}$$

Therefore the angular frequency at which it rotates is:

$$\omega_H = 2\pi f_H = 2\pi(2s^{-1}) = 12.6rad.s^{-1}$$

The modal speed of *D.Salina* is around:

$$V_s = 60\mu m s^{-1}$$

Substituting these values into the dimensionless coefficients gives:

$$\alpha = \frac{A_D}{H} = \frac{55 - 262\mu m}{400\mu m} = 0.14 - 0.66$$

$$\beta = \frac{V_s}{A_D \omega_D} = \frac{60\mu m s^{-1}}{(55 - 262\mu m)(3.1 - 38 s^{-1})} = 6 \times 10^{-3} - 0.35$$

$$\Omega_H = \frac{\omega_H}{\omega_D} = \frac{12.6 s^{-1}}{(3.1 - 38 s^{-1})} = 0.3 - 4.1$$

$$\Omega_G = \frac{\omega_G}{\omega_D} = \frac{0.05 s^{-1}}{(3.1 - 38 s^{-1})} = 10^{-3} - 0.016$$

As Ω_G is always low relative to the other terms (meaning gravity has little effect on the algae's swimming direction in such oscillatory flows), then Equation 81 and Equation 82 can be simplified into Equation 83 and Equation 84 respectively:

$$\frac{d\underline{p}}{dt} = \left[\Omega_H \underline{n} - \frac{1}{2}\alpha Cos(t)\underline{\hat{e}_z}\right] \wedge \underline{p}$$

Equation 83

$$\frac{d\underline{n}}{dt} = \left[-\frac{1}{2}\alpha Cos(t)\underline{\hat{e}_z} \wedge \underline{n}\right]$$

Equation 84

Chapter 4 Apparatus and Methods

4.1 Chapter Summary

This chapter describes the main apparatus developed in this work and used in experiments throughout this PhD. It starts with describing the electromechanical squeeze cell and how it was used to carry out oscillatory squeeze film flow on samples of particulate suspensions with a gap distance of 1000 microns, as well as algal suspensions with a gap distance of no more than 400 microns. A variety of squeezing frequencies and peak squeezing forces were used.

It then goes on to describe the electromechanical shear cell, which was used to carry out oscillatory shear flow on samples of algae with a gap distance of 400 microns at frequencies in the range of 0.5-6Hz at a variety of shearing amplitudes. It finishes by describing the piezoelectric squeeze cell that was used to squeeze samples of algae suspensions with a gap distance of 300 microns and at frequencies in the range of 0.5-3Hz.

A brief introduction is also given into to how particle tracking software works and in particular how particle tracking was used to track *Dunaliella Salina* in oscillatory flows and how the resulting data was then analysed.

4.2 Electromechanical Squeeze Cell Description

The electromechanical squeeze cell ESC, squeezes droplets of fluids between a mobile glass bottom plate and a glass cover slip supported by an aluminium stationary plate which is screwed on to an aluminium base plate. The glass plate is moved up and down in an oscillatory manner by electromechanical exciter drivers as illustrated in Figure 16. The apparatus was placed underneath a microscope objective so that the local deformation of samples within the ESC can be viewed and recorded using a high speed camera. The macroscopic deformation could be seen by using a camera without a microscope.

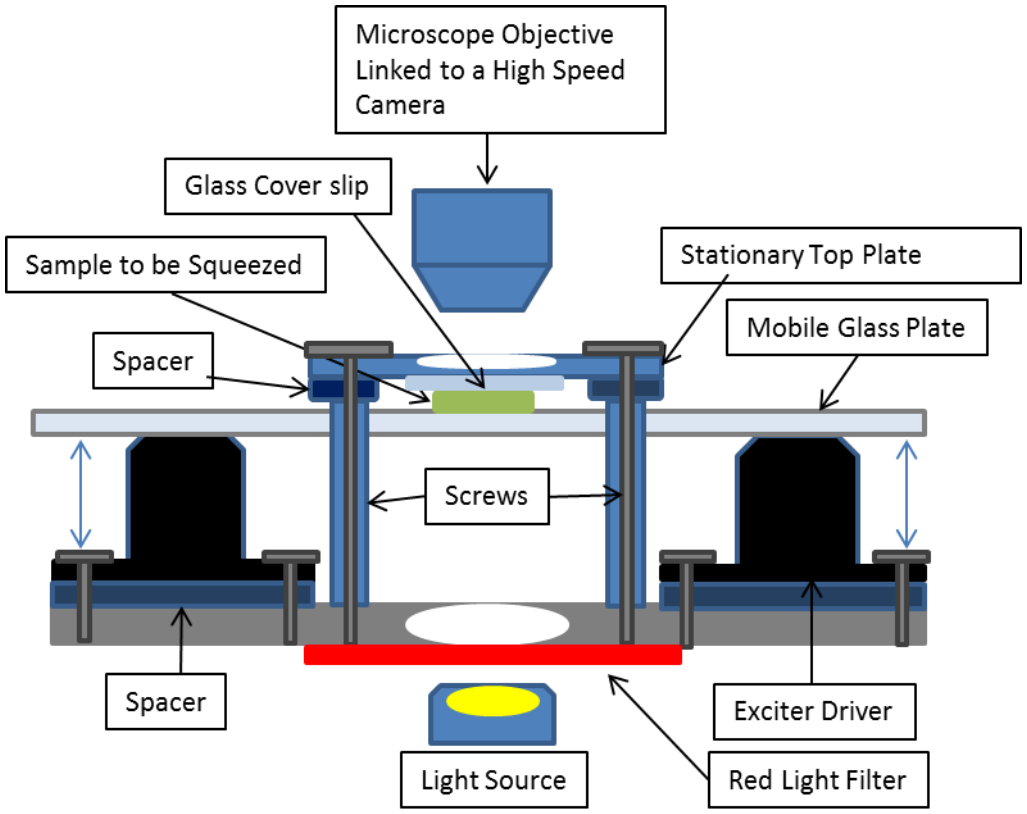

Figure 16 Labelled diagram of the electromechanical squeeze cell.

A sinusoidal DC voltage is applied by a TG310 function generator which is then amplified and then passed to the Visaton EX 45S exciter drivers as is illustrated in Figure 17. This causes the exciter drivers to oscillate upwards and downwards at the same frequency as the original applied voltage signal.

In order to prevent noise generated by one exciter driver from affecting the other, the signal from the function generator is split between 2 different amplifiers, each of which is powered by a separate DC power supply operating at 12 volts.

In order to prevent electrical noise in the mains supply from affecting the DC power supply, the power supplies were plugged into a Tacima gang socket containing an audio noise filter. The signal that reaches each separate exciter driver is in phase with the other.

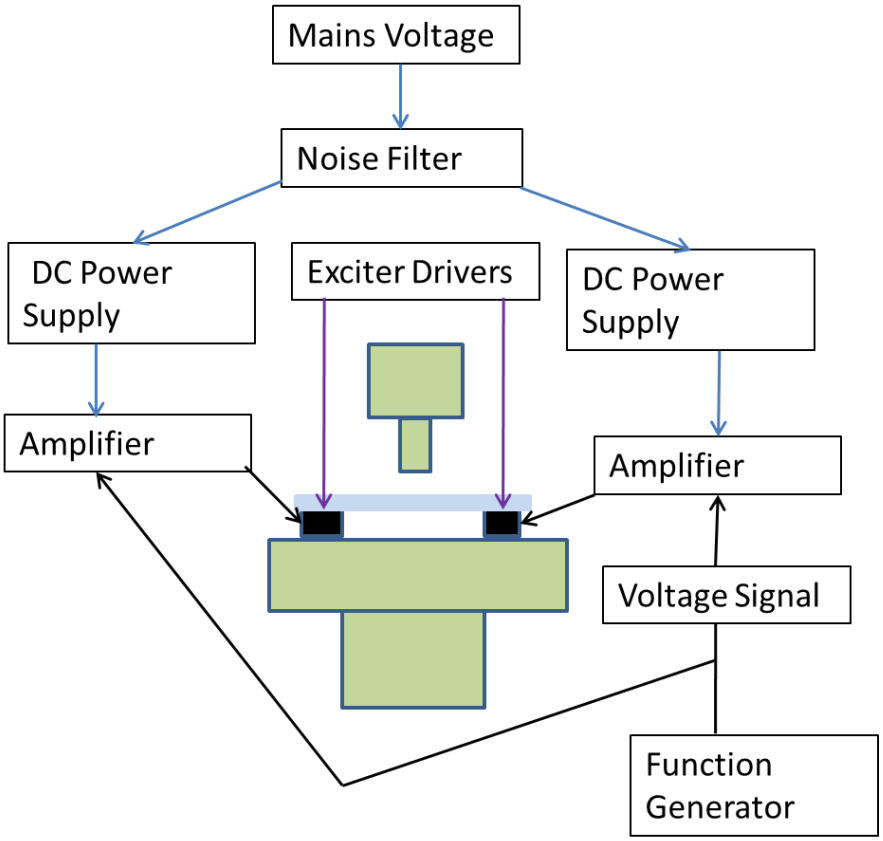

Figure 17 Diagram of the overall layout of the apparatus. Black lines show the direction of the signal from the function generator. Blue lines show where the power to the amplifiers comes from.

The peak force exerted by the glass plate at a given frequency of oscillation can be controlled within a limited range by altering the pre-amplified voltage from the function generator. The frequency of oscillation can be altered by changing the frequency of the applied voltage waveform using the function generator.

4.3 Calibration Issues with the Electromechanical Squeeze Cell

The amplifiers were required in the setup shown in Figure 17 because the function generator had a high internal resistance of 50 Ohms compared to the resistance of the exciter drivers which is only 8 ohms. The function generator could only apply a voltage of between 20 and -20 volts. This meant that only small voltages could be developed over the exciter drivers without an amplifier because most of the voltage would be developed over the function generator itself. Ideally the requirement for amplifiers could be avoided by the use of a function generator capable of producing much stronger voltage signals.

4.3.1 Peak Applied Force

A problem with amplifiers is that the degree to which they step up the power of the original signal passing through them is dependent on the frequency of the incoming signal. This means that as the frequency of the signal increases, the power passing through the exciter drivers increases. This means that the peak stress applied by the bottom plate increases with frequency for a given pre-amplified signal as illustrated in Figure 18:

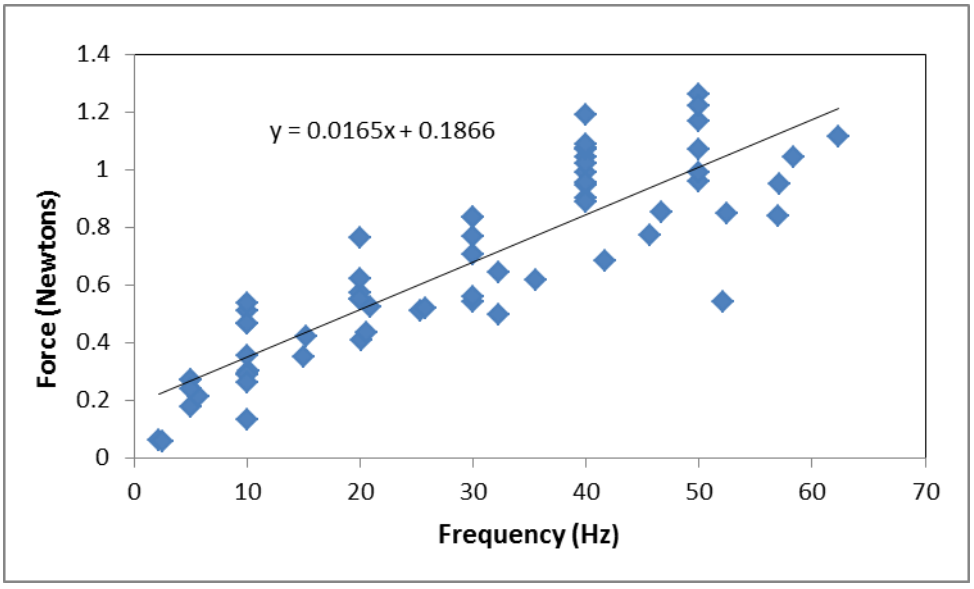

Figure 18 Frequency vs. Peak force detected by an A201 Force sensitive resistor at a fixed pre-amplified voltage of 112mV.

As frequency of a signal with a constant applied pre-amplified voltage is increased the detected force increases. These results were obtained by squeezing a metal puck against the force sensitive resistor (FSR) within the exciter driver squeezer and measuring the change of resistance (or conductance) using a National Instrument DAQ device. This is

illustrated in Figure 19. The peak squeezing force can be easily converted to a peak squeezing stress if the contact area between the plates and the material being squeezed is known.

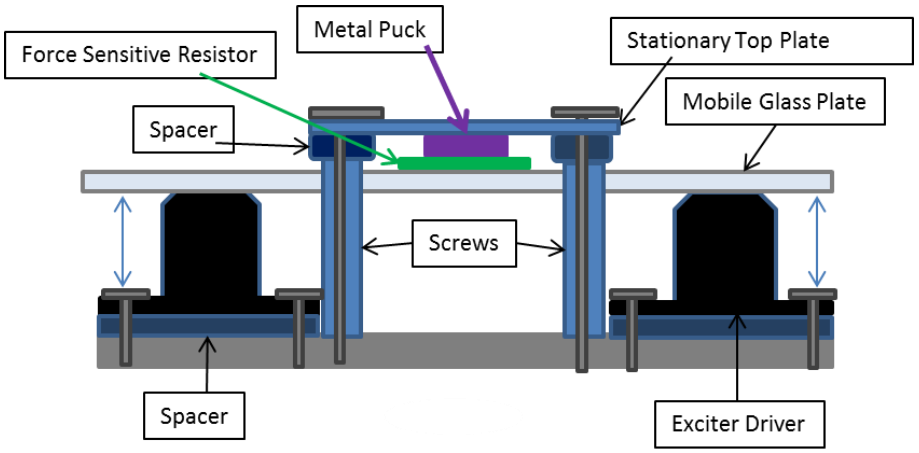

Figure 19 This is the arrangement used to determine the peak force applied by the ESC during squeezing.

The change of conductance of the FSR due to the applied squeezing force of the bottom plate can then be converted to a force by comparing with a calibration curve as shown in Figure 20. This curve was constructed by applying a known force to the FSR and measuring the change of the conductance.

The DAQ device used to monitor the resistance of the FSR was the NI-USB-6251, this has an extremely high sampling rate and is very sensitive so that it can detect small voltages developed over a resistor.

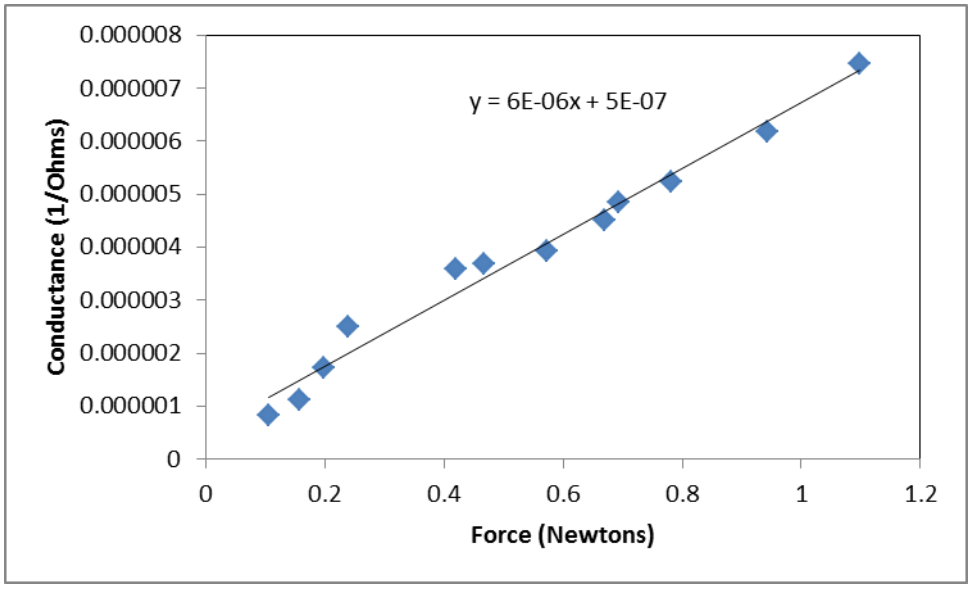

Figure 20 Calibration curve of the conductance of the A201 Force sensitive resistor at a given applied force. This curve was created by applying known forces to the FSR and noting the conductance.

Figure 21 shows that at a given applied frequency, the force from the ESC can be varied by altering the peak voltage. This means that it is possible to increase the frequency while keeping the applied peak force constant by adjusting the supplied voltage. It should be noted that above 40 Hz, it is more difficult to measure the peak force over such short squeezing cycles which accounts for the scatter in the recorded forces on both Figure 18 and Figure 21.

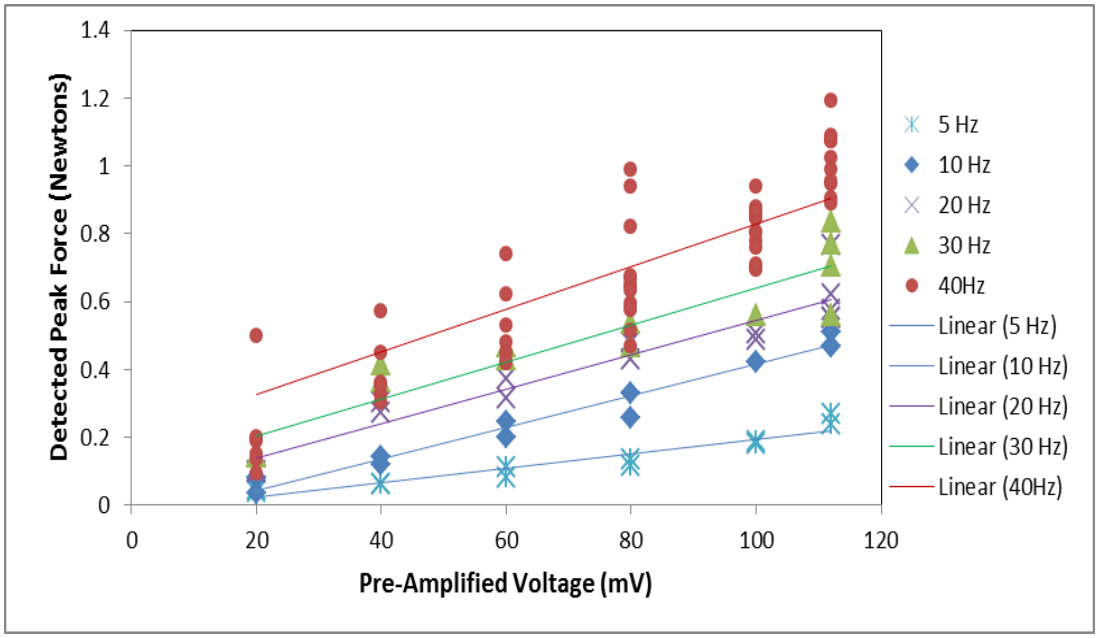

Figure 21 Detected peak force vs. applied pre-amplified voltage for a set of frequencies. Here the frequency of the applied voltage signal is held constant while the pre-amplified voltage is varied. As the pre-amplified voltage is increased for a given squeezing frequency, the detected force that is measured by the A201 force sensor increases.

Figure 18 and Figure 21 imply that the squeezing force is highly variable but this is not the case in practise. The reason for the relatively large spread in the detected forces is due to the difficulty in measuring the peak force, rather than the peak force exerted by the ESC at a given set of conditions being erratic. In practise the peak squeezing force applied by the ESC at a given applied voltage and frequency is highly consistent. This is known to be the case because consistent and reproducible deformation is observed when squeezing fluids at a given set of conditions.

In this PhD Figure 18 and Figure 21 were used as calibration curves to estimate the applied peak squeezing force at a given set of conditions. Although the peak squeezing forces are consistent which each other, it must be noted that the true value of the applied peak force and therefore peak stress is not precisely known. This is due to difficulties in using the FSR to measure rapidly changing forces.

4.3.2 Maximum Displacement

Another complication of the experimental set-up was that even when nothing but air was being squeezed, the maximum possible displacement of the bottom plate increased with frequency for a given pre-amplified voltage signal. This is once again because the gain of the amplifiers used to increase the power of the signal from the function generator increases with frequency. This is illustrated in Figure 22 and Figure 23:

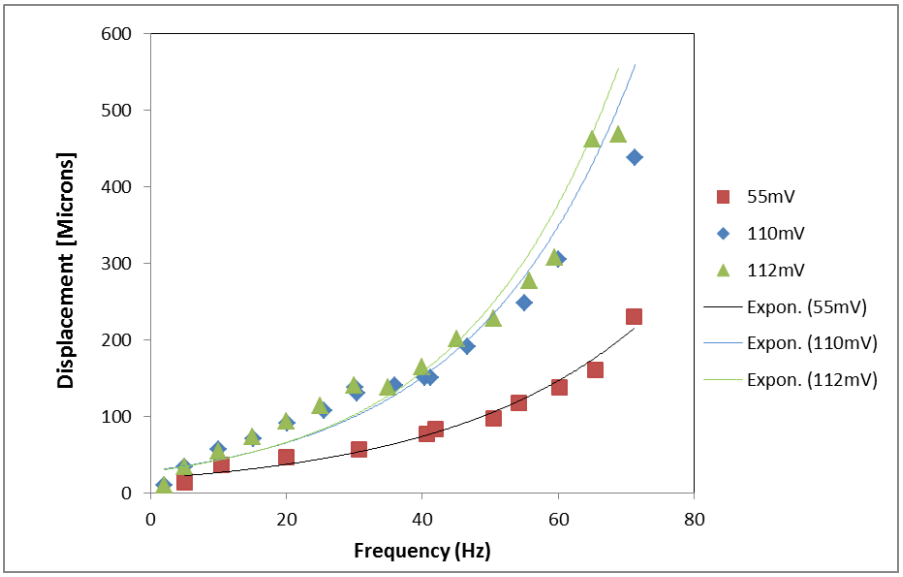

Figure 22 Frequency vs. observed peak to peak distance of an exciter driver for a given pre-amplified voltage. As frequency increases for a given pre-amplified voltage, the displacement increases. Obtained by observing one of the exciter drivers on its side while oscillating under underneath a microscope objective as illustrated in Figure 24.

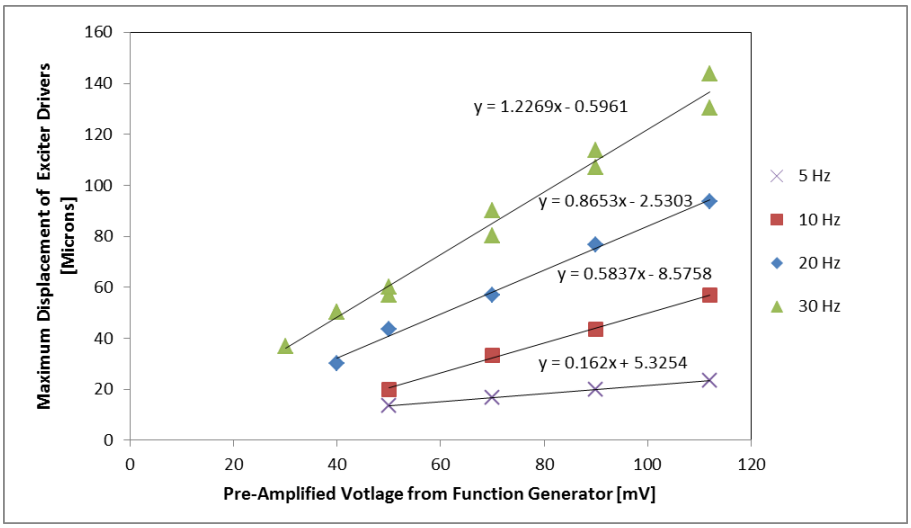

Figure 23 Displacement of a plate attached to set of electro dynamical exciter drivers as a sinusoidal waveform was passed through it. For each curve the frequency of the applied voltage waveform is constant. The displacement was noted as the applied voltage signal was varied.

The displacement of an electromechanical exciter driver was measured by placing one of the drivers side-ways under a microscope. A thin cover slip was attached to the top of the driver and the maximum peak to peak displacement of the cover slip was noted using a high speed camera to monitor its movement. This is illustrated in Figure 24.

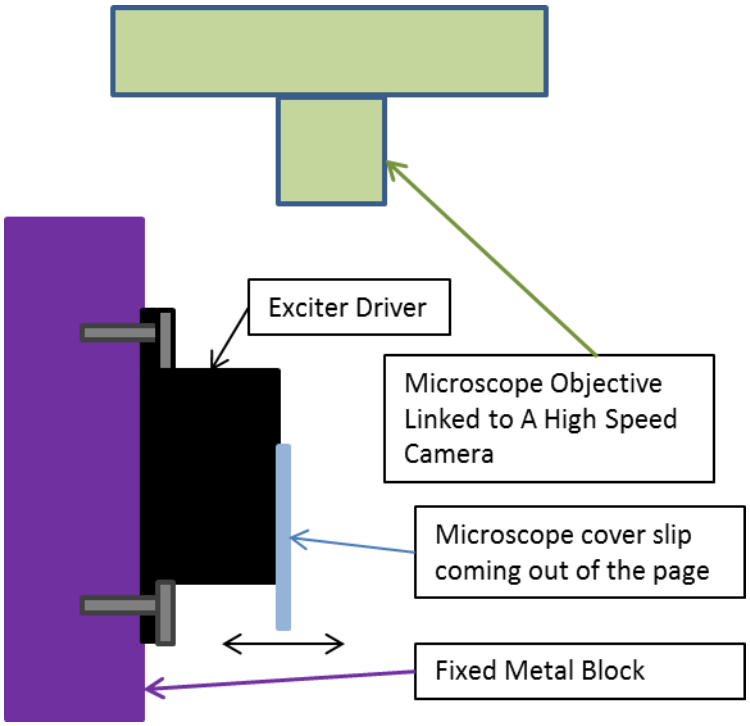

Figure 24 Arrangement used to determine maximum displacement of exciter drivers during oscilation.

To summarise, for a given applied voltage to the ESC, the force and maximum possible displacement of the bottom plate increases with frequency because the gain of the amplifiers increases with frequency. Additionally for a given applied voltage frequency, the force exerted by the bottom plate and maximum possible displacement of the bottom plate increases with the applied voltage in the range of parameters investigated.

The fact that the maximum displacement of the bottom plate for a given voltage and frequency shown in Figure 22 and Figure 23 appears low relative to a gap distance of 1000 microns is not ideal. This should be kept in mind as this essentially shows that equipment is limited in the maximum deformation of a sample at a given peak stress that can be achieved. However this issue has no real impact on squeezing the fluid samples in this PhD as in practise it is the peak force that can be applied by the apparatus that limits the maximum deformation over an OSFF cycle rather than the mechanical limitations of the equipment. This was illustrated in section 2.5.4.

4.4.1 General Experimental Procedure for the Use of the Electromechanical Squeeze Cell on Particle Suspensions

In order to ensure that the mobile plate in the electromechanical squeeze cell is flat, an engineering spirit level was used and the spacers underneath each exciter driver were adjusted. Thin metal sheets may also be placed underneath certain sides of the ESC to ensure the setup is flat. The gap distance between the stationary top plate and the mobile glass plate is controlled by inserting or removing spacers to move the top plate upwards or downwards.

It was important to wait until the sample is completely at rest before starting experiments as moving the apparatus onto the microscope can cause sample drift which takes time to dissipate. When squeezing a sample, it is best to view a section of the sample where particles are being cleanly translated back and forth over a straight line as this is what is expected for squeeze film flow. In order to check that particles are being cleanly translated, minimum intensity plots of a recorded video can be quickly taken using image processing software, Image J as shown in Figure 25. Minimum intensity plots of a stack of images essentially plot all the dark spots from all the images onto one picture. This is a quick way of mapping out a flow field because it results in tracer particles tracing out their own paths.

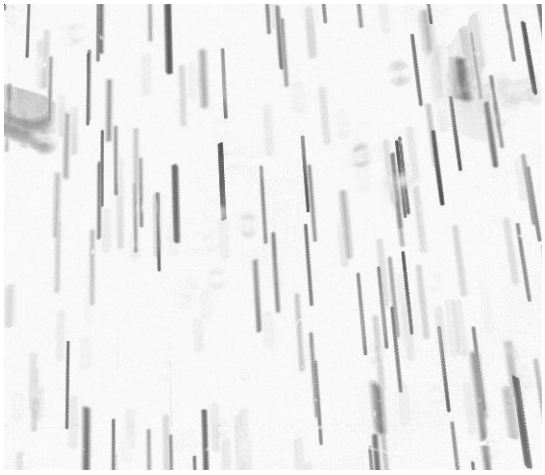

Figure 25 Minimum intensity plot of a dilute suspension of melamine particles (10.2 microns in diameter) suspended in glycerol over a period of 0.5 seconds while being squeezed. The gap distance was 900 Microns and the sample volume was approximately 1ml. The plot was taken at a squeezing frequency of 10.22Hz. The peak stress exerted by the bottom plate was roughly 600Pa. The black lines traced out the motion of the tracer particles. Different grey level or intensity indicates particles at different heights relative to the plane of focus.

Depending on factors such as; how the sample wets and spreads across the surface of the bottom plate, how parallel the top and bottom plates are relative to the gap distance and the extent of squeezing, it was often the case that particles were not cleanly translated across straight lines as shown in Figure 26A. Sometimes particles were seen to follow non-perfectly straight lines or elliptical paths as shown in Figure 26B.

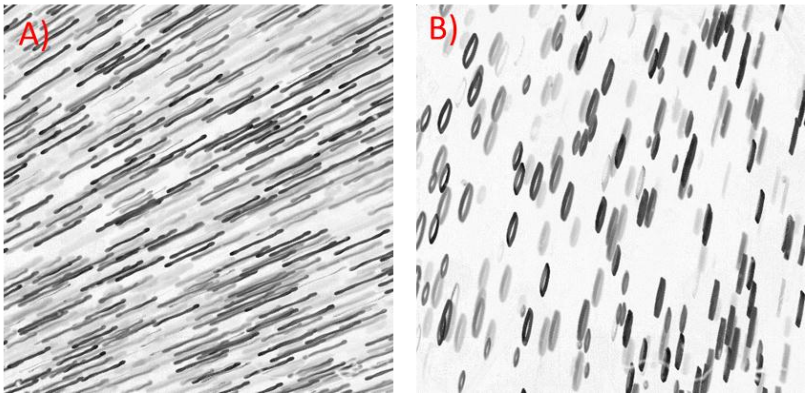

Figure 26 Minimum intensity plots of a dilute glycerol suspension with melamine particles (10.2 microns in diameter) over a period of 0.5 seconds. The gap distance was 1000 Microns and the sample volume was. a) (left) the plot was taken at a squeezing frequency of 20.32Hz. The black lines are not perfectly straight. b) (right) this plot was taken at a squeezing frequencies of 20.15Hz and the gap distance was 500 microns. Many of the tracer particles are following elliptical paths.

If the paths of particles are unsatisfactory as shown in Figure 26B then the section of the sample being viewed is changed in order to find the spot where the flow lines are the straightest so that deviations from the norm when squeezing concentrated colloidal dispersions would be easier to characterise. The areas viewed were at the edges of the sample where flow field resulting from OSFF is strongest.

Imperfections such as elliptical paths are more common at the lower end of gap distances used and get worse as the squeezing amplitude increases because the gap distance across the whole volume of the sample varies by a greater percentage if the plates are not perfectly parallel. In order to mitigate this effect a gap distance of 1000 microns was used for experiments where peak stresses of greater than 500Pa were being applied.

Another important reason for selecting a larger gap distance was to reduce the force required to squeeze a fluid between two parallel plates which is inversely proportional to the cube of gap distance as shown in chapter 2. Increasing the gap distance beyond 1000 microns also was not practical as many lower viscosity fluid samples would not be thick enough to wet the top surface. This can cause the fluid sample to wet and un-wet the

surface while squeezing is occurring which can contribute to the samples drifting out of the squeeze cell during squeezing.

4.4.2 Experimental Procedure for the Oscillatory Squeeze Film Flow of Concentrated Suspensions using the Electromechanical Squeeze Cell

Samples of colloidal dispersions of volume fractions in the range of 0.58-0.623 were subjected to two different sets of oscillatory squeeze film flow experiments.
In one set of experiments the peak oscillatory stress of roughly 600Pa was applied at frequencies in the range of 10-40Hz at a fixed initial gap distance of 1000 Microns. In another set of experiments a fixed squeezing frequency of 40Hz was applied and the peak squeezing stress was varied in the range of 600-1000Pa.

In both sets of experiments the flow field and sample shape were observed during squeezing and the conditions at which non-Newtonian behaviours were encountered were noted as is discussed in the results and discussion chapter in more detail. The preparation of samples is discussed in section 4.8.1.

4.4.3 Experimental Procedure for the Oscillatory Squeeze Film Flow of Dilute suspensions of *D.Salina* using the Electromechanical Squeeze Cell

Samples of *D. Salina* suspensions of number concentration of approximately 10^6 cells/ml were subjected to oscillatory squeeze film flow experiments with an initial gap distance of either 200 or 400 microns. Videos of the algae were recorded while the oscillatory squeeze film flow took place so that particle tracking software could be used to gather information on the swimming directions of individual algae.

Squeezing frequencies in the range of 1-3Hz were applied. The bottom plate would oscillate upwards and downwards with a peak to trough displacement of 9-18 microns to achieve a given maximum translation of individual algae on the central plane of the sample which is a measure of the extent of shear.

When tracking was carried out the plane of focus was 100 microns down from the top plate. When a gap distance of 200 microns was used the plane of focus was at the centre of the sample. However algae on other planes throughout the sample were clear enough to be viewed and subsequently tracked. When a gap distance of 400 microns was used the plane of focus was at the top quarter of the sample, though algae in the top half of the

sample could be seen clear enough to be tracked. The preparation of samples of *D. Salina* is discussed in section 4.8.4.

4.5 Experimental Setup and Procedure for the Electromechanical Shear Cell

Oscillation flow experiments have also been conducted with a parallel plate shear cell, for comparison with squeeze flow experiments.

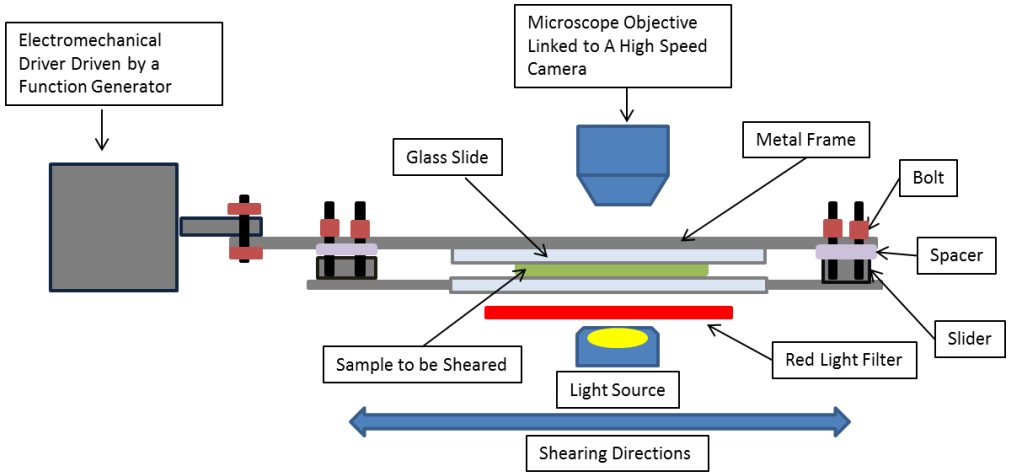

Figure 27 Simplified diagram of the shear cell. An oscillatory voltage from a function generator causes the arm of the electromechanical driver to extend and retract. This extension and retraction is done at the same frequency as the applied voltage. The displacement of the arm is proportional to the applied voltage. The frequency that the top plate oscillates at is the same as the frequency of the applied voltage waveform.

When an oscillatory voltage is applied by a function generator to the electromechanical driver, the arm moves in and out, causing the top plate to move with it. This shears the sample between the plates as shown in Figure 27. By varying the applied voltage waveform the displacement of the top plate per cycle varies and therefore the extent of the applied shear changes. The shearing frequency was altered by altering the frequency of the voltage waveform applied by the function generator. The gap distance is set using spacers of a desired thickness and can be accurately determined by focusing on the top plate using a microscope, and then moving the microscope focus down to the bottom plate and noting the distance that the microscope stage has moved.

As with the electromechanical squeeze cell, it is important to ensure that when a sample is being sheared, tracer particles follow straight paths. This can be checked using minimum intensity plots as shown in the previous section. It is also important to ensure that there is no drift of the sample. This can be mostly avoided by checking that the base of the shear

cell is flat by using a spirit level, and by waiting a few minutes after loading the shear cell and placing it on the microscope before carrying out an experiment.

To check that there is no sample drift, a minimum intensity plot can be quickly taken when no shear is being applied. If there is no drift, then the plot will show that all the stationary particles do not move, if not any non-motile particles will make straight lines in the direction of the drift.

The shear cell was used to apply oscillatory shear to suspensions of *D. Salina* at frequencies in the range of 0.5-6Hz and at peak to peak displacements of the top plate of up to 525 microns with a fixed gap distance of 400 microns. The number concentration of *D.Salina* within the suspensions was of the order of 10^6 cells/ml. The reason this approximate number concentration was used, was that at higher concentrations the particle tracking software had problems tracking all of algae at the same time.

The microalgae were observed using a mikotron high speed camera connected to the microscope in which the shear cell was placed. The plane of focus of the shear cell was 200 microns from the bottom plate. The reason for this was to reduce the effects of translation of the algae during shear to make it easier to track individual algae using particle tracking software. Throughout the gap the shear rate at a given point in time is the same however, the closer the plane of focus is to the moving top plate the greater the distance algae are being translated back and forth making individual algae harder to track.

4.6 Experimental Setup and Procedure for the Piezoelectric Squeeze Cell

A second method of applying oscillatory squeeze film flow was also developed, this one using piezoelectric devices to provide controlled displacement of a bottom plate.

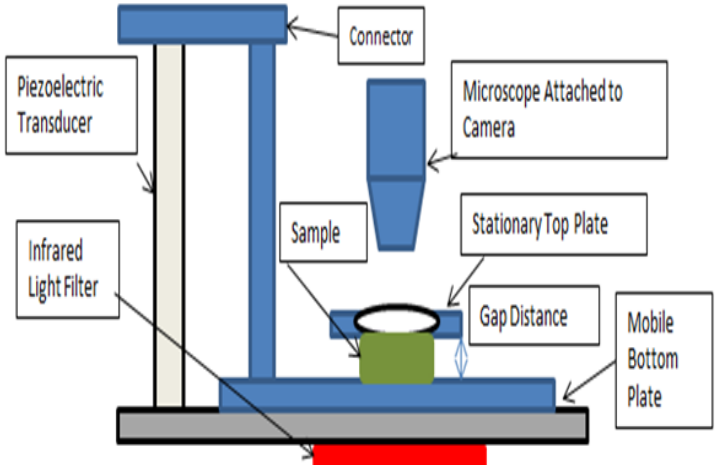

Figure 28 Diagram of the piezoelectric squeeze cell. It squeezes samples by moving a bottom plate towards a stationary top plate using a piezoelectric transducer.

The piezoelectric squeeze cell (PSC) is shown in Figure 28. This was used to squeeze suspensions of *D. Salina* in almost exactly the same way as the electromechanical squeeze cell. With this piece of apparatus, the bottom mobile plate was moved upwards a fixed distance by applying a corresponding voltage to the piezoelectric transducers causing it to move the mobile bottom plate upwards and squeeze a given sample.

In experiments using this piece of apparatus, a sinusoidal voltage wave form would be applied causing the mobile bottom plate to oscillate upwards from its starting off position. An example of a typical voltage wave form would be one with amplitude of roughly 2 volts, a peak voltage of 4 volts and a trough voltage of 0 volts. This means that the gap distance would never exceed its initial value which was kept fixed at 300 microns. The voltage waveforms were controlled and applied using a labview DAQ box connected to an amplifier.

The maximum displacement of the bottom plate was varied in the range of 9-18 microns in order to give a desired maximum translation of algae that occupy the centre plane. This is a measure of the extent of shear taking place at a given position in the sample and will be

explained in more detail in chapter 7. The applied squeezing frequency was varied in the range of 0.5-3Hz and the initial gap distance used in all experiments was 300 microns.

The main advantages of the PSC over the electromechanical squeeze cell were that the position of the bottom plate could be controlled extremely accurately, and a variety of squeezing waveforms could be applied. The relative disadvantages of the PSC were that it was vastly more expensive and prone to breaking leading to high repair costs. The PSC also was unable to operate over as wide a range of sinusoidal frequencies as the electromechanical squeeze cell.

4.7 Rheometry Experimental Arrangement

Measurements of the rheology of samples were also carried out using a standard commercial rheometer to explore the role of shear thickening in the particle systems investigated. The DHR2 strain controlled rheometer manufactured by TA instruments is shown in Figure 29. Attached to the device is a parallel disk geometry of 40mm in diameter, which was the only rheometer geometry used in this PhD.

Figure 29 A picture of the DHR2 strain controlled rheometer used for rheometry experiments in this PhD.

Both continuous shear ramps and large amplitude oscillatory shear experiments were carried out on concentrated particle suspensions.

In continuous shear ramp experiments, the shear rate was ramped up linearly between specified initial and final shear rates over a specified time period. If the torque required to meet the target shear rate at a given moment is too high for the motor to handle (due to a

increase in viscosity from shear thickening for example) then the shear rate will fall below its target value. The rheometer will however continue to try and meet the target shear rates at subsequent points in time.

In the large amplitude oscillatory shear experiments, a fixed maximum shear strain% of 200% was used and the angular frequency was ramped up from 0.1-400rad/s. It should be noted that a maximum shear strain of 200% corresponds to a maximum angular displacement of 0.1 radians.

The gap distance used in all experiments was 1000µm with the exception of experiments involving corn-starch suspensions in which case the gap distance used was 800µm. The reason for this is that samples of corn-starch suspensions wetted the surfaces more than the other samples used, meaning that the samples spread out so that their thickness was less than 1000µm. Therefore a gap distance of 1000µm could not be used here as the samples would not wet the top surface of the geometry.

It should be noted that all experiments in this PhD carried out using the DHR2 strain controlled rheometer were temperature controlled at 20 degrees Celsius.

4.8 Sample Preparation

In this section, the preparation of the samples used in experiments carried out in this PhD is discussed.

4.8.1 Preparation of Colloidal Dispersions Samples

The colloidal particles used were mono-disperse polymethylmethacrylate (PMMA) spheres of radius 574±4 nm (measured by dynamic light scattering). They were sterically stabilised with PHSA polymer hairs of roughly 10nm in length. When dispersed in a refractive index matched mixture of decalin and tetralin, van der waals and electrostatic interactions are extremely weak. Dispersions of this type are commonly used throughout the literature because they are a good representation of an ideal hard sphere dispersion as particles can be assumed to only interact through the hard sphere potential[188]. The steps required to prepare samples of PMMA colloidal dispersions are outlined here.

Step 1

A dilute dispersion of polymer stabilised PMMA particles dispersed in a refractive index matched solution of mixed decalin and tetralin is centrifuged for 2 hours 30 minutes at 4000 RPM. The refractive index matched solvent is 66% decalin and 33% tetralin by volume. After centrifugation, concentrated sediment at the bottom of a container is formed as shown in Figure 30:

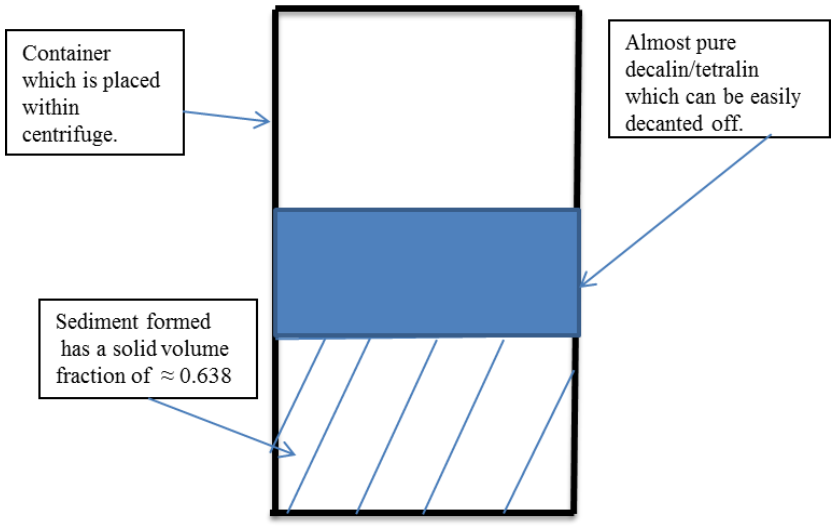

Figure 30 Illustration of the sediment formed after centrifugation.

Step 2

All excess solvent from container is then removed to leave only the sediment and then the container is then weighed to determine the mass of the sediment. This sediment is assumed to have a solid volume fraction of around 0.638; this is true for same sized spheres randomly packed together [31].

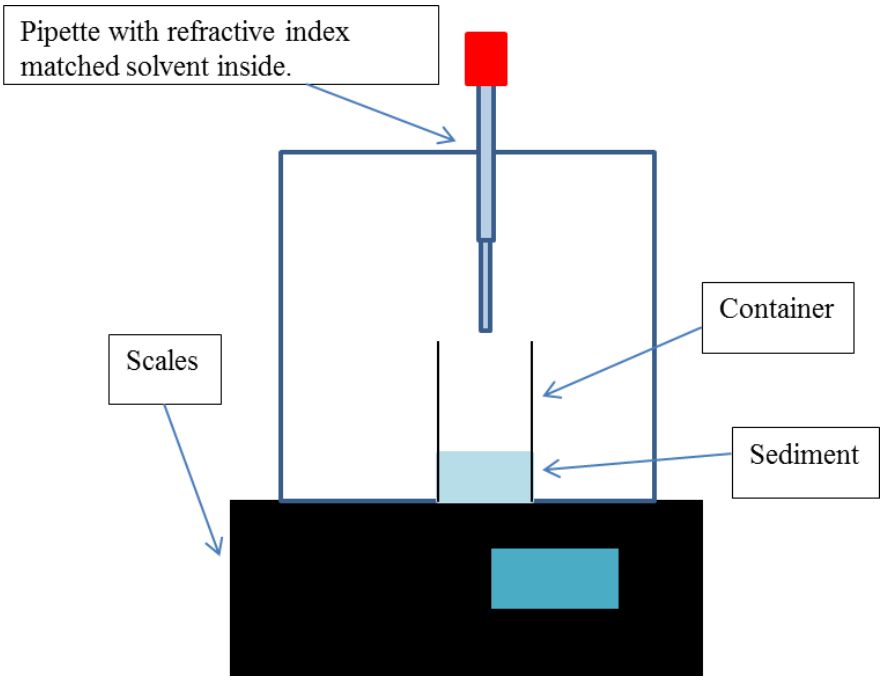

Figure 31 Illustration of the preparation of dispersions of known solid volume fraction.

Step 3

As the density of the PMMA particles and the index matched solvent are known, samples of a desired volume fraction were made by adding a known mass of solvent to the sediment of known volume fraction. The required mass of solvent to be added (denoted $Target\_dm_{solvent}$) was calculated by the following formula which is derived from a mass balance where ϕ is the solid volume fraction of the sediment, ϕ_T is the target volume fraction, ρ_c is the density of the colloidal particles, $\rho_{solvent}$ is the density of the suspending medium and M_O is the mass of the sediment:

$$Target\_dm_{solvent} = \frac{M_O\left[\frac{\Phi}{\Phi_T} - 1\right]}{\Phi\left[\frac{\rho_c}{\rho_{solvent}} - 1\right] + 1}$$

Equation 85

Step 4

The target amount of solvent to be added to the sediment to give the desired solid volume fraction was added by pipette while measuring the weight of solvent added using scales as shown in Figure 31.

Step 5

The actual mass of solvent added (denoted by $Actual\_dm_{solvent}$) was usually slightly different from the target mass to be added to give the desired solid volume fraction. Therefore the actual mass of solvent added was used to estimate the actual global solid volume fraction of the dispersion. Equation 86(which is a rearrangement of Equation 85) was used to calculate the actual global volume fraction of the sediment + solvent system (denoted ϕ_{new}):

$$\Phi_{new} = \frac{\Phi}{\frac{Actual\_dm_{solvent}}{M_0}\left[\left[\frac{\rho_c}{\rho_{solvent}} - 1\right]\Phi + 1\right] + 1}$$

Equation 86

Step 6

The sample was then mixed for 10 minutes using a vortex mixer in an attempt to make the sample as homogeneous as possible.

Step 7

Using a spatula, roughly 1ml of a given colloidal dispersion of known volume fraction is scooped up from the container and placed in the ESC. The refractive index matched solvent is placed around the ESC in order to saturate the surrounding air with the matched solvent. This reduces evaporation of the solvent from the sample within the ESC.

4.8.2 Uncertainty in Solid Volume Fractions

A detailed discussion on the difficulties and uncertainties involved in the preparing of colloidal dispersions of known volume fractions was given by Poon and co-workers. They proposed that even when the greatest care is taken in preparing colloidal dispersions of a known volume fraction, that the error in the solid volume fraction is likely to be at best in the range of 3-6% [42,188].

Error in samples prepared by centrifugation

In this PhD colloidal dispersions of a given volume fraction were prepared by centrifugation as described in the previous section, errors in the volume fraction of the sediment obtained are due to the following [42]:

1. The true value of the RCP is not known exactly however it likely falls in the region of ϕ=0.636-0.64 for a highly mono-disperse dispersion [31].
2. The sediment can potentially be compressed and expand with time after centrifugation ends which could potentially result in the value of the sediment being higher than expected if the supernatant fluid is decanted off too quickly.
3. The dependence on the value of the RCP on polydispersity is poorly known, however this was not expected to be a significant issue in this thesis as the colloidal particles used were highly mono-disperse.
4. The dependence of the sediment structure on centrifugation procedure is unknown.

As long as a consistent procedure is followed in the centrifugation of colloidal dispersions such as keeping the centrifugation speed and the time spent undergoing centrifugation constant then the volume fraction of the sediment takes on a reproducible value [42]. This essentially means that using this method there is a systematic error in knowing the true value of the solid volume fraction.

An inevitable source of error occurs when transferring a sample from a container holding a stock concentrated dispersion of a well known volume fraction to another container or into experimental apparatus. If a pipette were to be used to transfer a high volume fraction sample from one container to another, this could result in self-filtration where the volume fraction of the sample collected is of a lower volume fraction than the stock [144]. This

effect depends on the solid volume fractions and becomes more serious at high volume fractions near and above the glass transition. Within a stock container the local volume fractions may be different from the global volume fraction which can lead to errors even when scooping samples out from the stock [190]. Additionally due to difficulties in scooping out a highly viscous shear thickening dispersion that can jam during the act of scooping, it is likely that areas of lower viscosity and volume fractions are more likely to be transferred than the more viscous regions which essentially fight against the act of scooping to a greater extent. However as long as a consistent procedure is followed, the obtained sample volume fractions should be consistent and comparable even though the absolute value cannot be known exactly.

4.8.3 Preparation of Corn Starch Suspensions

The corn-starch used in all experiments was 27% amylose and 73% amylopectin by weight and was unrefined (purchased from Sigma Aldrich). The average particle size was measured to be roughly 14 microns using microscopy. Dry corn-starch particles are very hard with a compression modulus of the order of 10^{10} Pa and are very hydrophilic [13].

Corn-starch can be purchased refined or un-refined. Unrefined corn-starch suspensions generally show slightly higher viscosity in the shear thinning and continuous shear thickening regimes than refined corn-starch; however it is not yet clear why this is the case. It has been shown that in the discontinuous shear thickening regime the rheological behaviour does not appear to be affected by whether or not the corn-starch is refined or unrefined. The rheology of corn-starch suspensions has been known to change over time as particles absorb water [191].

Corn-starch suspensions of a desired mass fraction were created by adding a fixed mass of deionised water by pipette to a given mass of dry corn-starch within a small container to give a suspension with a desired solid mass fraction. The samples would then be mixed aggressively in a vortex mixer for 10 minutes. Roughly 1ml of corn-starch suspensions would be used immediately after being prepared to limit changes in the rheology of the suspensions.

In literature many experiments used corn-starch dispersed in a density matched solution of CsCl in water to prevent sedimentation; however this has the disadvantage that it induces

charges on the granular particles. Even without density matching it can take several hours for sedimentation to be significant within concentrated suspensions [13].

The most important variable as far as determining the rheological properties of a suspension is concerned is the solid volume fraction, however as this cannot be known accurately due to swelling of hydrated corn-starch suspensions, mass fractions were used instead as a more reliable indicator of concentration.

4.8.4 Preparation of Suspensions of *D. Salina* for Oscillatory Flow Experiments

Dunaliella Salina cultures were grown in medium corresponding to the commonly used recipe by Pick [192], which is also similar to recipe by Hejazi and Wijffels [193]. When inoculating, roughly 15 ml sample of a relatively highly concentrated 4 week old suspension of *D.Salina* is placed in fresh medium of volume 135ml in 500ml wide neck Erlenmeyer flasks. The initial culture of the specific strain of *D. Salina* (CCAP 19/18), which was used to create further cultures, was purchased from an organisation called CCAP (Culture Collection of Algae and Protozoa).

Cultures of *D. Salina* were exposed to white light at an intensity of approximately 1600-2000 lux. This is a good intensity for ensuring quick growth but not so high that the algae become stressed. The light source was a set of cool fluorescent white light bulbs. Automatic timers were used to ensure day/night cycles of 12 Hours each.

The whole setup was covered in such a way as to ensure that the only light reaching the algae came from the lighting. Cultures were grown in an enclosed hut due to the lab space being in a large open area surrounded by windows. Ideally algae cultures would be grown in an enclosed room.

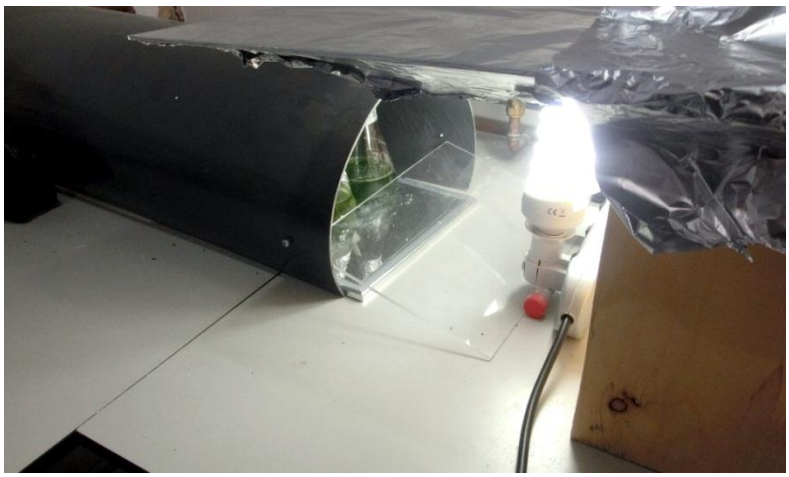

Figure 32 Set-up used to grow batches of *D. Salina*.

4.9 Basics of Particle Tracking

Particle tracking in videos relies on the simple fact that images made up of an array of individual pixels can be represented as a matrix of values where each pixel is represented by a numerical value. In a black and white image, each pixel is represented by a number indicating how intense the white colour of the pixel is. For example a value of 0 could represent black and a value of 256 could represent the maximum allowable intensity of white. Particle tracking generally involves three steps.

Step 1 Identification: In each frame of a given video, particles with desired characteristics are identified. Features of each identified object are recorded in every frame such as position, size, eccentricity and intensity of the pixels that represent a given object. At this stage every identified object in a given frame is assumed to be different from objects identified in other frames, even if it is obvious to any human observer that it is the exact same object just at a later point in time.

Step 2 Tracking: Using the information recorded on each identified object in a given frame, the program identifies which objects in a given frame are likely to be the same particles that have been identified in other frames. This is done by 1^{st} setting a maximum distance within which an identified particle can move between frames, this means that when a particle is identified in one frame, the program will only search for that same particle within a given maximum distance from its last known position in the next frame. This is to prevent it looking too far and mistaking the identified particle in the 1^{st} frame for a completely different particle in the next frame. Within this maximum distance, particle properties such as size and shape are used to determine which identified particles between consecutive frames are In fact the same.

Each unique object is then assigned an identification number and its properties such as positions in every frame are then associated with this identification number, allowing movements to be displayed frame by frame.

Step 3 Analysis: Once the co-ordinates and other properties of given particles have been identified, then how these properties change over time frame by frame can be analysed. For example by processing the initial and final position of a tracked particle the flow field and the direction of travel can be determined.

In this PhD a modified version of particle tracking software originally written by Maria Kilfoil in Matlab was used to track the positions of algae [194]. This was used to give positions of tracked algae at a given point in time. This data is then processed in Matlab using a program specifically designed to determine the speed and swimming directions of individual algae.

4.10 Identification of Algae Swimming Directions and Speed

When *D.Salina* is observed through a microscope, they are seen to swim in random directions in a given plane as long as there are no external factors that cause a bias to any particular directions, under such conditions they also tend to change their swimming directions over a period of around 10 seconds [185].

Figure 33 below shows the angle of trajectories of a batch of swimming *D.Salina* observed and recorded through a microscope in the plane of focus, as well as the corresponding histogram of the observed speed. The angle of trajectory of a given algae can take values between 0 and 360 degrees as is shown in Figure 33.

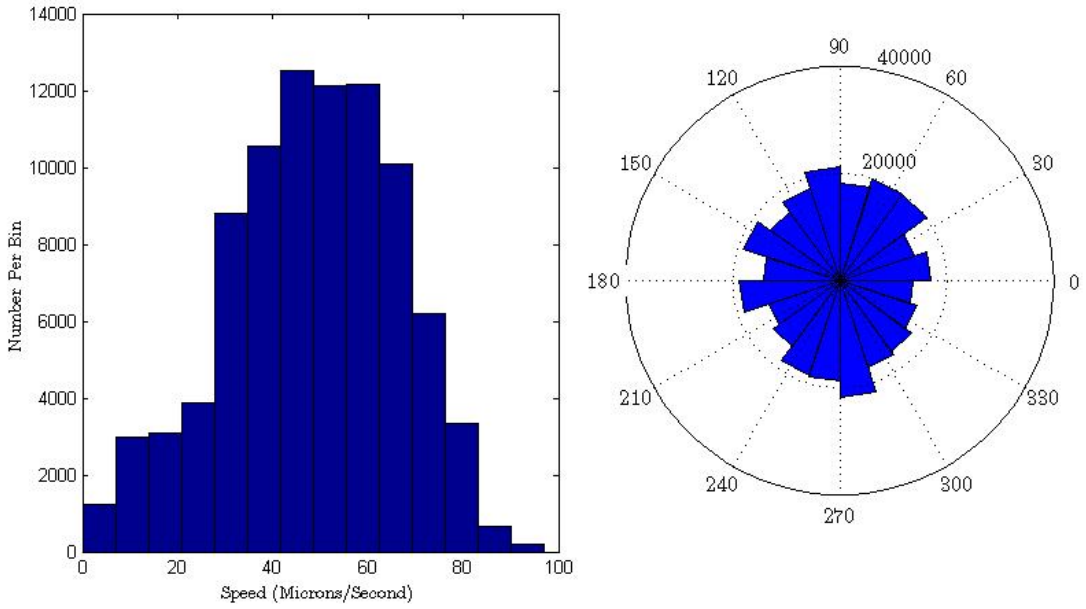

Figure 33 (left)Histogram of the speed of algae within the shear cell with no applied shear. (right) Angle of trajectory histogram of algae swimming directions over periods of 2 seconds with no applied shearing.

The angle of trajectory histogram is constructed by considering the starting and end points of each individual algae track from a collection of multiple videos and then finding the angle in which the displacement vector points. It can be seen that the distribution is mostly

circular corresponding to no preference in swimming direction, which shows the analysis is successful on this front.

The number per bin axis of the speed and angle of trajectory histograms corresponds to the number of algae tracks lasting a specified time period corresponding to a specific number of frames N. If a track lasts more than N frames, it is split into multiple tracks lasting N frames. For example if a track lasts N+2 frames then the track would be split into 3 tracks each of which would be represented in the histograms. The 1^{st} track corresponding to this specific alga would take place from the 1^{st} frame to the N^{th} frame and the 2^{nd} track would take place over the 2^{nd} frame to the $(N+1)^{th}$ frame and so on.

A histogram of speed is constructed by dividing the displacement achieved by each individual algae track by the time which the track lasted. *D. Salina* is known to have an instantaneous modal speed in the range of 60-80microns/s [185]. It is expected that when observing algae with a microscope that the observed speed will on average be lower as a component of the velocity vector of a given algae track will point in the vertical direction which can not be detected. Additionally if an individual alga changes direction over the time period which the speed is analysed, then the recorded speed will be lower than if it moved in a straight line. Figure 33 displays a modal speed of 50microns/s which is consistent with expectations, showing that the analysis is successful and *D. Salina* are behaving normally.

4.11 Identification of Algae Swimming Directions and Speed in Oscillatory Flows

When a sample is subjected to an oscillatory parallel shear, the flow field within the sample oscillates back and forth as is illustrated in Figure 34 .

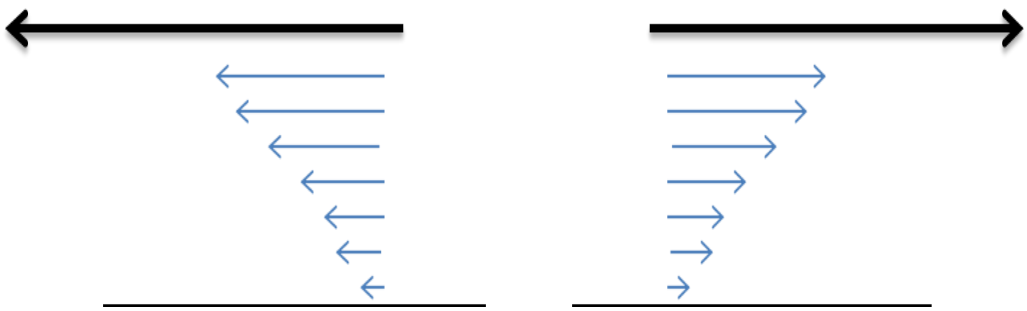

Figure 34 An illustration of oscillatory shear flow. The flow field can point in 2 different directions depending on the point in the cycle.

The oscillatory flow causes algae to be translated back and forth as they swim meaning that if they swim perpendicular to the flow field they trace out a sinusoidal shape, while lifeless tracer particles are simply translated back and forth over the same line as shown in Figure 35.

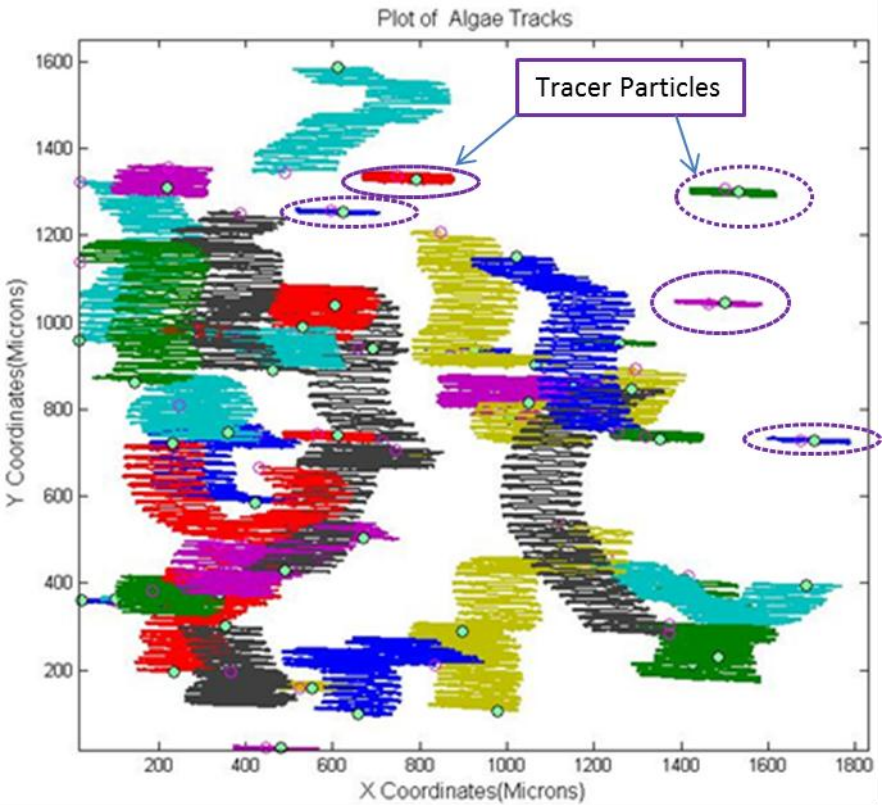

Figure 35 Plot of tracks made by *D.Salina* and tracer particles inside the shear cell at a shearing frequency of 2Hz over 5 Seconds. Maximum displacement of top plate of 200 microns with a gap distance of 500 microns.

Figure 36 shows example tracking plots of algae being subjected to an oscillatory shear of 1.5 Hz over 4 seconds and Figure 37 shows the corresponding speed and angle of trajectories of the swimming *D.Salina*. Both Figure 36 and Figure 37 show that the swimming directions preferentially point in the two directions perpendicular to the translations due to the oscillatory flow. This will be discussed in more detail in chapter 7.

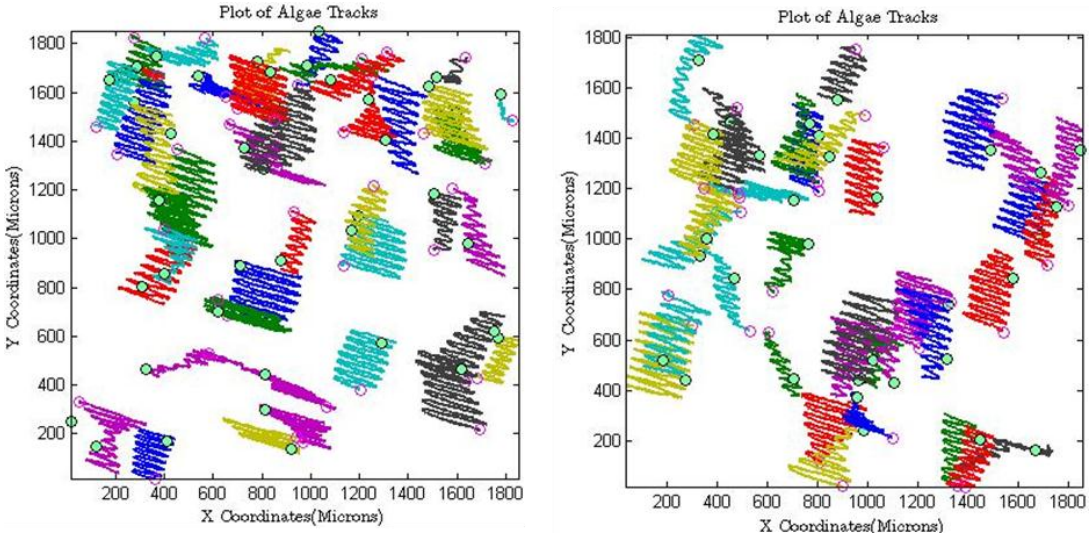

Figure 36 Plots of algae tracks over a period of 4 seconds over which a shearing frequency of 1.5Hz was applied. The average shear rate was 1.97s^{-1} where the maximum peak to peak displacement of the top plate was 524 microns. The gap distance between the plates was 400 microns. The video was recorded at a frame rate of 300 FPS.

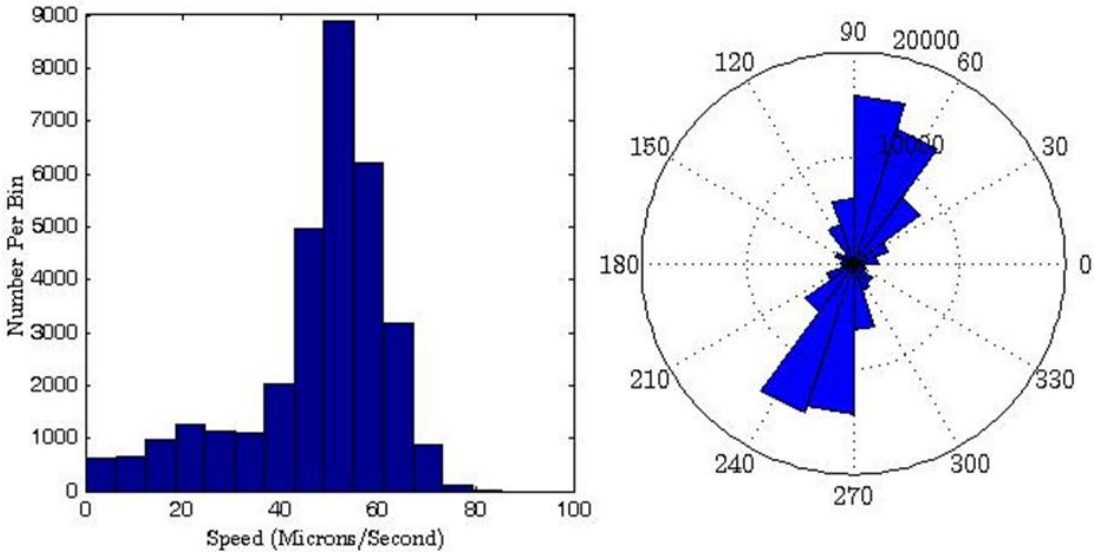

Figure 37 (left) Histogram of the speed of algae within the shear cell with shearing at a frequency of 1.5 Hz at an average shear rate of 1.97s^{-1} over a periods of 4 seconds. (right) shows the corresponding angle of trajectory histogram of algae swimming directions over a period of 4 seconds.

In order to determine the overall swimming directions of algae, the displacements must be analysed over a time period (represented by a number of frames) which is an integer multiple of the time taken for one oscillation to complete. By doing this any displacements due to the oscillatory shear are cancelled out and the resulting displacement is due to swimming alone. If this is not done, then part of the algae's displacement at any given time will be due to it being translated by the act of shearing.

In order to determine the shearing directions, the angles of trajectories of each *D.Salina* alga are analysed over a series of time scales much less than the time taken to complete a full oscillation. The displacement of a given algae's position due to the shear is generally much greater than displacement due to swimming if analysed over a short enough time period. This means that the angle of trajectory distribution will have peaks in the shear directions as shown in Figure 38. As expected the peaks are π radians apart as the directions are anti-parallel.

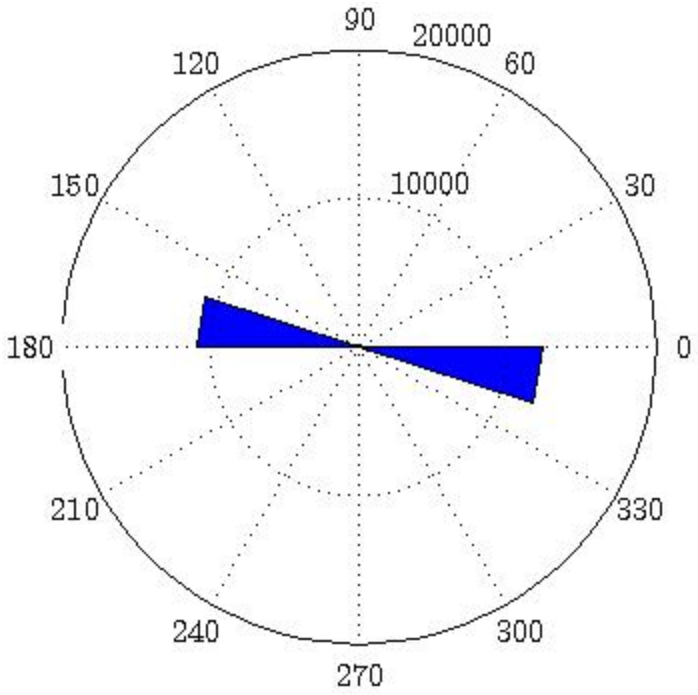

Figure 38 historgam of angle of trajectories of swimming *Dunaliella Salina* in oscillatory shear flow at a frequency of 1.5 Hz taken over intervals of 0.33 seconds which is smaller than the time taken for a full oscillation which is 0.66 seconds.The peaks here are in the the directions of the applied shear.

Chapter 5 Rheometry of Colloidal and Granular Suspensions Results

5.1 Chapter Summary

In this section, example continuous shear rheometry results that were carried out on concentrated particle systems using a strain controlled DHR2 rheometer with a parallel plate geometry are shown. This is followed by example large amplitude oscillatory shear results that were carried out on the same concentrated suspensions. These results are then discussed in the context of other results within the surrounding literature. Most of the systems examined here correspond closely to the systems used in the oscillatory squeezing experiments shown in chapter 6. The primary purpose of this chapter is to describe the rheology of the systems that are examined in chapter 6.

5.2 Continuous Shear of Concentrated Colloidal Dispersions Results

In this subsection the displayed results correspond to the application of continuous shear ramps (as described in 4.7) on a variety of sterically stabilised colloidal PMMA dispersions in a refractive index matched solution of Decalin and Tetralin.

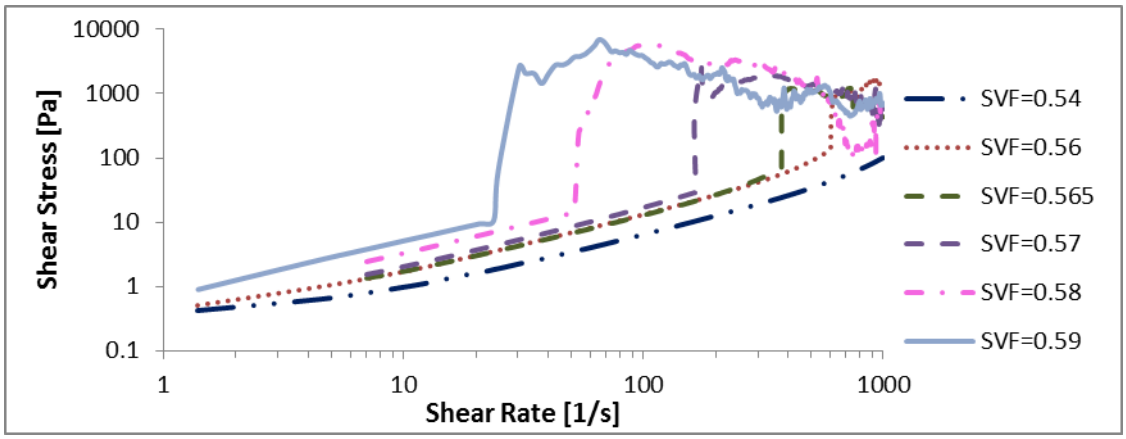

Figure 39 Shows how the resulting shear stress varies as the shear rate is continuously ramped up for concentrated colloidal dispersions of varying SVF. All dispersions consisted of PMMA particles of 574nm in radius. The gap distance used was 1000µm.

Figure 39 shows that as the solid volume fraction of the colloidal dispersions increases, then the shear rate at which DST begins decreases as expected [31,196]. It also shows that at low enough solid volume fractions, DST does not occur within the range of shear rates

examined, which is also expected [31]. At the end of the DST regime where the shear stresses reached values of around 2500-6000Pa, the sample would show fracture and distortion effects such as sharkskin [52] and would partially slide out of, or eject from the geometry. This resulted in the recorded shear stresses and viscosities decreasing due to the fact that there was less material being sheared. Figure 40 shows examples of samples of concentrated colloidal dispersions after and during DST.

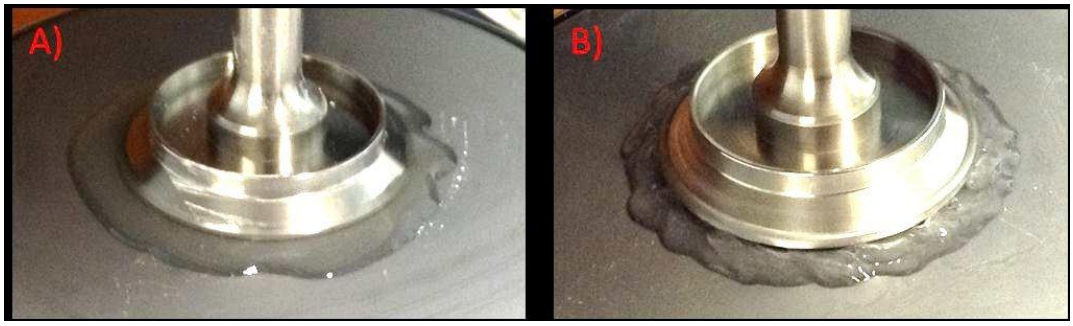

Figure 40A) Shows a sample of a colloidal dispersion of PMMA particles with a solid volume fraction of 0.57 after it had undergone continuous shear corresponding to Figure 39. After the period of extreme DST at around 200s^{-1}, the fluid partially flowed out of the gap smoothly with slight ripples in the surface being observed. Figure 40B) Shows a sample of a colloidal dispersion of PMMA particles with a solid volume fraction of 0.58 as it was undergoing DST during continuous shear corresponding to Figure 39. At a shear rate of around 50s^{-1}, the dispersion displayed ripples on its surface and also partially flowed out of the gap. The fluid that exited the gap remained distorted unlike in A).

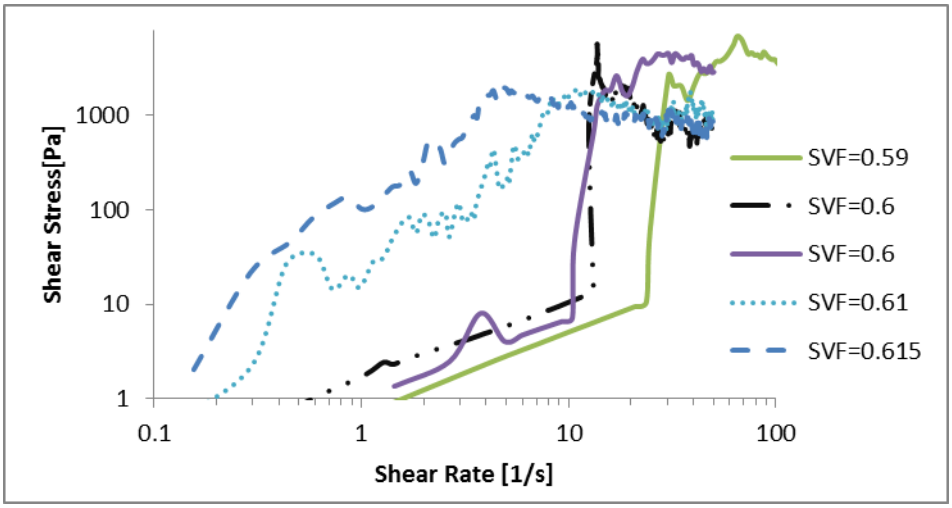

Figure 41 Shows how the resulting shear stress varies as the shear rate is linearly ramped up for a variety of highly concentrated colloidal dispersions consisting of PMMA particles of 574nm in radius (measured by DLS). The gap distance used was 1000μm.

Figure 41 shows that at high volume fractions above 0.6, the DST regime was less sharp. DST occurred over a wider range of shear rates and greater fluctuations in the resulting shear stress were observed. This was observed to be due to sample fracture and escape

from the geometry occurring more gradually and at lower stresses. This caused the large discontinuous jump in the shear stresses observed during DST to be less distinct than observed at lower solid volume fractions. This also caused the values of the peak stresses obtained during DST to decrease, as some of the sample had already escaped by the time the maximum peak shear stress (often referred to as τ_{MAX}) that the sample could sustain was reached.

It is important to note at this stage that the ejection of sample from the gap was not due to centrifugal forces as the ranges of shear rates were too low for this to be an issue.

Figure 42 shows how the value of the shear rate at which DST began varied with solid volume fraction, during shear ramp experiments. Figure 42 shows that as the solid volume fraction increases, the shear rate at which DST began decreases sharply.

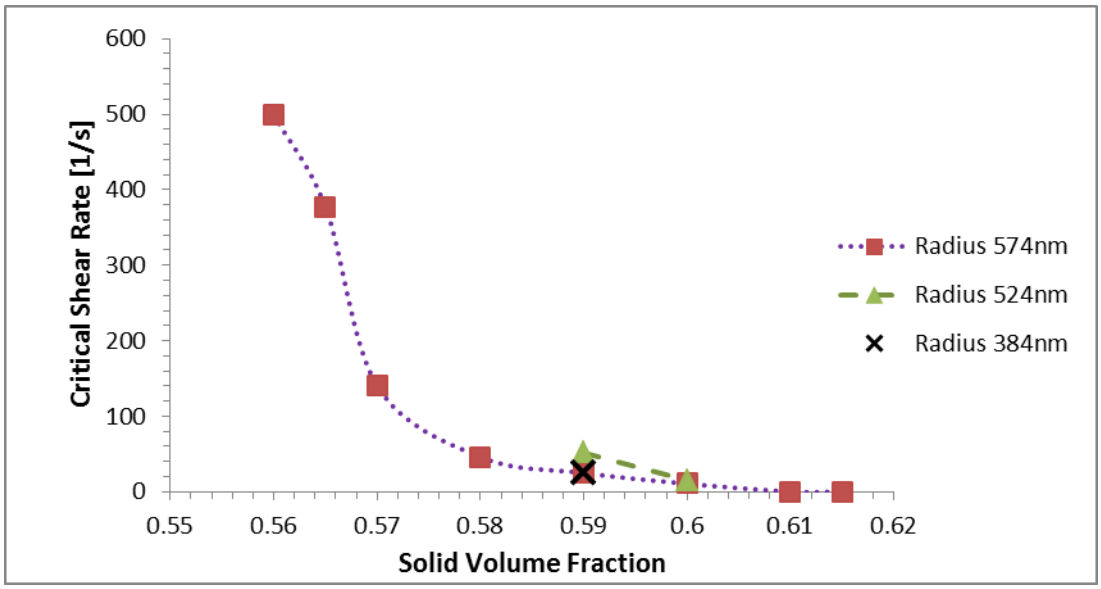

Figure 42 shows a plot of the shear rates at which DST began against the solid volume fraction of colloidal dispersions consisting of PMMA particles of radius 574nm. This figure was primarily derived from the same data used to construct Figure 39 and Figure 41. The particles were dispersed in refractive index matched solutions of decalin and tetralin. Some data from dispersions containing smaller colloidal particles is also included for comparison.

It was commonly observed that at high solid volume fractions, during DST, jammed granules would be expelled from gap as shown in Figure 43.

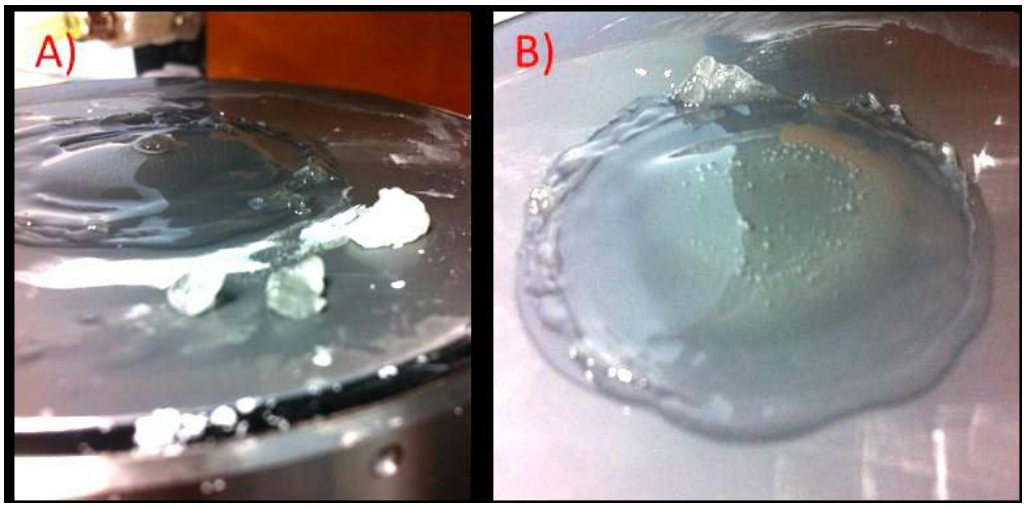

Figure 43A) and B) show permanently jammed granules that were expelled from the geometry gap during the DST of a dispersion of PMMA particles of radius 574nm and solid volume fraction of 0.59. The gap distance used was 1000µm.

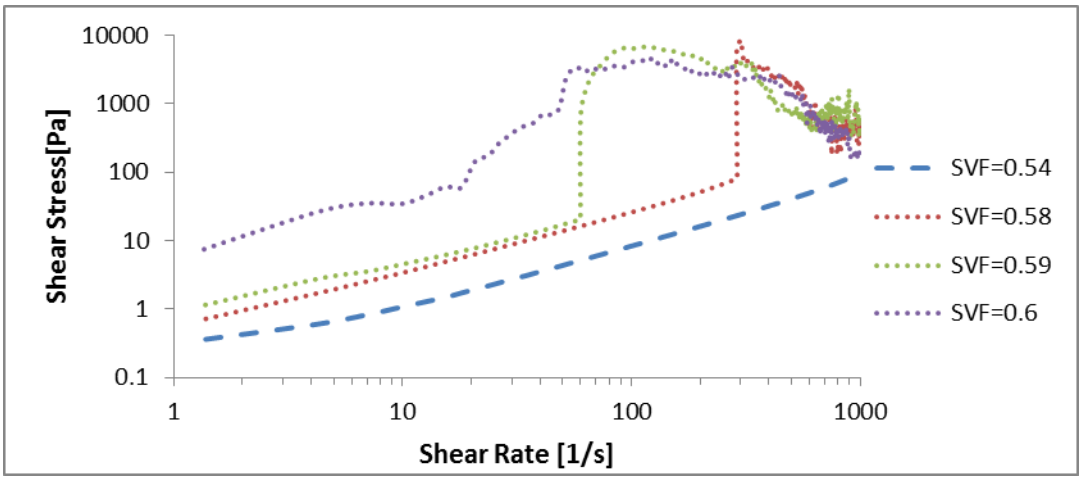

Figure 44 Shows how the resulting shear stress varies as the shear rate is increased for a variety of colloidal dispersions consisting of PMMA particles of 524nm in radius. The gap distance used was 1000µm.

Figure 44 confirms the findings displayed in Figure 39 and Figure 41 with colloidal dispersions consisting of particles with a slightly smaller radius. As the solid volume fraction increases, the DST regime becomes less distinct and occurs at lower shear rates. The peak stress sustainable by a given sample decreased as the solid volume fraction increased. At low enough concentrations no DST was observed and the initial viscosity increased with volume fraction as expected. The shear stresses observed at the onset of DST were very similar for dispersions of different volume fractions, which is expected from literature [13,15].

It was observed that when DST was occurring in a variety of highly concentrated colloidal dispersions, that large changes in the developed shear stresses correlated strongly with large fluctuations in the normal stress that could be either positive or negative as illustrated in Figure 45 and Figure 46.

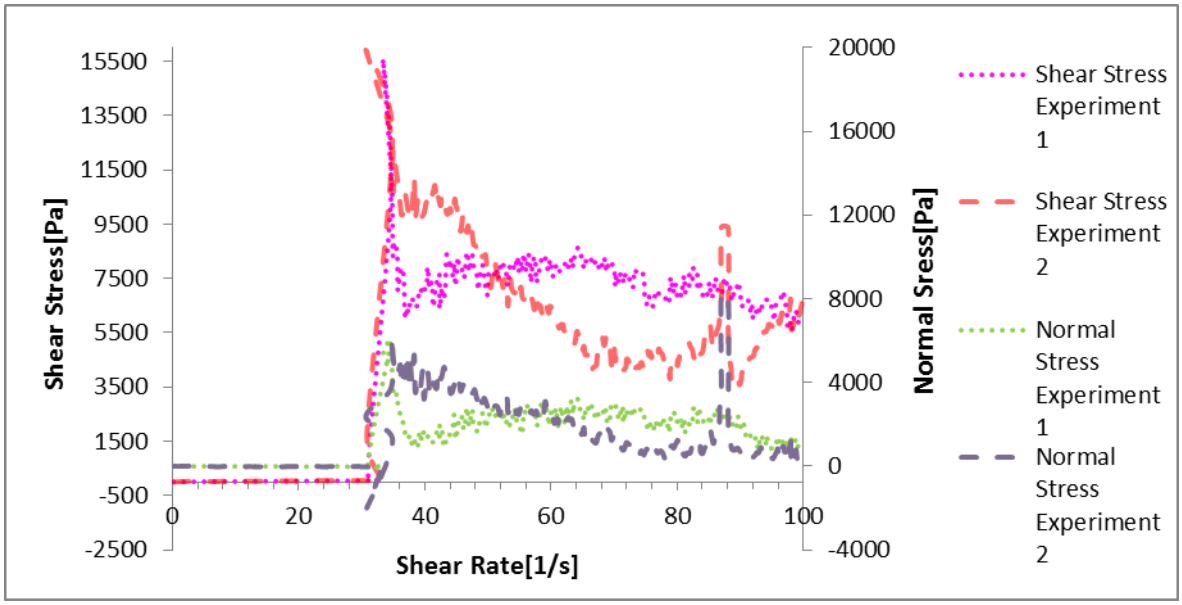

Figure 45 Shows how the resulting shear and normal stress varies as the shear rate is increased for colloidal dispersions consisting of PMMA particles of 384nm in radius with a solid volume fraction of 0.59. The gap distance used was 1000µm. Experiments 1 and 2 were carried out on separate samples from the same bulk dispersion with a solid volume fraction of 0.59. Both experiments give relatively consistent results.

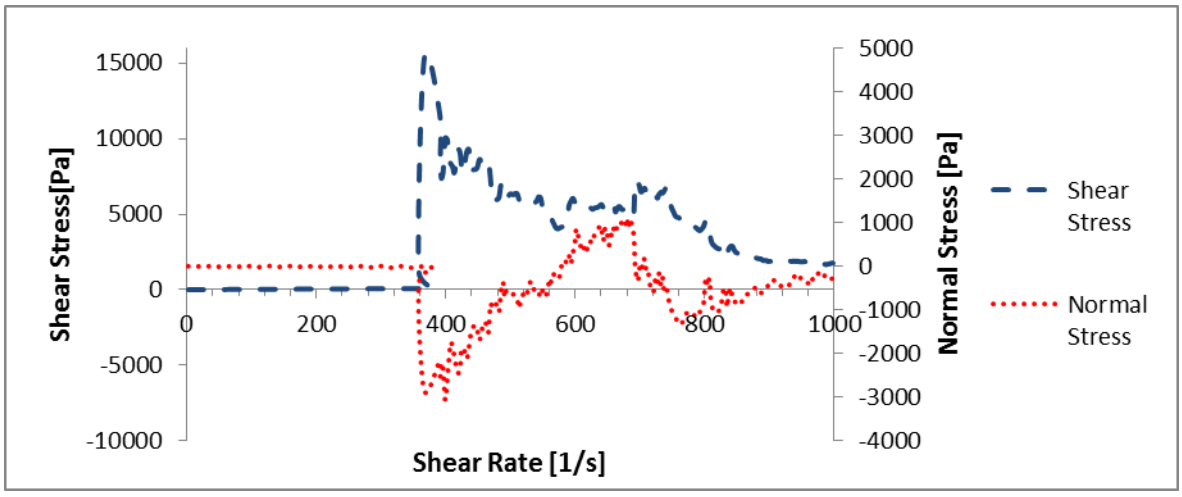

Figure 46 Shows how the resulting shear and normal stress vary as the shear rate is increased for a colloidal dispersion consisting of PMMA particles of 384nm in radius with a solid volume fraction of 0.55. The gap distance used was 1000µm.

Comparing Figure 45 and Figure 46 shows that the peak stress that marks the end of the extreme DST regime is almost identical despite the large difference in volume fraction between the samples. The signs of the peak normal stresses differ however.

In continuous shear experiments carried out on colloidal particles of radius 384, 524 and 574nm, it was generally found to be the case that when DST was observed at volume fractions of around and above 0.59-0.6, the normal stress fluctuations would be large and positive. At lower volume fractions, the normal stress fluctuations that would be observed during DST were generally large and negative.

Large negative peaks in the normal stress are generally observed during the end of the DST regime when the samples was breaking up or ejecting from the gap. The large negative values could therefore be the result of a pressure difference created within the sample as some fluid exits the gap leaving an empty pocket within the sample.

Interestingly it was found that when large and positive normal stresses were observed during the shear of highly concentrated dispersions, the recorded normal stresses at each point in time appeared to correlate with the corresponding shear stresses as shown in Figure 47. However this was not the case when large negative normal stresses were observed. In these cases no consistent relationship between the measured shear and normal stresses could usually be obtained without removing negative outliers.

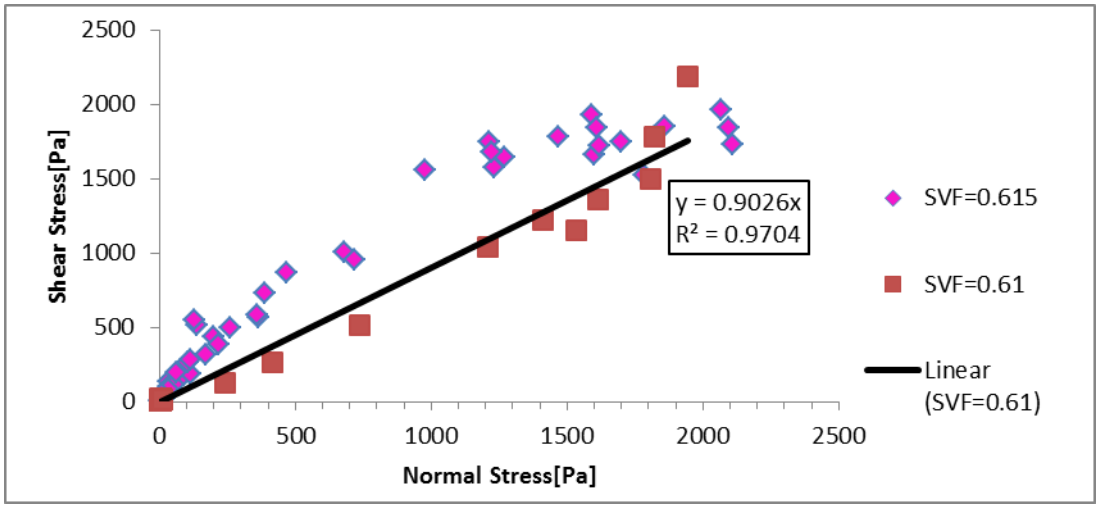

Figure 47 Shows the recorded shear stress values against the corresponding recorded normal stress values during at each instant during continuous shear ramp experiments on colloidal dispersion consisting of PMMA particles of 574nm in radius. The shear rate was varied from 0.1-1000[s^{-1}]. The gap distance used was 1000µm. The particles were dispersed in a refractivly index matched solution of decalin and tetralin.

Figure 47 shows that at very high volume fractions, the values of the shear and normal stresses recorded during a shear ramp experiments at each moment in time can be roughly correlated by a relationship of the form shown in Equation 87, where τ_{Shear}, is the shear stress, σ_{Normal} is the normal stress and μ_k is a best fit constant referred to as the macroscopic friction coefficient by Fall [15]. This will be discussed in detail in later sections.

$$\tau_{Shear} = \mu_k \sigma_{normal}$$

Equation 87

At slightly lower solid volume fractions however, it is not possible to relate the in phase shear and normal stresses values in such a simple way as shown in Figure 47, even though large changes in shear and normal stresses may be perfectly in phase, at lower volume fractions, the values of the normal and shear stresses cannot be neatly related to each other by an equation of the form given by Equation 87.

Figure 48 shows the shear and normal stress values obtained from a shear ramp experiment carried out on a suspension of PMMA particles with a solid volume fraction of 0.6. Figure 49 shows that even though the shear and normal stress fluctuations appear to be in phase as shown in Figure 48, the values of the shear stress are not a simple function of the normal stress, as was the case at higher volume fractions as shown in Figure 47.

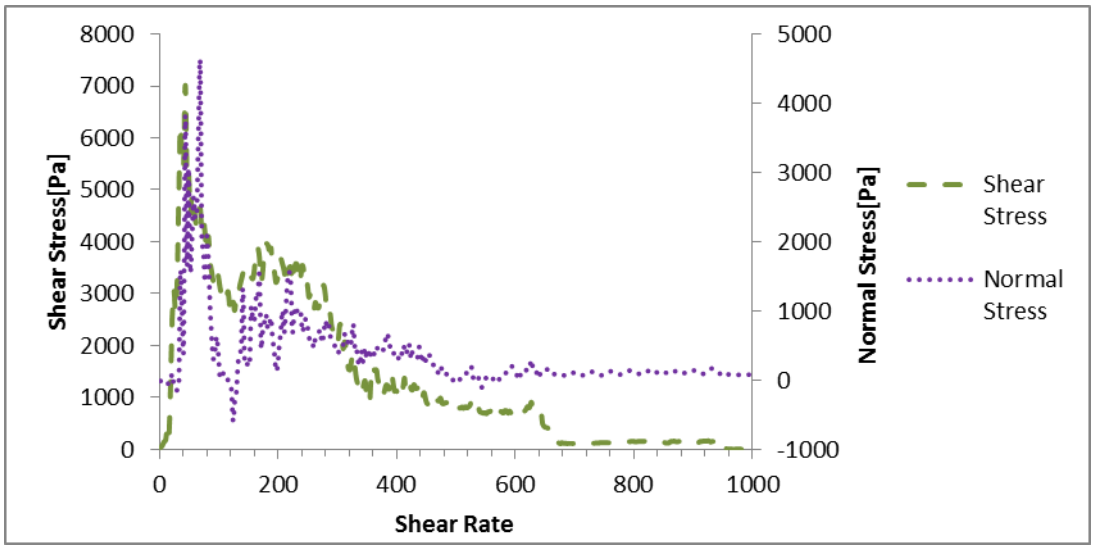

Figure 48 Shows how the resulting shear and normal stress varies as the shear rate is increased for a colloidal dispersion consisting of PMMA particles of 574nm in radius with a solid volume fraction of 0.6. The gap distance used was 1000µm. The particles were dispersed in a refractive index matched solution of decalin and tetralin.

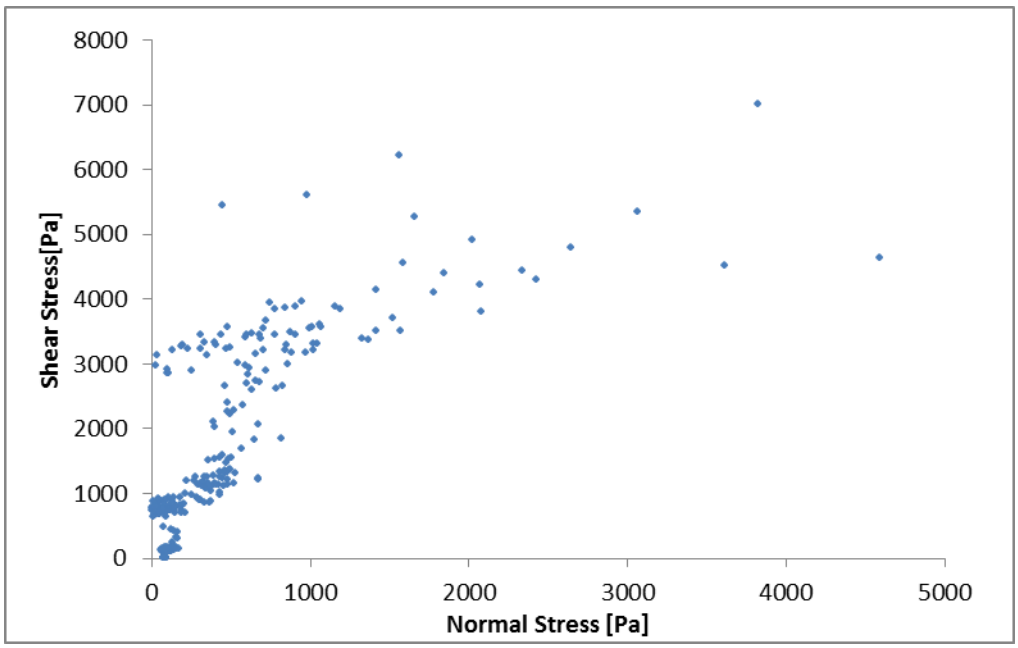

Figure 49 shows the recorded shear stress values against the recorded normal stress values during a continuous shear ramp experiment on colloidal dispersion with a solid volume fraction of 0.6 consisting of PMMA particles of 574nm in radius. The shear rate was varied from 0.1-1000 [s^{-1}]. The gap distance used was 1000µm. The particles were dispersed in a refractive index matched solution of decalin and tetralin.

To summarise, during and after the DST of colloidal dispersions where the shear stress increases drastically in response to a small increase in shear rate, large changes in the normal stress are observed. Below around 0.59, the colloidal dispersions generally displayed large negative changes in the normal stress during DST, while at 0.59-0.6 and above the large changes in normal stress were large and positive.

At extremely high values of the solid volume fractions of around 0.61, the in-phase values of the shear and normal stress appear to be correlated as shown in Equation 87. However they become less correlated as the volume fraction decreases as can be seen by comparing Figure 47 and Figure 49.

For clarity, it is important to highlight that it is very common for particle suspensions to display small negative normal stresses during shear, even when there are no stress fluctuations or shear thickening occurring as illustrated in Figure 50 over the range of shear rates of 0-600s^{-1} [197].

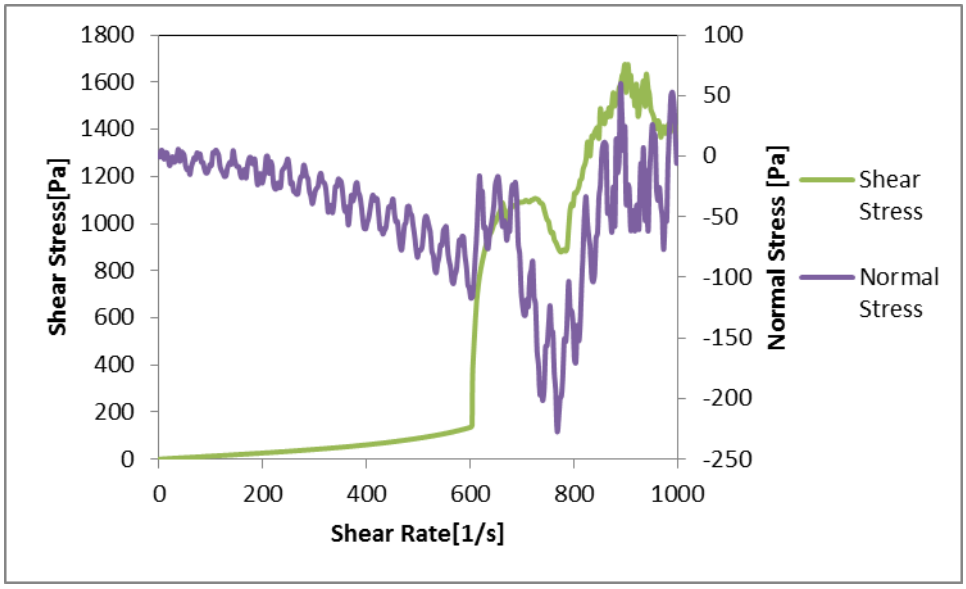

Figure 50 Shows how the resulting shear and normal stress varies as the shear rate is increased for a colloidal dispersion consisting of PMMA particles of 574nm in radius with a solid volume fraction of 0.56. The gap distance used was 1000µm. The particles were dispersed in a index matched solution of decalin and tetralin.

5.3 Continuous Shear of Concentrated Corn Starch Suspensions Results

In this subsection the displayed results correspond to the application of continuous shear ramps on corn-starch in water suspensions. Figure 51 and Figure 52 show that DST occurs for such suspensions with solid mass fractions at and above 0.5 within the range of shear rates examined. At mass fraction in the range of 0.5-0.54, the peak stresses observed during DST were all around 700Pa. At mass fractions above 0.54, much stronger DST was observed as can be seen in Figure 52 and Figure 55, and was accompanied by the ejection of jammed granules from the gap as shown in Figure 56.

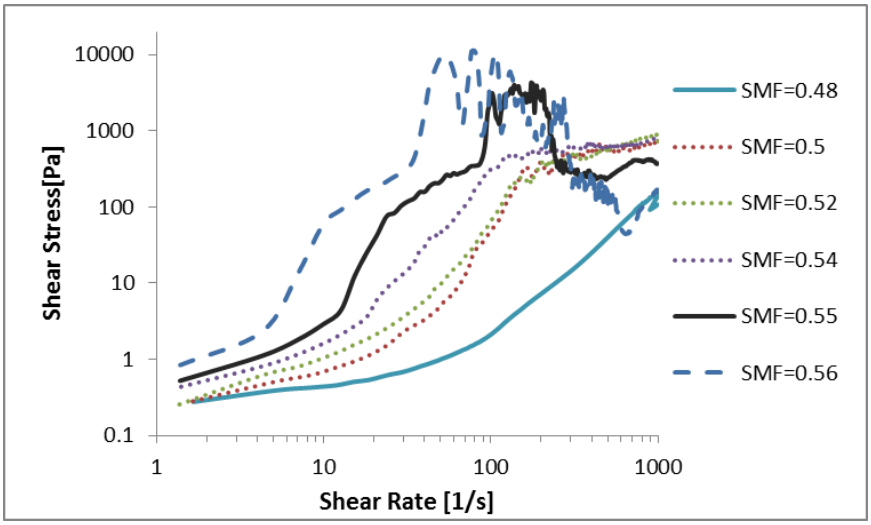

Figure 51 Shows how the resulting shear stress varies as the shear rate is increased for a variety of corn starch in water suspension of varying SMF. The gap distance used was 800µm.

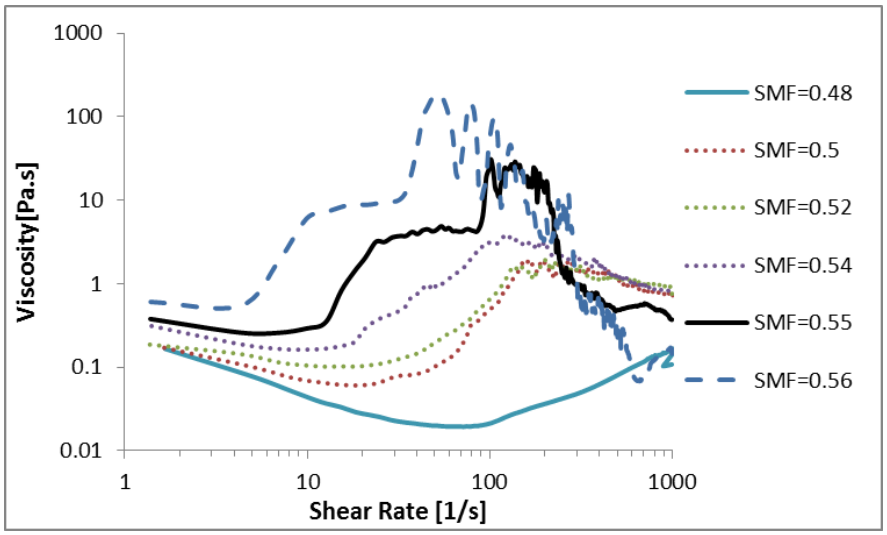

Figure 52 Shows how the resulting viscosity varies as the shear rate is increased for a variety of corn starch in water suspension of varying SMF. The gap distance used was 800µm.

Figure 52 uses the same data as in Figure 51, except that it is plotted as viscosity versus the applied shear rate. It shows that at lower mass fractions shear thinning was observed as expected from literature [31].

Figure 53 shows how the normal stress varied as the shear rate was ramped up. During and after DST, changes in normal stressed coincided very well with changes in the shear stress as was the case with PMMA colloidal dispersions.

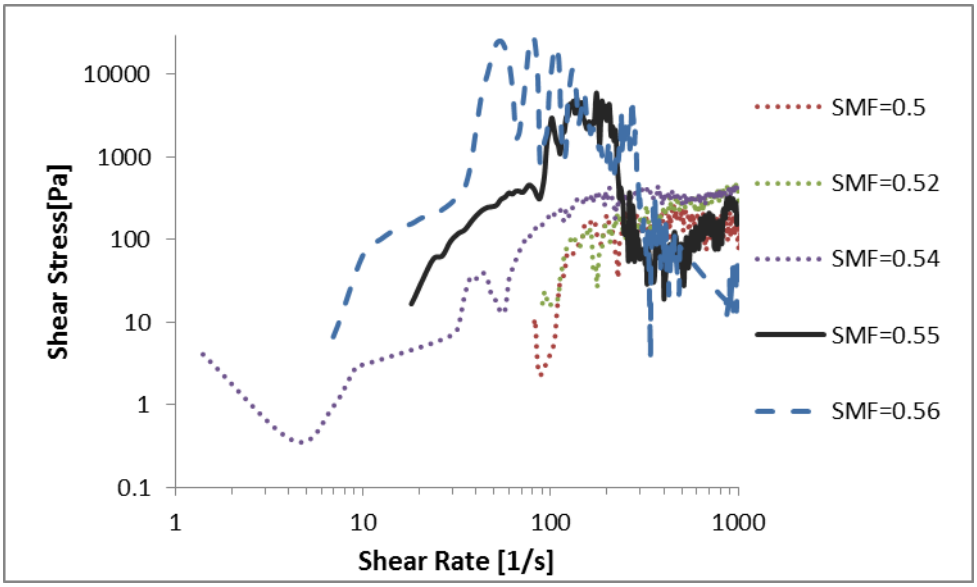

Figure 53 Shows how the resulting normal stress varies as the shear rate is increased for a variety of corn starch in water suspension of varying mass fraction. The gap distance used was 800µm.

Figure 54 shows the shear and normal stresses versus the applied shear rate for a corn-starch in water suspension with a solid mass fraction of 0.57. The curves in Figure 54 and Figure 55 appear strange as they loop back on themselves due to intermittent jamming causing the applied shear rate to rapidly decrease unexpectedly. It is easy to see that the changes in the shear stress directly correlate to changes in the observed normal stress. Figure 55 shows the same data used in Figure 54 but expressed in terms of viscosity versus shear rate.

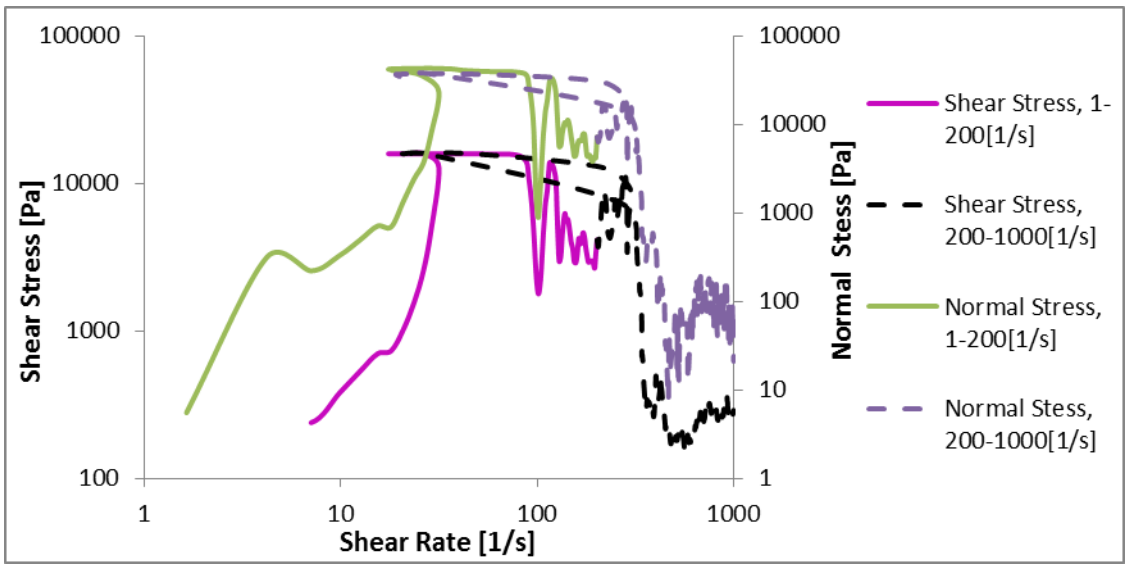

Figure 54 Shows how the resulting shear stress and normal stress varies as the applied shear rate is increased for a corn starch in water suspension with a solid mass fraction of 0.57. The same curves have been split into two different parts to improve clarity, as the curve loops back on itself at a roughly 200s^{-1} due to the DHR2 rheometer being unable to apply the necessary stress to maintain and increase the shear rate.

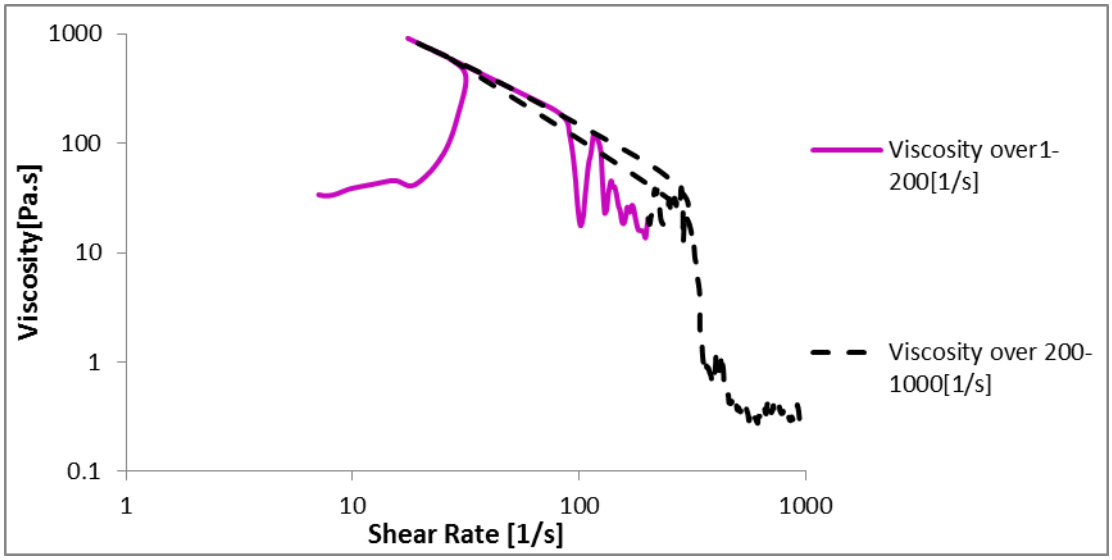

Figure 55 Shows how the resulting viscosity varies as the applied shear rate is increased for a corn starch in water suspension with a solid mass fraction of 0.57. The same curve has been split into two different parts to improve clarity.

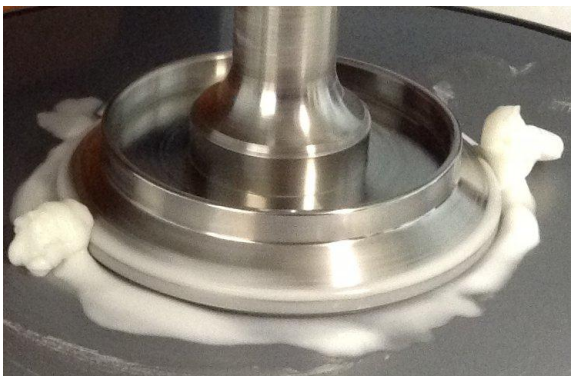

Figure 56 Shows an example of stable jammed granules that formed and were ejected from the geometry during DST of a sample of solid mass fraction of 0.57 at a shear rate of ~30s^{-1} corresponding to Figure 54 .

Figure 56 shows the formation and ejection of stable jammed granules from the sample geometry when DST was occurring. These granules remain jammed unless additional liquid is added to them in which case they appear to revert to being a fluid.

Relationship between Shear and Normal Stresses

Figure 57 and Figure 58 show how the values of the in-phase shear and normal stresses recorded at each point in time during shear ramp experiments on corn-starch suspensions compare to each other. As was the case with colloidal dispersions at high enough concentration, it can be seen that the shear and normal stresses are approximately related by Equation 87 for some constant μ_k.

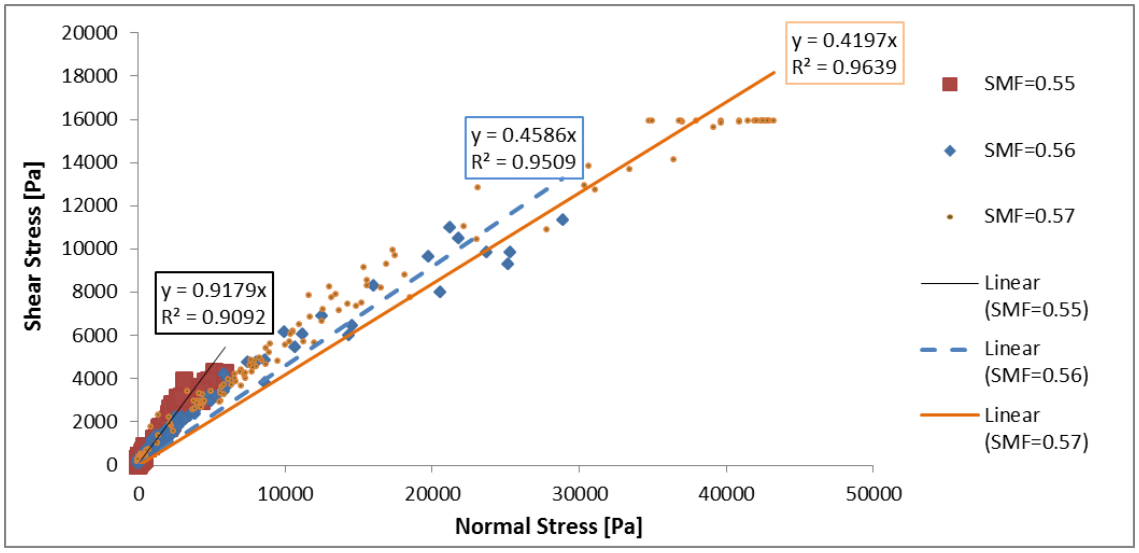

Figure 57 shows the recorded shear stress values against the recorded normal stress values during a continuous shear ramp experiment on highly concentrated corn-starch suspensions. The shear rate was varied from 0.1-1000[s^{-1}]. The R^2 values show how well the data fits the associated trend line.

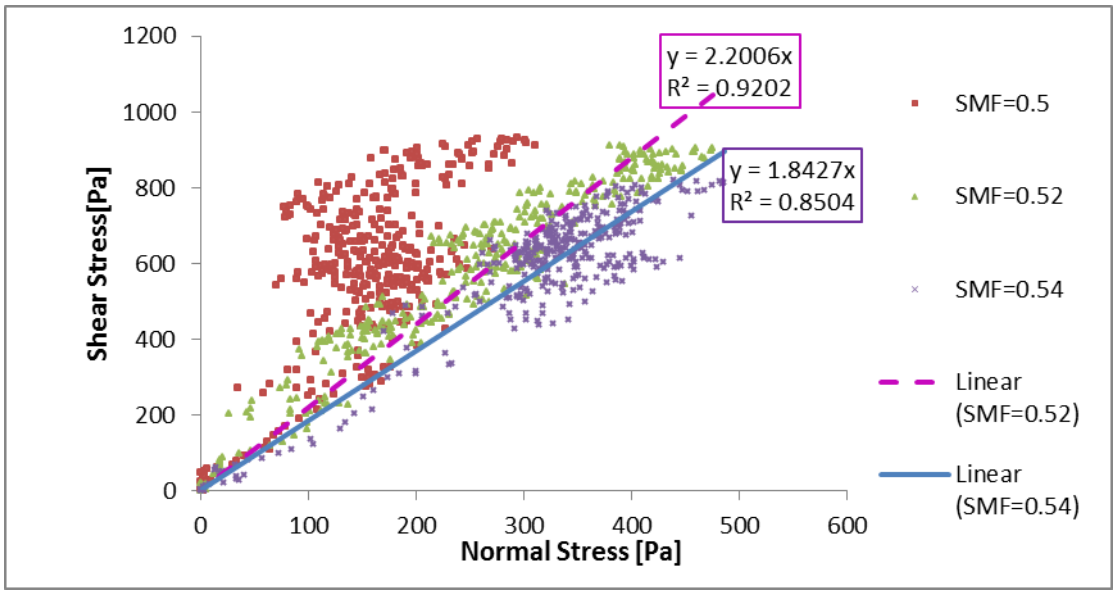

Figure 58 shows the recorded shear stress values against the recorded normal stress values during a continuous shear ramp experiment on corn-starch suspensions. The shear rate was varied from 0.1-1000 [s^{-1}]. The gap distance used was 800µm. The R^2 values show how well the data fits the associated trend line.

Figure 57 and Figure 58 show that as the solid mass fraction increases, the in phase normal and shear stress values generally become less well correlated. Additionally the fitting constant can be generally seen to decrease with increasing concentration, meaning that the normal stresses are increasing relative to the shear stress.

Figure 59 shows the viscosity and normal stresses obtained with a corn starch suspension of mass fraction of 0.48. Both shear thinning and continuous shear thickening was observed and the normal stress was always small and negative. The shear stresses did not show any correlation with the normal stresses as was observed at higher concentrations where DST was observed. This highlights that there is no such correlation between the shear and normal stresses at lower particle concentrations.

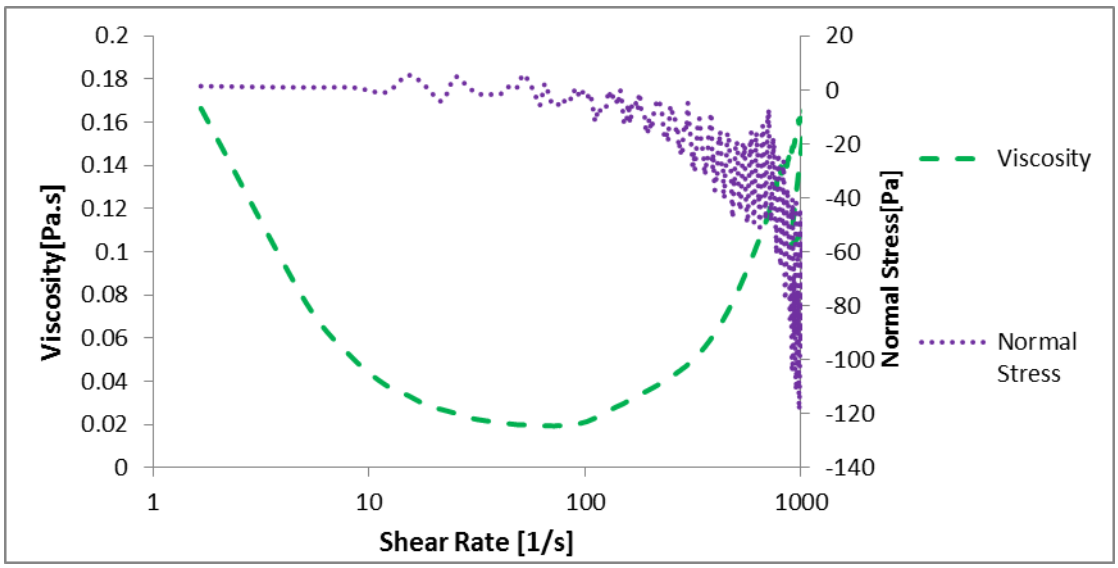

Figure 59 Shows how the resulting viscosity and normal stress varies as the applied shear rate is increased for a corn starch in water suspension with a solid mass fraction of 0.48. The gap distance used was 800µm.

5.4 Discussion of Continuous Shear of Concentrated Suspensions Results

A number of authors have suggested that DST is closely related to jamming [10,13,15,198]. The experiments displayed in section 5.2 support this. The fact that permanently jammed granules were formed during extreme DST, and that their formation corresponded with large increases in both shear and normal stress, implies that all three are linked.

5.4.1 Effect of Particle size and type on DST and Jamming

It was noticed that the peak stresses obtained during extreme DST before the sample gave a thinning response due to sample ejection, were much higher with dispersions of particles of radius 384nm than particles with radius of 574nm and 524nm.

When DST was observed in dispersions of particles of 384nm in radius, the peak stresses recorded were always greater than 15000Pa. Because the DHR2 rheometer was not designed to apply shear stresses above 15500P, it would often have difficulty maintaining the shear rate ramp and the shear rate would unexpectedly decrease as a result. When DST was observed in dispersions of particles of 574nm in radius, the peak stresses recorded varied from roughly 7000Pa at a volume fraction of 0.58 to 1500Pa at a volume fraction of 0.61. Similarly with dispersions of particles of 524nm in radius, the highest peak stress recorded was roughly 8000Pa at volume fractions of 0.58. This implies that samples consisting of smaller particles are capable of sustaining higher shear stresses before they fracture.

This agrees well with the theory that the maximum value of the stress τ_{MAX} observed during DST (in an open rheometer) scales linearly with the maximum capillary force that the fluid can exert on a particle during dilation, as this increases linearly with decreasing particle size [10,13,198]. As was mentioned in chapter 1, it has been proposed that maximum value of the confining capillary stress that limits τ_{MAX} in an open rheometer is given by the surface tension divided by the particle diameter (Γ/d). In practise it has been found that τ_{MAX} scales with $0.1\Gamma/d$ which agrees well with the values of τ_{MAX} presented in this chapter [13].

For example for the colloidal dispersions of PMMA particles of radius 574nm used in this PhD, $0.1\Gamma/d \approx$ 2500Pa which is well within the order of magnitude of the values of τ_{MAX} experimentally obtained.

The DST observed during the continuous shear of corn starch suspensions differed from that observed in the colloidal dispersions. At mass fractions of 0.5-0.54, DST was observed without any obvious sample breakup, and although the samples shear thinned after the DST region as shown in Figure 52, the resulting shear stress did not decease as shown in Figure 51 which was not the case for the colloidal dispersions. The reason the shear stress continued to increase slightly after DST was because the sample was not being ejected from the gap as was the case with colloidal dispersions.

Within this range of mass fractions examined, the peak stresses observed at the end of the DST regime were approximately 700Pa which compares relatively well with values found in and predicted from literature [13,15,191]. This again supports the idea that τ_{MAX} is inversely proportional to the particle size of the suspensions due to the value of the constraining capillary stress. The observed value of τ_{MAX} for corn-starch suspensions of mass fractions between 0.50-0.54, was roughly 10 times smaller than those observed with colloidal dispersions of roughly 1.1μm in diameter. As the colloidal PMMA particles were roughly 10 times smaller than the corn-starch particles (average diameter of around 14 microns), this again supports the theory that the value of τ_{MAX} is inversely proportional to the particle size of the suspended particles [10,13,198].

Additionally as the concentration of starch suspensions increased beyond solid mass fractions above around 0.54, the peak shearing and normal stresses observed during DST increased dramatically as shown in Figure 51 and Figure 53. As the solid volume fraction of colloidal dispersions was increased, the peak shearing and normal stresses stayed approximately constant except at very high solid volume fractions where it decreased slightly due to premature break up and escape of the sample.

During the continuous shear ramp experiments involving corn starch in water suspensions with mass fractions of 0.57, the normal stress values observed exceeded 40000Pa and were far beyond those observed during the continuous shear ramp experiments of any of the colloidal dispersions that were examined. The shear stress values during DST were also so high that the shear rate decreased rapidly because the rheometer could not apply enough force to even maintain its current shear rate until large jammed granules had been ejected from the gap.

For corn-starch in water suspensions of mass fractions of 0.56 and above, the shear and normal stresses observed were also far beyond values recorded or expected from literature which are of the order of 1000Pa [13,15]. The cause for these unexpectedly high values of the normal and shear stresses is possibly related to the formation of the jammed granules that were seen ejecting from the geometry gap. Given that individual corn-starch particles are relatively incompressible [13], it is likely that force chains could sustain normal stresses of the order of 40000Pa and that very high shear forces would be required to move large jammed granules past each other.

A possible reason for corn-starch samples of mass fraction of 0.56 and above showing such extreme DST and jamming behaviour compared to corn-starch suspensions of lower mass fractions, as well as highly concentrated PMMA suspensions is therefore the onset of granulation.

5.4.2 Relationship between Normal and Shear Stresses during DST

As was mentioned in chapter 1, Lootens carried out experiments using a cone and plate geometry operating at a fixed shear rate on concentrated suspensions of rough colloidal silica particles of 1 μm in diameter. He showed that large correlated fluctuations in both the shear and normal stresses occurred frequently [88]. Lootens observed that at volume fractions below a threshold value, the large normal stress fluctuations that were in phase with shear stress fluctuations were negative, but that at higher ϕ_S, the normal stress fluctuations were positive.

This agrees well with the results presented in section 5.2 involving the application of shear ramps on a variety of colloidal dispersions. In these experiments the large normal stress fluctuations that were in phase with large positive shear stress fluctuations during DST, were generally negative at volume fractions below around 0.59 and positive at higher volume fractions.

Using confocal microscopy, Lootens observed that the large positive normal stresses fluctuations were caused by the dilation of force chains made up of clusters of colloidal particles [88]. He suggested that the reason for the large negative normal stresses he observed at lower solid volume fractions to be due to flow anisotropy such as the

formation of ordered layers [54,197]. This is known to cause small negative normal stresses during the shear of suspensions at low shear rates where DST is not occurring [31].

Lootens also showed at high concentrations (where the normal stress fluctuations were always positive) the magnitude of the shear stress fluctuations appeared to be a linear function of corresponding positive normal stress values that were recorded at the same instant [54].

Similar large increases in the normal stresses in the DST regime during shear ramp experiments on density matched corn-starch suspensions have been reported by Fall [15], and by Chang and co-workers but using colloidal dispersion of particles of roughly 300nm in diameter [114]. Both sets of authors used parallel plate geometries. In these experiments however, the large fluctuations in the normal stress coinciding with DST were always positive, as was the case with the majority of results on corn-starch suspensions shown in section 5.3.

Fall showed that during a shear sweep experiment on a corn-starch suspension with a volume fraction 0.44, the shear stress was related to the normal stress by the following equation where μ_k=0.62:

$$\tau_{shear} = \mu_k \sigma_{normal}$$

This corresponds well to results experiments presented in section 5.2.

In section 5.2 it is shown that a similar relation can be used to describe the relationship between the shear and normal stresses for extremely concentrated PMMA colloidal dispersions during shear ramp experiments but that the relationship breaks down at lower solid volume fractions.

We also show that as the particle concentration increases, the value of μ_K generally decreases, meaning that the normal stresses corresponding to a given shear stress increase with concentration. We also show that as the concentration is increased, generally the magnitudes of the normal and shear stresses become increasingly correlated. This implies that the shear thickening at these high volume fractions is likely due to direct frictional contact between the particles[15]. If particles are closely packed then dilation has to occur in order for the suspension to flow, this results in the applied shear forces causing normal stresses.

5.5 Large Amplitude Oscillatory Shear (LAOS) of Concentrated Colloidal Dispersions

In this subsection the displayed results correspond to the application of LAOS on a variety of sterically stabilised colloidal PMMA dispersions that were dispersed in a refractive index matched solution of decalin and tetralin. LAOS is discussed in chapter 1.

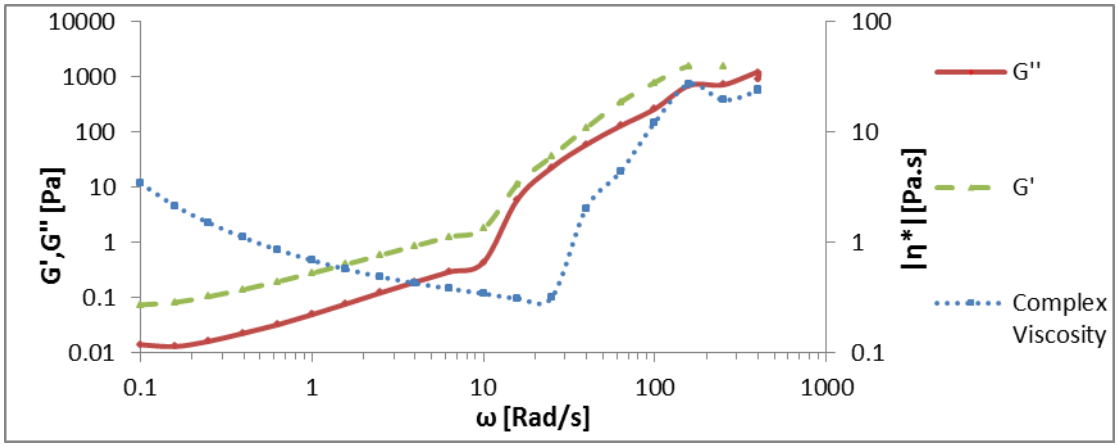

Figure 60 Shows how the elastic modulus (G')and viscous modus (G''), as well as the modulus of the complex viscosity varies with the angular frequency of oscillation applied to a colloidal disperion with a solid volume fraction of 0.56. The dispersion consisted of PMMA particles of 574nm in radius. The shear strain% every cycle was 200% which corresponds to a maximum angular displacement of 0.1 radians. The gap distance used was 1000µm.

Figure 60 shows that the colloidal dispersion with a solid volume fraction of 0.56 displays strong viscoelasticity in response to LAOS and that the modulus of the complex viscosity can show oscillatory DST during LAOS at angular frequencies beyond around 20rad/s.

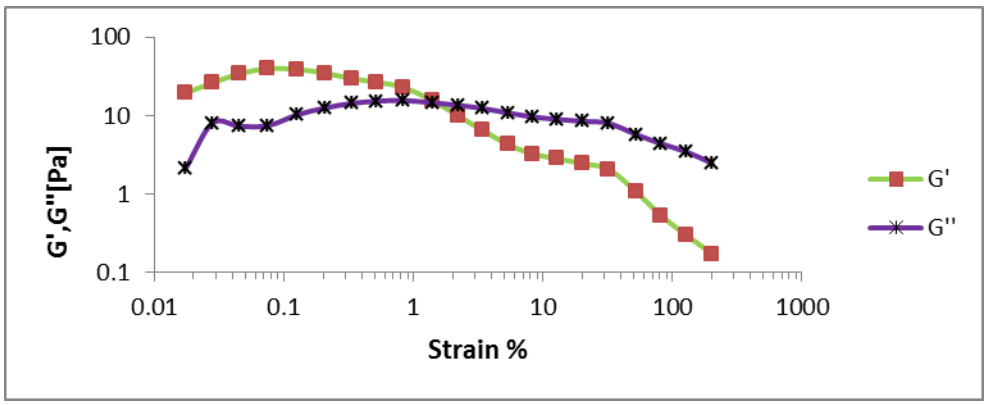

Figure 61 Shows how the elastic and viscous moduli of a colloidal disperion of PMMA particles varies as the peak strain% is increased. The angular frequency of the applied oscillatory strain was fixed at 20 rad/s. The solid volume fraction was 0.55 and the particle radius was 574nm.

Figure 61 shows that when the dispersion undergoes oscillatory shear strain at 20rad/s and at peak strains above around 2%, the response of the dispersion is out with the linear viscoelastic regime where G' and G'' are related roughly linearly [32,52] . It is therefore safe to refer to such oscillatory flows at higher peak strains as being LAOS rather than SAOS.

Figure 62 and Figure 63 show how the modulus of the complex viscosity varies with angular frequency during the LAOS of a variety of volume fractions of PMMA colloidal dispersions at a fixed shear strain of 200%. The angular frequency was increased from 0.1-400 rad/s.

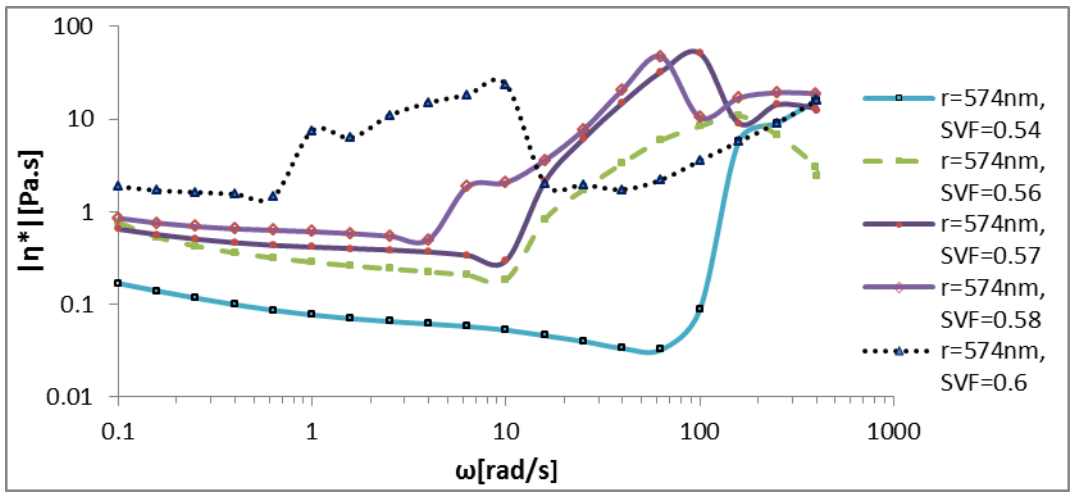

Figure 62 Shows how the modulus of the complex viscosity varies with the angular frequency of oscillation applied to colloidal disperions of PMMA particles of 574nm in radius. The shear strain% every cycle was 200% which corresponds to a maximum angular displacement of 0.1 radians.

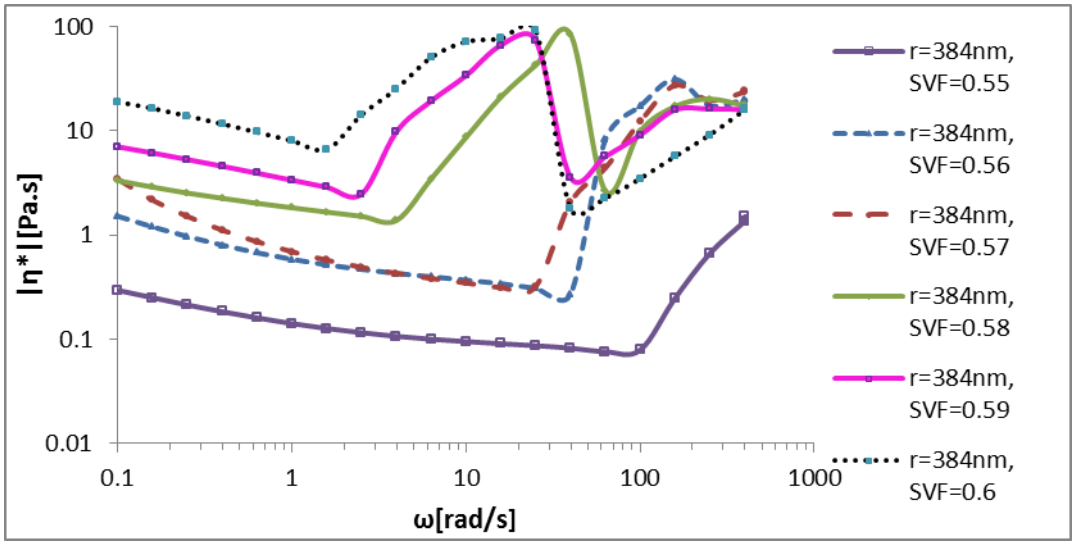

Figure 63 Shows how the modulus of the complex viscosity varies with the angular frequency of oscillation applied to colloidal disperions of PMMA particles of 384nm in radius. The shear strain% every cycle was 200% which corresponds to a maximum angular displacement of 0.1 radians.

It is important to note that some authors prefer to plot the complex viscosity and viscous and elastic moduli against a variable called the dynamic shear rate which is simply given by the peak strain multiplied by the angular velocity. In Figure 62 and Figure 63, it is simple to convert the x-axis from showing angular frequency of oscillation to showing the dynamic shear rate by simply multiplying the x-axis values by a factor of 2, this is because the strain every cycle is fixed at 2 (200 strain%).

Both Figure 62 and Figure 63 show that at solid volume fractions above and around 0.58, it was common for samples to display sharp decreases in the complex viscosity directly after oscillatory DST. This was observed to be caused by the sample partially ejecting from the geometry as shown in Figure 64.

Figure 64 Shows a picture of a sample of a colloidal disperions of PMMA particles of 384nm in radius with a volume fraction of 0.59, after it had undergone LAOS.

Figure 64 shows an example picture of a sample of a colloidal dispersion with a solid volume fraction of 0.59, after it had undergone LAOS. It can be seen that much of the sample from the centre of the gap has escaped and that some of the dispersion on the outer rim has formed a stable jammed structure.

Figure 65 shows that as the solid volume fraction of the dispersions increased, the angular frequency at which oscillatory DST began decreased sharply for both sets of dispersions. Figure 66 shows a plot of the complex viscosity at the onset of oscillatory DST versus the solid volume fraction. It shows that the critical complex viscosity increases sharply with the solid volume fraction.

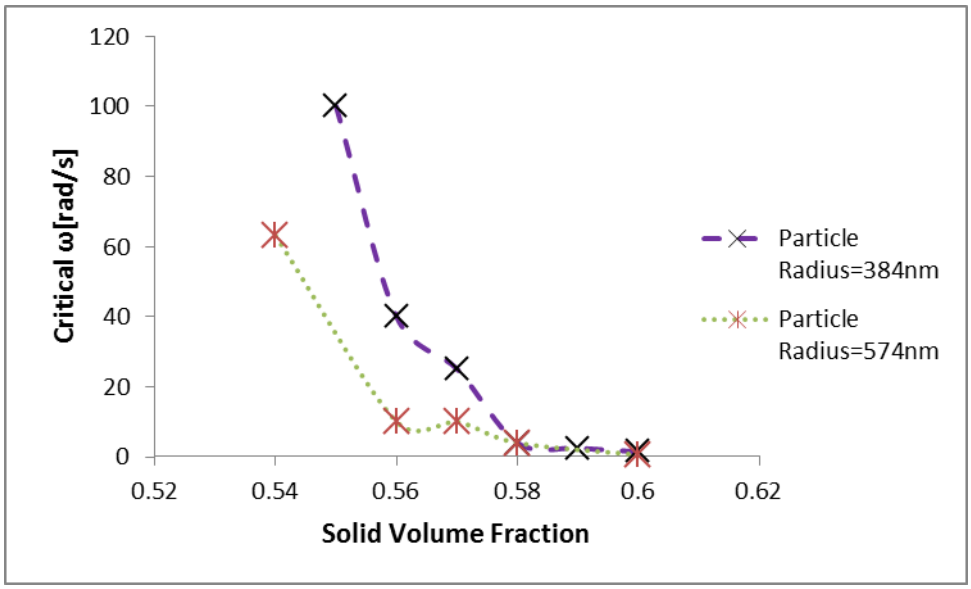

Figure 65 shows a plot of the critical angular frequency observed at which the onset of oscillatory DST is observed vs. the solid volume fraction during frequency sweeps at a fixed peak strain of 200%.

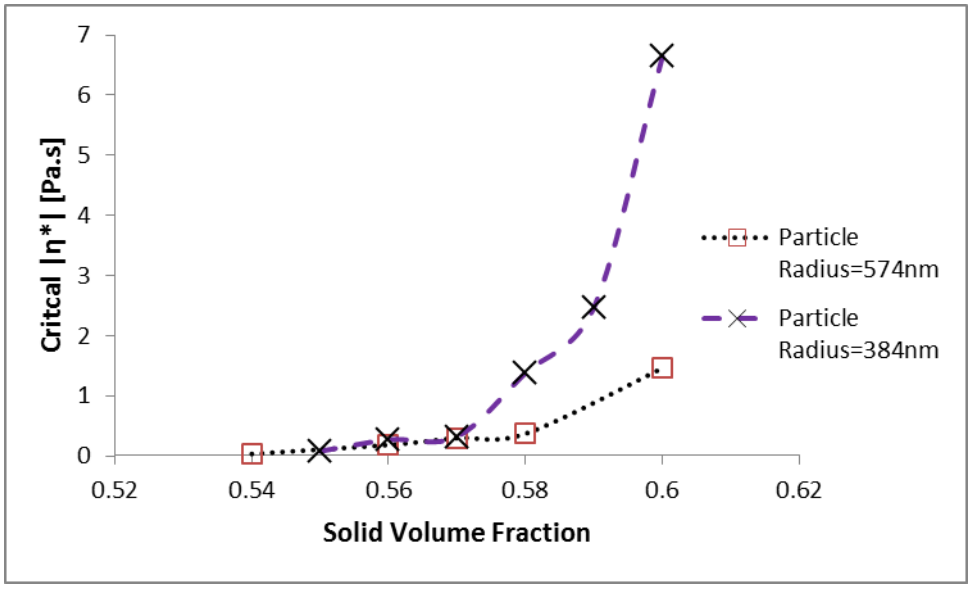

Figure 66 shows a plot of the critical complex viscosity observed at the onset of oscillatory DST vs. volume fraction during frequency sweeps at a fixed peak strain of 200%.

5.6 Large Amplitude Oscillatory Shear of Concentrated Corn Starch Suspensions

In this subsection, results corresponding to the application of LAOS on corn starch in water suspensions of solid mass fractions between 0.48-0.57 are displayed. The gap distance used for all such experiments was fixed at 800µm. The peak strain was fixed at 200% every cycle.

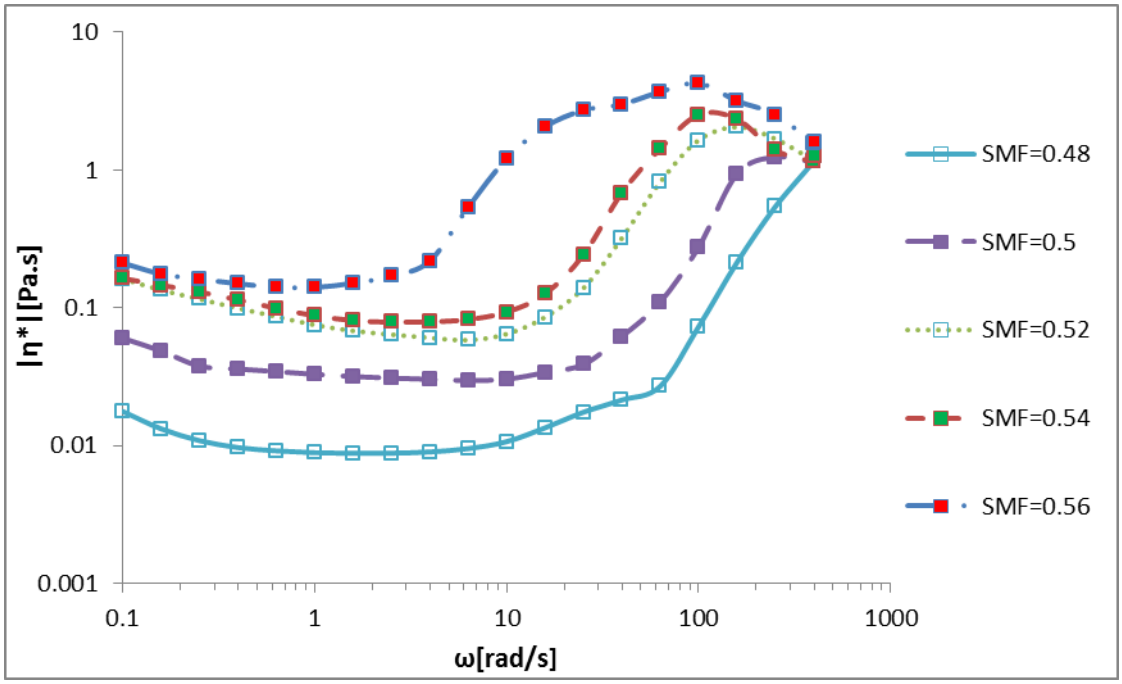

Figure 67 Shows how the modulus of the complex viscosity of corn starch in water suspension varies with the angular frequency of oscillation. The shear strain% every cycle was 200% which corresponds to a maximum angular displacement of 0.1 radians.

Figure 67 shows that as the solid mass fraction of the corn starch in water suspensions increases, oscillatory discontinuous shear thickening occurs at lower shearing frequencies. It also shows that the peak complex viscosity generally increases with the solid mass fraction as does the initial complex viscosity.

Figure 68 shows that as the solid mass fraction of the corn-starch in water suspensions increases, the critical angular velocity required to cause the onset oscillatory DST decreases sharply. Figure 69 shows that as the solid mass fraction of the corn starch in water suspensions, the critical complex viscosity at the onset of oscillatory DST increases exponentially.

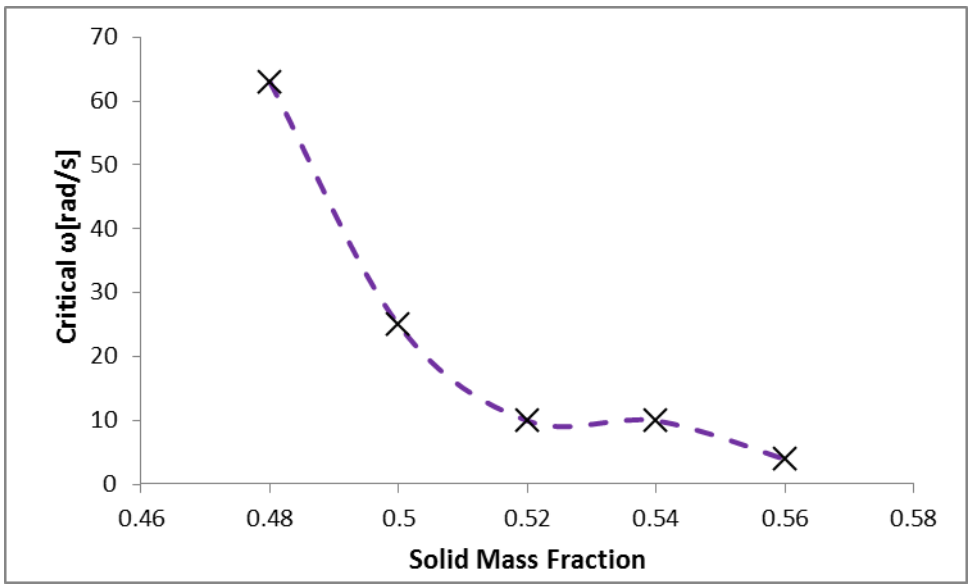

Figure 68 shows a plot of the critical angular frequency observed at which the onset of oscillatory DST is observed vs. the solid mass fraction during frequency sweeps at a fixed peak strain of 200%.

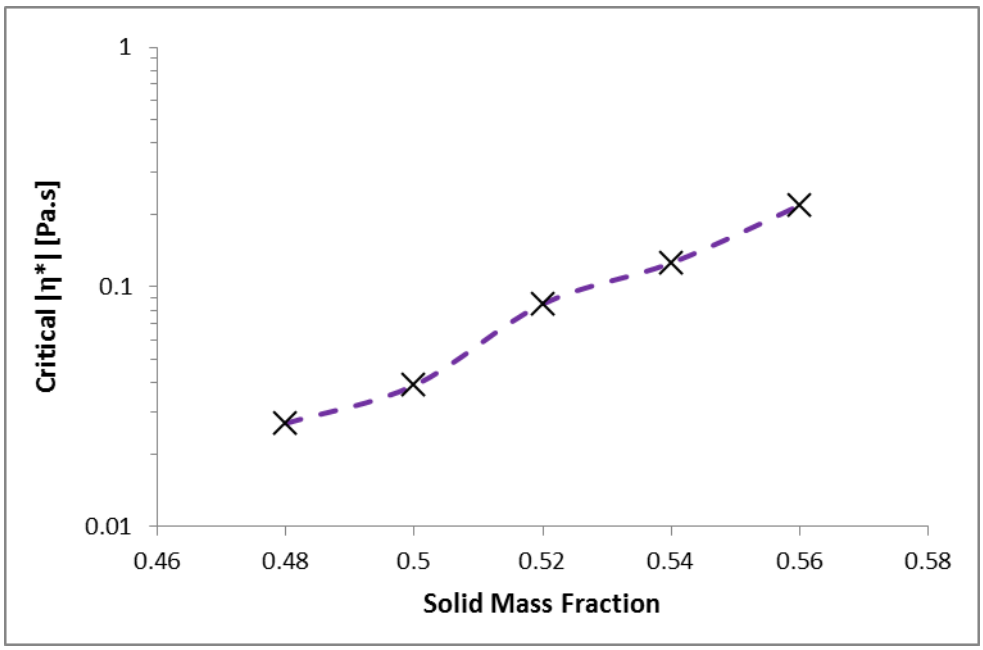

Figure 69 Shows a plot of the critical complex viscosity observed at the onset of oscillatory DST vs volume fraction during frequency sweeps at a fixed peak strain of 200%.

Comparing Figure 68 and Figure 69 with Figure 65 and Figure 66 shows similar trends between LAOS of colloidal dispersions and corn starch suspensions.

5.7 Discussion of LAOS of Concentrated Suspensions Results

Comparing Figure 62, Figure 63 and Figure 67, a clear trend is shown that oscillatory DST of the colloidal and granular suspensions used in this thesis becomes more severe and occurs at lower angular frequencies of oscillation as the volume fraction increases. This agrees well with the continuous shear experiments carried out on the same particle suspensions in section 5.2.

Additionally it was observed during the LAOS of concentrated colloidal dispersions that permanent jamming and sample ejection occurred just as it did in continuous shear experiments. This implies that DST, jamming and sample yielding/fracture can occur in oscillatory flows in a similar way as they do in continuous shear flows.

Comparing Figure 42,Figure 65 and Figure 68, it is shown that just as the critical shear rate for DST in continuous shear flows decreases sharply with volume fraction, so does the critical angular frequency for oscillatory DST of concentrated suspensions. It should be noted that Fall reported a linear decrease in the critical shear rate at which shear thickening occurred with increasing volume fraction , however those critical shear rates referred to the onset of CST not DST [15].

The vast majority of experiments involving the oscillatory shear of particle suspensions presented in the literature involve the application of strain or stress sweeps at fixed frequencies of oscillation, rather than the application of frequency sweeps at a fixed strain as was done in this PhD. The results presented in literature compare well with those presented in this chapter despite a significant number of experimental differences [103,114].

Oscillatory experiments were carried out by Lee and Wagner on colloidal dispersions of mono-disperse silica particles with radii of 223±4nm dispersed in both aqueous solution and ethylene glycol at volume fractions of 0.55 and 0.6 [103]. In their experiments they applied both oscillatory strain and stress sweeps at fixed angular frequencies in the range of 0.1-10 rad/s. They showed dramatic increases in viscous dissipation during oscillatory shear thickening which they attributed to the jamming of hydroclusters. They also showed that a critical average stress was required in order for shear thickening to be observed that decreased with the frequency of oscillation. The peak complex viscosities observed during

DST by Lee and Wagner were much higher than those observed in this PhD with all sets of particles. This is likely due to the size of the silica particles used by Lee and Wagner being considerably smaller, allowing them to sustain higher stresses without the suspensions fracturing [103].

Xu and co-workers carried out oscillatory strain sweeps experiments using a parallel disk geometry on granular suspensions of ZrO_2 particles of 100μm in radius suspended in a variety of standard oils of differing viscosity [112]. They used a solid volume fraction of approximately 0.54. Their results compare well with the oscillatory shear experiments on corn starch suspensions presented in Figure 67. Their experiments showed that as the viscosity of the suspending medium increases, the transition into oscillatory DST becomes less distinct [112]. The peak complex viscosities obtained by Xu and co-workers compare well to the peak values observed during the LAOS of corn starch in water suspensions during this PhD that can be extracted from Figure 67.

Raghavan and Khan carried out LAOS experiments on dilute suspensions of non-stabilised fumed silica particles of mass fractions of between 3-10% at large peak strains of 750% [105]. The particles were roughly spherical and roughly 14 microns in diameter which compares well to corn-starch suspensions. Their experiments showed that severity of oscillatory shear thickening increased with particle concentration as is shown in this chapter. However, their experiments also showed that the critical frequency for oscillatory shear thickening appeared relatively independent of the particle concentration. Additionally despite the low concentration of the suspensions used, the recorded complex viscosities were high compared to those observed during the LAOS of corn-starch suspensions in this thesis.

Chang and co-workers carried out both steady and oscillatory shear experiments using parallel disk geometry on colloidal dispersions at fixed volume fraction of 0.58 [114]. The dispersions consisted of polydisperse (irregularly shaped) polystyrene particles with an average diameter of 300nm dispersed in ethylene glycol. In their experiments they carried out steady shear and oscillatory strain sweeps at a range of fixed frequencies of oscillation, using a range of different gap distances. The largest gap distance they used was 800 microns and at this gap distance both the steady and oscillatory shear experimental results compare well to results presented in this chapter. Strong oscillatory DST was observed at similar conditions. They also showed that as the frequency of oscillation increased, lower

peak shear strains were required to cause oscillatory DST. It is interesting to note that the peak complex viscosities reported were higher than those presented in this thesis. This again could be related in some way to the fact that the particles used were not stabilised and were irregularly shaped, as well as being considerably smaller than those used in this PhD. This would likely mean the maximum containing capillary stress would be much larger, allowing the sample to sustain higher stresses before fracturing and ejecting from the rheometer.

5.8 Summary of Parallel Plate Rheometry Results

As long as the concentration of colloidal dispersions of PMMA particles and suspensions of corn starch suspensions were high enough, then discontinuous shear thickening was observed at high enough applied shear stresses during continuous shear as expected. As the solid volume fraction of both colloidal PMMA dispersions and granular suspensions of corn starch increases, then DST occurred at lower applied shear rates as expected. This proves that these systems display DST and that these systems are expected to show DST during oscillatory squeeze film flow experiments as long as the applied stresses and the system concentrations are high enough. It also implies that these systems are expected to show DST effects at lower squeezing frequencies as the particle concentration increases.

DST would often be accompanied by effects such as sharkskin, fracture and partial ejection of the sample from the geometry. Often at extremely high concentrations permanently jammed granules would eject from the geometry gap. This implies that if DST occurs during oscillatory squeeze film flow then similar effects may occur.

It was observed that as the size of the colloidal particles within the dispersion decreased, the peak shear stress obtained during DST tended to increase. This compares will predictions made by Cates and Brown as discussed in chapter 1 that the maximum stress jammed particle suspensions can sustain before fracture is proportional the confining stresses on the system.

It was generally the case that when DST occurred during the continuous shear of colloidal dispersions, the peak stress encountered before sample break up was approximately

constant regardless of the volume fraction as long as the solid volume fraction was below around 0.61. This implies that similar behaviour may be observed during OSFF experiments.

The onset of DST coincided with large fluctuations in the normal stresses that could be positive or negative depending on the solid volume fraction of the colloidal dispersion.
It was generally the case that when DST occurred during the continuous shear of corn starch suspensions, the peak stress encountered before sample ejection increased with the solid mass fraction of the suspension. At high enough mass fractions, intermittent jamming of the corn-starch suspensions temporarily brought the rheometer's motor to a halt. Intermittent jamming also unexpectedly slowed the rheometer's motor during the shear of colloidal dispersions.

Fluctuations in the normal stresses were generally in phase with fluctuations in the shear stresses during DST which agrees well with results observed by Fall and Lootens as discussed in chapter 1. At extremely high particle concentrations where the RCP is approached, the shear stresses and normal stresses observed during shear become increasingly related by a linear function. As the particle concentration increases, the strength of the in phase normal stresses generally increased relative to the shear stresses during DST. These observations support the idea that direct frictional interactions between particles and dilation are important in understanding DST.

During the large amplitude oscillatory shear of colloidal dispersions of PMMA particles and of corn starch suspensions, oscillatory DST was observed at high enough angular frequencies of oscillation. This also implies that these systems are expected to show DST during OSFF at high enough squeezing frequencies and peak squeezing stresses.

As the solid volume fraction of both colloidal PMMA dispersions and granular suspensions of corn starch increased, then the critical frequency at which oscillatory DST occurred decreased sharply while the magnitude of the complex viscosity at the onset of oscillatory DST increased sharply. This also implies that these systems are expected to show DST effects at lower squeezing frequencies as the particle concentration increases.

During the LAOS of colloidal dispersions of PMMA particles of high enough solid volume fraction, it was observed that they could give a shear thinning response after oscillatory DST due to the sample partially ejecting from the geometry. Sections of the sample were also observed to form stable jammed structures during LAOS. It was shown that there are a number of similarities between the DST of suspensions in both continuous shear and LAOS experiments. This implies that it is possible for jammed structures to be formed during OSFF.

Chapter 6 Results and Discussion of the Squeeze Film Flow of Concentrated Suspensions

6.1 Chapter Summary

In this chapter, it is shown that when concentrated enough colloidal dispersions and corn starch suspensions were subjected to oscillatory squeeze film flows using the electromechanical squeeze cell, they can show unusual non-Newtonian responses consistent with jamming. When a Newtonian fluid like glycerol or viscoelastic polyacrylamide solutions were subjected to the same oscillatory squeeze flows, no unusual responses were observed. At high enough peak stresses and squeezing frequencies, it was observed that the local flow field of colloidal dispersions became distorted. Macroscopically the sample shape of concentrated enough colloidal dispersions and corn starch droplets was observed to become continuously more distorted while subjected to such oscillatory squeeze film flows. These results are discussed in the context of the surrounding literature. Potential reasons for the cause of the observed flow field and sample shape distortions are also put forward.

6.2 Oscillatory Squeeze Film Flow (OSFF) of Glycerol

Before applying OSFF to concentrated dispersions of colloids using the electromechanical squeeze cell described in section 4.2, it is important to have a clear view of what happens when OSFF is applied to a Newtonian fluid in the same apparatus. As concentrated suspensions are highly viscous, it makes sense to use a viscous Newtonian liquid such as glycerol (which is roughly 1000 times more viscous than water) for comparison.

Being Newtonian, glycerol is not expected to show unusual behaviour as the rate of deformation or the peak squeezing force changes. Therefore it was important that when applying OSFF to glycerol that the expected results were observed, or it would indicate faults with the apparatus. For Newtonian fluids, at a given position within a sample, the oscillating flow field should not change from one cycle to the next over time. The overall shape of the flow field also should not change as the rate of deformation or the applied stress changes. This is what was observed as shown in Figure 70A and Figure 70B. Suspended melamine tracer particles within samples of glycerol being squeezed and

stretched traced out the same straight path lines back and forth (in the horizontal plane) every squeezing cycle without deviating.

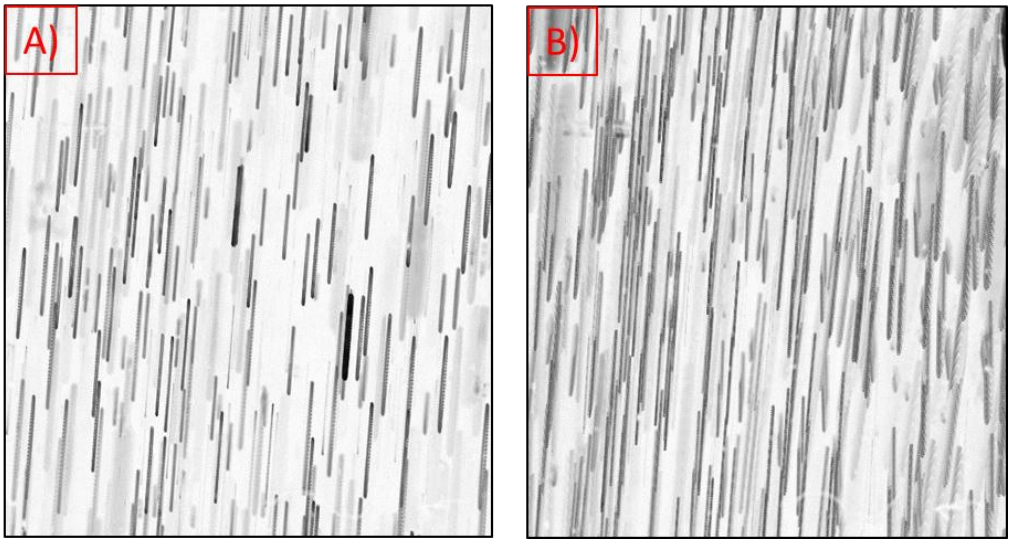

Figure 70 A) (left) Shows a minimum intensity plot of a glycerol sample squeezed at a frequency of 10.05Hz with a peak stess of around 600Pa. The gap distance was 1000 microns. The intensity plot was taken over 0.4 Seconds. B) (right) as for (A) but at a frequency of 50.5Hz with a peak stress of around 1000Pa.

As the peak squeezing force was increased, the distance the tracer particles were translated each cycle increased as expected as is illustrated in Figure 70B. Additionally, no memory effects are observed such that the history of the sample has no effect on its response to the applied squeezing.

Macroscopically the sample shape is seen to remain constant over time as it was being subjected to driving oscillatory squeeze film flow as shown in Figure 71.

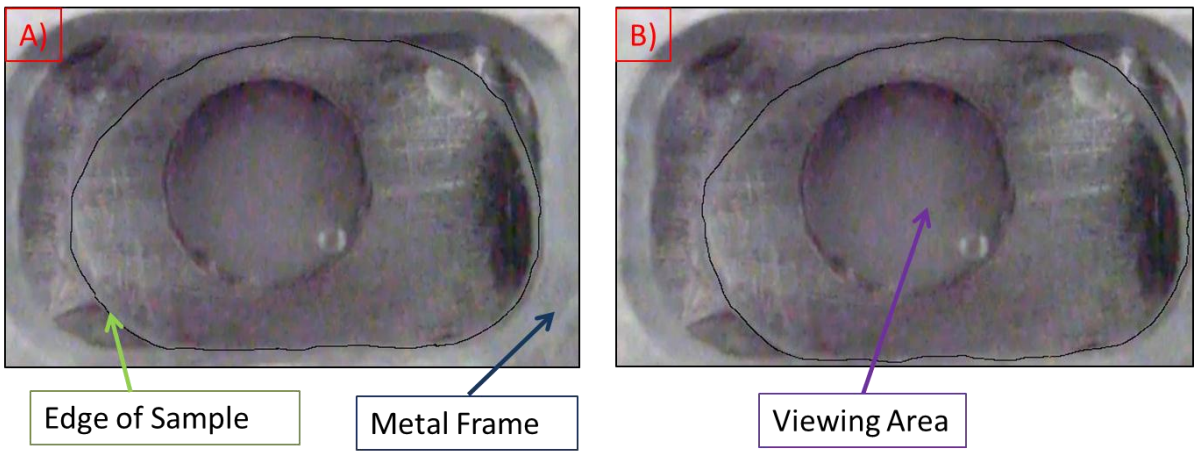

Figure 71A) Shows the initial shape of a sample of glycerol before any oscillatory squeezing had been applied. Figure 71B) Shows the shape of the same sample of glycerol as shown in Figure 71A after an oscillatory squeeze film flow of 50Hz with a peak stress of around 1000Pa had been applied for 4 minutes.

Figure 72 confirms that the glycerol samples used responded in a Newtonian manner as expected in response to a continuous shear ramp (using the DHR2 strain controlled rheometer described in chapter 4), as the viscosity essentially remained constant.

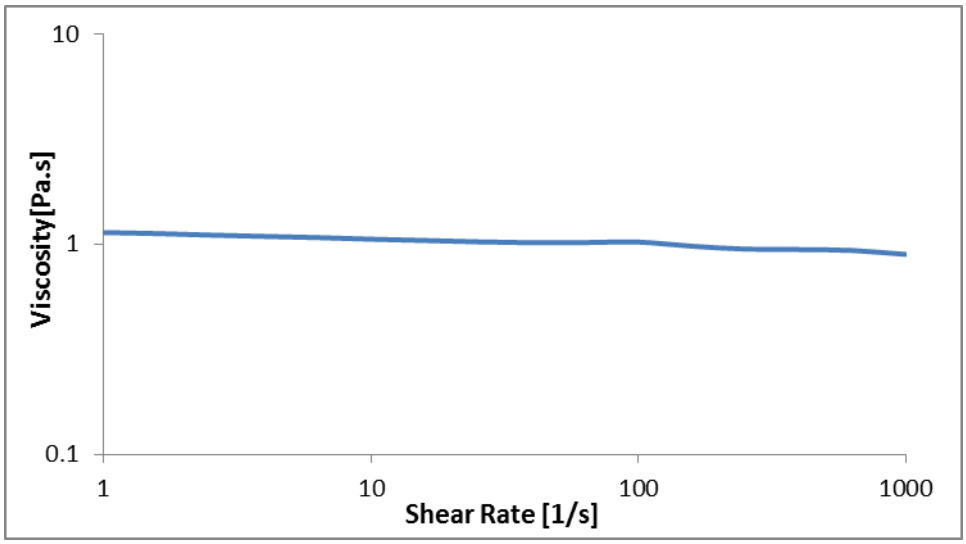

Figure 72 Shows the viscosity vs. shear rate curve of a sample of pure glycerol for comparison with concentrated particle suspensions. The temperature of the sample was controlled at 20 degrees Celsius.

6.3 OSFF and Shear Flow of Polyacrylamide in Water Solutions

In order to check that the slight viscoelasticity that particle suspensions possess was not a potential cause of any unusual behaviour observed during the oscillatory squeeze film flow squeezing of particulate systems, a slightly viscoelastic viscous substance was subjected to the same OSFF.

Polyacrylamide (PAM) solutions are commonly used as standard viscoelastic materials in experiments. PAM solutions of varying molecular weight and concentration have been extensively examined in literature using standard rheometers, showing slight shear thinning, shear thickening, and hysteresis in addition to viscoelasticity. These solutions have the added bonus of being transparent which means the flow field can be examined by dispersing tracer particles into the solution [199,200].

Solutions of PAM in water were squeezed over a wide range of frequencies. Even above 70 Hz with peak squeezing forces above 1000Pa no unusual behaviour (such as flow field distortion and sample shape change) was seen in either concentrated or dilute PAM solutions. Under squeezing, tracer particles dispersed in the solution follow straight path lines back and forth that do not change over time as is shown in Figure 73A) and Figure 73B).

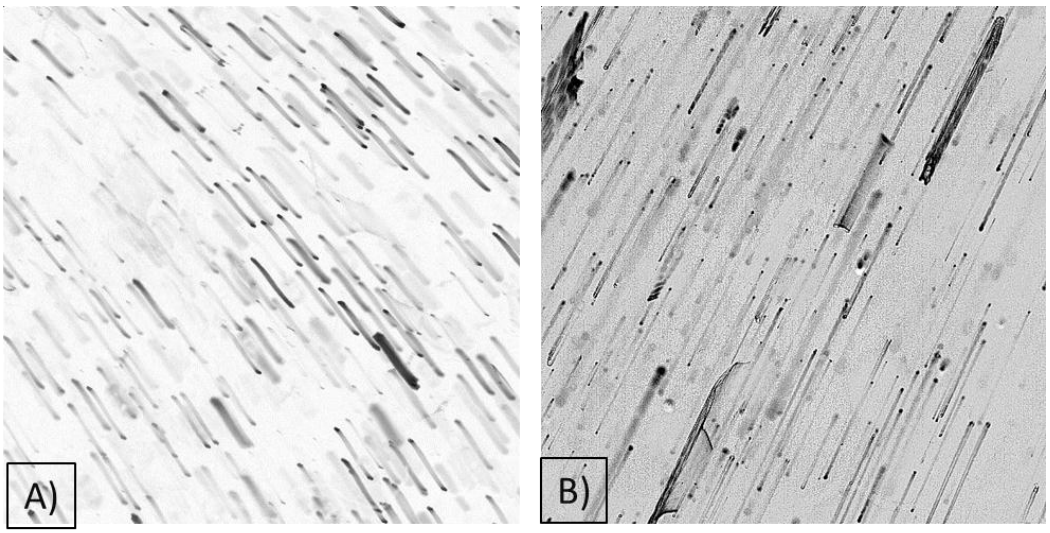

Figure 73A) (left) Minimum intensity plot obtained during squeezing of 50% PAM by weight. Average molecular weight of the polymer was 10000. The peak applied stress was 1000Pa at a frequency of 50Hz. The gap distance used was 1000 microns. The intensity plot was taken over 0.4 Seconds. B) (right) as for A) but using a 25% PAM by weight solution.

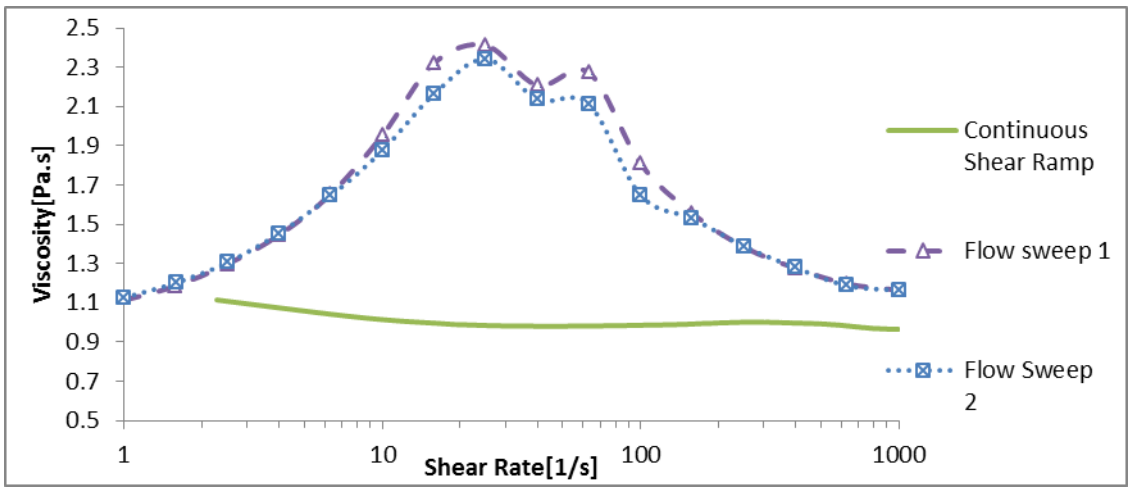

Figure 74 Shows viscosity vs shear rate curves of 50% by weight PAM in water solutions. The green curve, which corresponds to the shear rate continuously increasing with time differs from the other curves corresponding to flow sweeps, where the viscosity was analysed at only a few set shear rates but over a longer time period to ensure the samples had reached equilibrium at a given shear rate.

Figure 74 shows the PAM solution has a viscosity similar to that of glycerol and is potentially capable of showing both slight shear thinning and shear thickening behaviour.

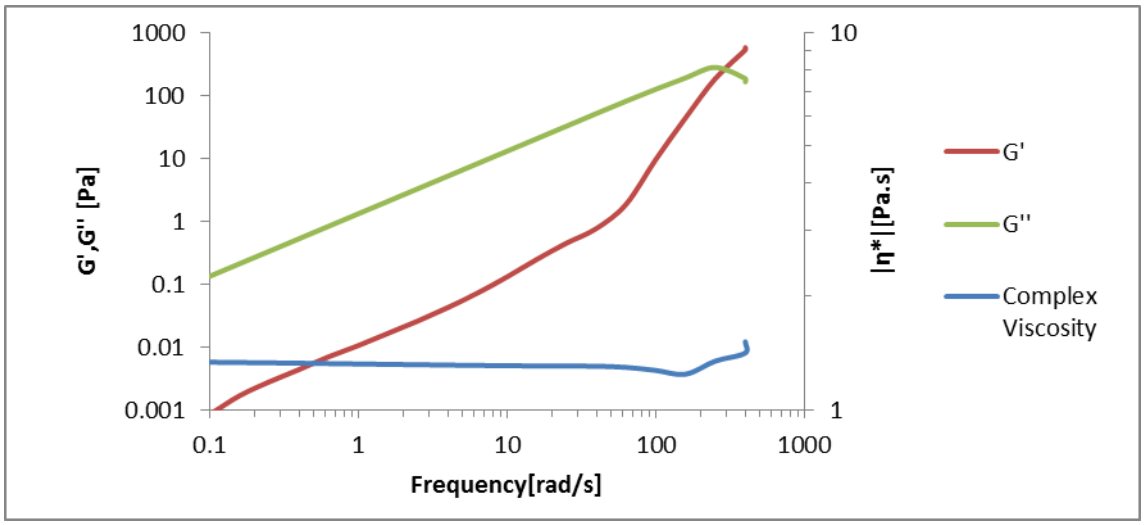

Figure 75 Shows the response of 50% by weight PAM in water solutions undergoing oscillatory shear flow within parallel plate geometry with a peak shear strain of 2(200%), which corresponds to a maximum angular displacement of 0.1 radians.

Figure 75 show that this PAM solution displayed some viscoelasticity at high frequencies of oscillation.

6.4 Squeezing of Concentrated Colloidal Dispersions Results

In these experiments, concentrated dispersions of solid PMMA particles dispersed in a refractive index matched mixture of mixed decalin and tetralin were subjected to oscillatory squeeze flow. Because the PMMA particles have the same refractive index as the medium in which they are dispersed, they are completely transparent. In order to see how the dispersion responds to OSFF, melamine tracer particles were added that were not refractive index matched to the dispersing medium.

The methodology of these experiments was to systematically vary the peak applied stress and squeezing frequency applied to colloidal dispersions of a given solid volume fraction. The motion of the tracer particles under the microscope was recorded to map out the flow field identifying responses that diverged from an expected Newtonian response.

6.4.1 Local Flow field Distortions in Concentrated Colloidal Dispersions

At high enough solid volume fractions, as the applied squeezing frequencies and/or peak squeezing stresses were increased, the local flow field was observed to change from a standard Newtonian like response with straight path lines as show in Figure 76A to a locally distorted field as shown in Figure 76B.

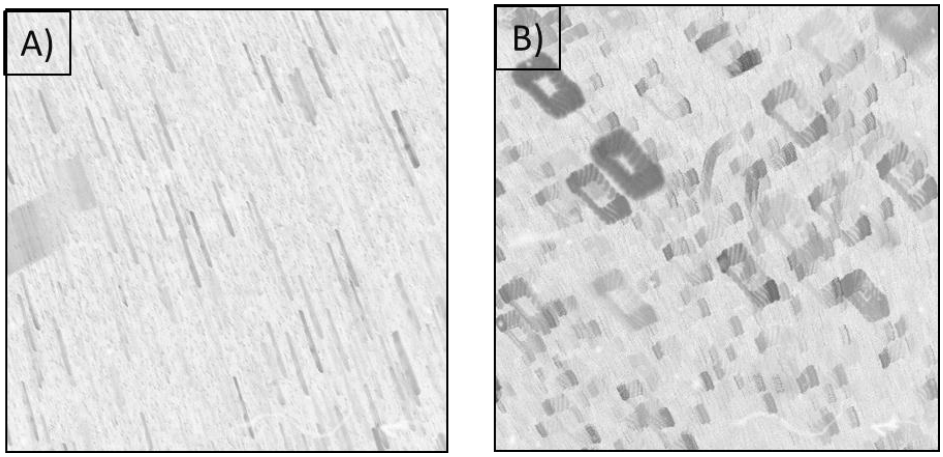

Figure 76A) (left) Shows a minimum intensity plot of a sample of a PMMA dispersion of volume fraction of 0.61 being squeezed at a frequency of 10Hz with a peak force of around 600Pa. B) (Right) as for (A) but at a frequency of 30Hz. As the squeezing frequency increased while keeping the peak squeezing force constant, the local flow field was observed to change. The radius of the dispersed particles was 574±4nm.

The observed flow field distortion usually appeared to be cyclic in that tracer particles follow a similar distorted path over each cycle as is shown in Figure 76B. This is true over a time period of a few seconds as long as the sample shape does not change too rapidly.

The observed flow field distortions are reversible. By reducing the peak stress or squeezing frequency during oscillatory squeeze film flow, the flow field reverts to a normal Newtonian response. This is illustrated in Figure 77.

Figure 77A shows a minimum intensity plot of a colloidal dispersion of ϕ=0.62 squeezed at a frequency of 30.2Hz with a peak force of 600Pa. The tracer particles trace out rectangular like paths each cycle. Figure 77B shows the same sample as shown in Figure 77A and at the same position in the sample after the applied squeezing frequency had been lowered to 9.9 Hz, while keeping the peak squeezing stress constant.

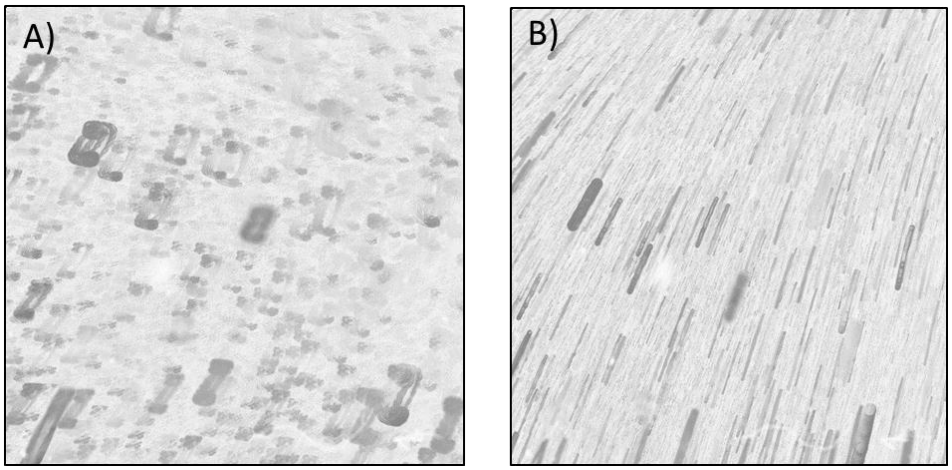

Figure 77A) (left) Shows a minimum intensity plot of a sample of a PMMA dispersion of volume fraction of 0.62 sample being squeezed at a frequency of 30.2Hz with a peak force of 600Pa.The gap distance used was 1mm.B)(right) as for (A) but with a peak squeezing/stretching stress of 600Pa and squeezing frequency of 9.91Hz. Both images were taken from the same experiment. The radius of the dispersed particles was 574±4nm.

6.4.2 Local Variation of Flow Field Distortion with Position

It was commonly observed that the shape of flow field distortions observed in a given region of a sample was not the same as flow field distortions observed in other similar regions near a different edge of the sample. In fact it was common for some regions to be heavily distorted and show clear bulk movement while other regions of a sample showed little in the way of distortion or bulk sample movement. This is illustrated in Figure 78 and Figure 79.

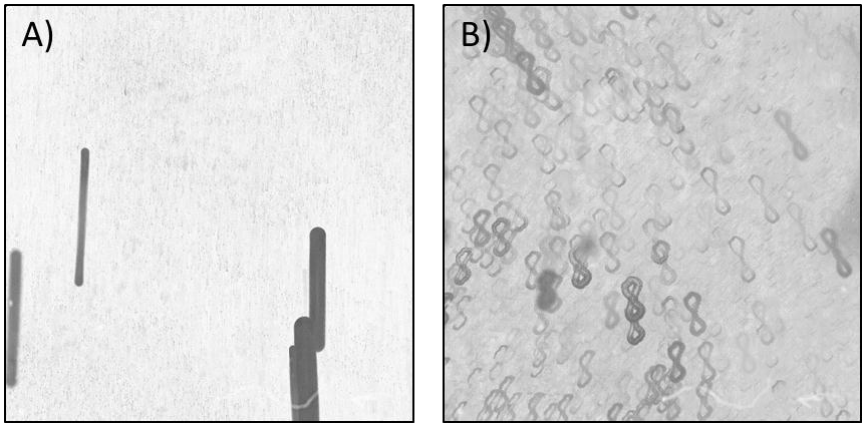

Figure 78A) shows a region of a sample of a colloidal dispersion of volume fraction 0.62 of PMMA particles of 574nm in radius. An oscillatory squeeze with a frequency of 20 Hz and a peak stress of 600Pa was applied. No unusual behaviour was observed here as can be seen by the straight path lines. Figure 78B) shows a different region on the other side of the same colloidal dispersion as in A). Unusual behaviour was observed here as can be seen by the distorted path lines.

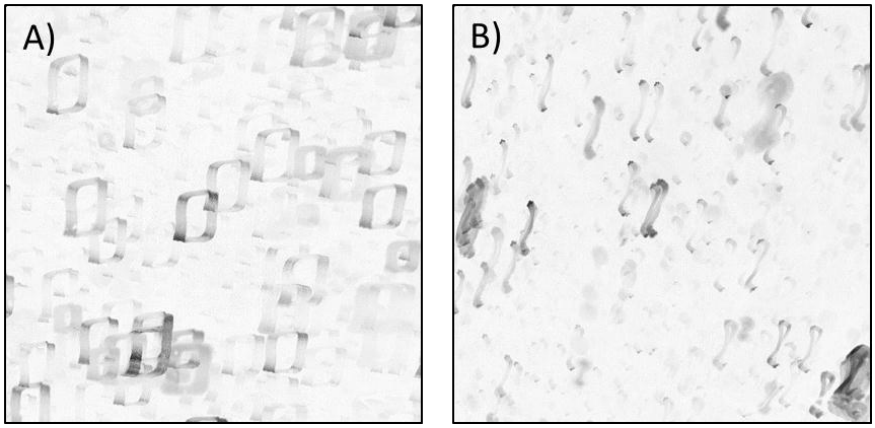

Figure 79A) shows a region of a sample of a colloidal dispersion of volume fraction 0.6 consisting of PMMA particles of 384nm in radius. An oscillatory squeeze with a frequency of 50 Hz and a peak stress of 1000Pa was applied. Strong flow field distortion was observed here as can be seen by the rectangular path lines. Figure 79B) shows a different region of the same sample as in A). The shape of the flow field distortion differed in this position.

6.4.3 Variations in Flow Field Distortions between Repeated Experiments

When an applied oscillatory squeeze flow brings about flow field distortion and the applied squeeze is ceased and then re-applied, it was common that the shape of the flow field distortion observed in the same region of the sample would change. Figure 80A and Figure 80B show how the observed flow field distortions in the same sample region at the same OSFF conditions can change by ceasing for 1 minute and then re-applying OSFF.

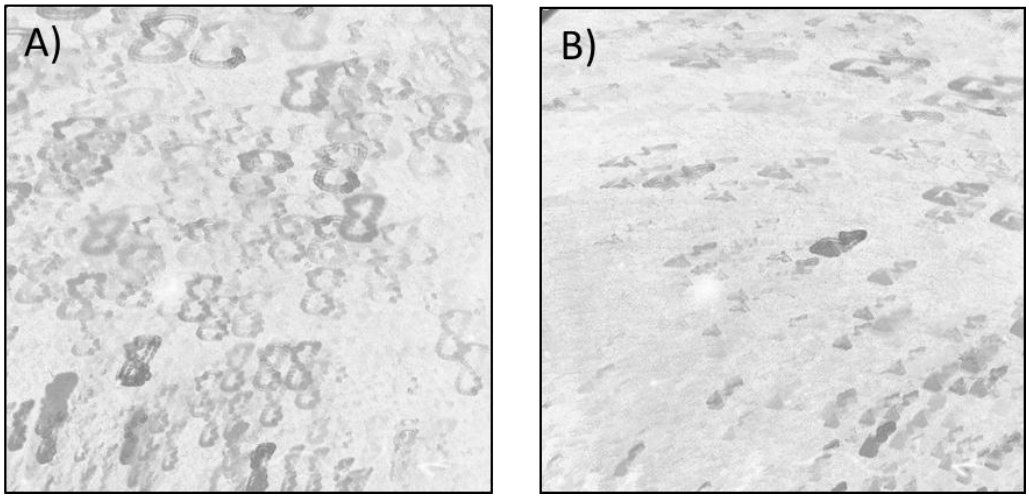

Figure 80A) shows a minimum intensity plot of a sample of a PMMA dispersion of volume fraction of 0.62 being squeezed at a frequency of 20.87Hz with a peak stress of 600Pa. B) shows a minimum intensity plot of the same sample after cessation of squeezing for 1 minute followed by squeezing at the same frequency and stress.

6.4.4 Particle Migration and Sample Shape Change of Colloidal Dispersions

When the flow field becomes distorted, tracer particles can be seen to migrate locally over time as the macroscopic sample shape changes. Figure 81 shows an example of such bulk movement over a period of 2 seconds.

Figure 81 shows two images superimposed on each other from a sample of solid volume fraction of 0.62. One image was taken at the beginning of a 2 second interval over which an applied a peak oscillatory stress of 1000Pa was applied at a frequency of 50.4Hz. The 2nd image superimposed into Figure 81 was taken at the end of the same 2 second interval. The initial and final position of tracer particles over a period of 2 seconds can be seen. In order to cancel out any differences in position due to the oscillatory flow without bulk movement, the pictures were taken at the same point in the squeezing cycle.

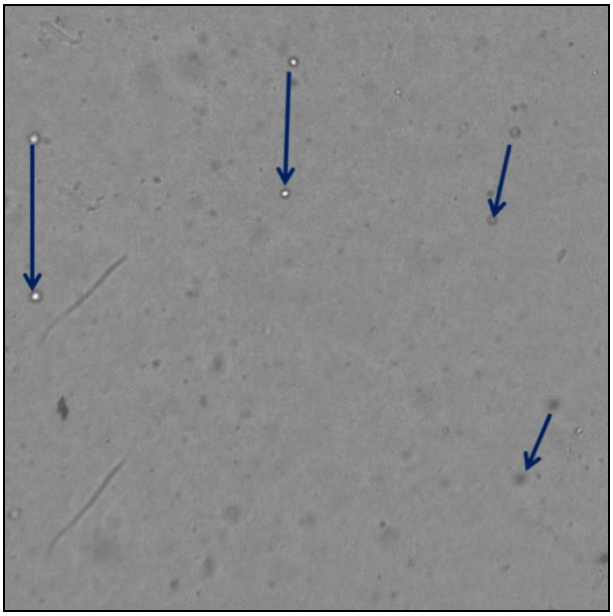

Figure 81 Movement of tracer particles over a period of 2 seconds during OSFF. The blue arrows show how particles positions have changed as the sample deformed.

Figure 82A shows the initial shape of a sample of volume fraction 0.615 and Figure 82B shows the sample shape after an oscillatory squeeze flow of 40Hz with a peak stress of 1000Pa had been applied for a period of 1 minute. Figure 82B shows that the sample shape became significantly distorted due to the application of OSFF.

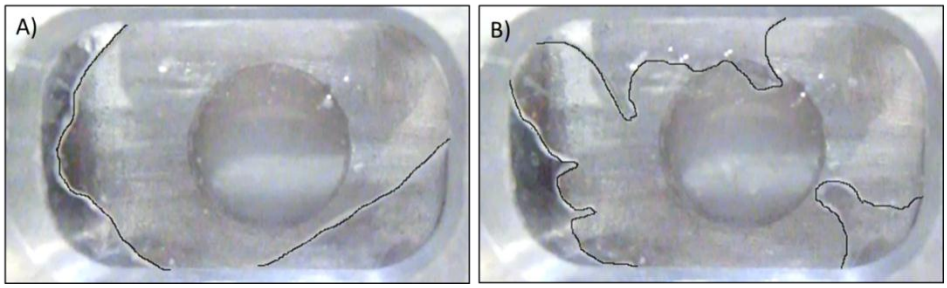

Figure 82A) Initial shape of colloidal dispersion with a volume fraction of 0.615 before any squeezing had been applied. B) Shape of same sample in Figure 82 after a period of 1 minute at a squeezing frequency of 40 Hz and a peak squeezing stress of 1000Pa.

Figure 83A shows the initial shape of a sample of volume fraction 0.605 and Figure 83B the sample later after an oscillatory squeeze flow of 30Hz with a peak squeezing stress of 700Pa had been applied for 1 minute. Figure 83C shows the sample shape after the same sample is allowed to rest without squeeze flow for a period of 14 minutes.

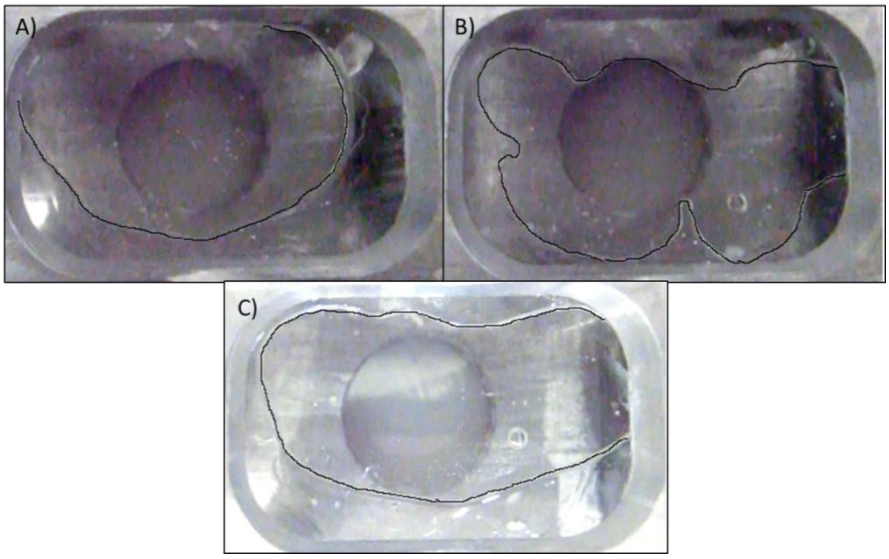

Figure 83A) Initial shape of colloidal dispersion with a volume fraction of 0.605 before any squeezing had been applied. B) Shape of same sample in Figure 83A) after a period of 1 minute at a squeezing frequency of 30 Hz and a peak squeezing stress of 700Pa. C) Shows the shape of same sample in Figure 83B) after a period of 14 minutes where no squeezing had been applied since Figure 83B) was taken.

Figure 83C shows that the sample shape distortion fades away over time after cessation OSFF, resulting in a decrease in the surface area due to surface tension. From Figure 83, it can also been seen that OSFF causes the fluid sample to move. It was commonly observed that the overall position of the samples could move across the plate in random directions as sample shape distortion was occurring.

To summarise, so far in this section it has been shown that when concentrated dispersions of PMMA are subjected to OSFF at high enough frequencies and peak squeezing and stretching stresses per cycle, reversible local flow field distortion and macroscopic sample shape distortion are observed.

6.5.1 Squeezing of Concentrated Corn-Starch Suspension Experiments

In this section, examples of the shape change of corn starch suspensions of varying solid mass fractions during the oscillatory squeeze film flow of corn starch suspensions are shown. It was not possible to examine the local flow field of corn-starch suspensions using a microscope because they are not transparent.

The peak applied oscillatory squeezing/stretching stresses at fixed frequencies at 40Hz and 50 Hz required to bring about deformation of a given samples shape are also summarised. Suspensions of corn starch in water of various mass fractions were squeezed at fixed frequencies of 40Hz and 50 Hz while varying the peak squeezing stress in the range of around 600-1000 Pa. The strategy of these experiments was to record macroscopic videos of corn starch samples and note down whether the sample shape was changing in response to the applied oscillatory squeeze film flow.

Initially the shapes of the corn starch samples were roughly circular filling the gap as a Newtonian fluid would as shown in Figure 84A. Figure 84B shows how the shape of a sample of a corn starch in water suspension of 0.59 changes after 4 minutes of an oscillatory squeeze at 50Hz and peak stress of 1000Pa. Figure 84C shows the same sample shown in Figure 84A after 6 minutes of applied OSFF.

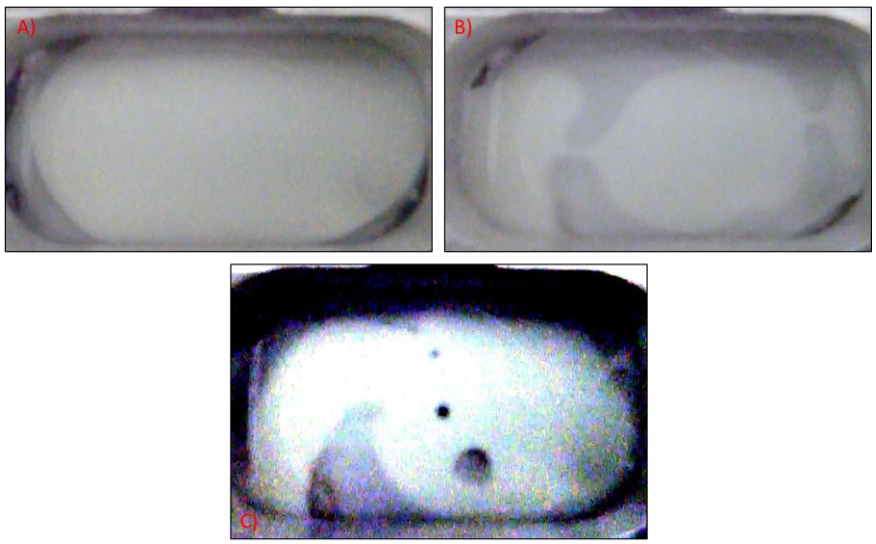

Figure 84A) A corn starch in water sample with a mass fraction of 0.59 before squeezing. The gap distance between the top and bottom plate was 1000 microns. B) Taken after 4 minutes of squeezing the same sample at 50Hz with a peak squeezing stress of 1000Pa. Note the formation of bridges that appear to hold sections of the sample together, a common observation. C) Sample after 6 minutes of squeezing.

Figure 84 shows that the sample shape of the corn starch in water suspension changes significantly over time. Note the presence of bubbles in Figure 84C but not in the previous photos. It is common that as the sample shape deforms, areas of the sample open up and close on themselves trapping air. The observed air pockets often appeared to shrink or collapse while making a surprisingly loud squeaking noise which will be discussed later. It was also common for bubbles to escape or to combine with other bubbles as the sample shape deformed.

Figure 85A shows the shape of a corn starch in water suspension of mass fraction 0.55 before any OSFF had been applied. Figure 85B shows how the same sample had deformed after 6 minutes of oscillatory squeeze film flow at 50Hz with a peak squeezing/stretching stress of 1000 Pa. Similar deformation to the more concentrated previous example is shown. Qualitatively the distortion of this sample was not as extreme as at higher mass fractions and when squeezing was ceased, the distortions in shape were eliminated more quickly.

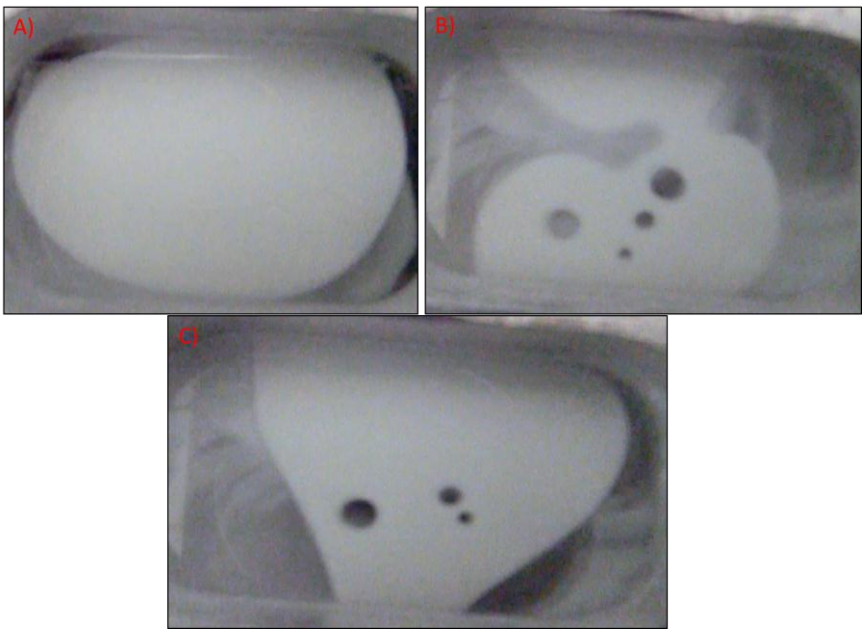

Figure 85A) A corn starch in water sample with a mass fraction of 0.55 before squeezing. The gap distance between the top and bottom plate was 1000 microns. B) Same sample with a mass fraction of 0.55 taken after 6 minutes of squeezing at 50Hz and a peak squeezing stress of 1000Pa. C) 1 minute after cessation of squeezing.

6.5.2 Bubble Formation and Escape in Corn-Starch Suspensions

In this section the behaviour of bubbles trapped within corn-starch suspensions undergoing OSFF is further discussed. During OSFF of corn starch suspensions, trapped bubbles often tend to steadily shrink or collapse on themselves while making a loud squeaking sound. Figure 86A shows a sample of corn-starch subjected to OSFF with a peak squeezing stress of 1000Pa at 50 Hz for a period of 3 minutes. Figure 86B) shows the same sample 2 seconds later, note the formation of the bubble highlighted in blue due to surfaces of the suspension merging and causing air to be trapped.

Figure 86C shows that the bubble highlighted in blue has vanished 4 seconds after it formed. Studying the disappearance frame by frame it was observed that the bubble randomly and suddenly shrank or collapsed in on itself while making a loud squeaking noise rather than escaping from a rupture in the side of the suspension (Figure 86D).

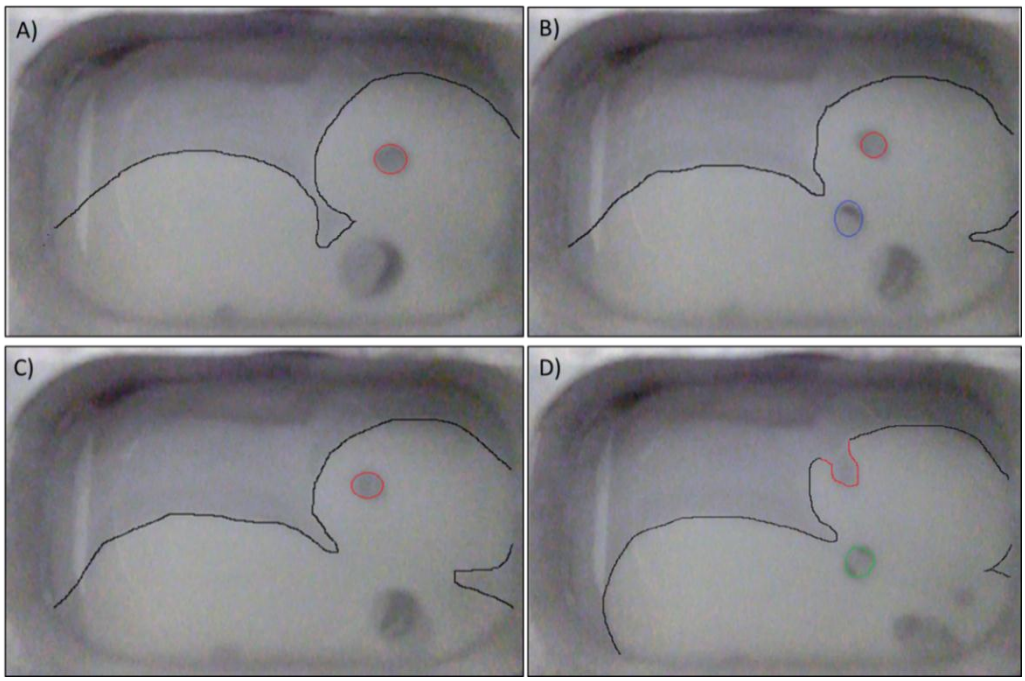

Figure 86A) A corn starch in water sample with a mass fraction of 0.59. The gap distance between the top and bottom plate is 1000 microns. After 3 minutes of squeezing at50Hz and a peak squeezing stress of 1000Pa. B) After 3 minutes and 2 seconds of squeezing. Another bubble was created over this 2 second time period and is highlighted in blue. C) After 3 minutes and 6 seconds of squeezing. Note that the bubble highlighted in blue in Figure 86B has collapsed while making a high pitched squeaking noise. D) After 3 minutes and 27 seconds of squeezing. The bubble highlighted in red in Figure 86C can be seen to escape here through the surface of the suspension. Note the bubble highlighted in green formed after the bubble highlighted in blue had collapsed in Figure 86B.

This shrinking/collapsing behaviour of trapped bubbles was commonly observed during the squeezing of corn starch suspensions but has not been observed during the squeezing of colloidal dispersions. A possible reason is that dilation causes greater surface roughening in the corn starch suspensions due to the larger particle size [13]. This means that dilation could cause greater gaps between the sample and the top or bottom boundaries, potentially allowing trapped air to escape when a suitable path becomes available.

Other potential causes for the bubble disappearance could be related to cavitation as this is known to occur during OSFF [201-203]. In industrial applications, cavitation is known to cause loud sounds as bubbles collapse and split up into smaller bubbles however the formation of smaller bubbles was not observed in experiments carried out in this thesis. Additionally the bubbles are often stable over periods of the order of tens of seconds and over hundreds of squeezing cycles, and so it is unclear why bubbles would suddenly undergo cavitation.

Esmonde and co-workers studied the cavitation of Newtonian fluids during oscillatory squeeze flow [159]. They showed that the conditions for cavitation to be avoided in OSFF can be summarised by Equation 88, where $P_{Atmospheric}$ is the atmospheric pressure, $F_{tensile}$ is the maximum force during the stretching phase or squeezing phase of the oscillatory flow, and the contact area is the area of contact between the fluid and the plates.

$$\frac{F_{tensile}}{P_{Atmospheric} \times Contact\_Area} < 0.5$$

Equation 88

Substituting in the maximum force applied by the electromechanical squeeze cell and the minimum contact area of the ESC with the fluid into Equation 88, it can be shown that cavitation is unlikely as shown below:

$$\frac{1.2[N]}{1.01325 \times 10^5[N/m^2] \times 8 \times 10^{-4}[m^2]} = 0.015$$

It should be noted however that if dilation occurs, it is possible that this could decrease the effective contact area due to particles poking out of the surface. This could therefore result in higher stresses being exerted near bubbles that could cause cavitation.

Yet another cause of such an effect could be the dissolving of the entire air bubbles into the suspending liquid but this requires extremely high pressures far beyond any that could be supplied by the apparatus.

6.5.3 Summary of Qualitative Observations

- For a PMMA colloidal dispersion at a high enough solid volume fraction, at high enough peak squeezing frequencies and peak squeezing stresses, sample shape and local flow field distortions were observed over time.
- The local flow field distortion was completely reversible as distortions faded away if the squeezing frequency or peak squeezing stress were decreased enough.
- For corn starch suspensions at high enough solid mass fractions, peak squeezing frequencies and peak squeezing forces, distortion of the sample shape was observed over time.
- The observed sample shape distortion was shown to be reversible as distortions faded away after the OSFF had been ceased. This was due to surface tension acting to reduce the additional surface area created during the oscillatory squeeze film flow of concentrated enough particle suspensions.
- Trapped bubbles were observed to spontaneously disappear while making a loud squeaking noise which possibly indicates dilation. Dilation could create gaps between the top and bottom surfaces allowing air bubbles to escape.

6.6 Squeezing of Concentrated Colloidal Dispersions: Phase Diagrams

In this section a summary of the roles of the peak stress and squeezing frequency in the response of concentrated dispersions using 'phase diagrams' to map sample behaviour.

In one set of experiments, a peak oscillatory stress of 600Pa was applied and the frequency was altered over the range of 10-40Hz. At a given frequency and sample volume fraction it would be noted whether or not flow field distortion and/or particle migration was observed. Results are shown in Figure 87 and Figure 88.

In another set of experiments the applied squeezing frequency was fixed at 40Hz and the behaviour across a range of peak stresses and volume fractions was noted as shown in Figure 89.

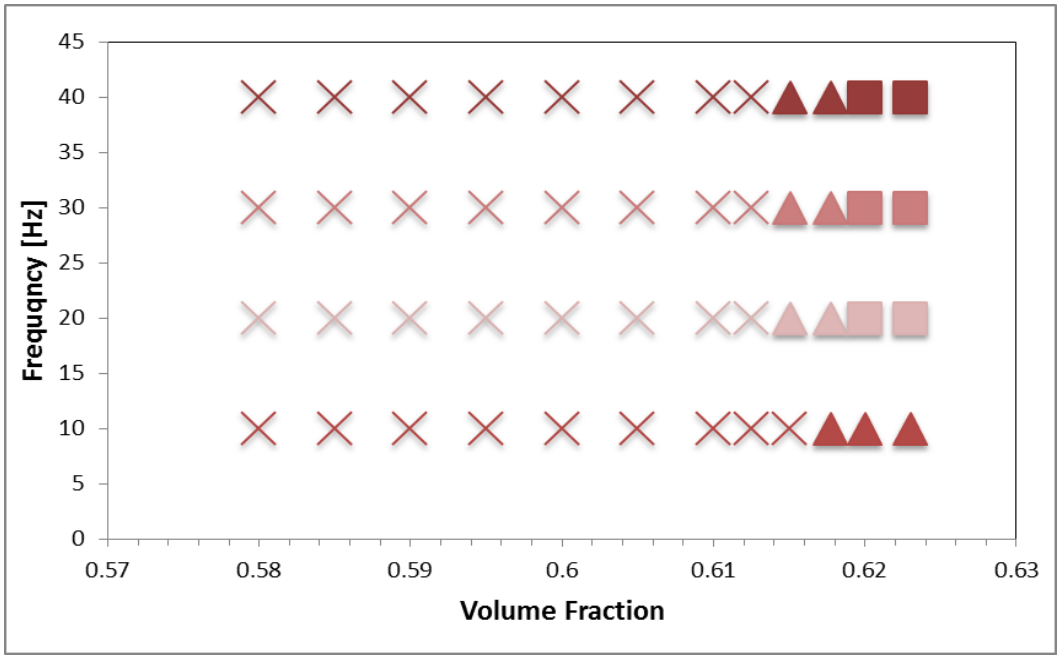

Figure 87 Shows a table describing the peak squeezing stresses and volume fractions field distortion was observed in PMMA colloidal dispersions of particles of 574nm in radius at a fixed squeezing frequency of 40Hz. Crosses denote conditions where no local flow field distortions were observed anywhere in the sample. Squares denote conditions where clear flow field distortion were consistently observed somewhere within the sample. Triangles denote conditions where mild flow field distortion was observed but not consistently throughout the sample between repeated experiments.

Figure 87 and Figure 88 imply that for a given peak squeezing and stretching stress, as the solid volume fraction of the colloidal dispersions increases and as the applied squeezing frequency increases, then observed flow field and sample shape distortion are more likely to be observed.

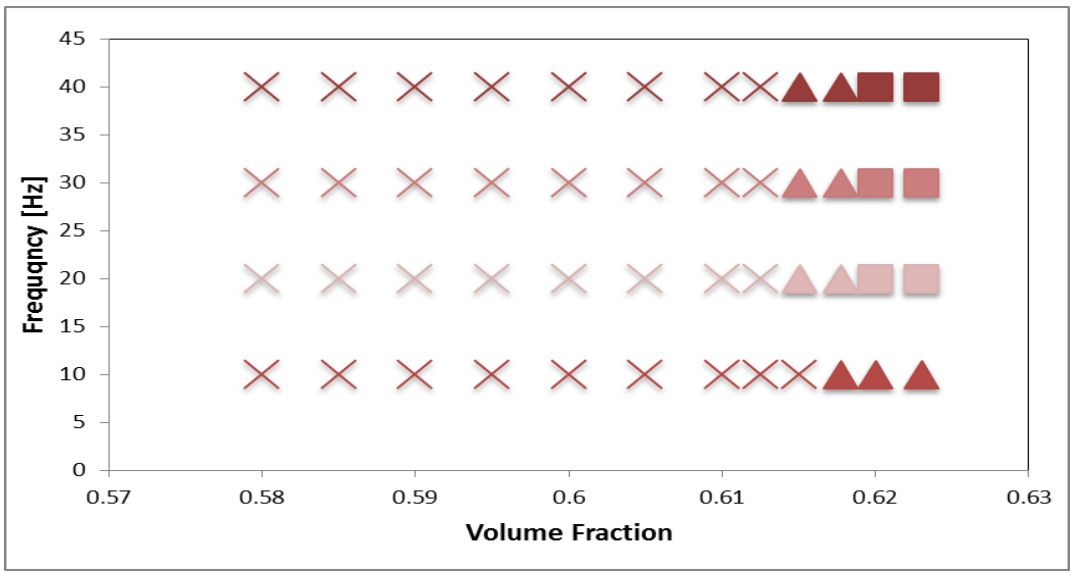

Figure 88 Shows a table describing the peak squeezing stresses and volume fractions that sample shape change was observed in PMMA colloidal dispersions of particles of 574nm in radius at a fixed squeezing frequency of 40Hz. Crosses denote conditions where no particle migration or shape change were observed anywhere in the sample. Squares denote conditions where clear particle migration and shape change were consistently observed somewhere in the sample. Triangles denote conditions was mild shape change where observed but not consistently between repeated experiments.

Comparing Figure 87 and Figure 88 suggests that flow field distortion and particle migration/shape change occur together.

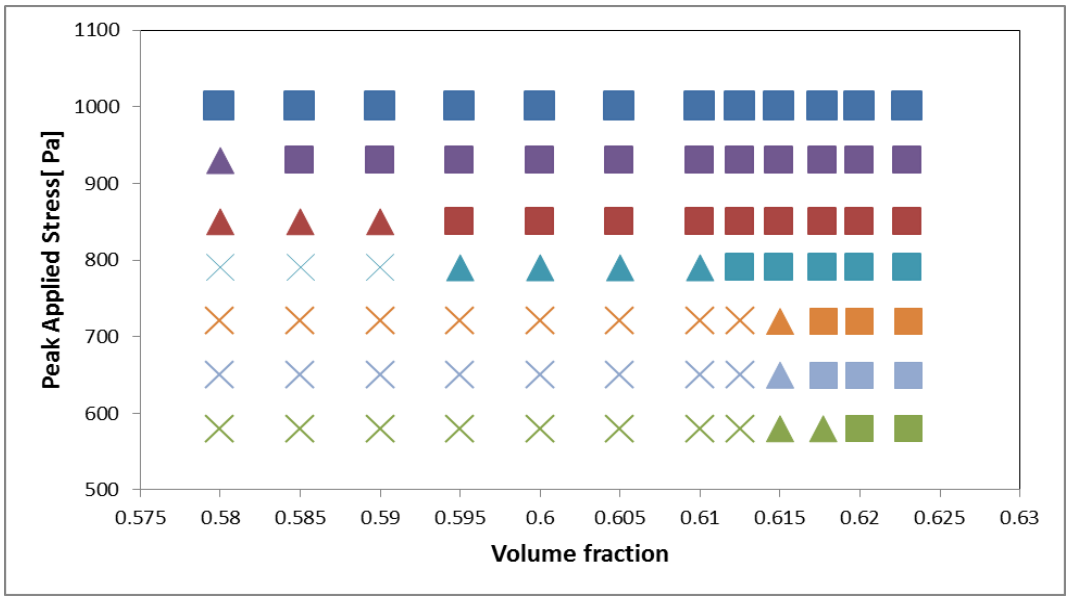

Figure 89 Shows a table describing the peak squeezing stresses and volume fractions that sample shape change and flow field distortion were observed in PMMA colloidal dispersions of particles of 574nm in radius at a fixed squeezing frequency of 40Hz. Crosses denote conditions where no local flow field distortions and particle migration/shape change were observed anywhere in the sample. Squares denote conditions where clear local flow field distortions and shape change were consistently observed somewhere in the sample. Triangles denote conditions where mild shape change or flow field distortions were observed but not consistently between repeated experiments.

Figure 89 shows that at a fixed squeezing frequency of 40Hz, as the solid volume fraction of the dispersions and the peak squeezing/stretching stresses increase then flow field and sample shape distortion are more likely to be observed.

Figure 90 shows the same experiments (at a fixed frequency of 40Hz) with colloidal dispersions of 384nm in diameter.

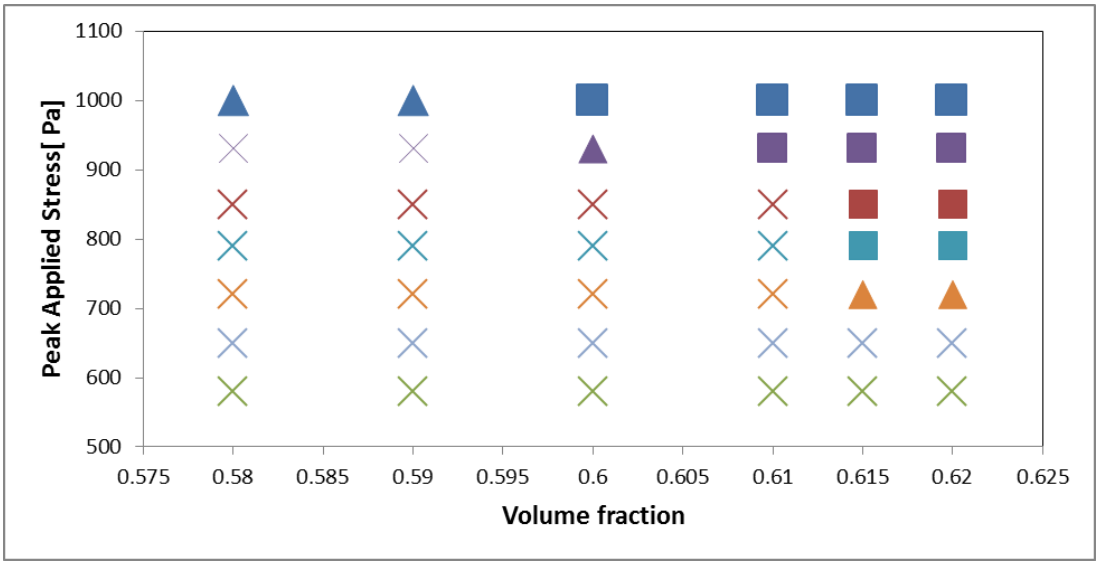

Figure 90 Shows a table describing the peak squeezing stresses and volume fractions that sample shape change and flow field distortion were observed in PMMA colloidal dispersions of particles of 384nm in radius at a fixed squeezing frequency of 40Hz. Crosses denote conditions where no local flow field distortions and particle migration/shape change were observed anywhere in the sample. Squares denote conditions where clear local flow field distortions and shape change were consistently observed somewhere in the sample. Triangles denote conditions where mild shape change or flow field distortions were observed but not consistently between repeated experiments.

Comparing Figure 89 and Figure 90, colloidal dispersions of radius of 384nm, at a given solid volume fraction, were less prone to show flow field and shape distortion compared to dispersions consisting of particles of radius 574nm. This could be in some way related to the fact that colloidal dispersions of smaller particles showed oscillatory DST at higher shearing frequencies as shown in Figure 65. Additionally it could in some way be related to the fact that colloidal dispersions of radius of 384nm could sustain higher stresses during DST before fracturing than colloidal dispersions of radius of 574nm at a given solid volume fraction.

6.7 Squeezing of Concentrated Corn-Starch Suspensions Results

Figure 91 summarises the peak oscillatory stresses at a fixed squeezing and stretching frequency of 50Hz required to bring about sample shape change for a given solid mass fraction of corn-starch.

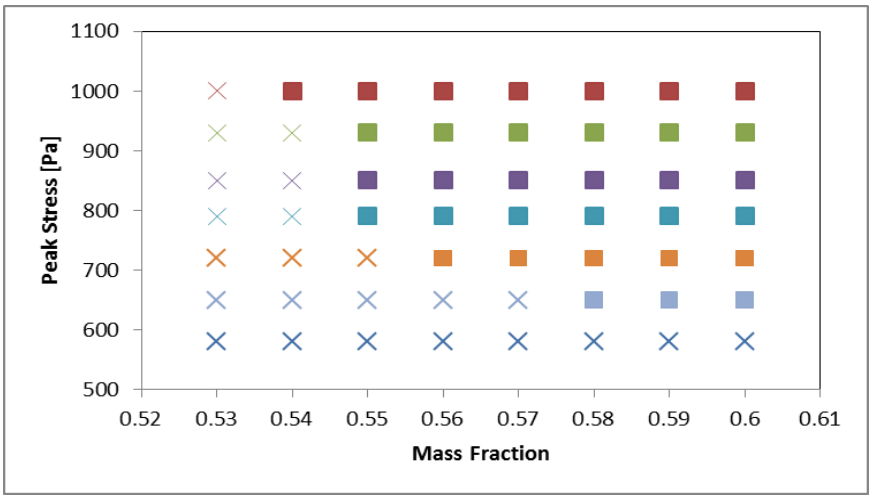

Figure 91 Shows a table describing the peak squeezing stresses and mass fractions that sample shape change was observed at a fixed squeezing frequency of 50Hz. Crosses denote conditions where sample shape change were not observed anywhere in the sample. Squares denote conditions where clear shape change was consistently observed.

Figure 92 summarises the peak oscillatory stresses at a squeezing and stretching frequency of 40Hz required to bring about sample shape change for a given solid mass fraction of corn starch.

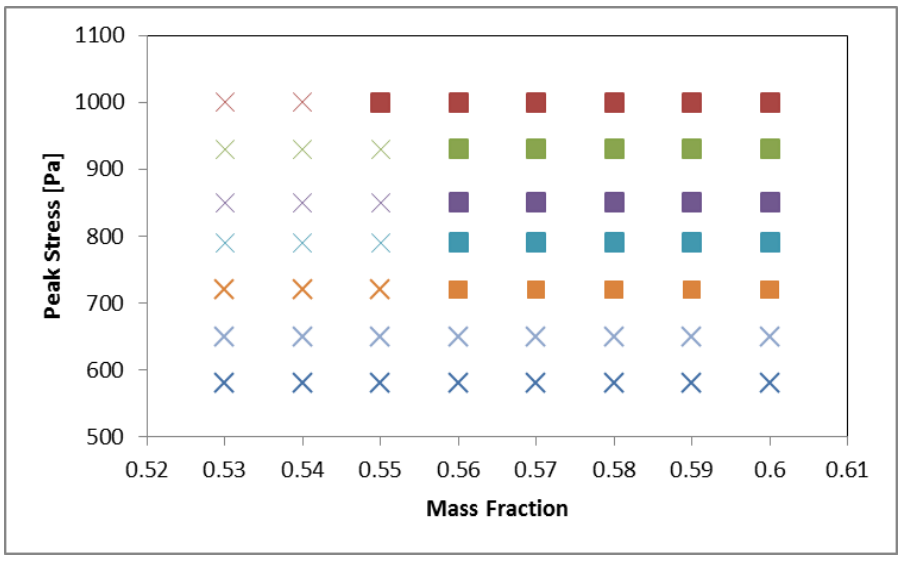

Figure 92 Shows a table describing the peak squeezing stresses and mass fractions that sample shape change was observed at a fixed squeezing frequency of 40Hz. Crosses denote conditions where no sample shape change were not observed anywhere in the sample. Squares denote conditions where clear shape change was consistently observed.

Comparing Figure 91 and Figure 92, it can be seen that at higher frequencies, sample shape change occurs at lower applied peak stresses and lower mass fractions.

6.8 Comparison of Colloidal Dispersions and Corn Starch Suspensions Results

Figure 91 and Figure 92 compare well with Figure 89. They show that sample shape distortion only occurred at high enough squeezing frequencies and peak squeezing stresses for both systems. They also showed for both sets of particle systems, that the frequencies and stresses required to cause distortions decreased as the particle concentration increased.

While the results relating to the OSFF of corn starch suspensions implied higher stresses are required for unusual behaviour to be displayed, this cannot be said for certain since the local flow field cannot be observed, which could have shown distortions before sample shape change is visible.

At this stage it is important keep in mind that the PMMA particles were mono-disperse and a relatively close representation of non-interacting hard spheres, while corn starch particles are poly-disperse and are of a variety of shapes. As was mentioned in chapter 1, these factors are known to strongly effect the transition into the shear thickening regime during shear flow, this could have some effect on the unusual behaviours observed during oscillatory squeeze film flow of suspensions [31,53,80,81].

6.9 Comparison of Results with Literature

In the literature, there are no direct comparisons with the oscillatory squeeze flow experiments described in this chapter. There are however some experiments in the literature with different geometries and types of flow that could potentially help to explain the results presented in this thesis. In the following sections related work is discussed, although the difference in flow geometries means there is no attempt here to make any quantitative comparisons at this stage.

6.9.1 Relation to Work done on DST, Dilation and Fracture of Concentrated Particle Suspensions

As was mentioned in chapter one, Smith and co-workers carried out extensional flow experiments using a HAAKE CaBER 1 Extensional Rheometer on concentrated dispersions of sterically stabilised PMMA of 608nm in radius [90]. It was observed for dispersions of $\phi \approx 0.6$, extensional DST, dilatancy and distortion of the shape of the filament were observed at rates of extension of around $1.3s^{-1}$. At higher rates of extension, jamming followed by fracture of the filament was observed, while at lower rates of extension the colloidal dispersion essentially behaved as a viscous liquid. Using a cone and plate rheometer to carry out continuous shear flow on the same colloidal dispersions, Smith showed that DST began at shear rates of approximately $2s^{-1}$ which corresponds well with extensional flow. Smith and co-workers summarised the rates of extension required to cause dilation and distortion of colloidal dispersions with solid volume fractions of between 0.59 and 0.62. They showed that the higher the solid volume fraction, then dilation and other effects such as cracking, shape distortion and jamming of filaments of colloidal particles occurred at lower rates of extension [90].

The results obtained by Smith and co-workers agree well with the results in this thesis in that unusual non-Newtonian effects displayed by particulate systems are most apparent as the rate of deformation and the solid volume fraction are increased. The colloidal particles used by Smith and co-workers and the range of solid volume fractions explored were almost identical to those used in this PhD [90].

It is however difficult to make comparisons as the experiments carried out by Smith involved applying steady elongation rates, while experiments carried out in this PhD were oscillatory and the peak stress and squeezing frequencies were controlled. There is

however circumstantial evidence to link the observed flow field distortion and sample shape changes to DST and jamming [90].

6.9.2 Relation to Work done on the Vibration of Complex Fluids

As was mentioned in chapter one, a significant amount of work has been done on the vibration of complex fluids (such as concentrated particle suspensions) resting on an oscillating bottom plate. In these experiments, it was shown that stable fingers and holes would form in concentrated enough suspensions and in yield stress fluids when the acceleration of the bottom plate exceeded a critical value [135]. It was shown that these unusual effects become more pronounced as the amplitude and frequencies of the oscillation of the bottom plate increased. This has similarities with the findings presented in this chapter which showed that above a given critical squeezing stress and squeezing frequency, the sample shape change and flow field distortion of particulate suspensions became more pronounced as the peak squeezing stress and squeezing frequency were increased.

The main difference between these vibration experiments and the oscillatory squeeze flow presented in this thesis is the presence here of a constraining stationary top plate which samples are squeezed against and which prevents the formation of fingers. It could be that the sample shape and flow field changes presented in this chapter are the oscillatory squeeze flow equivalent of the formation of stable fingers and holes observed by various authors in vibration experiments [135-137].

It has been shown that these unusual effects are caused by stress hysteresis by Deegan and co-workers [138,139]. In the case of concentrated suspensions it was shown that the onset of the formation of stable fingers and holes coincided with the onset of shear thickening. In the case of yield stress fluids the onset of the unusual behaviour was observed when the applied stresses reached the yield stress value of the fluids being examined. Hysteresis may be a result of the formation of jammed regions of a sample formed at one stage of the oscillation cycle, persisting through to the next cycle even though the stress and shear have changed. Hence hysteresis due to jamming and unjamming of regions within the samples during the cycle may cause the flow field and sample shape distortions presented in this chapter. This remains to be investigated further, for example by studying precisely what happens locally during the oscillation cycle in more detail.

6.9.3 Relation to Work done on the Dynamic Jamming of Particle Suspensions

In chapter one, dynamic jamming was described which relates to the temporary solidification of a fluid like system upon a fast enough impact, which then unjams over time and becomes fluid like again. At a first glance, dynamic jamming could very well be related to the shape change and flow field distortion of particle systems shown in this chapter.

- When squeeze film flow is ceased, the distorted shape of the particle system reverts to the initial fluid state over time. In dynamic jamming experiments, once the impact has ceased the particle system becomes fluid like again and any observed distortions in the shape of the suspension such as cracks fade away [133]. The behaviours are therefore similarly reversible on the removal of stress.
- In impact experiments, if the impacts are too slow then the system doesn't jam, similarly to squeeze film flow experiments where no non-Newtonian behaviour is observed at low squeezing and stretching frequencies and stresses.

6.10 Discussion of Potential Mechanisms

In this section, potential causes for the local flow field and sample shape distortion of concentrated particle suspensions are put forward, based on the comparisons with other 'unusual' flow responses of concentrated suspensions.

Dynamic jamming due to high frequency oscillatory flow

Squeezing and stretching at high frequencies could be analogous to dynamic jamming due to high velocity impacts, in that it is likely that particles will be forced into close contact during high stress portions of the cycle forming concentrated jammed regions. These jammed regions could then unjam as the suspending fluid de-concentrates these regions once the impact stress or the applied squeezing changes. If a section of the system being subjected to OSFF becomes jammed and does not flow then, this will affect the flow field in other regions causing distortions depending on local position. Once dynamically jammed regions have un-jammed and randomised their structure on cessation of squeezing re-application of squeezing would lead to different regions of jamming, explaining why the shape of flow field distortions would often change when the squeezing was ceased and re-applied after a period where the samples were left to rest.

Static jamming and unjamming due to high frequency oscillatory flow

Applying even very small forces with a spatula is enough to cause concentrated suspensions of PMMA colloidal particles of $\phi>0.6$ to undergo static jamming. It is likely that static jamming could have been occurring during squeeze flow as the applied stresses varied from 0 to above that required for DST. Under oscillatory squeezing/stretching force chains could continuously form and then buckle and break as the applied stress exceeds a critical level. Additionally as static jamming is fragile in that it can only sustain compressive stresses in certain directions, the stretching phase of a cycle would likely unjam statically jammed structures formed during the squeezing stage and *vice versa*.

The shear and elongational stress can vary greatly with position throughout the sample at a given moment in time. It is therefore likely that jamming and buckling could be occurring at different stages in a given cycle at different positions. This could result in jammed regions forming in one region while they are buckling and flowing in another region resulting in flow field distortion.

Speculative mechanism for flow field/sample shape distortion and reversal

Jamming of some regions of a suspension at the high stress regions of squeezing cycles could cause hysteresis if jammed structures do not dissipate rapidly relative to the time period of oscillation. Over a large number of cycles, such hysteresis could have the long term cumulative effect of causing the extreme sample shape change presented in this chapter.

Both of the particle systems used in the experiments were highly concentrated. In the case of corn-starch in water suspensions, the suspending particles were non-Brownian and therefore Brownian motion does not randomize the microstructure after deformation. However in the case of the PMMA dispersions Brownian motion may also be insignificant as caging effects prevent particles from diffusing past each other at such high volume fraction. This means that hysteresis is certainly a factor as any structures formed during one stage of a squeezing cycle will dissipate very slowly and therefore the flow response is the most significant factor.

This implies that the only driving force that resists and reverses shape distortion is surface tension after the cessation of deformation. It must also be the case that surface tension is responsible for the surface area of distorted samples shrinking as their shape became more ‘normal’ once the applied squeezing had ceased.

6.11 Summary of Results

When dispersions of PMMA particles at high enough concentration were subjected to oscillatory squeeze film flows with a high enough peak squeezing stress, and high enough squeezing frequency, the observed local flow fields within the sample became highly distorted. This distortion was accompanied by the sample shape changing significantly over time. These distortions were shown to be reversible over time when the peak squeezing stress and/or squeezing frequencies were reduced. The flow field distortion and shape change is likely a result of local changes in the microstructure of regions within the sample that is consistent with jamming. This observed flow field distortion and shape change could be related to the DST observed in continuous shear flows where jammed granules can be formed within samples being subjected to high enough shear stresses.

Similarly when suspensions of corn starch particles in water at high enough concentration, were subjected to oscillatory squeeze film flows with a high enough peak squeezing stress and high enough squeezing frequency, the shape of the sample changed significantly over time. These distortions were reversible and faded away when the peak squeezing stress and/or squeezing frequencies were reduced. Sample shape change was observed to begin at the edges of the sample where the shear stress and strain is greatest. This shape change is likely a result of stress hysteresis as a consequence of the jamming of regions within the sample. This is likely analogous to DST and jamming observed in continuous and oscillatory shear flows when strong enough shear stresses were applied.

As the concentration of the particle suspensions increases, sample shape and flow field distortions were observable at lower peak squeezing stresses and squeezing frequencies. This is likely analogous to the observation in continuous and oscillatory shear flows that DST occurs at lower rates of deformation as the particle concentration increases.

As the squeezing frequency was increased, sample shape distortions could be observed at lower peak squeezing stresses. All the above observations are consistent with the known jamming behaviour of the systems studied and the various observations from other complex flow scenarios. However a detailed understanding of the roles of dynamic jamming and hysteresis needs to be further investigated.

Chapter 7 Results and Discussion of the Response of *D.Salina* to Oscillatory Flows

7.1 Chapter Summary

In this chapter, it is shown that when suspensions of *D.Salina* are exposed to oscillatory shear at certain frequencies and magnitudes, *D.Salina* can preferentially order their swimming direction in the vorticity direction of the induced oscillatory flow field. This is demonstrated in 3 different experimental arrangements including both shear and squeeze film flows.

For each experimental arrangement, it is shown that ordering of swimming directions only occurs at certain shearing frequencies and shear magnitudes, otherwise *D.Salina* swims in random directions similarly to when no oscillatory flow is applied. These results are discussed in the context of the surrounding literature.

7.2 Response of *D.Salina* to Oscillatory Parallel Plate Shear Flows

Using the shear cell described in section 4.5, oscillatory shear flows were applied to suspensions of *D.Salina* and the movements of individual algae were tracked and analysed as described in section 4.10. Shearing frequencies in the range of 0.5 Hz to 6 Hz were applied. The gap distance between the top and bottom plates was fixed at 400 microns. The maximum peak to peak displacement of the top plate was varied between 110-525 microns in order to alter magnitude of the applied shear per cycle. The maximum displacement of the top plate from the initial position which it oscillated around was therefore varied in the range of $\pm$55-263 microns. The plane of focus was at the centre of the gap.

7.2.1 Behaviour of *D.Salina* within Shear Cell Before Any Applied Shear

When a suspension of *D.Salina* was placed within the shear cell with no applied shearing taking place, the modal speed was around 50-80 microns/second which means the algae being observed were healthy. The swimming directions of algae showed no preference to any given direction as is illustrated by Figure 93 and Figure 94:

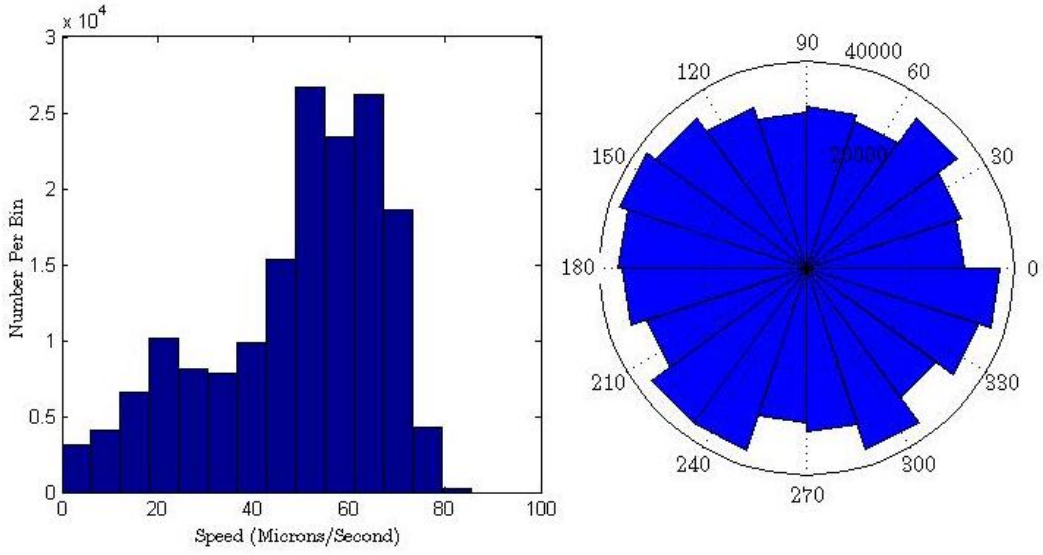

Figure 93 Histograms of the speed of a collection of algae and their corresponding swimming directions over a period of 7 seconds with no applied shear.

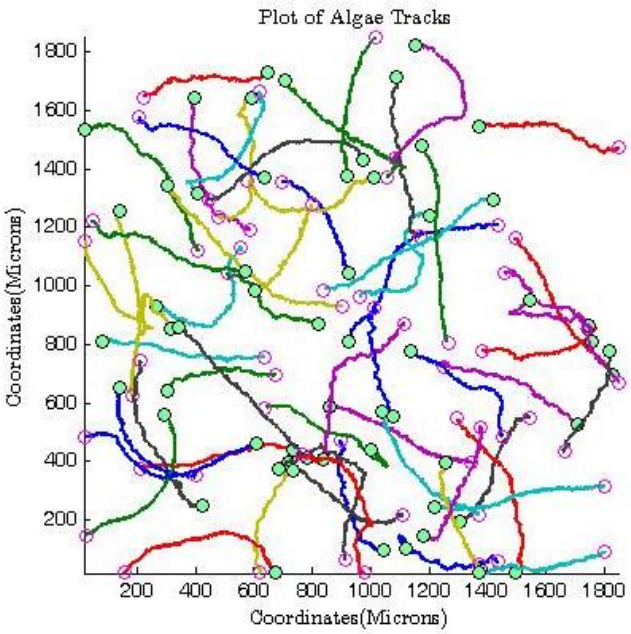

Figure 94 Tracks of algae over a period of 10 seconds within the shear cell with no applied shear, showing no obvious bias to a particular direction. Filled green circles represent the starting point of a given track and hollow pink circles represent the end of a given track.

It should be noted at this stage that the exact value of the modal speed and the shape of the speed histogram of a collection of algae can be affected by a wide range of parameters such as age of culture, time of day and exact handling history. The reason why speed histograms are shown throughout this chapter is to confirm that the algae being observed were healthy.

7.2.2 Response of *D.Salina* to Oscillatory Parallel Plate Shear Flows at Low Shear

At a low shear strain (relatively low displacements of the top plate per cycle), the algae swimming directions were distributed randomly as was the case when no shearing was being applied. The modal speed of the algae distributions was also within the expected range for *D.Salina*. This is illustrated in Figure 95 and Figure 96:

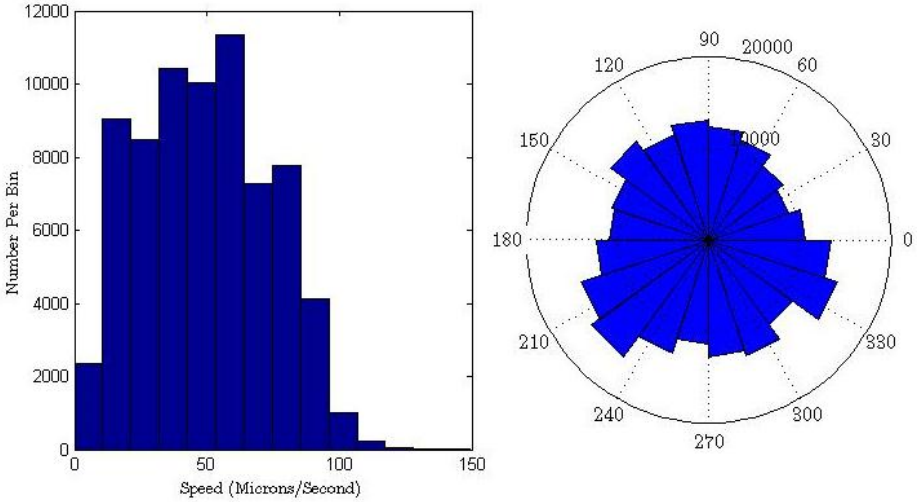

Figure 95 Histogram of speed of a collection of algae and their corresponding swimming directions over a period of 4 seconds, with shear being applied at a frequency of 6Hz and a maximum peak to peak displacement of the top plate of 110 microns.

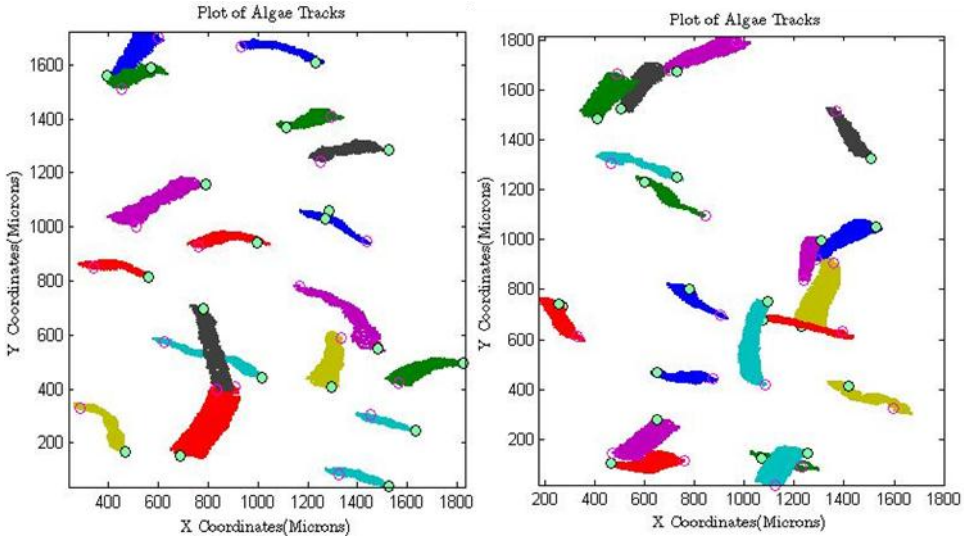

Figure 96 Tracking plots of algae over a period of 4 seconds with shear at a frequency of 6Hz and a maximum peak to peak displacement of the top plate of 110 microns. Filled green circles represent the starting point of a given track and hollow pink circles represent the end of a given track.

7.2.3 Ordering of D. Salina due to Pure Oscillatory Shear Flows

At certain squeezing frequencies and maximum translations of the top plate, ordering of the swimming directions of *D.Salina* is visually observed as shown in Figure 97 and Figure 98. Despite the observed ordering, the modal speed of the algae was similar to the case where there was no applied shear. Figure 97 also shows that the swimming direction of *D.Salina* is strongly focused perpendicular to the oscillatory flow field (which flipped between the in 0 and π radian (0 and 180 degree) directions).

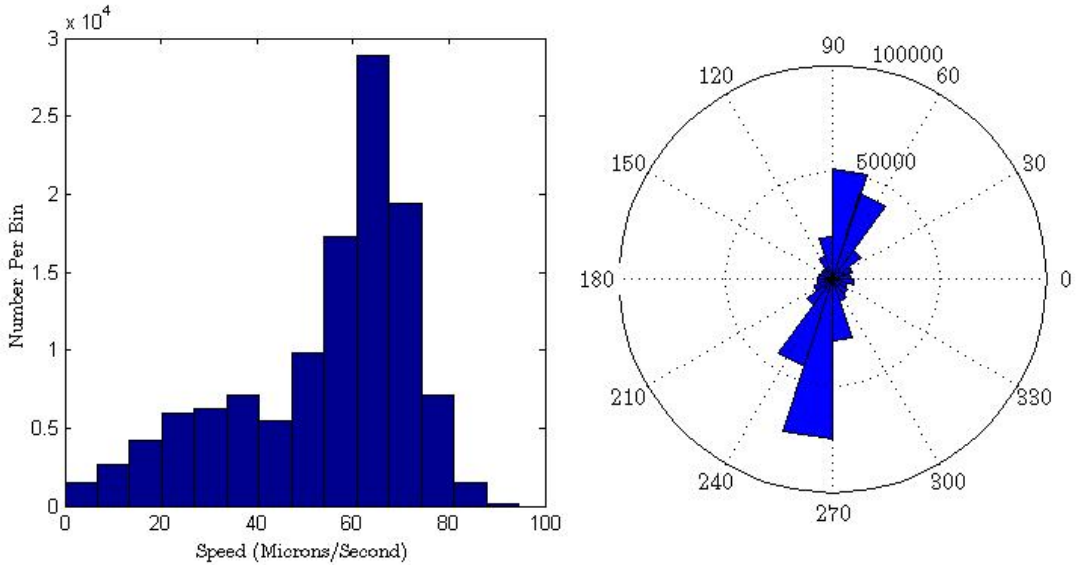

Figure 97 Histogram of the speed of a collection of algae and their corresponding swimming directions over a period of 4 seconds, with shear being applied at a frequency of 2Hz and a maximum peak to peak displacement of the top plate of 224 microns. The swimming direction distribution shows a preference to the two directions perpendicular to the oscillatory flow field.

Figure 98 shows track plots of *D. Salina* that correspond to Figure 97, demonstrating the strong preference for swimming approximately perpendicular to the flow field.

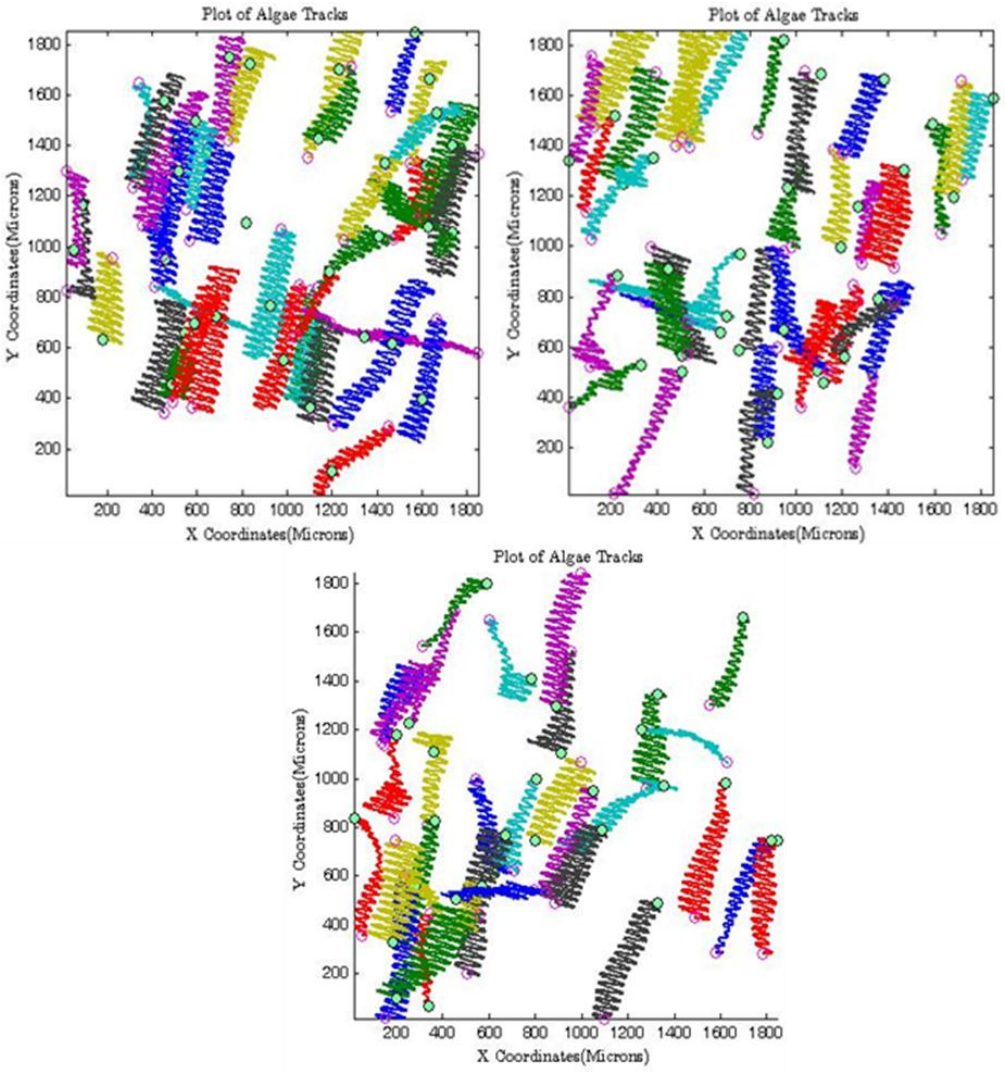

Figure 98 Tracking plots of algae over a period of 7 seconds within the shear cell, with shear being applied at a frequency of 2Hz and a maximum displacement of the top plate of 224 microns. These plots show a bias to directions perpendicular the oscillatory flow field in the plane of focus. Filled green circles represent the starting point of a given track and hollow pink circles represent the end of a given track.

The above track plots were taken from the same experiment over different time periods and plotted separately for clarity. Note that not all algae are swimming perpendicularly to the flow field.

7.2.4 Disappearance of Ordering of *D.Salina* after Cessation of Oscillatory Shear

The observed ordering during oscillatory shear vanishes if the applied shearing is ceased as is shown in Figure 99.

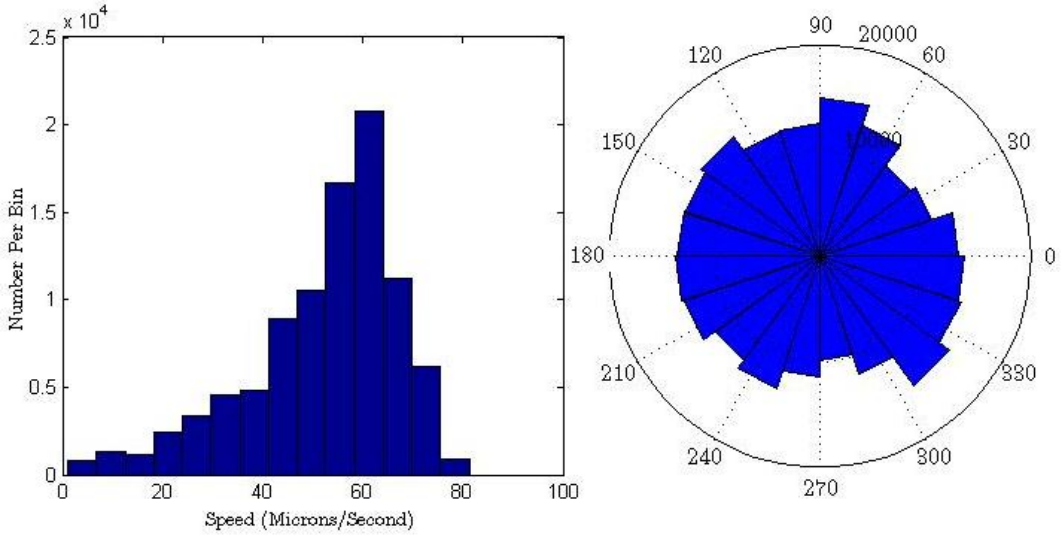

Figure 99 Histograms of speed of a collection of algae and their corresponding swimming directions over a period of 7 seconds measured 1 minute after the cessation of shearing. The algae swimming directions had previously ordered perpendicular to the flow field prior to the cessation of shear.

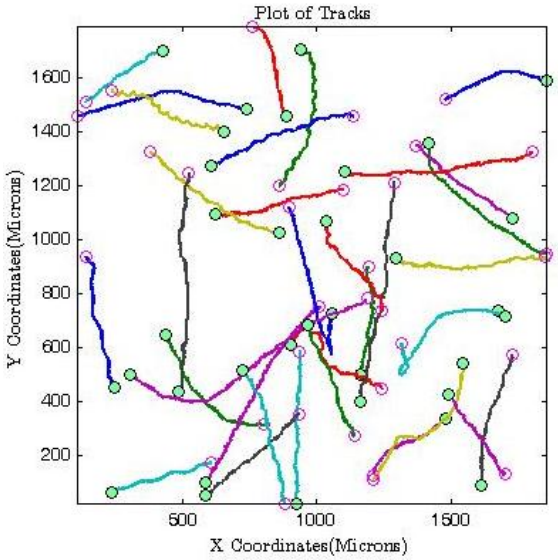

Figure 100 Tracks of algae over a period of 10 seconds 1 minute after the cessation of shearing, showing a return to random swimming directions. Filled green circles represent the starting point of a given track and hollow pink circles represent the end of a given track.

7.2.5 Results and Conclusions: Response of *D.Salina* to Oscillatory Pure Shear Flows

To quantify the degree of ordering of swimming direction, R is used which is the ratio (R) of algae with swimming directions within π/2 radians of the direction perpendicular to the oscillatory flow field to those with directions within π/2 radians of the flow field direction across the range of shearing conditions.

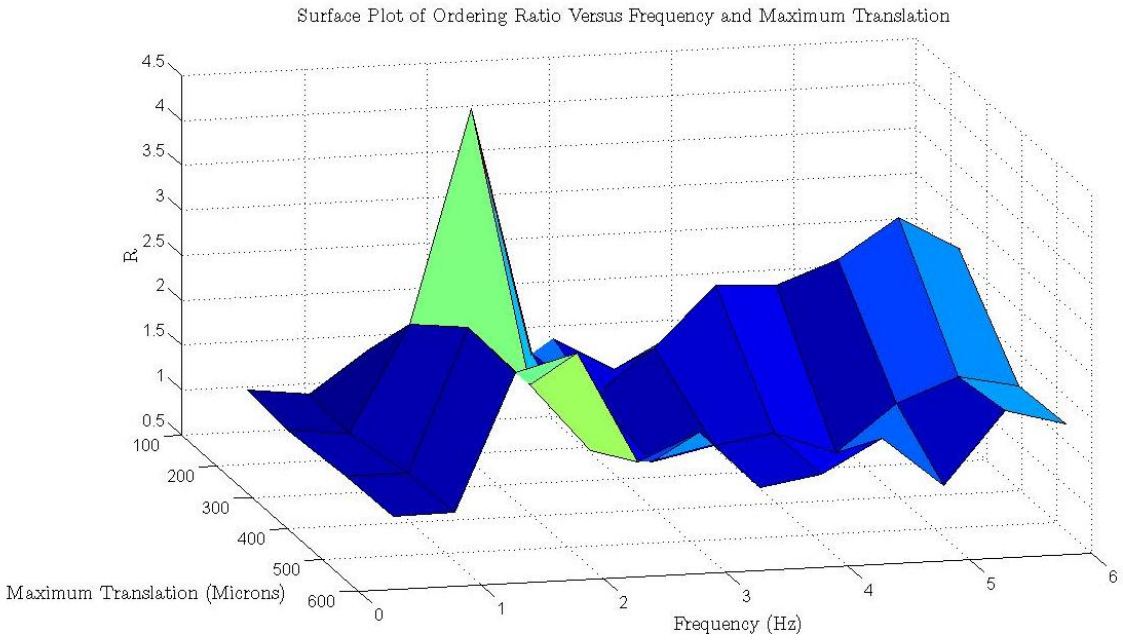

Figure 101 Surface plot of the ordering ratio R as a function of maximum peak to peak translation of the top plate and frequency of oscillation for shearing flows. The gap distance used was 400 microns. The plane of focus was at the centre of the sample.

Figure 101 shows that the strength of ordering depends on the maximum translation and on frequency. This can be more clearly seen by examining plots where the maximum displacement of the top plate is fixed and the shearing frequency varied, this is illustrated in Figure 102.

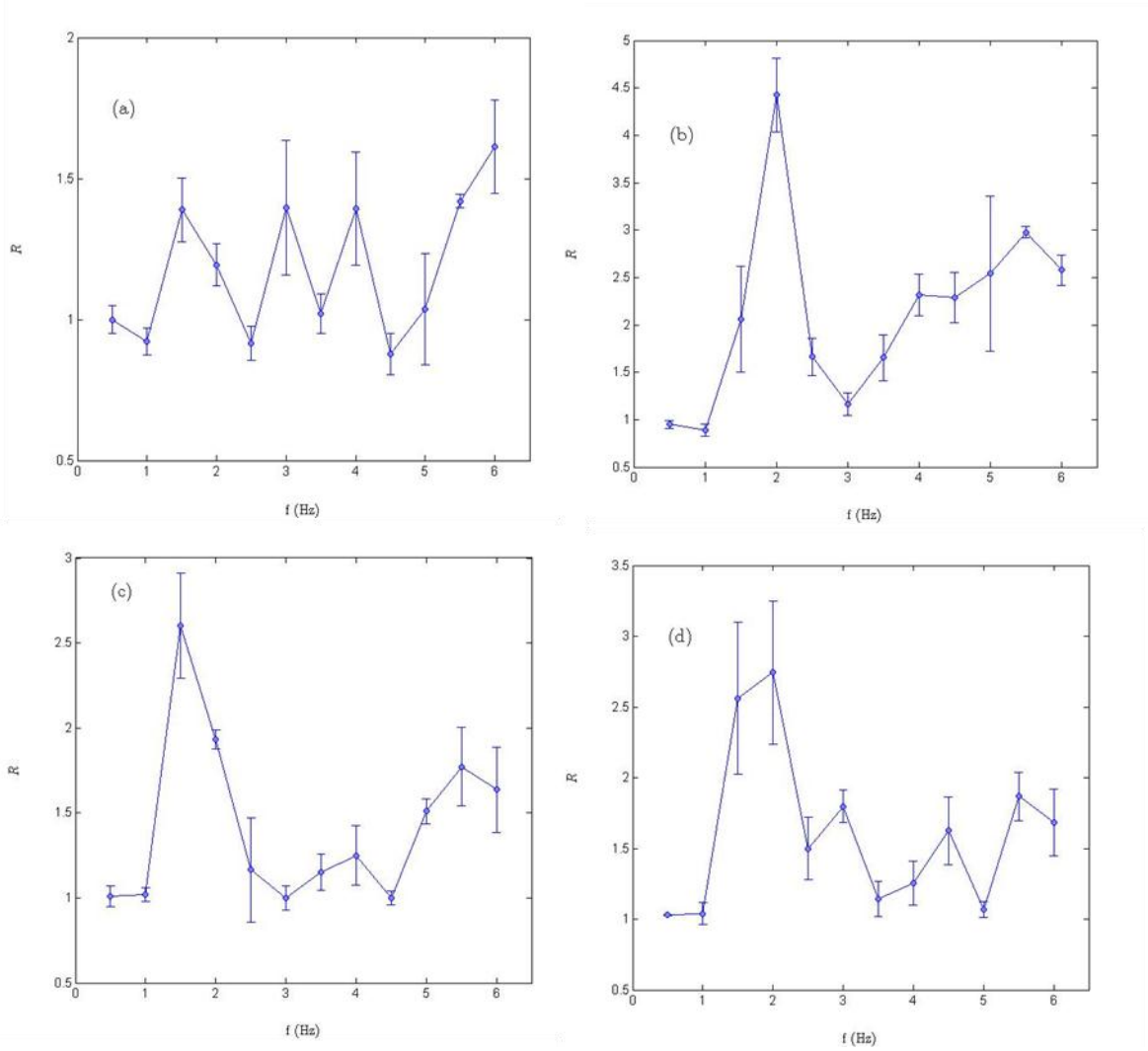

Figure 102 Variation of R with shearing frequency at a fixed maximum peak to peak translation of the top plate. a) Maximum peak to peak displacement of the top plate of 110 microns. b) Maximum top plate displacement of 224 microns. c) Maximum peak to peak top plate displacement of 391 microns. d) Maximum top plate displacement of 524 microns. Note that the scale used in each figure is different.

Figure 102a shows no ordering or at the very most weak ordering at low shearing magnitudes. This indicates that imposed shear flow needs to be of an appropriate magnitude before ordering is observed. Figure 102b to Figure 102d show that the ordering ratio appears to be highest at frequencies in the range of 1.5 Hz to 2 Hz. The error bars correspond to the standard error in the mean value of R from multiple experiments at a given set of conditions.

7.3 Squeeze Film Flow of Algae Suspensions

In the next section, results showing the response of *D.Salina* during oscillatory squeeze film are displayed.

In the parallel plate shear experiments shown previously, the extent of the shear strain and the average shear rate per cycle is defined by the gap distance and how far the top plate moves per cycle. At a given moment in time, the shear rate and shear strain is constant throughout the sample being sheared.

In squeeze film flow experiments, defining the shear strain/shear rate is more complicated. As was discussed in chapter 2, during OSFF at a given moment in time, the shear strain and shear rate varies with both radial and vertical position throughout the sample. It is therefore important to be able to have a measure of shear strain/rate in the specific local region being observed during an OSFF experiment.

In these experiments the extent of the local shear occurring per squeezing cycle is related to the maximum translation of algae on the local central horizontal plane of the sample during a squeezing cycle in the region of observation. This as opposed to the maximum translation of the top plate which defines the extent of shear in the case of parallel plate shear flows. For the OSFF experiments detailed in this chapter, when the term maximum translation is used, it is defined as the maximum peak to peak displacement of an individual alga on the local central horizontal plane of the sample as it is translated as a result of the shearing caused by OSFF.

As a suspension of algae is squeezed and un-squeezed, algae are translated back and forth by the flow field. The larger the distance they are translated on the central horizontal plane in a given region of observation, the larger the shear strain/rate per cycle at a given vertical position within the sample.

Figure 103 shows that as a fluid with suspended particles is squeezed or stretched in the y-direction it causes suspended particles to be translated back and forth in the x-z plane along a straight path line. It is important to note that for a given maximum translation, algae being observed near the top or bottom plates experience greater shear strain and shear rates of the surrounding fluid compared to algae being observed near the central plane.

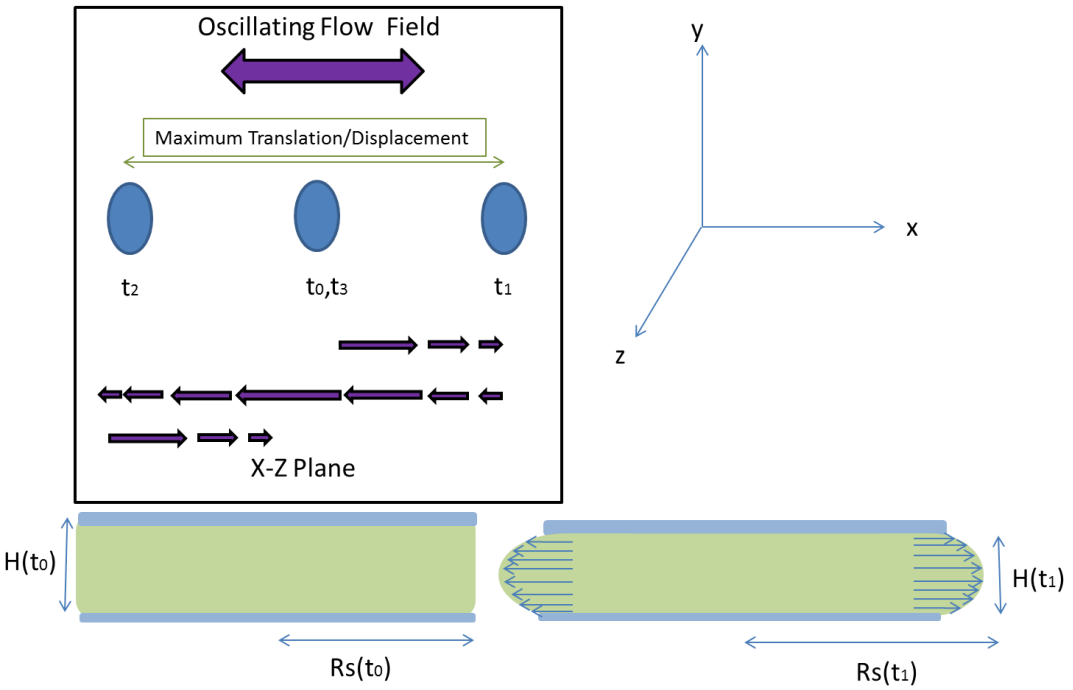

Figure 103 shows that during squeeze film flow, suspended particles are translated back and forth with the translation being the strongest on the central horizontal plane of the sample.

7.4 Response of *D.Salina* to Oscillatory Squeeze Film Flows using the Piezoelectric Squeeze Cell

Using the apparatus and procedures described in chapter 4, oscillatory squeeze film flows were applied to suspensions of *D.Salina* using the piezoelectric squeeze cell. Squeezing frequencies in the range of 0.5 Hz to 3 Hz were applied. The initial gap distance used was fixed at 300 microns. The maximum upward displacement of the bottom plate was varied between 9 to 18 microns in order to achieve a desired maximum translation of the algae on the local central horizontal plane. In these experiments, the plane of focus was either at the centre of the gap or 75 microns down from the top plate. As was discussed in chapter 2, the shear rate depends on the position within the sample being squeezed.

7.4.1 Behaviour of *D Salina* within Piezoelectric Squeeze Cell before Any Squeezing

Before squeezing, the algae swimming directions were distributed randomly the speed distributions were also as expected for *D.Salina*. This is illustrated in Figure 104, and Figure 105.

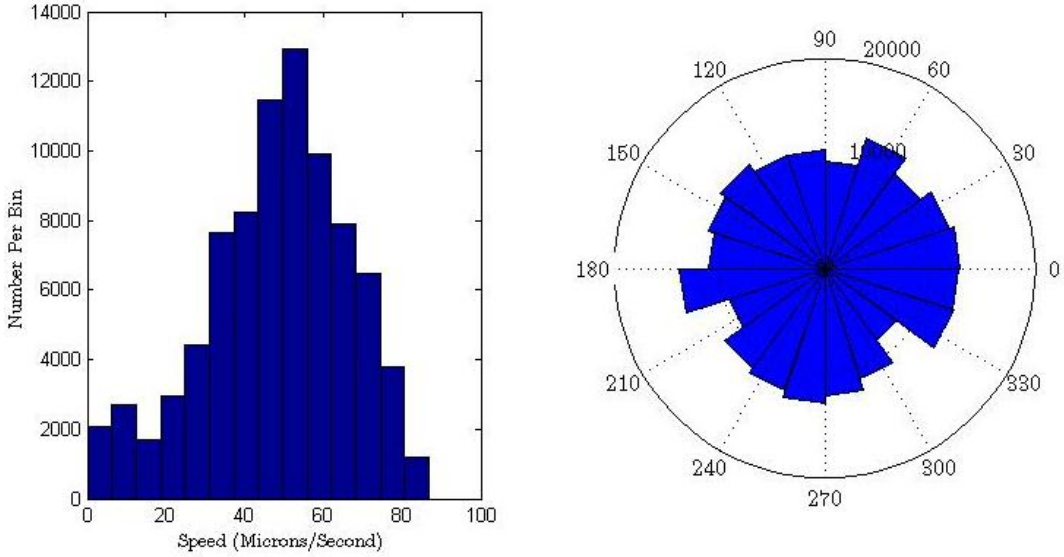

Figure 104 Histograms of speed of a collection of algae and their corresponding swimming directions over a period of 7 seconds. The algae were in the piezoelectric squeeze cell with no squeezing was being applied.

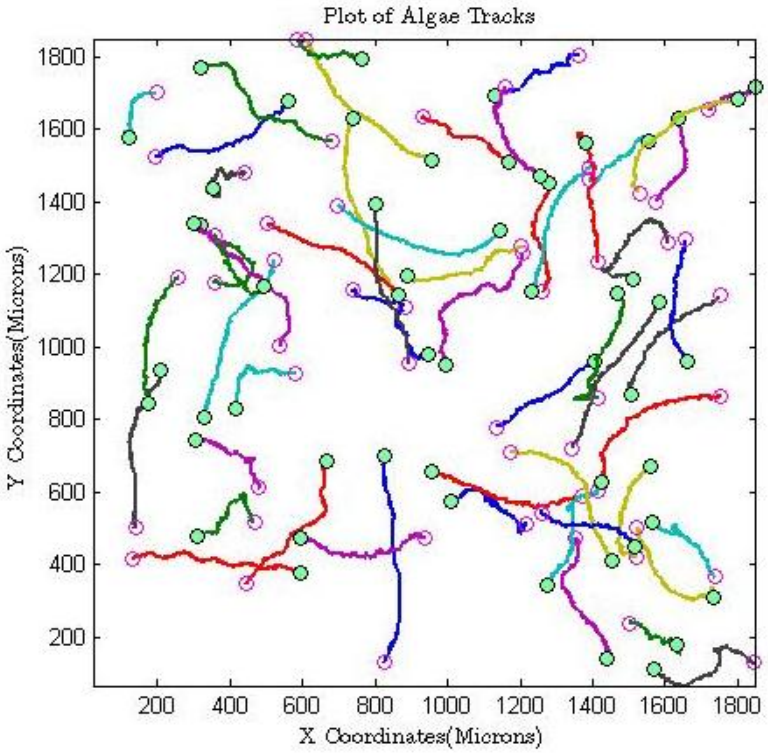

Figure 105 Tracks of algae over a period of 10 seconds within the piezoelectric squeeze cell before any squeeze film flow was applied. Filled green circles represent the starting point of a given track and hollow pink circles represent the end of a given track.

7.4.2 Ordering of *D. Salina* due to Oscillatory Squeeze Film Flow

At high enough squeezing frequencies and maximum translation ordering was visually observed. This is illustrated in Figure 106 which shows that the majority of the algae travel in directions perpendicular to the oscillating flow field in the 0 and π radian (0 and 180 degrees) directions:

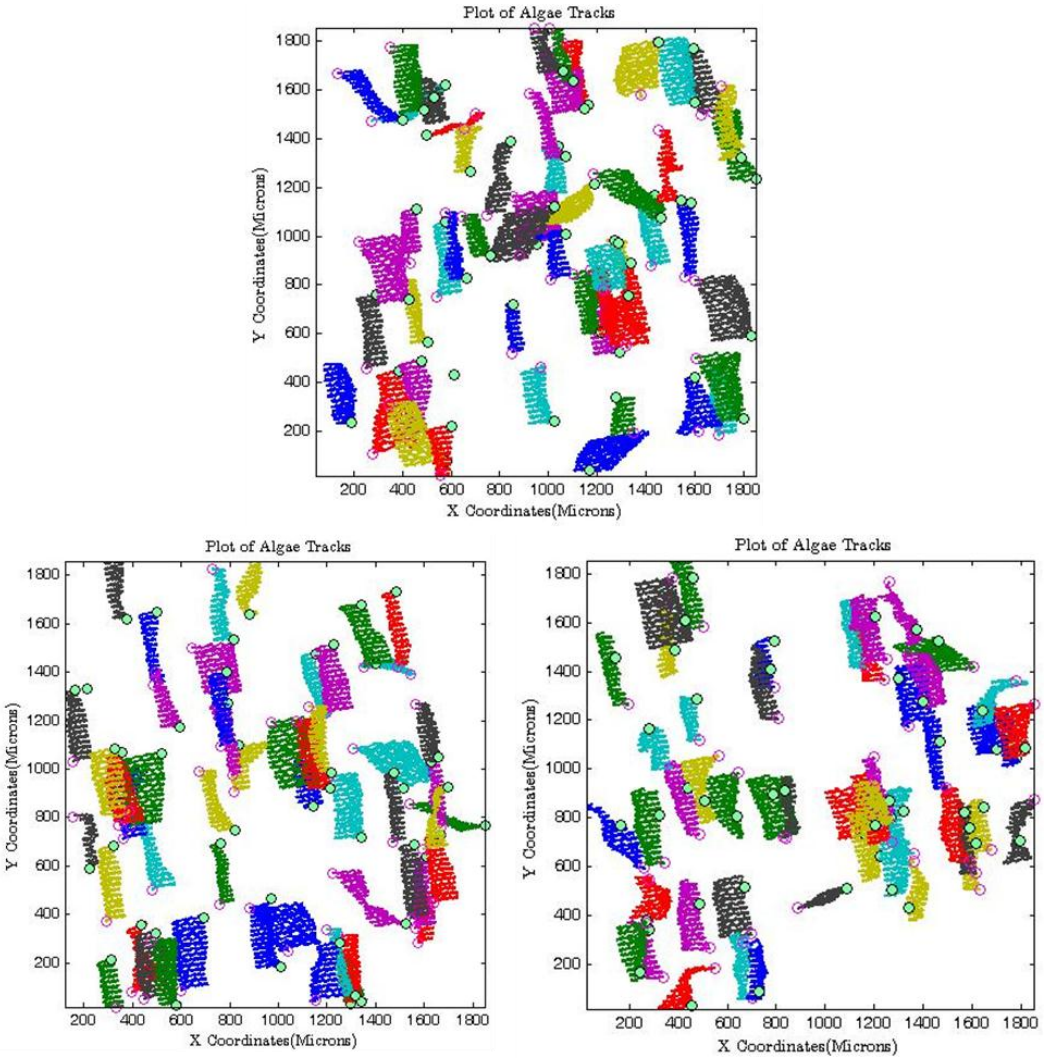

Figure 106 Tracking plots of algae over a period of 3 seconds individual swimming algae over a period of 3 seconds that were being subjected to a squeezing frequency of 3 Hz where the plane of focus was 75 microns down from the top plate.

The above track plots were taken from the same experiment over different time periods and plotted separately for clarity.

Figure 107 shows a distribution of the speed and angles of trajectory for the plots in Figure 106.

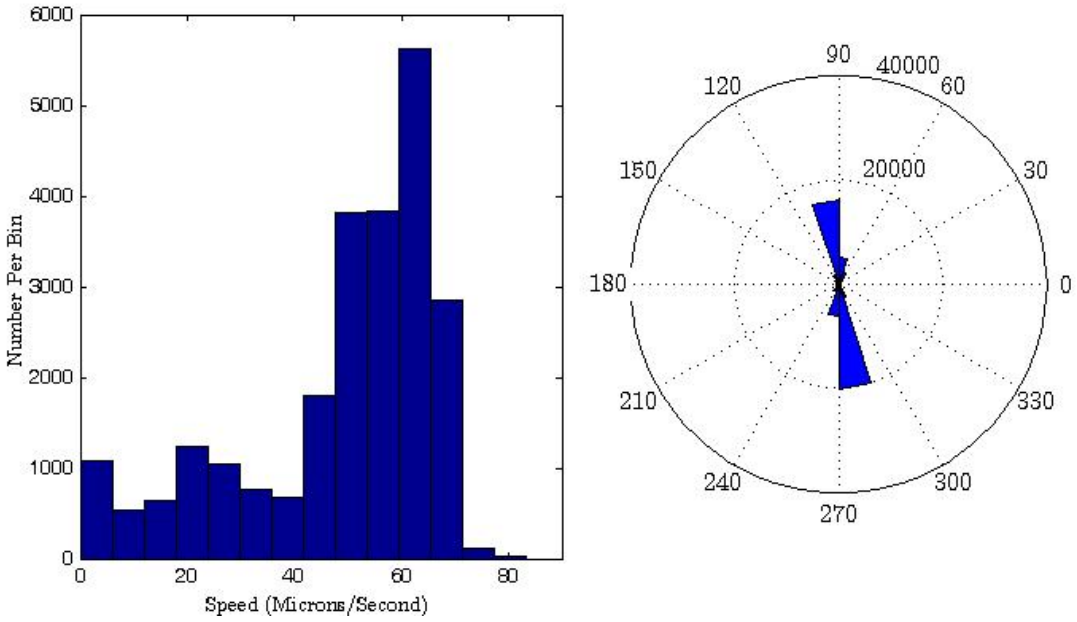

Figure 107 Histograms of speed of a collection of algae and their corresponding swimming directions over a period of 4 seconds, with squeezing being applied at a frequency of 3Hz with a maximum displacement of the algae of 160 microns. The swimming direction distribution shows a preference to the two directions perpendicular to the oscillatory flow field.

This ordering vanishes if the applied squeezing is ceased (Figure 108).

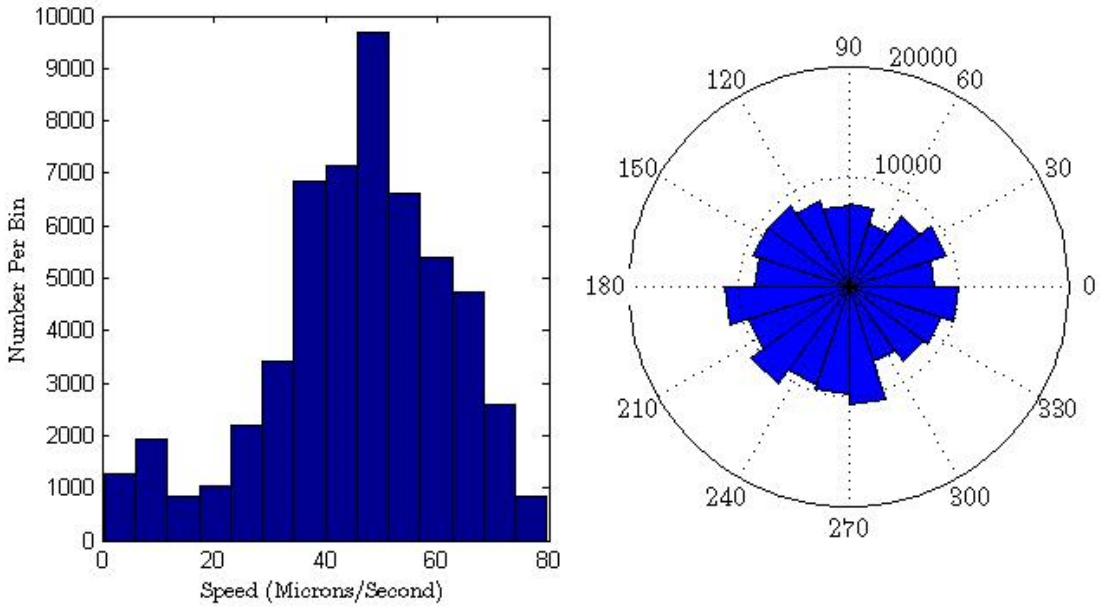

Figure 108 Histogram of swimming speed of a collection of algae and their corresponding swimming directions over a period of 4 seconds. The algae were within the piezoelectric squeeze cell with no squeezing being applied. The swimming direction distribution shows no preference to any particular directions.

7.4.3 Results and Conclusions: Response of *D.Salina* to Oscillatory Squeeze Flows Using the Piezoelectric Squeeze Cell

Figure 109 summarises how the ordering ratio(R) of tracked algae over a wide range of experiments as the squeezing frequency and shear strain per cycle were varied. The gap distance used in all experiments was 300 microns, where the plane of focus used was 75 microns below the top plate. It is important to note however that algae within around 60 microns of the plane of focus could still be tracked.

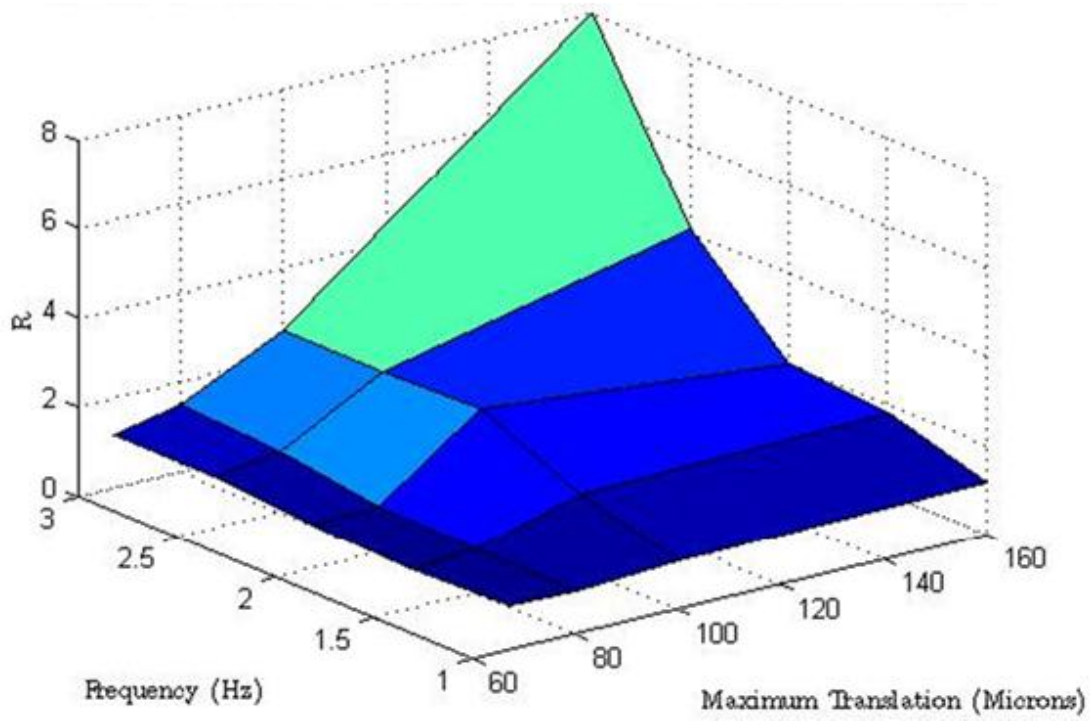

Figure 109 Surface plot of the ordering ratio R as a function of the maximum translation and frequency of oscillation for squeezing flows using the piezoelectric squeeze cell. The initial gap distance used was 300 microns. The plane of focus was 75 microns from the top plate.

As was mentioned in section 7.3, it is important to remember here that the maximum translation is the translation of a given algae on the local central horizontal plane of the sample over a squeezing cycle due to the flow field. As this increases, the shear strain per cycle and average shear rate increases.

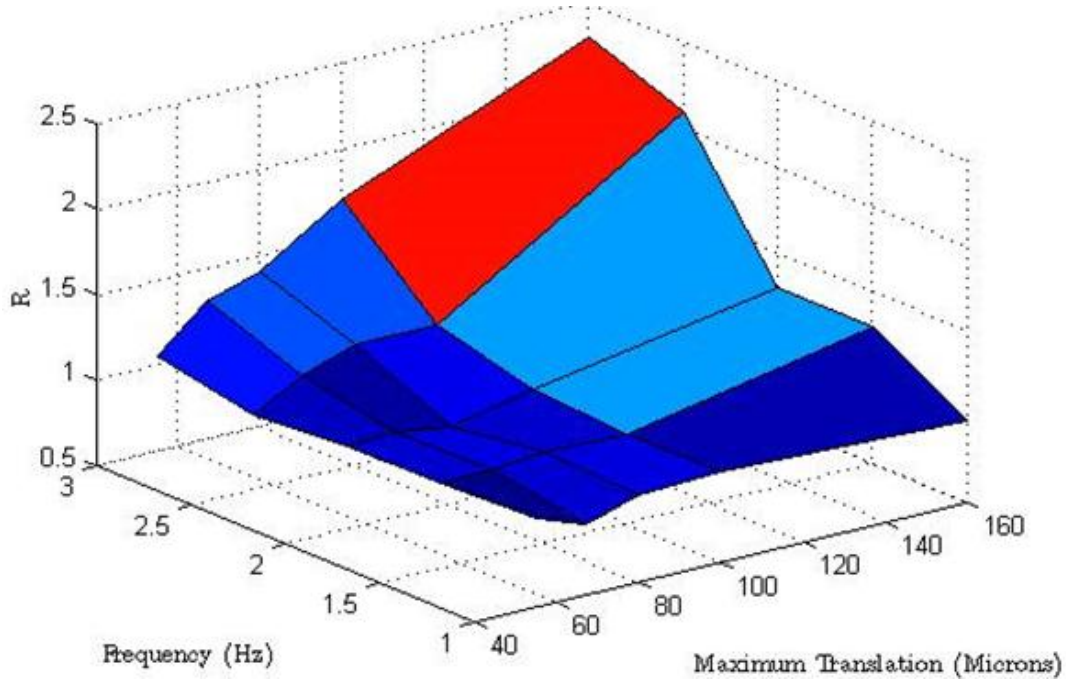

Figure 110 Surface plot of the ordering ratio R as a function of maximum translation and frequency of oscillation for squeezing flows using the piezoelectric squeeze cell. The initial gap distance used was 300 microns. The plane of focus was at the centre of the gap.

Figure 110 summarises how the ordering ratio of tracked algae varied over a wide range of experiments as the squeezing frequency were changed. The plane of focus used was at centre of the gap where the shear effects are weakest.

Both Figure 109 and Figure 110 shows that for experiments using the piezoelectric squeeze cell, as the squeezing frequency and the maximum translation increase, the extent of the ordering increases.

Comparing Figure 109 and Figure 110 shows that the ordering of *D. Salina* during OSFF using the piezoelectric squeeze was stronger in regions near the top plate of the piezoelectric squeeze cell where the shear strain and average shear rate were stronger. From chapter 2 it was shown that in OSFF shear is strongest near the top and bottom plates and weakest near the central horizontal plane.

7.5 Response of *D.Salina* to Oscillatory Squeeze Film Flows using the Electromechanical Squeeze Cell

Using the electromechanical squeeze cell, further oscillatory squeeze film flows were applied to suspensions of *D.Salina*. Squeezing frequencies in the range of 1Hz to 3Hz were applied. The initial gap distance used was fixed at either 200 microns or 400 microns. When a gap distance of 200 microns was used, the plane of focus was at the centre of the sample. When a gap distance of 400 microns was used, the plane of focus was 100 microns from the top plate. The maximum peak to trough displacement of the oscillating bottom plate was altered between 0 to 18 microns in order to achieve a desired maximum translation of the algae on the local horizontal central plane of the sample in the region being observed. This can be used as a measure of the extent of shear occurring away from the central horizontal plane at a given radial distance from the centre.

7.5.1 Behaviour of *D.Salina* within Electromechanical Squeeze Cell before any Applied Squeezing

When a suspension of *D.Salina* was placed within the electromechanical squeeze cell with no applied squeezing taking place, the modal speed was as expected for *D.Salina*. The swimming directions of algae showed no preference to any given direction as is illustrated in Figure 111 and Figure 112:

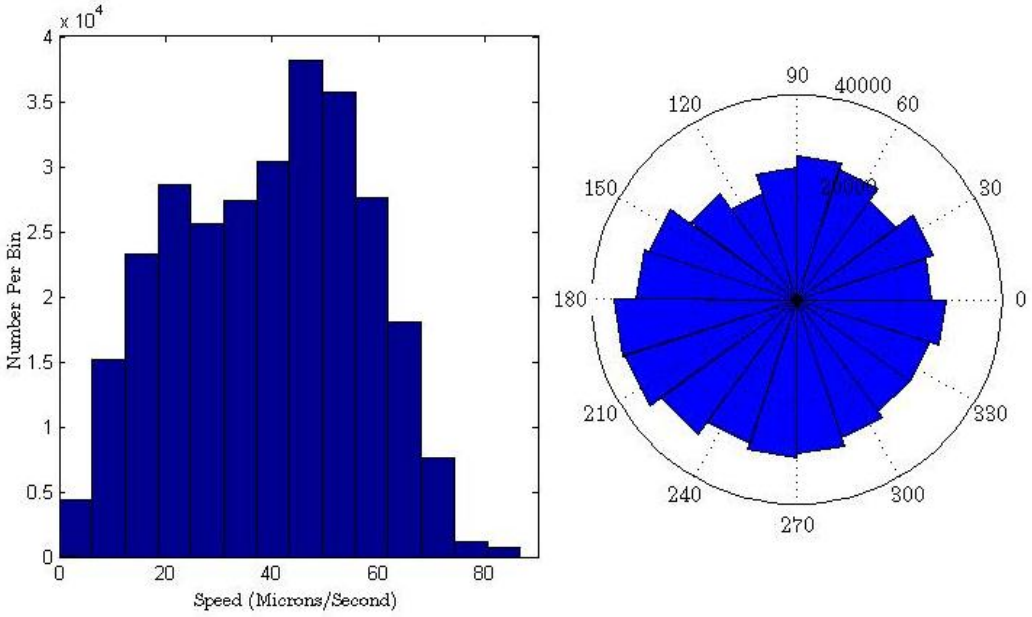

Figure 111 Histogram of speed of a collection of algae and their corresponding swimming directions over a period of 7 seconds. The algae were in the electromechanical squeeze cell with no squeezing being applied.

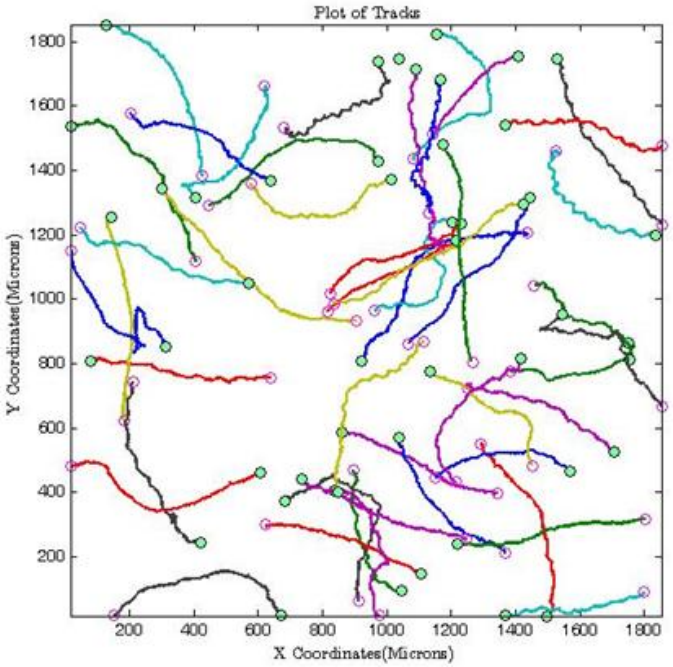

Figure 112 Tracks of algae over a period of 10 seconds within the electromechanical squeeze cell with no squeezing being applied. Filled green circles represent the starting point of a given track and hollow pink circles represent the end of a given track.

7.5.2 Ordering of *D. Salina* due Oscillatory Squeeze Film Flows

At certain squeezing frequencies and maximum translations, strong ordering of swimming directions could be visually observed as shown in Figure 114 and Figure 113. Despite the observed ordering, the modal speed of the algae was similar to the case where there was no applied squeezing.

Figure 113 also shows that the swimming direction of *D.Salina* was strongly focused perpendicular to the oscillatory flow field, which flipped between the in 0 and π radian (0 and 180 degrees) directions.

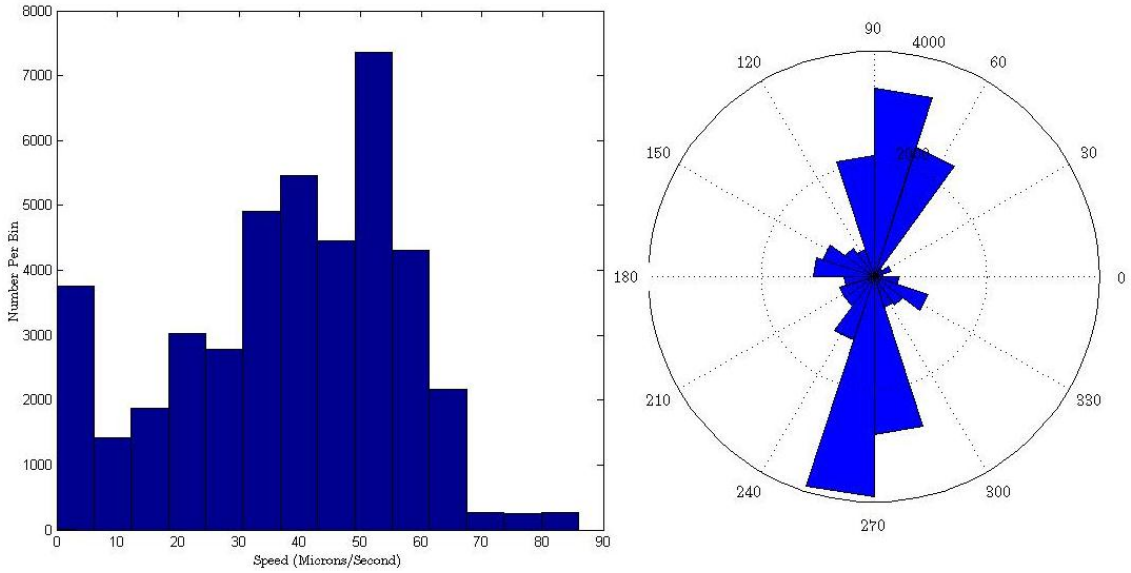

Figure 113 Histograms of speed of a collection of algae and their corresponding swimming directions over a period of 4 seconds. The algae were within the electromechanical squeeze cell with shear being applied at a frequency of 2Hz and a maximum displacement of the algae of 220 microns. The swimming direction distribution shows a preference to the directions perpendicular to the oscillatory flow field.

Figure 114 shows track plots of *D. Salina* that correspond to Figure 113, demonstrating the strong preference for swimming approximately perpendicular to the flow field.

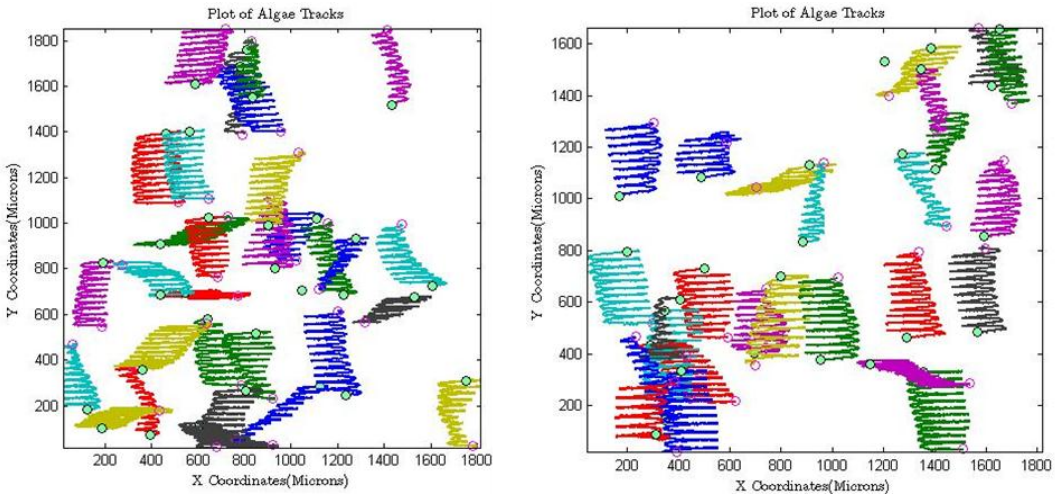

Figure 114 Tracks of algae over a period of 7 seconds within the shear with shear being applied at a frequency of 2Hz and a maximum translation of the algae of 220 microns. These plots show a bias of swimming directions perpendicular to the oscillatory flow field in the plane of focus. Filled green circles represent the starting point of a given track and hollow pink circles represent the end of a given track.

7.5.3 Disappearance of Ordering of *D.Salina* after Cessation of Oscillatory Squeeze Flow

This ordering vanishes if the applied squeezing shown is ceased as is shown in Figure 115 and Figure 116.

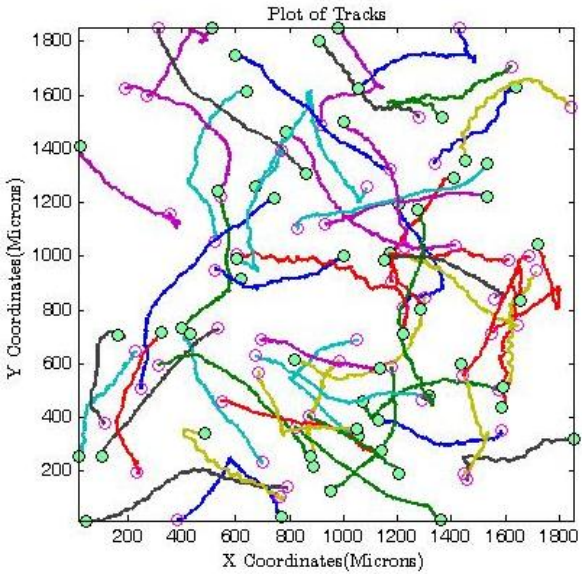

Figure 115 Shows a track of algae over a period of 10 seconds within the shear cell before any shear was applied. This shows no obvious bias to a particular direction. Filled green circles represent the starting point of a given track and hollow pink circles represent the end of a given track

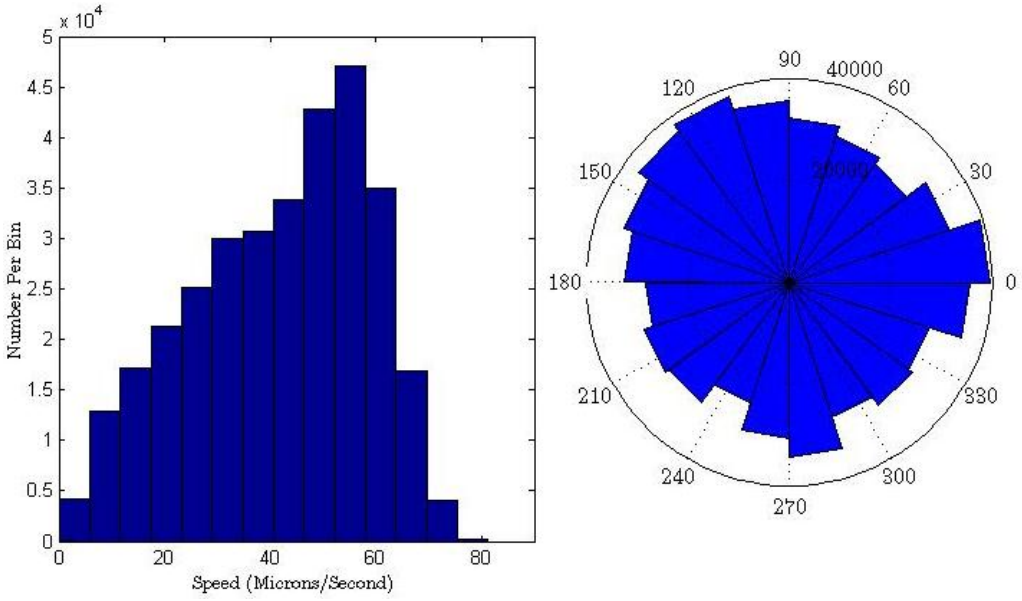

Figure 116 Histograms of speed of a collection of algae and their corresponding swimming directions over a period of 7 seconds, measured 1 minute after the cessation of squeezing. The algae swimming directions had previously ordered perpendicular to the flow field prior to the cessation of squeezing.

7.5.4 Results and Conclusions: Response of *D.Salina* to Oscillatory Squeeze Flows Using the Electromechanical Squeeze Cell

Figure 117 and Figure 119 summarise the average value of the ordering ratio as the applied squeezing frequency and the maximum translation of algae are varied at two different initial gap sizes, using the electromechanical squeeze cell.

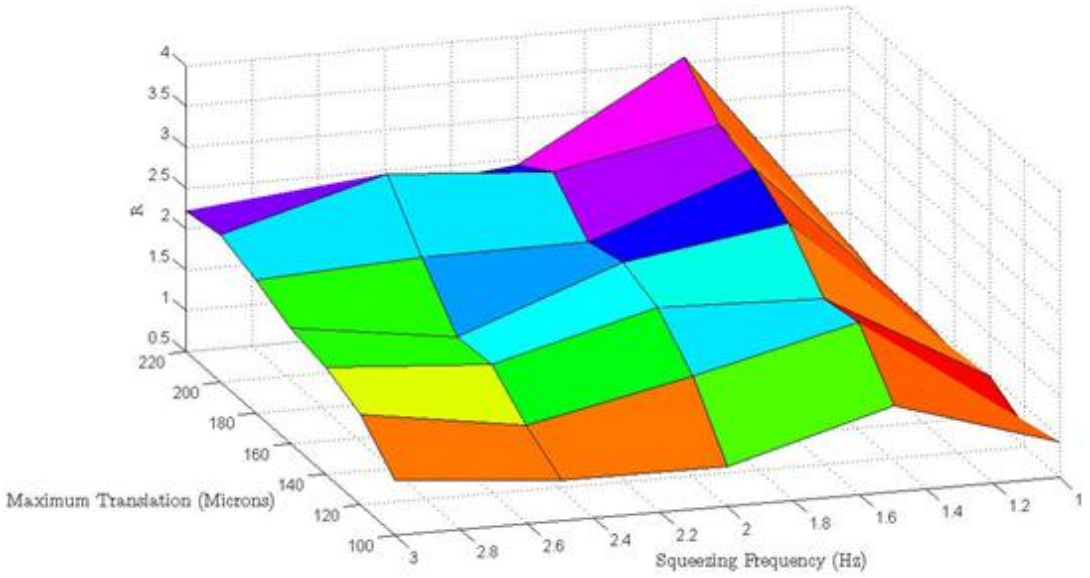

Figure 117 Surface plot of the ordering ratio R as a function of the maximum translation and the frequency of oscillation for squeezing flows using the electromechanical squeeze cell. The initial gap distance used was 200 microns. The plane of focus was at the central horizontal plane.

Figure 117 shows an increase in the ordering ratio (R) as the maximum translation is increased with a peak in the region of squeezing frequencies of 1.5 Hz. The plane of focus was at the centre of the sample, however algae within around 60 microns of this central plane could be identified as tracked. It indicates that the ordering ratio increases with the maximum translation which is a measure of the extent of shear per cycle over the range of parameters used.

Figure 118 shows segments of fixed maximum translation (effectively constant shear strain per cycle) from Figure 117 highlighting that the ordering ratio is highest at frequencies in the region of 1.5-2Hz.

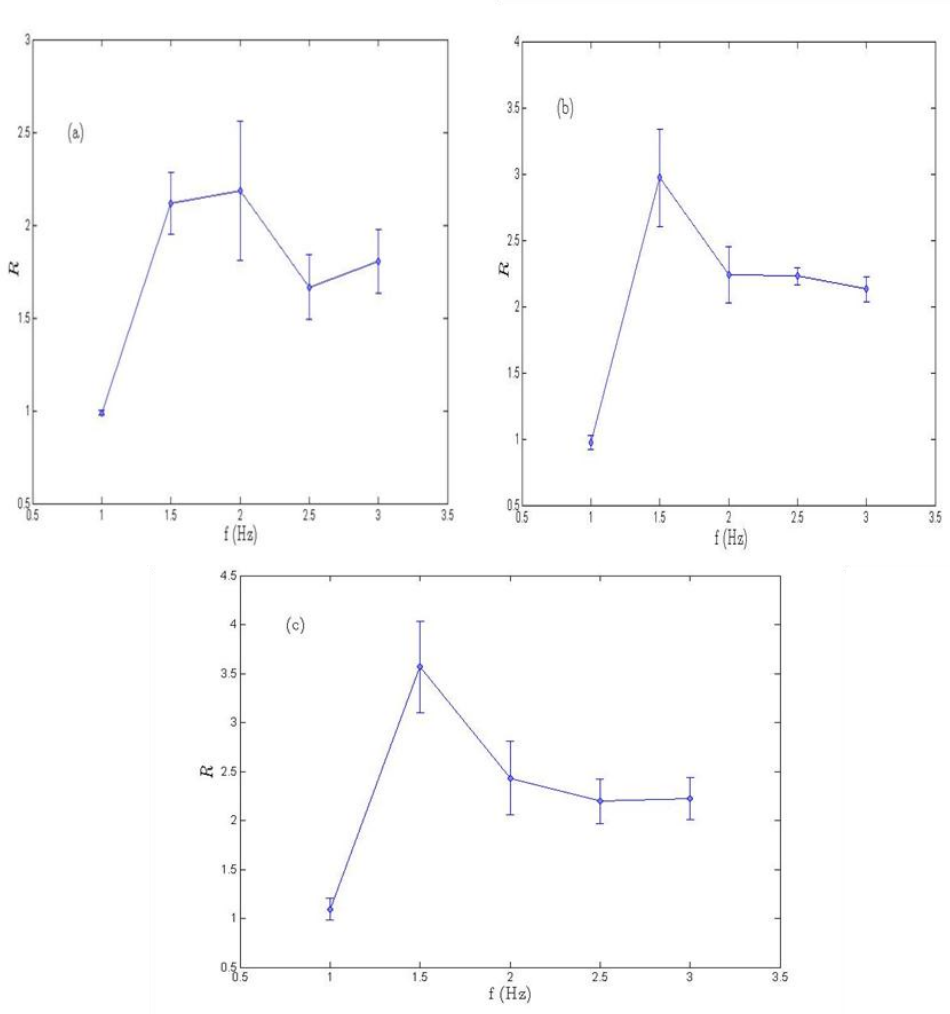

Figure 118a) Varation of R with squeezing frequency at a fixed maximum translation of algae of 140 microns. b) Maximum translation of algae of 180 microns. c) Maximum fixed translation of algae of 220 microns. The gap distance was 200 microns and the plane of focus was at the centre of the gap. The error bars correspond to the standard error in the mean value of R from multiple experiments at a given set of conditions. Note that the scale used in each figure is different.

Figure 119 summarises how the average value of the ordering ratio as the squeezing frequency and the maximum translation are varied at a larger gap distance of 400 microns. Ordering was also observed using the electromechanical squeeze cell at this larger gap distance of 400 microns, however it is more difficult to identify a clear trend in from this set of experiments.

The ordering was in general weaker than at the lower gap distance of 200 microns (as shown in Figure 117) where the shear strain and shear rate corresponding to a given maximum translation is higher. The shear is weaker because the velocity gradient from the centre of the sample where the shear rate is zero to the top and bottom plates increases with decreasing gap distance as was mentioned in chapter 2.

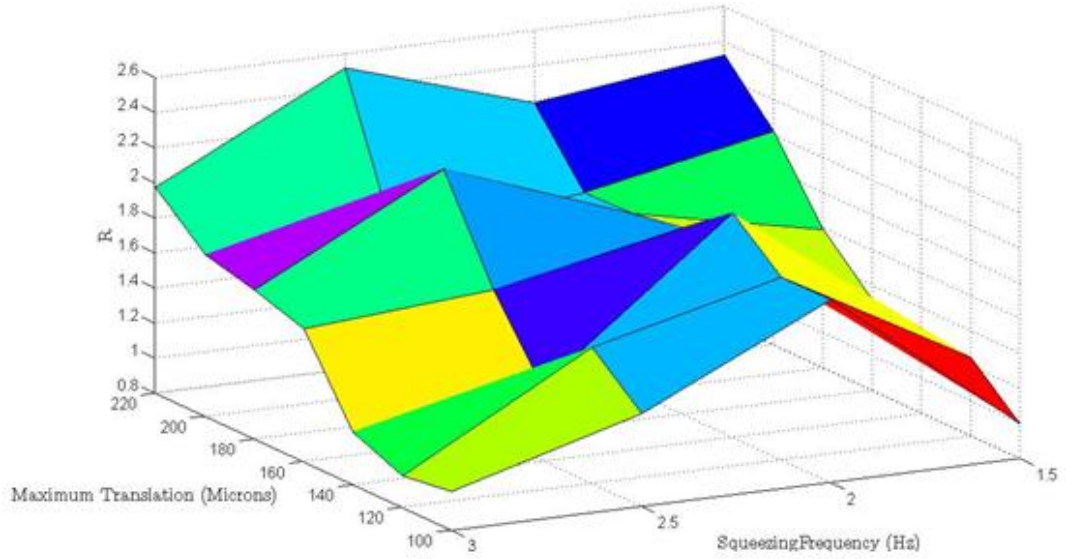

Figure 119 Surface plot of the ordering ratio R as a function of the maximum translation and frequency of oscillation for squeezing flows using the electromechanical squeeze cell. The initial gap distance used was 400 microns. The plane of focus was 100 microns down from the stationary top plate.

Comparing Figure 117 and Figure 119 also implies that the ordering is dependent to some extent on shear strain per cycle. Both show that in general that R increases with the maximum translation as was the case with squeeze flow experiments using the piezoelectric squeeze cell.

7.6 Discussion of Results

In this subsection, the results obtained in this chapter are discussed in the context of the surrounding literature.

7.6.1 Ordering of *D.Salina* Dependence on Shearing Frequency

Here the dependence of the ordering of *D.Salina* on the shearing frequencies of the applied flow fields is summarised. All three experimental arrangements showed that were was a minimum frequency, below which no ordering was observed. Results obtained from using the electromechanical shear cell showed that ordering was strongest in the region of 1.5-2Hz. Results obtained from using the electromechanical squeeze cell at a gap distance of 200 microns also showed a peak in the ordering ratio in the 1.5Hz region.

Using the electromechanical squeeze cell to apply OSFF with a fixed gap distance 400 microns, local maxima were seen at 2Hz and 2.5Hz, however at this gap distance the observed ordering was less than at a gap distance of 200, making it difficult to conclusively define any frequency dependence.

Results obtained using the piezoelectric squeeze cell at a gap distance of 300 microns showed that in the range of 0-3Hz and maximum translations up to 160 microns, the ordering ratio increased with both frequency and shearing magnitude, which partially contradicts other results as no strong peak in the ordering was observed in the region of 1.5-2Hz.

It is difficult to make direct comparisons between the different set-ups as a number of parameters such as gap and distance and the plane of focus (which have a great effect on the forces acting on the algae), were different. This means that it is to be expected that in different shearing geometries that different shearing frequencies and maximum translations cause the same ordering effect on *D.Salina*.

Some sets of experiments using the electromechanical squeeze and shear cell display peaks in the ordering ratio around 2Hz. There is a possibility this could be related to the fact that *D.Salina* rotates at a frequency of around 2Hz but simulations so far have implied that this is unlikely to be the case [204].

7.6.2 Ordering Dependence on Maximum Translation/Shear Strain

All three arrangements showed that as the extent of shearing was decreased far enough (represented by decreasing by the maximum translation), no ordering was observed.

The ordering ratio also varies with distance from the centre of the gap during oscillatory squeeze flow as is illustrated by comparing Figure 109 and Figure 110. This gives evidence that ordering is related to the average or maximum shear rate in the region under observation.

Results using electromechanical and piezoelectric squeeze cells showed in general that increasing the strength of the shear strain per cycle (by increasing the maximum translation of the algae for a given gap distance), while keeping the frequency fixed resulted in an increase in the ordering ratio.

Results obtained using the shear cell showed that ordering ratio R was strongest with a maximum translation of 224 microns. This contradicts squeezing results to some extent which normally showed the ordering ratio increasing with maximum translation at any given frequency. However this could be related to the fact that the induced flow fields have a number of differences which could potentially have an impact on the behaviour of *D.Salina*. For example in OSFF experiments there is a slight elongation component present in the flow and for a given maximum translation and gap distance, the shear strain and shear rate was greater in OSFF experiments.

From the results obtained it is not possible to obtain a full understanding on how this ordering is dependent on the frequency of oscillation and the shear strain per cycle until a model is found that fits experimental data. This is discussed more at the end of this chapter. The fact that R is dependent on a range of parameters implies that induced ordering is a result of a delicate balance between viscous torque of the flow acting on the algae and the torques due to its physical characteristics such as gravitactic and intrinsic torques as described in chapter 3.

To summarise, it is clear that ordering of *D.Salina* was observed in oscillatory shears flows during this PhD, and that this ordering is dependent on the frequency of oscillation of the flow field and the shear strain per cycle.

7.6.3 Comparison of Experimental Results with Results Found in Literature

Experiments carried out by Chengala and co-workers have shown that a species of swimming algae called *Dunaliella Primolecta* which is very similar to *D. Salina*, can order its swimming directions during continuous shearing flows [205]. In their experiments they used a syringe pump to drive algae suspensions through a rectangular channel at various flow rates. They observed algae at 2 fixed positions near the top and bottom planes of the rectangular channel. By altering the overall flow rate they also altered the shear rates at these fixed planes. Within a certain range of shear rates, they showed that *D. Primolecta* orders its swimming directions perpendicular to the flow field, in the vorticity direction.

The direction of the vorticity at the top plane during such laminar channel flow is anti-parallel to the bottom plane and so the algae observed in each of the planes ordered their swimming directions in opposite directions to algae in the other plane.

In oscillatory shear flow experiments the direction of the vorticity direction flips back and forth every cycle and it is along these 2 directions that the algae preferentially swim along. There is therefore some agreement between the oscillatory shear and the continuous shear experiments carried out by Chengala, both experiments showed algae swimming in the vorticity directions. Chengala and co-workers also showed that there was a minimum shear rate below which no ordering was observed which corresponds well with the results in this thesis.

The model proposed by Chengala to describe the ordering that they observed does not really fit the oscillatory flow results presented in this chapter as it implies that *D.Salina* should change their swimming direction as the vorticity direction changes. Additionally Chengala only observed ordering near the top and bottom planes which means that interactions with the boundaries could have been responsible.

A theoretical study on micro-swimmers in oscillatory shears flows with noise in the velocity gradient by Guzman-Lastra and co-workers predicted a mean displacement of swimmers in the direction of the vorticity [206]. In their model the extent of this ordering increased with the shearing frequency for a given noise intensity which potentially agrees well with the results in this thesis. However this predicted ordering was independent of the shear rate

which disagrees with the results in this thesis. It is therefore unclear to what extent this theoretical study can be related to the results presented in this chapter.

7.6.4 Discussion of a Potential Mechanism

Here the most likely cause that has so far been suggested for the ordering observed in this thesis is discussed.

When individual *D.Salina* are observed to be swimming with or against the oscillating shear flow that is translating them back and forth as they swim, they often seem to be forced into a tumble. During and shortly after this tumble, their ability to propel themselves is greatly reduced and they are then prone to orientate themselves perpendicular to the oscillating flow field. It is likely that this tumbling issue is caused by the viscous torque resulting from the oscillating flow field. *D.Salina* that swim perpendicular to the flow field don't appear to be forced into a tumble by the oscillating flow field, or at least do so less often.

As algae that are swimming against or with the flow field are more likely to tumble than those swimming perpendicular to the flow field, this could provide an effective driving force for the observed ordering. There is preliminary simulation evidence that supports this mechanism as the cause of the observed ordering [204].

7.6.5 Chapter Summary

To summarise, in this chapter it is shown using 3 different sets of experimental apparatus that when *D.Salina* is subjected to oscillatory shear flows at certain frequencies and shear strains per cycle, they can order their swimming directions in the vorticity directions. This implies that forces exerted by the oscillating flow fields on individual algae can have the effect of preferentially encouraging algae to swim in the vorticity directions.

A proven mechanism for this behaviour is still under investigation, however the most probable model is one in which *D.Salina* that are orientated parallel to the oscillating flow field are preferentially forced into a tumble which prevents swimming, while *D.Salina* orientated perpendicular to the oscillating flow field are not. This could result in an effective driving force that causes the algae to primarily move in the vorticity directions.

Chapter 8 Conclusions and Future Work

The conclusions that can be taken from this PhD are summarised and suggestions for future work are given here.

8.1 Conclusions from the Investigation of the Jamming of Particle Suspensions

The original goal of this PhD was to investigate the jamming of particle suspensions, particularly in squeeze film flows. This goal was met, although due to equipment issues, the methods used were very different from what was originally intended.

It was shown that when particle suspensions at high enough concentrations are subjected the oscillatory squeeze film flows of high enough frequencies and peak forces, the flow field within the suspensions becomes distorted and the sample shape changes. These changes were shown to be reversible. Surface tension forces were shown to act against sample shape distortion during squeezing. Once the applied squeezing is halted the sample shape becomes less distorted due to surface tension over time. It was concluded that the observed flow field and sample shape distortions were most likely a result of intermittent jamming occurring within the suspensions, given that Newtonian and viscoelastic fluids show no such effects.

The flow field and shape distortions observed during the oscillatory squeeze film flow of concentrated suspensions at high enough applied peak stresses and frequencies is likely analogous to the discontinuous shear thickening and jamming observed in shear flows. DST and jamming was observed in the same concentrated particle systems during parallel plate continuous and oscillatory shear flow rheometry. This confirms that the suspensions used in the oscillatory squeeze flow experiments were prone to DST at mild shearing conditions giving strong evidence that DST and jamming could have been the cause of the unusual observations.

A range of useful rheological data regarding the continuous and large amplitude oscillatory shear of highly concentrated stabilised colloidal dispersions and corn starch suspensions was obtained. Results implied that jamming evolves from DST and is caused by the formation of clusters of particles that transmit forces through direct particle contact.

Results also gave evidence supporting the idea that the maximum shear stress a particle suspension can sustain without fracturing in an open rheometer is proportional to the maximum capillary forces that act against dilation. Extreme DST and jamming was seen experimentally to lead to granulation- the formation of stable jammed granules.

Future work in this area could involve the investigation of the mechanism by which granulation of suspensions evolves from DST at high enough particle concentrations. This could be approached by determining the conditions required to cause granulation in a wide range of different particle suspensions with different properties such as particle size, dispersing medium and polydispersity.

8.2 Design of Electromechanical Squeeze Cell

A cost effective method for applying smooth and consistent oscillatory squeeze film flow was shown to be successful. The apparatus allowed samples to be squeezed and stretched at a given peak stress and allows samples to be microscopically viewed using a microscope and camera. The apparatus is also very robust, and it easy to upgrade and replace its constituent parts.

Further improvements in this area could involve enhancing the electromechanical squeeze cell so that it can record the position of the bottom plate during squeezing, this would allow the resulting strains to be measured during squeezing. Relationships between the stress and strain in this geometry could then be obtained while the flow field is being viewed. This would also allow rheological properties of fluids to be analysed.

8.3 Swimming of Algae in Oscillatory Shear Flows Conclusions and Future Work

The original aim of this set of work was to investigate the behaviour the species of swimming algae *D.Salina* in oscillatory shear flows. This objective was met.

Experimental evidence suggests that when *D.Salina* is exposed to oscillatory shear flows, the algae preferentially swim in directions coinciding with the vorticity axis of the oscillating flow field. This is likely due to the forces exerted by the oscillating flow fields on individual *D.Salina* encouraging them to become preferentially aligned with the vorticity directions of the oscillating flow field. There is also observational evidence to suggest that

oscillating shear flows can cause *D.Salina* that are orientated parallel to the flow field to be forced into a tumble by the flow, while those oriented perpendicular to the flow are less prone to be forced into a tumble and continue swimming. This has potential applications in the design of energy efficient algal self-concentration processes.

Future work would be to develop a model that predicts the observed experimental behaviour and determine the exact mechanism behind the ordering. Investigation of how other species of swimming algae and bacteria respond to oscillatory shear flows could also yield clues into what characteristics are necessary for ordering in the vorticity directions to be observed. It could also be useful to investigate whether the observed ordering in the direction of the vorticity could have practical applications in encouraging *D.Salina* and other species into self-concentrating by the action of oscillating shear flows.

References

[1] R. A. L. Jones, *Soft Condensed Matter* (Oxford University Press, 2002).
[2] R. J. Hunter, *Foundations of Colloid Science* (Oxford University Press, 1999), 2nd edn.
[3] V. Trappe, V. Prasad, L. Cipelletti, P. N. Segre, and D. A. Weitz, Nature **411**, 772 (2001).
[4] T. K. Haxton, M. Schmiedeberg, and A. J. Liu, Physical Review E **83** (2011).
[5] Eric Weeks, Soft Jammed Materials(2007), http://www.physics.emory.edu/~weeks/lab/papers/sendai2007.pdf.
[6] A. J. Liu and S. R. Nagel, Nature **396**, 21 (1998).
[7] M. E. Cates, J. P. Wittmer, J. P. Bouchaud, and P. Claudin, Physical Review Letters **81**, 1841 (1998).
[8] M. E. Cates, J. P. Wittmer, J. P. Bouchaud, and P. Claudin, Chaos **9**, 511 (1999).
[9] M. E. Cates, Annales Henri Poincare **4**, S647 (2003).
[10] M. E. Cates, M. D. Haw, and C. B. Holmes, Journal of Physics-Condensed Matter **17**, S2517 (2005).
[11] C. B. Holmes, M. Fuchs, and M. E. Cates, Europhysics Letters **63**, 240 (2003).
[12] E. Bertrand, J. Bibette, and V. Schmitt, Physical Review E **66**, 060401 (2002).
[13] E. Brown and H. M. Jaeger, Journal of Rheology **56**, 875 (2012).
[14] A. Fall, N. Huang, F. Bertrand, G. Ovarlez, and D. Bonn, Physical Review Letters **100** (2008).
[15] A. Fall, F. Bertrand, G. Ovarlez, and D. Bonn, Journal of Rheology **56**, 575 (2012).
[16] E. Brown and H. M. Jaeger, Reports on Progress in Physics **77**, 046602 (2014).
[17] A. Mehta, *Granular Physics* (Cambridge University Press, 2007).
[18] F. Toussaint, C. Roy, and P.-H. Jezequel, Rheologica Acta **48**, 883 (2009).
[19] D. Feys, R. Verhoeven, and G. De Schutter, Cement and Concrete Research **39**, 510 (2009).
[20] D. Lootens, P. Hebraud, E. Lecolier, and H. Van Damme, Oil & Gas Science and Technology-Revue D Ifp Energies Nouvelles **59**, 31 (2004).
[21] J. R. Amend, Jr., E. Brown, N. Rodenberg, H. M. Jaeger, and H. Lipson, IEEE Transactions on Robotics **28**, 341 (2012).
[22] E. Brown, N. Rodenberg, J. Amend, A. Mozeika, E. Steltz, M. R. Zakin, H. Lipson, and H. M. Jaeger, Proceedings of the National Academy of Sciences of the United States of America **107**, 18809 (2010).
[23] Y. S. Lee, E. D. Wetzel, and N. J. Wagner, Journal of Materials Science **38**, 2825 (2003).
[24] N. J. Wagner and J. F. Brady, Physics Today **62**, 27 (2009).
[25] M. J. Decker, C. J. Halbach, C. H. Nam, N. J. Wagner, and E. D. Wetzel, Composites Science and Technology **67**, 565 (2007).
[26] E. D. Wetzel and N. J. Wagner, Journal of Aircraft **49**, 671 (2012).
[27] X. Gong, Y. Xu, W. Zhu, S. Xuan, W. Jiang, and W. Jiang, Journal of Composite Materials **48**, 641 (2014).
[28] Victoria Gill, Liquid Armour Can Stop Bullets(2010), http://www.bbc.co.uk/news/10569761.
[29] M. Jenkins, *PhD thesis (unpublished)* (University of Edinburgh, 2005).
[30] G. L. Hunter and E. R. Weeks, Reports on Progress in Physics **75**, 066501 (2012).

[31] J. Mewis and N. J. Wagner, *Colloidal Suspension Rheology* (Cambridge University Press, 2012).
[32] R. G. Larson, *The Structure and Rheology of Complex Fluids* (Oxford University Press, 1999).
[33] J. W. Swan and J. F. Brady, Journal of Fluid Mechanics **687**, 254 (2011).
[34] J. F. Brady, Journal of Chemical Physics **98**, 3335 (1993).
[35] M. P. Ciamarra, R. Pastore, M. Nicodemi, and A. Coniglio, Physical Review E **84**, 041308 (2011).
[36] S. Henderson, S. Mitchell, and P. Bartlett, Physical Review E **64**, 061403 (2001).
[37] T. Cosgrove, *Colloid Science: Principles, Methods and Applications* (Wiley, 2010), 2nd edn.
[38] M. Jerkins, M. Schroeter, H. L. Swinney, T. J. Senden, M. Saadatfar, and T. Aste, Physical Review Letters **101** (2008).
[39] P. Ribiere, P. Philippe, P. Richard, R. Delannay, and D. Bideau, Journal of Physics-Condensed Matter **17**, S2743 (2005).
[40] K. J. Dong, R. Y. Yang, R. P. Zou, and A. B. Yu, Physical Review Letters **96** (2006).
[41] G. Y. Onoda and E. G. Liniger, Physical Review Letters **64**, 2727 (1990).
[42] W. C. K. Poon, E. R. Weeks, and C. P. Royall, Soft Matter **8**, 21 (2012).
[43] S. Torquato, T. M. Truskett, and P. G. Debenedetti, Physical Review Letters **84**, 2064 (2000).
[44] S. Torquato and F. H. Stillinger, Reviews of Modern Physics **82**, 2633 (2010).
[45] E. Brown and H. M. Jaeger, Physical Review Letters **103** (2009).
[46] V. T. O'Brien and M. E. Mackay, Langmuir **16**, 7931 (2000).
[47] R. G. Egres and N. J. Wagner, Journal of Rheology **49**, 719 (2005).
[48] P. N. Pusey, W. C. K. Poon, S. M. Ilett, and P. Bartlett, Journal of Physics-Condensed Matter **6**, A29 (1994).
[49] W. C. K. Poon and P. N. Pusey, in *Observation, Prediction and Simulation of Phase Transitions in Complex Fluids*, edited by M. R. L. F. R. J. P. Baus1995), pp. 3.
[50] C. Valeriani, E. Sanz, E. Zaccarelli, W. C. K. Poon, M. E. Cates, and P. N. Pusey, Journal of Physics-Condensed Matter **23** (2011).
[51] C. B. Holmes, M. E. Cates, M. Fuchs, and P. Sollich, Journal of Rheology **49**, 237 (2005).
[52] F. Morrison, *Understanding Rheology* (Oxford University Press, 2001).
[53] H. A. Barnes, Journal of Rheology **33**, 329 (1989).
[54] D. Lootens, H. Van Damme, and P. Hebraud, Physical Review Letters **90**, 178301 (2003).
[55] W. Loose and S. Hess, Rheologica Acta **28**, 91 (1989).
[56] B. J. Ackerson and P. N. Pusey, Physical Review Letters **61**, 1033 (1988).
[57] R. P. A. Dullens and C. Bechinger, Physical Review Letters **107** (2011).
[58] S. D. Kulkarni and J. F. Morris, Journal of Rheology **53**, 417 (2009).
[59] M. D. Haw, W. C. K. Poon, and P. N. Pusey, Physical Review E **57**, 6859 (1998).
[60] X. L. Xu, S. A. Rice, and A. R. Dinner, Proceedings of the National Academy of Sciences of the United States of America **110**, 3771 (2013).
[61] A. B. Metzner and M. Whitlock, Transactions of the Society of Rheology **2**, 239 (1958).
[62] R. V. Williamson and W. W. Heckert, Industrial and Engineering Chemistry **23**, 667 (1931).
[63] H. Freundlich and H. L. Roder, Transactions of the Faraday Society **34**, 0308 (1938).
[64] J. Delhommelle, European Physical Journal E **15**, 65 (2004).
[65] H. M. Laun, Journal of Non-Newtonian Fluid Mechanics **54**, 87 (1994).

[66] R. Seto, R. Mari, J. F. Morris, and M. M. Denn, Physical Review Letters **111**, 218301 (2013).
[67] H. M. Laun, R. Bung, and F. Schmidt, Journal of Rheology **35**, 999 (1991).
[68] D. Lootens, N. S. Martys, W. George, S. Satterfield, and P. Hebraud, in *Xvth International Congress on Rheology - the Society of Rheology 80th Annual Meeting, Pts 1 and 2*, edited by A. Co *et al.*2008), pp. 677.
[69] J. Vermant and M. J. Solomon, Journal of Physics-Condensed Matter **17**, R187 (2005).
[70] D. P. Kalman and N. J. Wagner, Rheologica Acta **48**, 897 (2009).
[71] J. Bender and N. J. Wagner, Journal of Rheology **40**, 899 (1996).
[72] Y. S. Lee and N. J. Wagner, Industrial & Engineering Chemistry Research **45**, 7015 (2006).
[73] B. J. Maranzano and N. J. Wagner, Journal of Chemical Physics **117**, 10291 (2002).
[74] H. M. Laun *et al.*, Journal of Rheology **36**, 743 (1992).
[75] J. W. Bender and N. J. Wagner, Journal of Colloid and Interface Science **172**, 171 (1995).
[76] G. Bossis and J. F. Brady, Journal of Chemical Physics **91**, 1866 (1989).
[77] J. F. Brady and G. Bossis, Annual Review of Fluid Mechanics **20**, 111 (1988).
[78] X. Cheng, J. H. McCoy, J. N. Israelachvili, and I. Cohen, Science **333**, 1276 (2011).
[79] R. G. Egres, F. Nettesheim, and N. J. Wagner, Journal of Rheology **50**, 685 (2006).
[80] B. J. Maranzano and N. J. Wagner, Journal of Rheology **45**, 1205 (2001).
[81] B. J. Maranzano and N. J. Wagner, Journal of Chemical Physics **114**, 10514 (2001).
[82] J. S. Chong, Christia.Eb, and A. D. Baer, Journal of Applied Polymer Science **15**, 2007 (1971).
[83] S. S. Shenoy and N. J. Wagner, Rheologica Acta **44**, 360 (2005).
[84] E. Brown, H. Zhang, N. A. Forman, B. W. Maynor, D. E. Betts, J. M. DeSimone, and H. M. Jaeger, Physical Review E **84** (2011).
[85] E. Brown, N. A. Forman, C. S. Orellana, H. Zhang, B. W. Maynor, D. E. Betts, J. M. DeSimone, and H. M. Jaeger, Nature Materials **9**, 220 (2010).
[86] M. E. Cates, J. P. Wittmer, J. P. Bouchaud, and P. Claudin, Physica A **263**, 354 (1999).
[87] M. E. Cates, in *Jamming, Yielding, and Irreversible Deformation in Condensed Matter*, edited by M. C. R. J. M. Miguel2006), pp. 3.
[88] D. Lootens, H. van Damme, Y. Hemar, and P. Hebraud, Physical Review Letters **95**, 268302 (2005).
[89] E. Brown, H. Zhang, N. A. Forman, B. W. Maynor, D. E. Betts, J. M. DeSimone, and H. M. Jaeger, Journal of Rheology **54**, 1023 (2010).
[90] M. I. Smith, R. Besseling, M. E. Cates, and V. Bertola, Nature Communications **1**, 114 (2010).
[91] E. E. B. White, M. Chellamuthu, and J. P. Rothstein, Rheologica Acta **49**, 119 (2010).
[92] D. Doraiswamy, A. N. Mujumdar, I. Tsao, A. N. Beris, S. C. Danforth, and A. B. Metzner, Journal of Rheology **35**, 647 (1991).
[93] M. Chellamuthu, E. M. Arndt, and J. P. Rothstein, Soft Matter **5**, 2117 (2009).
[94] R. L. Hoffman, Journal of Colloid and Interface Science **46**, 491 (1974).
[95] A. S. Lim, S. L. Lopatnikov, N. J. Wagner, and J. W. Gillespie, Journal of Non-Newtonian Fluid Mechanics **165**, 1342 (2010).
[96] W. J. Frith and A. Lips, Advances in Colloid and Interface Science **61**, 161 (1995).
[97] W. J. Frith, A. Lips, J. R. Melrose, and R. C. Ball, Modern Aspects of Colloidal Dispersions: Results from the Dti Colloid Technology Programme, 123 (1998).
[98] S. Adams, W. J. Frith, and J. R. Stokes, Journal of Rheology **48**, 1195 (2004).

[99] B. Wolf, S. Lam, M. Kirkland, and W. J. Frith, Journal of Rheology **51**, 465 (2007).
[100] T. G. Mason and D. A. Weitz, Physical Review Letters **75**, 2770 (1995).
[101] R. A. Lionberger and W. B. Russel, Journal of Rheology **38**, 1885 (1994).
[102] N. J. Wagner, Journal of Colloid and Interface Science **161**, 169 (1993).
[103] Y. S. Lee and N. J. Wagner, Rheologica Acta **42**, 199 (2003).
[104] C. Fischer, C. J. G. Plummer, V. Michaud, P.-E. Bourban, and J.-A. E. Manson, Rheologica Acta **46**, 1099 (2007).
[105] S. R. Raghavan and S. A. Khan, Journal of Colloid and Interface Science **185**, 57 (1997).
[106] C. O. Klein, H. W. Spiess, A. Calin, C. Balan, and M. Wilhelm, Macromolecules **40**, 4250 (2007).
[107] R. Buscall, Journal of Rheology **54**, 1177 (2010).
[108] L. Isa, R. Besseling, and W. C. K. Poon, Physical Review Letters **98**, 198305 (2007).
[109] P. Ballesta, G. Petekidis, L. Isa, W. C. K. Poon, and R. Besseling, Journal of Rheology **56**, 1005 (2012).
[110] F. Feuillebois, N. Ghalya, A. Sellier, and L. Elasmi, Microparticles in Stokes Flows: Symposium in Honor of Francois Feuillebois' 65th Birthday **392**, 012012 (2012).
[111] A. G. Chryss, S. N. Bhattacharya, and L. Pullum, Rheologica Acta **45**, 124 (2005).
[112] S. M. Qin Xu, Eric Brown, Heinrich M. Jaeger, *ArXiv14047181 Cond-Mat* (2014).
[113] A. Fall, H. de Cagny, D. Bonn, G. Ovarlez, E. Wandersman, J. A. Dijksman, and M. van Hecke, Journal of Rheology **57**, 1237 (2013).
[114] L. Chang, K. Friedrich, A. K. Schlarb, R. Tanner, and L. Ye, Journal of Materials Science **46**, 339 (2011).
[115] S. Torquato and F. H. Stillinger, Journal of Applied Physics **102**, 093511 (2007).
[116] Q. Sun, F. Jin, J. Liu, and G. Zhang, International Journal of Modern Physics B **24**, 5743 (2010).
[117] A. Tordesillas, Q. Lin, J. Zhang, R. P. Behringer, and J. Shi, Journal of the Mechanics and Physics of Solids **59**, 265 (2011).
[118] J. Zhang, R. P. Behringer, T. S. Majmudar, and M. Sperl, in *Powders and Grains 2009*, edited by M. L. S. Nakagawa2009), pp. 527.
[119] M. E. Cates, J. P. Wittmer, J. P. Bouchaud, and P. Claudin, Philosophical Transactions of the Royal Society a-Mathematical Physical and Engineering Sciences **356**, 2535 (1998).
[120] A. Fall and D. Bonn, Soft Matter **8**, 4645 (2012).
[121] A. Tordesillas, Philosophical Magazine **87**, 4987 (2007).
[122] J. R. Melrose and R. C. Ball, Journal of Rheology **48**, 961 (2004).
[123] J. R. Melrose, Faraday Discussions **123**, 355 (2003).
[124] J. R. Melrose and R. C. Ball, Journal of Rheology **48**, 937 (2004).
[125] M. E. Cates, in *Slow Dynamics in Complex Systems*, edited by M. O. I. Tokuyama2004), pp. 33.
[126] M. E. Cates, C. B. Holmes, M. Fuchs, and O. Henrich, *Schematic mode coupling theories for shear thinning, shear thickening, and jamming* 2004), Unifying Concepts in Granular Media and Glasses.
[127] M. P. Ciamarra, M. Nicodemi, and A. Coniglio, Soft Matter **6**, 2871 (2010).
[128] C. S. O'Hern, S. A. Langer, A. J. Liu, and S. R. Nagel, Physical Review Letters **88** (2002).
[129] S. R. Waitukaitis, L. K. Roth, V. Vitelli, and H. M. Jaeger, Epl **102**, 44001 (2013).
[130] S. R. Waitukaitis and H. M. Jaeger, Nature **487**, 205 (2012).
[131] W. Jiang, X. Gong, S. Xuan, W. Jiang, F. Ye, X. Li, and T. Liu, Applied Physics Letters **102**, 101901 (2013).

[132] O. E. Petel, D. L. Frost, A. J. Higgins, and S. Ouellet, Physical Review E **85** (2012).
[133] M. Roche, E. Myftiu, M. C. Johnston, P. Kim, and H. A. Stone, Physical Review Letters **110**, 148304 (2013).
[134] S. von Kann, J. H. Snoeijer, D. Lohse, and D. van der Meer, Physical Review E **84**, 060401 (2011).
[135] F. S. Merkt, R. D. Deegan, D. I. Goldman, E. C. Rericha, and H. L. Swinney, Physical Review Letters **92**, 184501 (2004).
[136] H. Ebata and M. Sano, Physical Review Letters **107**, 088301 (2011).
[137] H. Ebata and M. Sano, Physical Review E **88**, 053007 (2013).
[138] C. Falcon, J. Bruggeman, M. Pasquali, and R. D. Deegan, Epl **98**, 24002 (2012).
[139] R. D. Deegan, Physical Review E **81**, 036319 (2010).
[140] H. Ebata, S. Tatsumi, and M. Sano, Physical Review E **79**, 066308 (2009).
[141] H. Shiba, J. E. Ruppert-Felsot, Y. Takahashi, Y. Murayama, O. Qi, and M. Sano, Physical Review Letters **98**, 044501 (2007).
[142] S. Brand, R. C. Ball, and M. Nicodemi, Physical Review E **83** (2011).
[143] R. Pastore, M. P. Ciamarra, and A. Coniglio, Philosophical Magazine **91**, 2006 (2011).
[144] M. D. Haw, Physical Review Letters **92** (2004).
[145] A. I. Campbell and M. D. Haw, Soft Matter **6**, 4688 (2010).
[146] R. Bureau, S. Brand, R. C. Ball, and M. Nicodemi, Granular Matter **14**, 175 (2012).
[147] S. Brand, M. P. Ciamarra, and M. Nicodemi, Advances in Complex Systems **13**, 339 (2010).
[148] H. A. Barnes, *Handbook of Elementary Rheology* (The University of Wales Institute of Non-Newtonian Fluid Mechanics, 2000).
[149] P. Coussot, *Rheometry of Pastes, Suspensions, and Granular Materials: Applications in Industry and Environment* (Wiley, 2005).
[150] N. Delhaye, A. Poitou, and M. Chaouche, Journal of Non-Newtonian Fluid Mechanics **94**, 67 (2000).
[151] M. Nikkhoo, K. Khodabandehlou, L. Brozovsky, and F. Gadala-Maria, Rheologica Acta **52**, 155 (2013).
[152] S. Mascia and D. I. Wilson, Journal of Rheology **52**, 981 (2008).
[153] S. Mascia and D. I. Wilson, Journal of Rheology **51**, 493 (2007).
[154] D. Cheneler, J. Bowen, M. C. L. Ward, and M. J. Adams, Journal of Micromechanics and Microengineering **21** (2011).
[155] D. Cheneler, J. Bowen, M. C. L. Ward, and M. J. Adams, Microelectronic Engineering **88**, 1726 (2011).
[156] D. Bell, D. M. Binding, and K. Walters, Rheologica Acta **46**, 111 (2006).
[157] D. Cheneler, PhD thesis (unpublished),The University of Birmingham, 2009.
[158] J. A. Glasscock, R. S. Smith, J. Vanajek, and J. G. Winter, Review of Scientific Instruments **74**, 4925 (2003).
[159] H. Esmonde, H. See, and M. V. Swain, Measurement Science & Technology **20** (2009).
[160] B. Debbaut and K. Thomas, Journal of Non-Newtonian Fluid Mechanics **124**, 77 (2004).
[161] J. S. Field, M. V. Swain, and N. PhanThien, Journal of Non-Newtonian Fluid Mechanics **65**, 177 (1996).
[162] R. S. Smith and J. A. Glasscock, Korea-Australia Rheology Journal **16**, 169 (2004).
[163] N. Phanthien and R. I. Tanner, Journal of Fluid Mechanics **129**, 265 (1983).
[164] N. Phanthien, J. Dudek, D. V. Boger, and V. Tirtaatmadja, Journal of Non-Newtonian Fluid Mechanics **18**, 227 (1985).

[165] J. Engmann, C. Servais, and A. S. Burbidge, Journal of Non-Newtonian Fluid Mechanics **132**, 1 (2005).
[166] A. S. Lim, S. L. Lopatnikoy, N. J. Wagner, and J. W. Gillespie, Journal of Non-Newtonian Fluid Mechanics **166**, 680 (2011).
[167] D. Konigsberg, T. M. Nicholson, P. J. Halley, and K. H. Ahn, Rheologica Acta **53**, 103 (2014).
[168] M. M. Denn, *Process Fluid Mechanics* (Prentice Hall, 1980).
[169] *Perry's Chemical Engineers Handbook* (McGraw-Hill, 1999), 7th edn.
[170] L. E. Graham and L. W. Wilcox, *Algae* (Prentice Hall, 2000).
[171] L. Brennan and P. Owende, Renewable & Sustainable Energy Reviews **14**, 557 (2010).
[172] A. L. Stephenson, E. Kazamia, J. S. Dennis, C. J. Howe, S. A. Scott, and A. G. Smith, Energy & Fuels **24**, 4062 (2010).
[173] X. Garcia, S. Rafai, and P. Peyla, Physical Review Letters **110**, 138106 (2013).
[174] D. M. Christiaan van den Hoek, H.M Jahns, *Algae: An Introduction to Phycology* (Cambridge University Press, 1996).
[175] S. O'Malley and M. A. Bees, Bulletin of Mathematical Biology **74**, 232 (2012).
[176] C. R. Williams and M. A. Bees, Journal of Experimental Biology **214**, 2398 (2011).
[177] T. J. Pedley and J. O. Kessler, Annual Review of Fluid Mechanics **24**, 313 (1992).
[178] J. T. Locsei and T. J. Pedley, Bulletin of Mathematical Biology **71**, 1089 (2009).
[179] O. A. Croze, E. E. Ashraf, and M. A. Bees, Physical Biology **7**, 046001 (2010).
[180] M. A. Bees and O. A. Croze, Proceedings of the Royal Society a-Mathematical Physical and Engineering Sciences **466** (2010).
[181] O. A. Croze, G. Sardina, M. Ahmed, M. A. Bees, and L. Brandt, Journal of the Royal Society Interface **10**, 20121041 (2013).
[182] S. Ramaswamy, Annual Review of Condensed Matter Physics, Vol 1 **1**, 323 (2010).
[183] J. E. W. P. Ami Ben-Amotz, D.V. Subba Rao, *The Alga Dunaliella* (CRC Press, 2009).
[184] D. B. Weibel, P. Garstecki, D. Ryan, W. R. Diluzio, M. Mayer, J. E. Seto, and G. M. Whitesides, Proceedings of the National Academy of Sciences of the United States of America **102**, 11963 (2005).
[185] O. A. Croze, R. N. Bearon, and M. A. Bees, *in preparation*.
[186] R. N. Bearon, Journal of Mathematical Biology **66**, 1341 (2013).
[187] W. M. Durham, J. O. Kessler, and R. Stocker, Science **323**, 1067 (2009).
[188] C. P. Royall, W. C. K. Poon, and E. R. Weeks, Soft Matter **9**, 17 (2013).
[189] O.A Croze, *Private communication*.
[190] M. D. Haw, Philosophical Transactions of the Royal Society a-Mathematical Physical and Engineering Sciences **367**, 5167 (2009).
[191] N. C. Crawford, L. B. Popp, K. E. Johns, L. M. Caire, B. N. Peterson, and M. W. Liberatore, Journal of Colloid and Interface Science **396**, 83 (2013).
[192] U. Pick, L. Karni, and M. Avron, Plant Physiology **81**, 92 (1986).
[193] M. A. Hejazi, E. Andrysiewicz, J. Tramper, and R. H. Wijffels, Biotechnology and Bioengineering **84**, 591 (2003).
[194] Marial Kilfoil lab software research tools, http://people.umass.edu/kilfoil/downloads.html.
[196] A. Fall, A. Lemaitre, F. Bertrand, D. Bonn, and G. Ovarlez, Physical Review Letters **105**, 268303 (2010).
[197] P. Hebraud, Rheologica Acta **48**, 845 (2009).
[198] M. E. Cates, R. Adhikari, and K. Stratford, Journal of Physics-Condensed Matter **17**, S2771 (2005).
[199] L.-n. Xu, Journal of Central South University of Technology **15**, 443 (2008).

[200] M. T. Ghannam and M. N. Esmail, Journal of Applied Polymer Science **69**, 1587 (1998).
[201] D. W. Parkins and R. Maymiller, Mechanical Engineering **105**, 93 (1983).
[202] M. Sun, Z. Zhang, X. Chen, W. Wang, K. Meng, and D. C. Sun, Tribology Transactions **51**, 341 (2008).
[203] X. Y. Chen, M. L. Sun, W. Wang, D. C. Sun, Z. M. Zhang, and X. J. Wang, Science in China Series G-Physics Mechanics & Astronomy **47**, 107 (2004).
[204] M. Bees, *Private communication*.
[205] A. Chengala, M. Hondzo, and J. Sheng, Physical Review E **87**, 052704 (2013).
[206] F. Guzman-Lastra and R. Soto, Physical Review E **86**, 037301 (2012).